Continuum Analysis of Multi-modal TEM propagation

by

CHAMLIAN Vatché Simon,
B.Eng., M.Eng.

A thesis submitted to the Faculty of Graduate Studies and
Research in partial fulfillment of the requirements
for the degree of Doctor of Philosophy

Computational Analysis and Design Laboratory

Department of Electrical Engineering
McGill University
Montréal, Québec, Canada
December, 1995

ISBN 0-612-12341-3

Abstract

This thesis develops a field theory of propagating TEM (transverse electric and magnetic) modes for a theoretically infinite number of extremely thin conductors on a flat dielectric substrate. These conductors possess an infinite number of distinct propagation modes which are determined by an operator eigenvalue problem. The modes of the infinitesimal conductor structure are used to approximate to the case of finite numbers of conductors. To compute modal patterns and propagation velocities, Green's functions are calculated in well-convergent series expressions. Furthermore, symbolic algebra packages are used in order to bypass the singular integrals arising in the Green's functions' kernels.

The quasi-TEM analysis yields very good results provided that two basic assumptions are fulfilled. First, the system's transverse dimensions must be small compared to the operating wavelengths. Second, the longitudinal electromagnetic field components must be very small compared to the transverse components.

The theory is illustrated by several structures accompanied by descriptions of their modal functions and velocity distributions. The propagation modes of the structures are shown to be substantially independent of structural details such as the number and placement of individual conductors. On the other hand, the modes are shown to be mainly dependent on the structure cross-sectional shape and size.

Résumé

Cette thèse développe une théorie basée sur les champs électro-magnétiques d'un nombre théoriquement infini de lignes de transmission très minces placées sur un fondement diélectrique plane. Ces lignes de transmission possèdent un nombre infini de modes de propagation distincts qui peuvent être déterminés par un problème de valeur propre exprimé sous forme d'opérateur. Les modes d'une structure composée de conducteurs infinitésimals sont utilisés pour avoir une approximation d'une structure qui contient un nombre déterminé de conducteurs. Afin d'être en mesure de calculer les modes de propagation ainsi que leur vitesse respective, les fonctions de Green sont calculées sous forme de série convergente. Des programmes d'algèbre symbolique sont utililisés afin d'évaluer analytiquement les intégrales singulières qui apparaissent dans les fonctions de Green.

L'analyse quasi-transversale donne de très bons résultats dans les cas où les deux suppositions suivantes sont satisfaites: premièrement, lorsque les dimensions transverses du système sont relativement petites comparées à la longueur d'onde; deuxièmement, lorsque les champs électrique et magnétique ont chacun une composante le long de la direction de propagation négligeable relativement à leur composantes transverses.

La théorie est illustrée par le biais de plusieurs structures pour lesquelles les modes de propagation ainsi que leur vitesse sont décrits. Les modes de propagation des structures sont démontrés étant complètement indépendants du nombre et de l'emplacement des conducteurs mais surtout dépendants de la forme et des dimensions de la structure.

Original Contributions to Knowledge

(a) The present work adopts a field theory approach to examine the fields of a flat structure containing an infinite or finite number of parallel wires.

(b) The problem is solved in **continuum** form by the use of ***operators***. The Telegrapher's equations as well as the wave equations are stated in operator form.

(c) The modal theory is applied to calculate the crosstalk of a multi-line structure. Minimum-crosstalk positions can be located in a structure even if the total number of conductors and their exact placement are unknown.

(d) The division of the power among the various propagation modes is described and exhibited in a ***power distribution diagram***.

(e) The Green's functions of new structures are calculated in well-convergent series expressions.

Acknowledgements

The author would like to thank his thesis supervisor, Dr. P.P. Silvester, for his guidance, encouragement and patience.

The author would also like to thank all his colleagues at the CADlab who kept the working atmosphere pleasant.

The author would like to thank especially his wife Sossé who supported and helped him to correct and edit the present thesis.

TABLE OF CONTENTS

CHAPTER 1
MODAL ANALYSIS OF MULTICONDUCTOR TRANSMISSION LINE STRUCTURES

Wave phenomena in multiconductor transmission lines have been an important engineering topic since the invention of the telegraph. In recent times the subject has been growing in importance since electronic systems are increasing in complexity both in terms of numbers and density of components. Particular attention is being paid to the electromagnetic interference (EMI) and the computation of the propagation characteristics of printed circuits, high-speed interconnects, microstrip lines, with numerous applications in VLSI, ULSI (ultra) and PWB (printed wire boards). The problem of EMI has become so important that the Federal Communications Commission (FCC) in the United States has elaborated rules and regulations in order to control it. As clock frequencies in digital circuits are increasing, practically all digital products today are subject to FCC regulations. Products that are intended to be marketed in other countries are also subject to FCC regulations. Therefore, companies test their product not only to control its electromagnetic emission, but also to control the susceptibility and to ensure the proper operation of the product under EMI.

Since the mid-sixties, with the emergence of digital computing, numerous numerical techniques have been employed to study the EMI. Just to mention a few: finite element, finite difference in time domain (FDTD), integral methods, moment method, spectral method, mode-matching method, conformal mapping, etc. As a consequence, there are numerous empirical charts and tabulated results.

In the early seventies, the electromagnetic compatibility (EMC) design has received a bad name, due to the empirical approach taken to it. That is, only considering it after the design is completed and the problem of incompatibility already exists. Around the mid-seventies, circuit theory has become prominent in analyzing EMC problems with the use of lumped circuit models. The well-known modal analysis approach has gradually been put aside as an alternative approach

in solving the EMC problems.

The circuit approach has been extensively studied through several numerical techniques both in time and frequency domains. Lumped-circuit models have been developed in order to be able to use them in CAD tools such as SPICE. Unfortunately, there are several problems associated with the use of lumped-circuit models. The length of the line must be divided into a number of electrically short sections which are in turn modeled with the lumped circuits. Therefore, adequate prediction usually results in a circuit of exorbitant size. Furthermore, for time domain excitation, the input contains theoretically an infinite number of frequency components (Fourier series). Consequently, the models are valid only for a certain range of frequencies for which the sections are electrically short compared to the wavelength.

The field approach has been less investigated and the existing works, after determining the propagation modes, tend to take a network theory viewpoint in an early stage of the development.

Both approaches have failed to produce a rigorous method for optimizing the design (reducing the EMI or *crosstalk*) due to the *bottom-up* characteristic. Indeed, any new configuration of the interconnections requires the re-computation of the solution from scratch.

The present chapter formulates telegrapher's equations, wave equations and Poynting's vector in continuum form with the use of operators. The beginning focuses on an infinite number of parallel lines, after which a discrete approximation is given for a finite number of lines. The last section examines the behavior of the waves at the boundaries by calculating the scattering coefficients and characteristic impedances.

1.1 INTRODUCTION

A transmission structure is shown in Figure 1.1: a thin, broad group of parallel

conductors separated from a ground plane by a dielectric sheet or substrate. They are assumed infinitely long in the z direction (normal to the paper), infinitesimally thin in the y direction (normal to the dielectric sheet and the ground plane), and of finite width w in the x direction. The group is assumed to be composed of a very large number of substrips or wires, parallel but separated by thin insulating spaces, so that all currents are confined to flow in the longitudinal or z direction. In general, the distribution of electric potential V on such conductors is a function of position x, y, z as well as of time t. Suppose now that $w \ll \lambda$, i.e., that the variation of V is fairly slow in the z direction but may be quite rapid in x. In this case, quasi-TEM propagation is assumed to be taking place.

The structure of Figure 1.1 is a generalization of the classical problem of a multiconductor transmission line which has been treated by a variety of authors. The difficulties encountered in solving a multiconductor transmission structure are of a *mechanical* rather than mathematical nature, in that the large bulk of equations soon discourages the analyst to pursue his or her work with conventional methods. Two approaches have been used to solve this problem: one based on circuit theory, the other on field theory.

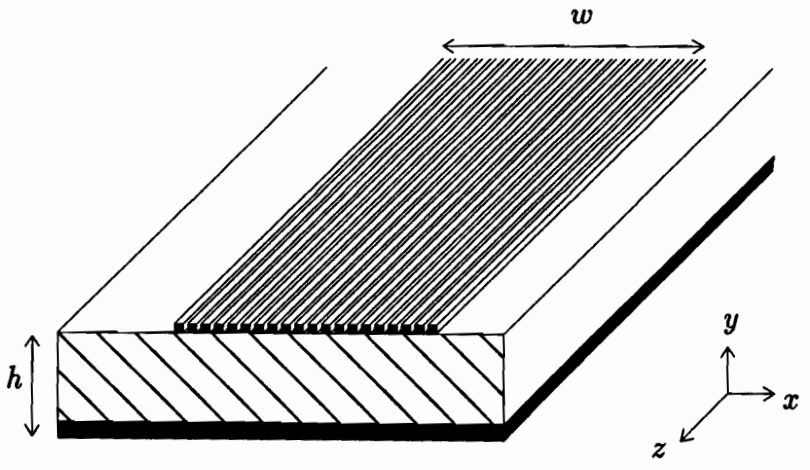

Figure 1.1 Transmission structure composed of many parallel wires or strips, separated by small gaps.

The circuit-theoretic formulation originated with William Thomson (Lord Kelvin) [1884], who stated it in a form very similar to what most authors have used since the middle of the twentieth century — even though *mutual inductance* was hardly a well-developed concept at the time, and the notion of *displacement current* was yet to be appreciated. By the middle of the twentieth century, electrical engineering gradually retreated from field theory to focus on formulations based on Laplace transforms and matrix notations. The use of matrix algebra has been first advanced by Pipes [1937]. Despite an erroneous statement (the product of two symmetric matrices $\mathbf{Z}$ and $\mathbf{Y}$ is interchangeable, i.e., $\mathbf{ZY} = \mathbf{YZ}$) leading to false results, Pipes' work is nevertheless valuable since it shows the simplicity of the solution by the use of matrix methods. In the seventies, the general multi-wire case was treated by Marx [1973] with great care and detail, and key points of the published work (up to about 1965) of this school were summarized in a book by Frankel [1977].

On the field-theoretic side, a somewhat comparable though less detailed overview is given in the monograph by Kuznetzov and Stratonovich [1964]. Recently, a few monographs review the key papers of the past thirty years, including Brandao Faria [1993] who has selected works based on a field approach, and C.R. Paul [1994] who in turn summarizes circuit-approach works.

Multimodal propagation in transmission structures first attracted interest in the area now called *electromagnetic compatibility*: the elimination of crosstalk and the design of transpositions in telegraph lines. Much of the available field-theoretic works throughout the long history of this problem have been directed to applications in the power industry — balancing of polyphase transmission lines and their concurrent use for signaling. The major portion of this work is formulated in the frequency domain. In recent decades there has been a resurgence of interest in time-domain formulations, as electromagnetic compatibility problems in digital circuits have moved into prominence.

The now very extensive literature on modal propagation studies is mainly characterized by what might be termed a "bottom-up" approach: the multiconductor transmission line is seen as a generalization of the two-wire line.

The present work takes the contrary, or "top-down" approach. It first considers the problem of a continuum containing an infinite number of wires, i.e., it presupposes continuous distributions of potentials and longitudinal current densities. The N-conductor problem is then seen as a specialization of the general case. In keeping with the application areas of current interest, it takes a field-theoretic viewpoint and formulates the problem entirely in the time domain.

1.2 TELEGRAPHER'S EQUATIONS

The classical telegrapher's equations of transmission line theory may be stated in an operator form that follows directly from field theory, without reference to a circuit interpretation. As compared to the conventional circuits-based derivation, this approach has the advantage of shedding light on field-theoretic assumptions hidden in the circuit formulation. This allows some assessment of error and may eventually permit still further generalization of the work.

In the TEM formulation of traveling waves, it is assumed that the waves propagate in a direction normal to both **E** and **H**, i.e., that the longitudinal field components E_z and H_z are vanishingly small. This assumption will be accepted here, whereby all the following refers strictly to quasi-TEM waves.

Independently of the TEM assumption, any electric field anywhere must satisfy the potential relationship

$$\mathbf{E} = -\frac{\partial \mathbf{A}}{\partial t} - \nabla V, \tag{1.1}$$

where **A** and V are the usual vector and scalar potentials. These are determined from the distributions of current densities and charges respectively. Taking the magnetic vector potential first, it is given by

$$\mathbf{A}_P = \int G_M(P;Q)\left(\mathbf{J} + \frac{\partial \mathbf{D}}{\partial t}\right) d\Omega_Q, \tag{1.2}$$

where $G_M(P;Q)$ is the Green's function appropriate to magnetic fields. In a TEM

wave, the longitudinal (z-directed) electric field must vanish, therefore for quasi-TEM waves, (1.1) requires that

$$\frac{\partial V}{\partial z} = -\frac{\partial A_z}{\partial t}. \tag{1.3}$$

Substituting (1.2) into (1.3) yields

$$\frac{\partial V}{\partial z} = -\frac{\partial}{\partial t}\int G_M(P;Q)\Big(J_z + \frac{\partial}{\partial t}D_z\Big)d\Omega_Q. \tag{1.4}$$

If all dielectric and magnetic materials are taken to be isotropic with respect to the direction of propagation z, then

$$D_z = \epsilon E_z. \tag{1.5}$$

Therefore, when the longitudinal electric field vanishes, so does D_z. Consequently (1.4) becomes

$$\frac{\partial V}{\partial z} = -\int G_M(P;Q)\frac{\partial J}{\partial t}d\Omega_Q. \tag{1.6}$$

Note that the subscript z on J_z has been dropped, for $\mathbf{J}$ has only a longitudinal component. This amounts to assuming that all conductor material in the transmission structure is anisotropic, with zero conductivity in both transverse directions. Note that this assumption is well approximated by a sheet of many fine parallel wires.

Consider the electric charge distribution $\rho(x,y,z,t)$ next. Without making any simplifying approximations, the scalar potential is

$$V_P = \int G_E(P;Q)\rho_Q d\Omega_Q, \tag{1.7}$$

where $G_E(P;Q)$ is the Green's function appropriate to electric fields. Differentiating with respect to time,

$$\frac{\partial V}{\partial t} = \int G_E(P;Q)\frac{\partial \rho}{\partial t}d\Omega_Q. \tag{1.8}$$

At an arbitrary space point, the law of conservation of electric charge may be written

$$\operatorname{div} \mathbf{J} = -\frac{\partial \rho}{\partial t}. \tag{1.9}$$

Substituting (1.9) into (1.8) yields

$$\frac{\partial V}{\partial t} = -\int G_E(P;Q) \operatorname{div} \mathbf{J}\, d\Omega_Q. \tag{1.10}$$

The TEM assumption restricts the current density vector to be purely longitudinal. Hence

$$\operatorname{div} \mathbf{J} = \frac{\partial J}{\partial z}. \tag{1.11}$$

Substituting (1.11) into (1.10), the time derivative of potential is therefore given by

$$\frac{\partial V}{\partial t} = -\int G_E(P;Q) \frac{\partial J}{\partial z} d\Omega_Q. \tag{1.12}$$

For notational brevity in further discussions, let the linear integral operator $\mathfrak{P}$ be defined by

$$\mathfrak{P}u = \int G_E(P;Q)\, u\, d\Omega_Q \tag{1.13}$$

where the integration domain Ω is the structure cross-section, in a plane orthogonal to the direction of propagation. In analogy with the potential coefficients that arise in the circuit theory of transmission lines, $\mathfrak{P}$ will be referred to as the *potential operator*. In a similar way, let the *inductance operator* $\mathfrak{L}$ be defined by

$$\mathfrak{L}u = \int G_M(P;Q)\, u\, d\Omega_Q \tag{1.14}$$

where $G_M(P;Q)$ is the Green's function appropriate to magnetic fields. The

integrals here must in principle be taken over all space. However, the quantity u represents a source (charge or current) density, which is nonzero only in the conductors themselves. Integration over the conductors themselves is therefore all that is required.

Note that the potential operator $\mathfrak{P}$ is semidefinite. However, it becomes definite once a potential reference has been chosen for V. Choosing $V = 0$ at some fixed point establishes the reference and makes $\mathfrak{P}$ positive definite, hence invertible. Its inverse will be denoted by $\mathfrak{C}$,

$$\mathfrak{C}\mathfrak{P}u = \mathfrak{P}\mathfrak{C}u = u \tag{1.15}$$

and will be referred to as the *capacitance operator*. Using this operator notation, (1.6) and (1.12) can be written as

$$\frac{\partial V}{\partial z} = -\mathfrak{L}\frac{\partial J}{\partial t}, \tag{1.16}$$

$$\frac{\partial J}{\partial z} = -\mathfrak{C}\frac{\partial V}{\partial t}. \tag{1.17}$$

These two equations represent none other than the generalized telegrapher's equations.

The underlying assumptions are: (1) all materials are homogeneous with respect to the direction of propagation, (2) the fields **E** and **H** are essentially transverse, (3) all currents **J** are purely longitudinal. These constitute the *TEM assumption*, which cannot ever hold exactly. If all vectors are strictly transverse, then there can be no longitudinal potential variation and no wave propagation — hence no problem. It is imperative to understand that the TEM assumption implies negligibly small longitudinal vector components compared to their transverse counterparts. A better definition of the TEM assumption is to state that *the Green's functions $G_E(P;Q)$ and $G_M(P;Q)$ shall be taken as two-dimensional*, i.e., as the Green's functions appropriate to the transverse electrostatic and transverse magnetostatic problem respectively. This means that the suppression of longitudinal vector components is made automatic. The

operators $\mathfrak{P}$, $\mathfrak{C}$ and $\mathfrak{L}$ are then transverse operators, thereby operating on the transverse coordinates and on quantities dependent on the transverse coordinates, not z or t.

1.3 WAVE EQUATIONS

The scalar potential V and the longitudinal current density J which satisfy the telegrapher's equations also satisfy a pair of operator wave equations. To arrive at these, the first step is to differentiate the telegrapher's equations given by (1.16) and (1.17) with respect to distance, then interchange time and distance differentiations:

$$\frac{\partial^2 V}{\partial z^2} = -\mathfrak{L}\frac{\partial}{\partial t}\left(\frac{\partial J}{\partial z}\right), \tag{1.18}$$

$$\frac{\partial^2 J}{\partial z^2} = -\mathfrak{C}\frac{\partial}{\partial t}\left(\frac{\partial V}{\partial z}\right). \tag{1.19}$$

Replacing $\partial J/\partial z$ by $-\mathfrak{C}(\partial V/\partial t)$ and $\partial V/\partial z$ by $-\mathfrak{L}(\partial J/\partial t)$, as given by the telegrapher's equations (1.17) and (1.16), then produces

$$\frac{\partial^2 V}{\partial z^2} = \mathfrak{L}\mathfrak{C}\frac{\partial^2 V}{\partial t^2}, \tag{1.20}$$

$$\frac{\partial^2 J}{\partial z^2} = \mathfrak{C}\mathfrak{L}\frac{\partial^2 J}{\partial t^2}. \tag{1.21}$$

These may be regarded as wave equations in operator form. It should be noted that there is no reason to expect the two operators $\mathfrak{L}$ and $\mathfrak{C}$ to commute; they may, but in most cases this is highly unlikely, $\mathfrak{L}\mathfrak{C} \neq \mathfrak{C}\mathfrak{L}$. Although similar in form, the two wave equations are therefore distinct.

An interesting special case arises when the transmission structure contains only a single isotropic dielectric material, and only a single isotropic magnetic material. In that circumstance the Green's functions G_E^0 and G_M^0 are identical except for material constants:

$$\mu G_E^0 = \epsilon G_M^0, \tag{1.22}$$

with the consequence that

$$\mathfrak{Q}\mathfrak{C}u = \mathfrak{C}\mathfrak{Q}u = \mu\epsilon. \tag{1.23}$$

The operator wave equations then become simply the scalar equations

$$\frac{\partial^2 V}{\partial z^2} = \mu\epsilon\frac{\partial^2 V}{\partial t^2}, \tag{1.24}$$

$$\frac{\partial^2 J}{\partial z^2} = \mu\epsilon\frac{\partial^2 J}{\partial t^2}. \tag{1.25}$$

This special case is well known in traveling-wave theory, as are its solutions.

1.4 SOLUTIONS TO THE WAVE EQUATIONS

Suppose that a traveling wave of potential V or longitudinal current density J is a possible solution of the wave equation. That is, suppose

$$J = \psi(x,y)f(ct \mp z) \tag{1.26}$$

where the upper sign denotes propagation in the $+z$ direction. Substituting this trial solution into the wave equation (1.21) becomes

$$\psi(x,y)\frac{\partial^2}{\partial z^2}f(ct \mp z) = \mathfrak{C}\mathfrak{Q}\psi(x,y)\frac{\partial^2}{\partial t^2}f(ct \mp z). \tag{1.27}$$

To simplify (1.27), rewrite and collect terms:

$$\frac{\partial^2 f(ct \mp z)}{\partial(ct \mp z)^2}\psi(x,y) = c^2\frac{\partial^2 f(ct \mp z)}{\partial(ct \mp z)^2}\mathfrak{C}\mathfrak{Q}\psi(x,y). \tag{1.28}$$

Clearly, any twice differentiable function $f(ct \mp z)$ will satisfy the wave equation. A similar development holds for the wave equation that governs the scalar potential. Substituting

$$V = \phi(x,y) f(ct \mp z) \tag{1.29}$$

into (1.20) yields

$$\phi(x,y)\frac{\partial^2 f(ct \mp z)}{\partial(ct \mp z)^2} = c^2 \mathfrak{Q}\mathfrak{C}\phi(x,y)\frac{\partial^2 f(ct \mp z)}{\partial(ct \mp z)^2}. \tag{1.30}$$

Equations (1.28) and (1.30) represent the pair of eigenvalue problems

$$\mathfrak{C}\mathfrak{Q}\psi_k(x,y) = \frac{1}{c_k^2}\psi_k(x,y), \tag{1.31}$$

$$\mathfrak{Q}\mathfrak{C}\phi_k(x,y) = \frac{1}{c_k^2}\phi_k(x,y). \tag{1.32}$$

The solution of this pair will produce two families of eigenfunctions associated with a single set of eigenvalues. The eigenfunctions represent modal distributions of current density and potential respectively; their corresponding eigenvalues represent the (squared inverse) propagation velocities associated with each mode. The two operators $\mathfrak{Q}$ and $\mathfrak{C}$ are positive and self-adjoint, but cannot be assumed to commute, therefore their compositions $\mathfrak{Q}\mathfrak{C}$ and $\mathfrak{C}\mathfrak{Q}$ are adjoints, but not necessarily self-adjoint. Hence their two sets of eigenfunctions $\{\phi_k\}$ and $\{\psi_k\}$ will be different, but will form biorthogonal sets,

$$\int_\Omega \psi_i(x,y)\phi_j(x,y)d\Omega = 0, \quad i \neq j. \tag{1.33}$$

They may of course be scaled so that the integral actually yields the Kronecker delta, i.e., so that the integral has unity value for $i = j$. However, this does not uniquely fix the amplitudes of the eigenfunctions, i.e., making ψ_i smaller can always be compensated by making ϕ_i bigger.

1.5 POYNTING'S VECTOR AND WAVE PROPAGATION

Consider now a cross-section of the transmission structure, $z =$ constant. The Poynting vector, popularly interpreted as a measure of power flow density, is

given by the usual expression

$$\mathbf{N}(x,y) = \mathbf{E} \times \mathbf{H}. \tag{1.34}$$

The longitudinal components of both **E** and **H** are zero, therefore both vectors are purely transverse; hence the power flow is everywhere purely z-directed. The electric field **E** is therefore given by

$$\mathbf{E}(x,y) = -\nabla_{xy} V \tag{1.35}$$

where ∇_{xy} is the (two-dimensional) transverse gradient operator. Thus

$$\mathbf{N}(x,y) = -\nabla_{xy} V \times \mathbf{H} \tag{1.36}$$

which may be converted, using standard vector identities, into

$$\mathbf{N}(x,y) = -\operatorname{curl}(V\mathbf{H}) + V \operatorname{curl} \mathbf{H}. \tag{1.37}$$

But $\operatorname{curl} \mathbf{H} = \mathbf{J} + \partial \mathbf{D}/\partial t$, so

$$\mathbf{N}(x,y) = -\operatorname{curl}(V\mathbf{H}) + V\mathbf{J} + V\frac{\partial \mathbf{D}}{\partial t}. \tag{1.38}$$

This vector is immediately decomposable into longitudinal and transverse components. By the TEM assumption, **H** and **D** are both purely transverse, **J** purely longitudinal. Hence the longitudinal portion of the Poynting vector is

$$N_z(x,y) = V(x,y)J(x,y), \tag{1.39}$$

leaving the transverse part as

$$\mathbf{N}(x,y) - \mathbf{1}_z N_z(x,y) = V\frac{\partial \mathbf{D}}{\partial t} - \operatorname{curl}(V\mathbf{H}). \tag{1.40}$$

Let $\mathbf{dS} = \mathbf{1}_z dS$ represent an area element of the cross-sectional area of the structure. The conventional (Poynting) power flow is then

$$W = \int V(x,y)J(x,y)\,dS\,. \tag{1.41}$$

For the function spaces containing potential and current density functions, the power is a suitable inner product, for it satisfies the usual conditions that an inner product must satisfy. The conventionally abbreviated notation

$$\langle \phi, \psi \rangle = \int \phi(x,y)\psi(x,y)\,dS \tag{1.42}$$

will therefore be used in the following sections.

The relationship of potentials to current densities in a propagating wave needs to be investigated next. Suppose that the lateral current density distribution $J(x,y)$ of a traveling wave is given by only one of the eigenfunctions $\psi_j(x,y)$,

$$J(x,y,z,t) = J_j\psi_j(x,y)\,f(z \mp c_j t). \tag{1.43}$$

The propagation velocity c_j must of course correspond to the eigenfunction ψ_j, for it represents an eigenvalue of the wave problem. On substituting (1.43), the first telegrapher's equation (1.16) becomes

$$\frac{\partial V}{\partial z} = -J_j \frac{\partial}{\partial t} f(z \mp c_j t)\mathfrak{L}\psi_j(x,y), \tag{1.44}$$

for the inductance operator $\mathfrak{L}$ acts only on the transverse coordinates. Simplifying,

$$\frac{\partial V}{\partial z} = \pm c_j J_j f'(z \mp c_j t)\mathfrak{L}\psi_j(x,y). \tag{1.45}$$

Now, the eigenfunctions ϕ_k of the potential wave equation constitute a basis for all possible potential distributions. Consequently the propagating potential that accompanies the current density $J(x,y,z,t)$ may be written as an eigenfunction expansion,

$$V(x,y,z,t) = \sum_k V_k \phi_k(x,y) h_k(z \mp c_k t) \tag{1.46}$$

where the precise nature of the functions $h_k(z \mp c_k t)$ remains to be determined. Differentiating (1.46) with respect to z,

$$\frac{\partial V}{\partial z} = \sum_k V_k \phi_k(x,y) h_k'(z \mp c_k t). \tag{1.47}$$

Combining (by setting $\partial V/\partial z = \partial V/\partial z$) the potential (equation (1.47)) and current density expressions (equation (1.45)) yields

$$\sum_k V_k \phi_k(x,y) h_k'(z \mp c_k t) = \pm c_j J_j f'(z \mp c_j t) \mathfrak{Q} \psi_j(x,y). \tag{1.48}$$

Equality can only be assured if both sides propagate with equal velocity. Consequently,

$$c_k = c_j, \tag{1.49}$$

$$h_k'(z \mp c_k t) = f'(z \mp c_j t). \tag{1.50}$$

Thus (1.48) becomes

$$\sum_k V_k \phi_k(x,y) = \pm c_j J_j \mathfrak{Q} \psi_j(x,y). \tag{1.51}$$

If the eigenvalues are distinct, then $k = j$. In other words, the summation on the left of (1.51) collapses into a sum that contains only as many terms as the degeneracy of the eigenvalue c_j. With eigenvalues distinct, it becomes only a single term,

$$V_j \phi_j(x,y) = \pm c_j J_j \mathfrak{Q} \psi_j(x,y). \tag{1.52}$$

The degenerate case poses no particular problem, so long as the eigenfunctions have been orthogonalized with respect to each other. Taking inner products with ψ_i on both sides of (1.51),

$$\sum_k V_k \langle \psi_i, \phi_k \rangle = \pm c_j J_j \langle \psi_i, \mathfrak{Q} \psi_j \rangle. \tag{1.53}$$

The two sets of eigenfunctions $\{\phi_k\}$ and $\{\psi_k\}$ are biorthogonal with respect to the power inner product. The only term to survive in (1.53) is therefore that for $i = j = k$, and

$$V_k\langle\psi_k, \phi_k\rangle = \pm c_k J_k \langle\psi_k, \mathfrak{Q}\psi_k\rangle. \tag{1.54}$$

In simple words, this argument says: A current density distribution describable by a single eigenfunction ψ_k may propagate in either the $+z$ or $-z$ direction, provided it propagates with velocity c_k, and provided it is accompanied by a potential distribution that propagates with the same velocity and has a spatial distribution describable by ϕ_k. The ratio of amplitudes of the two distributions is given by

$$\frac{V_k}{J_k} = \pm c_k \frac{\langle\psi_k, \mathfrak{Q}\psi_k\rangle}{\langle\psi_k, \phi_k\rangle} \tag{1.55}$$

where the positive sign is taken if propagation takes place in the positive z direction.

A similar development may be carried out beginning with the potential distribution. It begins by assuming a unimodal potential distribution to propagate,

$$V(x, y, z, t) = V_j \phi_j(x, y) f(z \mp c_j t). \tag{1.56}$$

The propagation velocity c_j must again correspond to the eigenfunction ϕ_j. On substituting (1.56) into the second telegrapher's equation (1.17) yields

$$\frac{\partial J}{\partial z} = \pm c_j V_j f'(z \mp c_j t) \mathfrak{C}\phi_j(x, y). \tag{1.57}$$

The propagating current density $J(x, y, z, t)$ that accompanies the potential may be written

$$J(x, y, z, t) = \sum_k J_k \psi_k(x, y) h_k(z \mp c_k t). \tag{1.58}$$

Differentiating (1.58) with respect to z and then combining (by setting

$\partial J/\partial z = \partial J/\partial z$) the potential (equation (1.57)) and current density expressions (equation (1.58)) yields

$$\sum_k J_k \psi_k = \pm c_j V_j \mathfrak{C} \phi_j \tag{1.59}$$

and equality of propagation velocity requires, in the nondegenerate case,

$$c_k = c_j, \tag{1.60}$$

$$h_k'(z \mp c_k t) = f'(z \mp c_j t). \tag{1.61}$$

Hence

$$J_j \psi_j(x,y) = \pm c_j V_j \mathfrak{C} \phi_j(x,y). \tag{1.62}$$

Biorthogonality finally requires that

$$J_k \langle \psi_k, \phi_k \rangle = \pm c_k V_k \langle \phi_k, \mathfrak{C} \phi_k \rangle \tag{1.63}$$

whence

$$\frac{J_k}{V_k} = \pm c_k \frac{\langle \phi_k, \mathfrak{C} \phi_k \rangle}{\langle \psi_k, \phi_k \rangle}. \tag{1.64}$$

Because the ratio of potential coefficient to current density coefficient must clearly be the same whichever way it is calculated, it follows that

$$\frac{J_k V_k}{V_k J_k} = c_k^2 \frac{\langle \psi_k, \mathfrak{L} \psi_k \rangle \langle \phi_k, \mathfrak{C} \phi_k \rangle}{\langle \psi_k, \phi_k \rangle^2} = 1, \tag{1.65}$$

thus,

$$\frac{1}{c_k^2} = \frac{\langle \psi_k, \mathfrak{L} \psi_k \rangle \langle \phi_k, \mathfrak{C} \phi_k \rangle}{\langle \psi_k, \phi_k \rangle^2}. \tag{1.66}$$

Alternatively, substituting (1.66) into (1.55) and simplifying,

$$\frac{V_k}{J_k} = \pm\sqrt{\frac{\langle\psi_k, \mathfrak{L}\psi_k\rangle}{\langle\phi_k, \mathfrak{C}\phi_k\rangle}}. \tag{1.67}$$

The ration V_k/J_k can be viewed as a modal characteristic impedance. However, a note of caution is in order. The current and potential eigenfunctions (ψ_k and ϕ_k) are scaled arbitrarily. Therefore, absolute impedance values have no objective meaning although relative values may. Brews [1987] has discussed this point in extensive detail. Of course, (1.67) remains valid regardless of how the eigenfunctions are normalized, even if the numerical *value* depends on the normalization. The velocity c_k^2 is normalization-independent so long as the functions remain biorthonormal. In other words, to keep the power the same, if ψ_k is made to have an amplitude larger by some factor K, then ϕ_k must be smaller by the same factor; therefore c_k^2 remains invariant. The ratio V_k/J_k, on the other hand, grows by K^2 under such a rescaling.

Note that in the nondegenerate case, substituting (1.67) into (1.52) and (1.62) gives the relation between the current and voltage distributions:

$$\phi_j(x,y) = \frac{c_j}{z_j}\mathfrak{L}\psi_j(x,y), \tag{1.68}$$

$$\psi_j(x,y) = c_j z_j \mathfrak{C}\phi_j(x,y) \tag{1.69}$$

where

$$z_k = \sqrt{\frac{\langle\psi_k, \mathfrak{L}\psi_k\rangle}{\langle\phi_k, \mathfrak{C}\phi_k\rangle}}. \tag{1.70}$$

It should be noted that the eigenfunctions (ψ_k and ϕ_k) are dimensionless. On the other hand, the operator $\mathfrak{L}$ has units of *henries/meter* because it contains the permeability μ. Similarly, the operator $\mathfrak{C}$ has units of *farads/meter*. Therefore, z_k (the ratio V_k/J_k) has units of *ohms*.

1.6 DISCRETE APPROXIMATION

To find the modes of a transmission structure a numerical approximation

technique is required. The problem is to determine the sets of eigenfunctions that satisfy the pair of eigenvalue problems

$$\mathfrak{C}\mathfrak{Q}\,\psi_k(x,y) = \frac{1}{c_k^2}\psi_k(x,y), \tag{1.71}$$

$$\mathfrak{Q}\mathfrak{C}\,\phi_k(x,y) = \frac{1}{c_k^2}\phi_k(x,y) \tag{1.72}$$

where

$$\mathfrak{Q}u(x) = \int G_M(x;\xi)\,u(\xi)\,d\xi \tag{1.73}$$

and

$$\mathfrak{C}^{-1}u(x) = \int G_E(x;\xi)\,u(\xi)\,d\xi\,. \tag{1.74}$$

It will be assumed here that all conductors are very thin, so the density functions $u(\xi)$ may be regarded as sheet densities, and integration is required only in a single coordinate lying in the plane of the dielectric substrate, say x. To simplify analysis, all coordinate values will be expressed in normalized coordinates, defined by

$$\overline{x} = \frac{x}{2h} \tag{1.75}$$

and

$$\overline{\xi} = \frac{\xi}{2h}, \tag{1.76}$$

the normalization being taken with respect to double the substrate thickness h. To proceed, select a convenient basis $\{p_i(\overline{x}) \mid i = 1,...\infty\}$ for the ψ_k or ϕ_k. For example, some convenient set of linearly independent polynomials or orthogonal polynomials may be a good choice. That is to say,

$$\psi_k(\overline{x}) = \sum_m a_{km}p_m(\overline{x}), \tag{1.77}$$

$$\phi_k(\overline{x}) = \sum_m b_{km} p_m(\overline{x}). \tag{1.78}$$

Then

$$\mathfrak{Q}\psi_k(\overline{x}) = 2h \sum_m a_{km} \int G_M(\overline{x};\overline{\xi})\, p_m(\overline{\xi})\, d\overline{\xi} \tag{1.79}$$

and

$$\mathfrak{C}^{-1}\psi_k(\overline{x}) = 2h \sum_m a_{km} \int G_E(\overline{x};\overline{\xi})\, p_m(\overline{\xi})\, d\overline{\xi}. \tag{1.80}$$

The eigenvalue problem therefore takes the form

$$\mathfrak{C}^{-1}\psi_k(\overline{x}) = c_k^2 \mathfrak{Q}\psi_k(\overline{x}) \tag{1.81}$$

or

$$\sum_m a_{km} \int G_E(\overline{x};\overline{\xi})\, p_m(\overline{\xi})\, d\overline{\xi} = c_k^2 \sum_m a_{km} \int G_M(\overline{x};\overline{\xi})\, p_m(\overline{\xi})\, d\overline{\xi}. \tag{1.82}$$

If this is to hold true for all k and m, then inner products taken with any $p_n(\overline{x})$ must also yield equality. Thus

$$\sum_m a_{km} \int\int G_E(\overline{x};\overline{\xi})\, p_m(\overline{\xi}) p_n(\overline{x})\, d\overline{\xi} d\overline{x} = c_k^2 \sum_m a_{km} \int\int G_M(\overline{x};\overline{\xi})\, p_m(\overline{\xi}) p_n(\overline{x})\, d\overline{\xi} d\overline{x} \tag{1.83}$$

or, regrouping terms,

$$\sum_m \left\{ \int\int G_E(\overline{x};\overline{\xi})\, p_m(\overline{\xi}) p_n(\overline{x})\, d\overline{\xi} d\overline{x} \right\} a_{km} =$$

$$c_k^2 \sum_m \left\{ \int\int G_M(\overline{x};\overline{\xi})\, p_m(\overline{\xi}) p_n(\overline{x})\, d\overline{\xi} d\overline{x} \right\} a_{km}. \tag{1.84}$$

The latter is immediately recognized as a conventional matrix eigenvalue problem,

$$\mathbf{C}^{-1}\mathbf{a}_k = c_k^2 \mathbf{L}\mathbf{a}_k, \tag{1.85}$$

where $\mathbf{C} = \mathbf{P}^{-1}$ and the matrices are given by

$$P_{mn} = \int\int G_E(\bar{x};\bar{\xi})\, p_m(\bar{\xi}) p_n(\bar{x})\, d\bar{\xi} d\bar{x} \tag{1.86}$$

$$L_{mn} = \int\int G_M(\bar{x};\bar{\xi})\, p_m(\bar{\xi}) p_n(\bar{x})\, d\bar{\xi} d\bar{x}. \tag{1.87}$$

The two Green's functions are known, and integration techniques for evaluating the integrals are available. As stated here, this is of course an infinite eigenvalue problem; to compute actual values it will be necessary to truncate it at some convenient point, i.e., to use a finite basis set $\{p_i(\bar{x}) \mid i = 1,...,N\}$ instead of $\{p_i(\bar{x}) \mid i = 1,...,\infty\}$.

1.7 TEM "STATIC" SOLUTIONS

The details of Green's functions can be checked and the correctness of matrix formulation verified by solving the static problem of a TEM line at very low frequency, i.e., by computing the static per-unit-length capacitance and inductance of a line. This is possible to calculate when it is assumed that *all* conductors are connected to the same source, i.e., when the structure is electrically equivalent to a flat strip. In the absence of any time variation the resistive anisotropy assumed in this analysis has no effect, so the results should exactly reproduce the propagation velocities and characteristic impedances given by Bryant and Weiss [1968] or Silvester [1968].

To develop the capacitance per unit length of a single line, return to the defining equation for the potential operator, writing it in the explicit form

$$V(\bar{x}) = 2h \int G_E(\bar{x};\bar{\xi})\, \rho(\bar{\xi})\, d\bar{\xi}, \tag{1.88}$$

where $G_E(\bar{x};\bar{\xi})$ is the Green's function appropriate to electric fields, $\bar{x}$ and $\bar{\xi}$ are coordinate values normalized to $2h$; the multiplier $2h$ arises from the normalization, since $d\xi = 2h d\bar{\xi}$. The solution procedure follows that in the early papers. Suppose the charge density ρ is given the finite representation

$$\rho(\bar{\xi}) = \sum_m \rho_m p_m(\bar{\xi}). \tag{1.89}$$

Then

$$V(\bar{x}) = 2h \sum_m \rho_m \int G_E(\bar{x};\bar{\xi})\, p_m(\bar{\xi})\, d\bar{\xi}. \tag{1.90}$$

To obtain a projective solution, form inner product projections with the same basis functions on both sides:

$$2h \int V(\bar{x}) p_n(\bar{x})\, d\bar{x} = \sum_m \rho_m 4h^2 \int\int G_E(\bar{x};\bar{\xi})\, p_m(\bar{\xi}) p_n(\bar{x})\, d\bar{x}\, d\bar{\xi}. \tag{1.91}$$

The integral on the right is immediately recognized as

$$P_{mn} = \int\int G_E(\bar{x};\bar{\xi})\, p_m(\bar{\xi}) p_n(\bar{x})\, d\bar{\xi} d\bar{x}. \tag{1.92}$$

On the left, some simplification results from the fact that $V(\bar{x}) = V_0$ is a constant, so that

$$2h \int V(\bar{x}) p_n(\bar{x})\, d\bar{x} = 2hV_0 \int p_n(\bar{x})\, d\bar{x} = 2hV_0 \overline{p_n} \tag{1.93}$$

where

$$\overline{p_n} = \int p_n(\bar{x})\, d\bar{x}. \tag{1.94}$$

Thus (1.91) takes the form

$$2hV_0 \overline{p_n} = 4h^2 \sum_m P_{mn} \rho_m \tag{1.95}$$

or in matrix form,

$$\rho = \frac{V_0}{2h} \mathbf{P}^{-1} \overline{\mathbf{p}} = \frac{V_0}{2h} \mathbf{C} \overline{\mathbf{p}}. \tag{1.96}$$

The charge per unit length on a single line is obtained by integrating the charge density distribution across the breadth of the strip,

$$\begin{aligned} q &= \int \rho(\overline{x})\, dx = 2h \int \rho(\overline{x})\, d\overline{x} \\ &= 2h \sum_m \rho_m \int p_m(\overline{x})\, d\overline{x} = 2h \sum_m \rho_m \overline{p_m} \end{aligned} \tag{1.97}$$

where the abbreviation

$$\overline{p_m} = \int p_m(\overline{x})\, d\overline{x} \tag{1.98}$$

is understood. Substituting the explicit expression for $\boldsymbol{\rho}$,

$$q = V_0 \sum_m \sum_n \overline{p_n} C_{mn} \overline{p_m}. \tag{1.99}$$

The line capacitance per unit length C is obtainable as the quotient of the charge q and the constant potential value $V(\overline{x}) = V_0$, i.e., as $C = q/V_0$:

$$C = \frac{q}{V_0} = \sum_m \sum_n \overline{p_n} C_{mn} \overline{p_m}. \tag{1.100}$$

The inductance per unit length may be found in exactly the same way. However, it is probably easier to proceed by the equivalent route of finding the capacitance per unit length C_0 for a similar line with $\epsilon_r = 1$,

$$C_0 = \sum_m \sum_n \overline{p_n} C_{(0)mn} \overline{p_m} \tag{1.101}$$

where

$$C_{(0)mn} = \left[C_{mn}\right]_{\epsilon_r = 1}. \tag{1.102}$$

The propagation velocity v_0 is always related to the per-unit-length inductances and capacitances by $v_0^2 LC = 1$. Compare now two similar lines, one with relative substrate permittivity ϵ_r, the other with unit relative permittivity. The latter will have a propagation velocity of c, the former v_0. So long as the substrates are always nonmagnetic, L has the same value in both cases. Hence

$$v_0^2 LC = c^2 LC_0 = 1. \tag{1.103}$$

It follows immediately that

$$\frac{v_0}{c} = \sqrt{\frac{C_0}{C}}. \tag{1.104}$$

The characteristic impedance is obtainable in a similar fashion. In general, for a true TEM transmission line, the characteristic impedance Z is

$$Z = \sqrt{\frac{L}{C}}. \tag{1.105}$$

But the line with $\epsilon_r = 1$ has $c^2 L C_0 = 1$, so L can be substituted directly to yield

$$Z = \frac{1}{c\sqrt{C C_0}}. \tag{1.106}$$

For the line with $\epsilon_r = 1$, this reduces to

$$Z_0 = \frac{1}{cC_0}. \tag{1.107}$$

For other lines, comparison yields

$$\frac{Z}{Z_0} = \sqrt{\frac{C_0}{C}} = \frac{v_0}{c}. \tag{1.108}$$

These relations should permit direct checking of both programs and theoretical analysis against already published work.

1.8 SCATTERING COEFFICIENTS AND CHARACTERISTIC IMPEDANCES

Notions of reflection coefficients and wave or characteristic impedances are firmly ensconced in the lore of transmission structures so the question naturally arises whether a structure of infinitely many conductors possesses such things as scattering matrices or a characteristic impedance. If it does, it is naturally of interest to discover how to calculate these quantities.

Consider a semi-infinite structure as depicted in Figure 1.1 which starts at $z = 0$ and continues in the positive z direction until $z = L$. In discrete approximation, an impedance matrix of order M is required to describe an M-conductor system. For single conductors, it has been conventional to give curves or tables of impedances. This manner of description is rather difficult, though still possible, for multiconductors since it amounts to a large amount of data even for a moderate number M. Here, a brief description applied to the formulation of this work will be given in the conventional matrix notation when the basis functions are considered piecewise constant (order 0 finite elements). Once again, it will be assumed that all conductors are very thin, so the density variations in the y direction may be neglected and the modeling in the x direction is sufficient.

In matrix notation, a wave traveling in the $+z$ direction can be characterized at any point in time and space by

$$\boldsymbol{v}(x, z, t) = \mathbf{M}_v \mathbf{v} \tag{1.109}$$

where the matrix $\mathbf{M}_v$ has its columns formed by the potential eigenfunctions ($\mathbf{M}_v = [\phi_1(x) \ \ldots \ \phi_n(x)]$) and the entries of the column vector $\mathbf{v}$ are the unknown coefficients V_k. Similarly, the current can be characterized at any point in time and space by

$$\boldsymbol{i}(x, z, t) = \mathbf{M}_i \mathbf{j} \tag{1.110}$$

where the matrix $\mathbf{M}_i$ has its columns formed by the current eigenfunctions ($\mathbf{M}_i = [\psi_1(x) \ \ldots \ \psi_n(x)]$) and the entries of the column vector $\mathbf{j}$ are the unknown coefficients J_k. Biorthogonality of the eigenfunctions requires the following relation for the two matrices, for which the columns are formed by the potential and current eigenfunctions:

$$\mathbf{M}_v^{-1} = \mathbf{M}_i^{\mathrm{T}}, \tag{1.111}$$

and

$$\mathbf{M}_i^{-1} = \mathbf{M}_v^{\mathrm{T}}. \tag{1.112}$$

In section 1.5, the relationship between the voltage and current coefficient have been found to be

$$\frac{V_k}{J_k} = \pm\sqrt{\frac{\langle\psi_k, \mathfrak{L}\psi_k\rangle}{\langle\phi_k, \mathfrak{C}\phi_k\rangle}}, \tag{1.113}$$

where the + sign indicates a wave traveling in the positive z direction and the − sign indicates a wave traveling in the negative z direction. For brevity, let

$$z_k = \sqrt{\frac{\langle\psi_k, \mathfrak{L}\psi_k\rangle}{\langle\phi_k, \mathfrak{C}\phi_k\rangle}}. \tag{1.114}$$

as in section 1.5. Therefore, in vector notation, the voltage and current coefficients are related by

$$\mathbf{v} = \mathrm{diag}(z_k)\mathbf{j} \tag{1.115}$$

where $\mathrm{diag}(z_k)$ is a diagonal matrix. Upon substitution of (1.115) into (1.109) yields

$$\boldsymbol{v}(x,z,t) = \mathbf{M}_v \mathrm{diag}(z_k)\mathbf{j}. \tag{1.116}$$

The current coefficients are implied by (1.110) as

$$\mathbf{j} = \mathbf{M}_i^{-1}\boldsymbol{i}(x,z,t). \tag{1.117}$$

Substituting (1.117) into (1.116) yields

$$\boldsymbol{v}(x,z,t) = \mathbf{M}_v \mathrm{diag}(z_k)\,\mathbf{M}_i^{-1}\boldsymbol{i}(x,z,t), \tag{1.118}$$

or,

$$\boldsymbol{v}(x,z,t) = Z_0\boldsymbol{i}(x,z,t) \tag{1.119}$$

where,

$$\boldsymbol{Z_0} = \mathbf{M_v}\,\mathrm{diag}(z_k)\,\mathbf{M_i^{-1}} = \mathbf{M_v}\,\mathrm{diag}(z_k)\,\mathbf{M_v^T}. \tag{1.120}$$

The matrix $\boldsymbol{Z_0}$ given by (1.120) can be viewed as the characteristic impedance matrix. The latter is formed by multiplying an orthogonal matrix times a diagonal matrix times the transpose of the orthogonal matrix. Therefore, $\boldsymbol{Z_0}$ can always be inverted unless z_k is zero for a given k. But z_k will be equal to zero if and only if $\psi_k(x)$ is zero which is impossible. Therefore, $\boldsymbol{Z_0}$ is always invertible.

The characteristic admittance matrix can be easily obtained by

$$\boldsymbol{Y_0} = \boldsymbol{Z_o^{-1}} = \mathbf{M_i}\,\mathrm{diag}(\tfrac{1}{z_k})\mathbf{M_i^T}. \tag{1.121}$$

Once the characteristic matrices are calculated, it is a simple matter (procedures are similar to those in the early papers) to derive the matrix equivalents of the transmission and reflection coefficients. The transmission matrix is given by

$$\tau = 2\boldsymbol{Z_L}(\boldsymbol{Z_L} + \boldsymbol{Z_0})^{-1} \tag{1.122}$$

where $\boldsymbol{Z_L}$ is the load impedance matrix. The reflection matrix is given by

$$\Gamma = \tau - \boldsymbol{U} = (\boldsymbol{Z_L} - \boldsymbol{Z_0})(\boldsymbol{Z_L} + \boldsymbol{Z_0})^{-1} \tag{1.123}$$

where $\boldsymbol{U}$ is the identity matrix.

Therefore, in order to eliminate all reflections, a resistive (since $\boldsymbol{Z_0}$ is real) network is required at the load ($\boldsymbol{Z_L}$) equal to the characteristic impedance matrix. It is yet to be proven if such a resistive network is physically realizable in order to eliminate all possible reflection. The book by Weinberg [1962] has an extensive study on the possibility for the realization of such a network. In summary, the book states that:

1) The dominance condition (dominant diagonal entries[1]) is sufficient (but not necessary) for the realization of a $n \times n$ real matrix as a short-circuit admittance matrix of n-port network composed entirely of resistances. The network in general contains $2n$ nodes.

The dominance condition is sufficient (but not necessary) for the realization as on open-circuit impedance matrix for the case $n \leq 3$. At the present time no known procedure exists for realizing a dominant matrix as an open-circuit impedance matrix when $n \geq 4$.

2) A necessary condition (but not sufficient) for realizability of a $n \times n$ real matrix as a short-circuit admittance matrix or an open-circuit impedance matrix of an n-port network composed entirely of resistances is that the matrix should be a *paramount*[2] matrix. When the order is not greater than 3, the condition is both necessary and sufficient.

3) Special case: A $n \times n$ real matrix is realizable as a short-circuit conductance matrix of a n-port resistive network containing only $n+1$ terminals, one of which is a ground terminal for all the ports, if and only if the matrix is dominant[3] and each of the off-diagonal terms nonpositive. Furthermore, the $(n+1)$ terminal network may be synthesized to have only $n+1$ nodes (very easy to realize).
If this restriction is not specified (in the presence of a dominant admittance matrix, irrespective of the distribution of the signs in the off-diagonal or mutual terms), then the first case (network with $2n$

[1]Symbolically, a dominant matrix of order n is defined by

$$a_{ii} \geq \sum_{\substack{j=1 \\ j \neq i}}^{n} |a_{ij}| \quad i = 1, 2, \ldots, n \, .$$

[2]When the *paramount* matrix arises in the topological analysis and synthesis of networks (matrices with integer elements: $1, -1$ and 0) it is also designated as a *unimodular* matrix.

[3]If a matrix is dominant, it is also paramount. However, the converse is not true.

terminals and $2n$ nodes where a common ground no longer exists) should be reconsidered.

Marx [1973] has addressed this problem and states that the admittance matrix $\boldsymbol{Y_0}$ must be real, symmetric, dominant (therefore positive definite) and have positive diagonal entries and negative off-diagonal entries. This affirmation actually corresponds to the special case mentioned above. Marx [1973] has also proven that $\boldsymbol{Y_0}$ is always realizable in two special cases, namely, lines with homogeneous dielectrics and three conductor lines (two conductors and a ground plane). Marx has proven that with homogeneous dielectrics,

$$\boldsymbol{Y_0} = v_0 \mathbf{C} \tag{1.124}$$

where $\mathbf{C}$ is the capacitance matrix which is symmetric positive definite with dominant diagonal entries and v_o is equal to $1/\sqrt{\mu\epsilon}$.

The strong criterion (the special case mentioned above) in the physical realization of the termination network does not need to hold. It is always possible to realize a resistive network with the weak sufficient condition, i.e. in the presence of a dominant admittance matrix, irrespective of the distribution of the signs in the off-diagonal or mutual terms. In the present work, it is yet to be proven if the admittance matrix ($\boldsymbol{Y_0} = \mathbf{M_i}\text{diag}(\frac{1}{z_k})\mathbf{M_i^T}$) has dominant diagonal entries. Note that the entries of the matrix $\boldsymbol{Y_0}$ are independent of the scaling of the eigenfunctions though very much dependent on the structure under investigation (the Green's functions). Indeed, as mentioned in section 1.5, the characteristic impedance z_k can be rescaled to any desired value since absolute impedance values have no objective meaning, contrary to relative values. Therefore, rescaling the columns of the matrix $\mathbf{M_i}$ by a factor K results in having z_k multiplied by K^2 under such a rescaling. Therefore, the factor K will cancel out in the evaluation of the entries of the matrix.

This matrix notation has a strong reference to a circuit interpretation and is restricted to piecewise constant basis functions whereas this work is based on field theory. Therefore, in the following pages the behavior of the waves at the

boundaries will be analyzed in continuum form. In fact, the circuit theory does not explicitly make clear the behavior of the modes at the boundaries. On the other hand, the field approach is capable of explicitly describing the behavior of the fields on the boundaries. Each mode traveling at a different velocity in the $+z$ direction reaches the termination of the line and is scattered in an infinite number of modes which travel in the $-z$ direction. Therefore, at the end of the line ($z = L$), the voltage and current functions are the sum of the forward and backward traveling waves:

$$v(L,x,t) = v^{+}(L,x,t) \; + v^{-}(L,x,t), \tag{1.125}$$

$$i(L,x,t) \; = i^{+}(L,x,t) \; + i^{-}(L,x,t) \tag{1.126}$$

where v^{+}, i^{+} are the waves traveling in the forward (positive z) direction and v^{-}, i^{-} the waves traveling in the backward (negative z) direction. The coefficients of the forward and backward traveling waves can be expressed as

$$\frac{V_k^{+}}{J_k^{+}} = +z_k \tag{1.127}$$

and

$$\frac{V_k^{-}}{J_k^{-}} = -z_k \tag{1.128}$$

where z_k is given by (1.114).

Let a resistive termination $R(x)$ be a function in continuum form such that

$$R(x) \geq 0, \forall x \in [-w/2; w/2] \tag{1.129}$$

where w is the width of the channel where the group of numerous parallel conductors are placed, as depicted in Figure 1.1. The function $R(x)$ gives the resistance (a real number) at any position x_i between the conductor and the ground plane or any other reference point in the absence of a ground plane. Since the function $R(x)$ gives the resistance at any position, therefore it can have values

equal to 0 (short circuit) or infinity (open circuit) at some positions x_i. At the end of the line ($z = L$), the voltage and current functions are related throughout this resistive function,

$$\frac{v(L,x,t)}{i(L,x,t)} = R(x). \tag{1.130}$$

Note that the resistive function is somewhat different from the load impedance matrix used with the circuit approach. Indeed, with the latter approach, the characteristic impedance (or admittance) matrix and the load matrix represent the mutual resistances between the conductors. With the field approach, the resistive function, at any position x_i, represents the self resistance of the terminating conductor. Therefore, the formulation with this resistive function is restricted to a particular case rather than a general formulation.

Without loss of generality, unimodal propagation can be considered since each mode has a different velocity. In other words, each mode, independent of all the others, arrives at the end of the line and is scattered to travel in the backward direction. Therefore, starting with (1.125), the problem can be stated as

$$v(L,x,t) = V_k^+ \phi_k(x) + \sum_j V_{kj}^- \phi_j(x), \tag{1.131}$$

where $V_k^+ \phi_k(x)$ is one of the modes, along with its coefficient, reaching the end of line. The scattered modes traveling backward have coefficients V_{kj}^- where the subscript k indicates coefficients of backward traveling modes associated to the incident mode k. Indeed, each incident mode might have a different set of backward coefficients. In detail, (1.131) can be written as

$$\sum_i V_i \phi_j(x) = V_k^+ \phi_k(x) + \sum_j V_{kj}^- \phi_j(x). \tag{1.132}$$

Since $v(L,x,t) = i(L,x,t)\,R(x)$, (1.132) becomes

$$R(x) \sum_i J_i \psi_i(x) = V_k^+ \phi_k(x) + \sum_j V_{kj}^- \phi_j(x). \tag{1.133}$$

Taking the inner product with $\phi_k(x)$ yields

$$J_k\langle R(x)\psi_k, \phi_k\rangle = V_k^{+}\langle \phi_k, \phi_k\rangle + V_{kk}^{-}\langle \phi_k, \phi_k\rangle. \tag{1.134}$$

Now, for simplicity the double subscript kk can be dropped to a single k. If the eigenfunctions are scaled to be orthonormal, then $\langle \phi_k, \phi_k\rangle = 1$. Thus,

$$J_k\langle R(x)\psi_k, \phi_k\rangle = V_k^{+} + V_k^{-} \tag{1.135}$$

A similar development may be carried out beginning with the current distribution at the end of the line (equation (1.126)):

$$i(L,x,t) = i^{+}(L,x,t) + i^{-}(L,x,t). \tag{1.136}$$

Once again, without loss of generality, unimodal propagation can be considered. Therefore (1.136) can be expressed as

$$\sum_i J_i\psi_i(x) = J_k^{+}\psi_k(x) + \sum_j J_{kj}^{-}\psi_j(x). \tag{1.137}$$

Since $v(L,x,t) = i(L,x,t)\,R(x)$, (1.137) can be written as

$$\frac{1}{R(x)}\sum_i V_i\phi_i(x) = J_k^{+}\psi_k(x) + \sum_j J_{kj}^{-}\psi_j(x). \tag{1.138}$$

Taking the inner product with $\psi_k(x)$,

$$V_k\langle \frac{\phi_k}{R(x)}, \psi_k\rangle = J_k^{+}\langle \psi_k, \psi_k\rangle + J_k^{-}\langle \psi_k, \psi_k\rangle, \tag{1.139}$$

where the double subscript kk has been dropped to a single k. Once again, when the eigenfunctions are scaled to be orthonormal, then $\langle \psi_k, \psi_k\rangle = 1$. Thus,

$$V_k\langle \frac{\phi_k}{R(x)}, \psi_k\rangle = J_k^{+} + J_k^{-}. \tag{1.140}$$

Let Γ_k be the reflection coefficient associated with the incident mode k. Therefore,

$$\frac{V_k^-}{V_k^+} = +\Gamma_k \quad \text{and} \quad \frac{J_k^-}{J_k^+} = -\Gamma_k. \tag{1.141}$$

Equations (1.135) and (1.140) can now be rewritten as

$$J_k\langle R(x)\psi_k, \phi_k\rangle = V_k^+ + \Gamma_k V_k^+ \tag{1.142}$$

and

$$V_k\langle \frac{\phi_k}{R(x)}, \psi_k\rangle = J_k^+ - \Gamma_k J_k^+. \tag{1.143}$$

Factorizing (1.143) and substituting V_k^+ by $z_k J_k^+$ in (1.142) yields

$$J_k\langle R(x)\psi_k, \phi_k\rangle = z_k J_k^+ (1+\Gamma_k), \tag{1.144}$$

$$V_k\langle \frac{\phi_k}{R(x)}, \psi_k\rangle = J_k^+ (1-\Gamma_k). \tag{1.145}$$

Dividing (1.144) by (1.145) yields

$$\frac{J_k\langle R(x)\psi_k, \phi_k\rangle}{V_k\langle \frac{\phi_k}{R(x)}, \psi_k\rangle} = z_k \frac{1+\Gamma_k}{1-\Gamma_k}. \tag{1.146}$$

Therefore,

$$\Gamma_k = \frac{\langle R(x)\psi_k, \phi_k\rangle J_k - \langle \phi_k/R(x), \psi_k\rangle V_k z_k}{\langle \phi_k/R(x), \psi_k\rangle V_k z_k + \langle R(x)\psi_k, \phi_k\rangle J_k}. \tag{1.147}$$

In order to eliminate all reflections it is necessary to find a function $R(x)$ so that the numerator of (1.147) is equal to zero. Thus,

$$\langle R(x)\psi_k, \phi_k\rangle J_k = \langle \phi_k/R(x), \psi_k\rangle V_k z_k \tag{1.148}$$

or

$$J_k \int R(x)\psi_k(x)\phi_k(x)\,dx = z_k V_k \int \frac{1}{R(x)}\psi_k(x)\phi_k(x)\,dx \qquad \forall k. \tag{1.149}$$

It is preferable to eliminate the coefficients of the total voltage and current (V_k/J_k) from (1.149). In order to do so, take once again the voltage and current functions as the sum of the forward and backward traveling waves at the end of the line:

$$v(L,x,t) = v^+(L,x,t) \ + v^-(L,x,t), \tag{1.150}$$

$$i(L,x,t) \ = i^+(L,x,t) \ + i^-(L,x,t). \tag{1.151}$$

Without loss of generality, the eigenfunctions can be scaled to be biorthonormal. Therefore, taking the inner product either with $\phi_k(x)$ or $\psi_k(x)$ in (1.150) and (1.151) will give the relation between the coefficients:

$$V_k \ = V_k^+ \ + V_k^- = V_k^+ \ (1+\Gamma_k), \tag{1.152}$$

$$J_k \ = J_k^+ \ + J_k^- = J_k^+ \ (1-\Gamma_k). \tag{1.153}$$

Dividing (1.152) by (1.153) yields

$$\frac{V_k}{J_k} = z_k \frac{1+\Gamma_k}{1-\Gamma_k}. \tag{1.154}$$

Substituting (1.154) into (1.146) will result in

$$\frac{\langle R(x)\psi_k, \phi_k\rangle}{\langle \frac{\phi_k}{R(x)}, \psi_k\rangle} = \left(z_k \frac{1+\Gamma_k}{1-\Gamma_k} \right)^2. \tag{1.155}$$

The reflection coefficient has now two different solutions:

$$\Gamma_k = \frac{\sqrt{\langle R(x)\psi_k, \phi_k\rangle} - \sqrt{\langle \phi_k/R(x), \psi_k\rangle}\, z_k}{\sqrt{\langle R(x)\psi_k, \phi_k\rangle} + \sqrt{\langle \phi_k/R(x), \psi_k\rangle}\, z_k}, \tag{1.156}$$

and

$$\Gamma_k = \frac{\sqrt{\langle R(x)\psi_k, \phi_k\rangle} + \sqrt{\langle \phi_k/R(x), \psi_k\rangle}\, z_k}{\sqrt{\langle R(x)\psi_k, \phi_k\rangle} - \sqrt{\langle \phi_k/R(x), \psi_k\rangle}\, z_k}. \tag{1.157}$$

The first solution of Γ_k is practically the same as the solution given by (1.149) where V_k/J_k is considered to be equal to $+z_k$. Since z_k is a positive scalar given by (1.114), it is impossible to render the second solution of Γ_k (unless it is complex), given by (1.157), equal to zero. Furthermore, for realistic functions of $R(x)$ (for instance $R(x)=z_k, \forall x$), Γ_k given by (1.157) is infinite, which is unrealistic. Consequently, the solution given by (1.157) must be ignored.

In conclusion, the expression of the reflection coefficient of mode k is given by

$$\Gamma_k = \frac{\sqrt{\langle R(x)\psi_k, \phi_k\rangle} - \sqrt{\langle \phi_k/R(x), \psi_k\rangle}\, z_k}{\sqrt{\langle R(x)\psi_k, \phi_k\rangle} + \sqrt{\langle \phi_k/R(x), \psi_k\rangle}\, z_k}. \tag{1.158}$$

The analogy of the expression of Γ_k, given by (1.158), with the reflection coefficient of a TEM wave is now obvious. Indeed, when $R(x)$ is equal to infinity (open circuit) for all positions of x, Γ_k is equal to 1. Similarly, when $R(x)$ is equal to zero (short circuit) for all positions of x, Γ_k is equal to -1.

For each incident mode k, it is always possible to eliminate its reflection Γ_k by setting

$$R(x) = z_k, \forall x \in [-w/2; w/2] \tag{1.159}$$

in (1.158) where the numerator can be written as

$$\int R(x)\psi_k(x)\phi_k(x)\,dx = z_k^2 \int \frac{1}{R(x)}\psi_k(x)\phi_k(x)\,dx. \tag{1.160}$$

However, it is yet to be proven if there exists a single function $R(x)$ which can eliminate the reflections of all incident modes by satisfying (1.160) for all k.

CHAPTER 2
GREEN'S FUNCTIONS

The Green's function of a structure is the solution of the partial differential equation of a unit charge and with specified homogeneous boundary conditions. To find the Green's function, the first step is to determine the potential due to the source charge everywhere in the region of interest. The Green's functions depend very much upon the particular problem being solved.

If there is more than one interface in a problem, the formation of image charges about the interface, by a process known as multiple imaging, must be considered. Each image of the real charge also images across all other interfaces. For example, if we consider charged interconnections printed on a dielectric substrate placed on a conducting ground plane, the real charge q will form an image across the dielectric interface as $q(\epsilon_1 - \epsilon_2)/(\epsilon_1 + \epsilon_2)$. This image will then form another image about the bottom ground plane as $-q(\epsilon_1 - \epsilon_2)/(\epsilon_1 + \epsilon_2)$. This new charge will in turn image back across the dielectric interface with its magnitude changed by a factor of $(\epsilon_1 - \epsilon_2)/(\epsilon_1 + \epsilon_2)$ and so on. This process will continue until infinity, producing an infinite number of images.

Although this process is well-known and widely used in the literature, it is rather difficult to use it in slightly complicated structures. A more systematic method of obtaining the image representation and therefore calculating the Green's functions consists of applying flux lines associated with the charge. Subsequently, the flux lines are treated as electromagnetic waves with all the characteristics of an incident wave getting reflected and transmitted on the interface of the two regions with different permittivity values.

After recapitulating the method of flux lines, the present chapter focuses on the calculation of the Green's function of several structures such as conductors printed on a dielectric substrate (with and without a ground plane) and those embedded in the substrate (with and without a ground plane). Also, the structure

of embedded conductors with a finite dielectric width is examined. The latter can be used as an approximation of a ribbon cable. Special care has been taken in expressing the Green's function in the most effective and numerically stable form.

2.1 METHOD OF PARTIAL IMAGES FOR A DIELECTRIC SLAB

Obtaining an image representation through the method of treating flux lines as electromagnetic waves is considerably easier due to the absence of refraction phenomena. In order to prove the absence of refraction, as well as to calculate the image coefficient K, consider a half space filled with a homogeneous dielectric of permittivity ϵ_1 and a line charge of q coulombs per meter lying at a certain distance from the interface, as illustrated in Figure 2.1. This charge will emit electric flux uniformly in all radial directions.

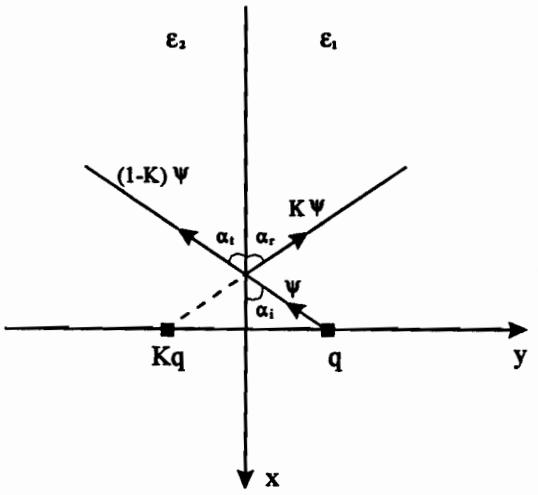

Figure 2.1 Flux lines associated with a line charge.

As in the case of an electromagnetic wave, some fraction of the flux, $K\psi$, will get reflected while the remainder $(1-K)\psi$ will be transmitted. Therefore, the image coefficient can be considered as playing the role of the reflection coefficient. Since the incident and reflected flux are in the same medium in the right half plane, they have the same velocity. Hence, it is a well-known result that the angles of incidence and reflection are equal,

$$\alpha_i = \alpha_r. \tag{2.1}$$

This equality can also be demonstrated with the next few equations.

The continuity conditions of electrostatics require the normal component of the flux density to be continuous across the interface, thus

$$\psi \sin\alpha_i - K\psi \sin\alpha_r = (1-K)\psi \sin\alpha_t, \tag{2.2}$$

and the tangential electric field component continuous across the interface, thus

$$\frac{1}{\epsilon_1}\psi\cos\alpha_i + \frac{1}{\epsilon_1}K\psi\cos\alpha_r = \frac{1}{\epsilon_2}(1-K)\psi\cos\alpha_t. \tag{2.3}$$

By substituting (2.1) into (2.2),

$$(1-K)\psi\sin\alpha_r = (1-K)\psi\sin\alpha_t, \tag{2.4}$$

from which it follows that $\alpha_i = \alpha_t$, therefore there is no refraction. By substituting (2.1) into (2.3),

$$\frac{1}{\epsilon_1}(1+K)\psi\cos\alpha_i = \frac{1}{\epsilon_2}(1-K)\psi\cos\alpha_t, \tag{2.5}$$

therefore,

$$\frac{(1+K)}{\epsilon_1} = \frac{(1-K)}{\epsilon_2}, \tag{2.6}$$

so that K must have the value

$$K = \frac{\epsilon_1 - \epsilon_2}{\epsilon_1 + \epsilon_2}. \tag{2.7}$$

Note that the expression of the image coefficient is equal to the negative of the reflection coefficient of an electromagnetic wave.

This approach can be used to determine the images of the real charge q i.e the flux line on the right side of the interface appears to be due to the result of two distinct line sources q and Kq as illustrated in Figure 2.1. Therefore, to calculate

the potential at the right side of the interface, the existence of two charges, q and an image Kq, must be considered. In the same manner, to calculate the potential at the left side of the interface, the existence of a single charge of strength $(1-K)q$, located at the right side, must be considered.

2.1.1 Potentials of multiple images

The method of flux lines can be used to determine the Green's function of a slab of finite thickness. The method is flexible enough to allow the calculation of the potential not only in the region where the real charge is located but also in all of the regions. Figure 2.2 illustrates the imaging for the right region where the real charge is located at $y = h + a$. The image coefficients associated with the first and second surface are K and $-K$ respectively.

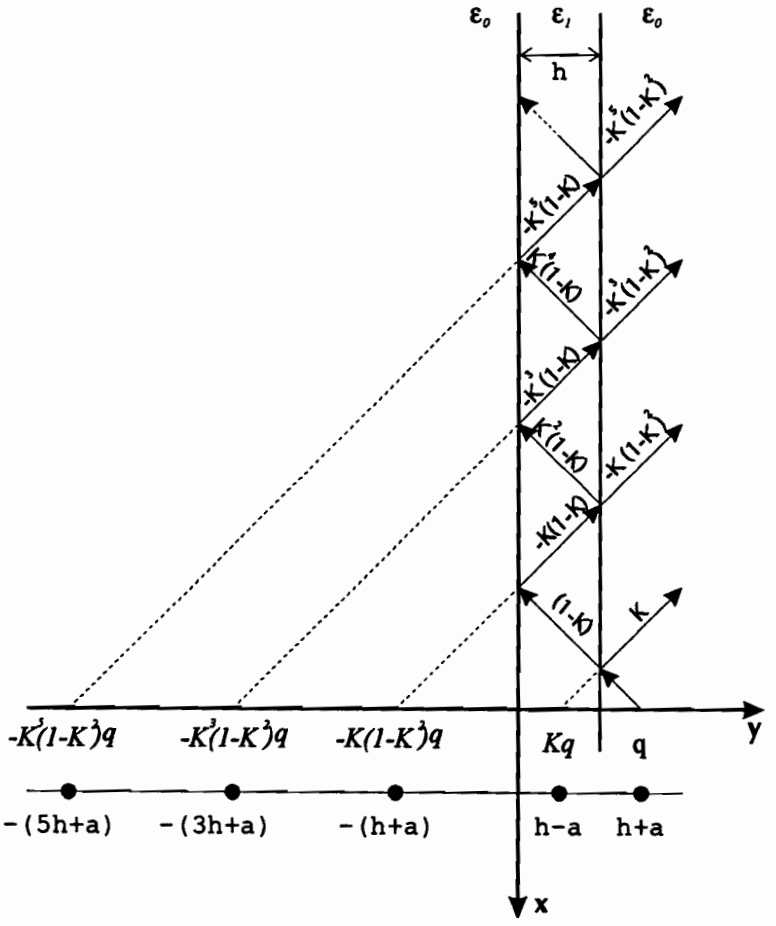

Figure 2.2 Equivalent image representation valid in the right region.

By simple geometrical proofs, it can be shown that the images are spaced $2h$ apart, except the first image Kq, which is at the location $y = h - a$. Therefore, the potential in the right region $(y > h)$, due to a single charge q placed at $(x = 0, y = h + a)$, is given by

$$V(x,y) = -\frac{q}{4\pi\epsilon_0}\log\{[y-(h+a)]^2 + x^2\} - \frac{Kq}{4\pi\epsilon_0}\log\{[y-(h-a)]^2 + x^2\}$$
$$+\frac{(1-K^2)q}{4\pi\epsilon_0}\sum_{n=1}^{\infty} K^{2n-1}\log\{[y+(2n-1)h+a]^2 + x^2\}. \tag{2.8}$$

In the center region $(0 < y < h)$ the equivalent image representation is illustrated in Figure 2.3.

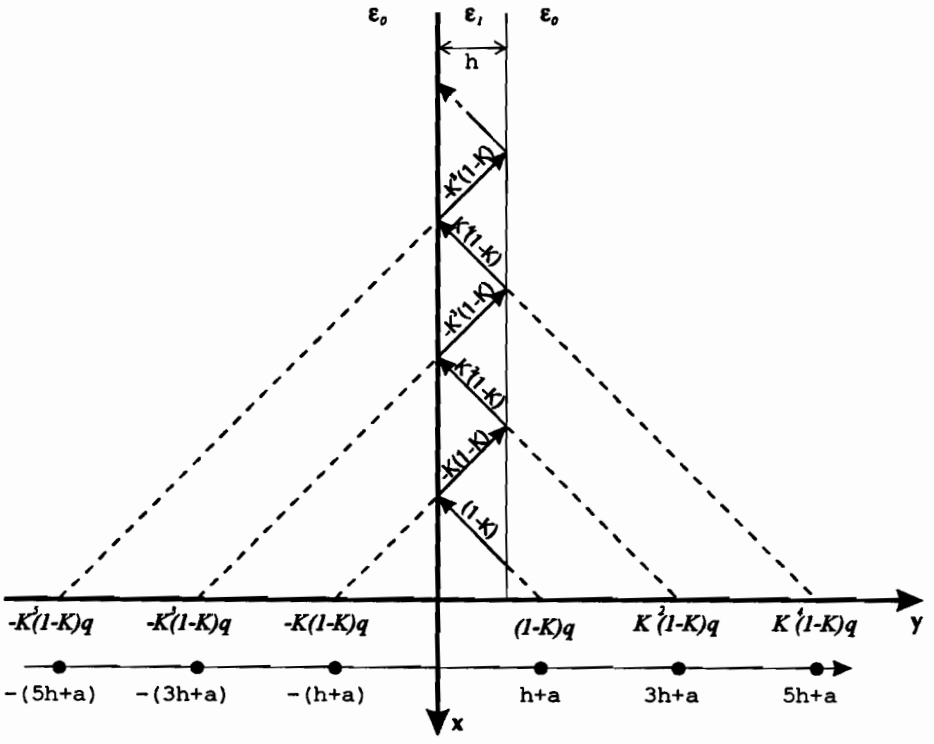

Figure 2.3 Equivalent image representation valid in the center region.

Therefore, the potential in the center region due to the same charge q located at $y = h + a$, is given by

$$V(x,y) = -\frac{(1-K)q}{4\pi\epsilon_1}\sum_{n=0}^{\infty} K^{2n}\log\{[(2n+1)h+a-y]^2+x^2\}$$
$$+\frac{(1-K)q}{4\pi\epsilon_1}\sum_{n=1}^{\infty} K^{2n-1}\log\{[(2n-1)h+a+y]^2+x^2\}. \qquad (2.9)$$

In the left region ($y < 0$), the equivalent image representation is illustrated in Figure 2.4.

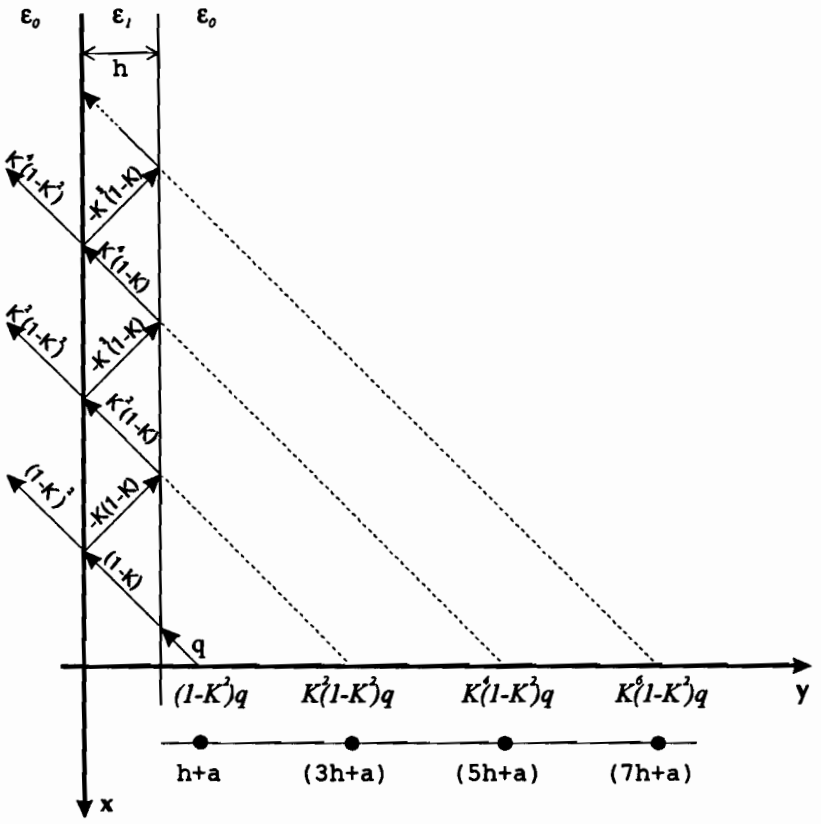

Figure 2.4 Equivalent image representation valid in the left region.

The potential in the left region, due to the same charge q, is given by

$$V(x,y) = -\frac{(1-K^2)q}{4\pi\epsilon_0}\sum_{n=1}^{\infty} K^{2(n-1)}\log\{[(2n-1)h+a-y]^2+x^2\}. \qquad (2.10)$$

The potential on the surface of the dielectric, $V_s(x)$, can be calculated using either expressions (2.8) or (2.9). At first glance, obtaining the same expression

with both equations seems unlikely. Starting with (2.8),

$$\lim_{a\to 0} V(x,h) = -\frac{q}{4\pi\epsilon_0}\log\{(h-h)^2+x^2\} - \frac{q}{4\pi\epsilon_0}K\log\{(h-h)^2+x^2\} + \frac{q}{4\pi\epsilon_0}(1-K^2)\sum_{n=1}^{\infty}K^{2n-1}\log\{(h+2nh-h)^2+x^2\}. \quad (2.8.1)$$

Simplifying and factorizing (2.8.1),

$$V_s(x) = -\frac{(1+K)q}{4\pi\epsilon_0}\log(x^2) + \frac{q}{4\pi\epsilon_0}(1-K^2)\sum_{n=1}^{\infty}K^{2n-1}\log\{(2nh)^2+x^2\}. \quad (2.8.2)$$

Starting with (2.9),

$$\lim_{a\to 0} V(x,h) = -\frac{(1-K)q}{4\pi\epsilon_1}\sum_{n=0}^{\infty}K^{2n}\log\{[(2n+1)h+0-h]^2+x^2\} + \frac{(1-K)q}{4\pi\epsilon_1}\sum_{n=1}^{\infty}K^{2n-1}\log\{[(2n-1)h+0+h]^2+x^2\}, \quad (2.9.1)$$

simplifying,

$$V_s(x) = -\frac{(1-K)q}{4\pi\epsilon_1}\sum_{n=0}^{\infty}K^{2n}\log\{(2nh)^2+x^2\} + \frac{(1-K)q}{4\pi\epsilon_1}\sum_{n=1}^{\infty}K^{2n-1}\log\{(2nh)^2+x^2\}. \quad (2.9.2)$$

Isolate the first term,

$$V_s(x) = -\frac{(1-K)q}{4\pi\epsilon_1}\log(x^2) - \frac{(1-K)q}{4\pi\epsilon_1}\sum_{n=1}^{\infty}K^{2n}\log\{(2nh)^2+x^2\} + \frac{(1-K)q}{4\pi\epsilon_1}\sum_{n=1}^{\infty}K^{2n-1}\log\{(2nh)^2+x^2\}. \quad (2.9.3)$$

Factorizing,

$$V_s(x) = -\frac{(1-K)q}{4\pi\epsilon_1}\log(x^2) + \frac{(1-K)q}{4\pi\epsilon_1}\sum_{n=1}^{\infty}K^{2n-1}\Big(\log\{(2nh)^2+x^2\} - K\log\{(2nh)^2+x^2\}\Big), \quad (2.9.4)$$

or,

$$V_s(x) = -\frac{(1-K)q}{4\pi\epsilon_1}\log(x^2) + \frac{(1-K)^2 q}{4\pi\epsilon_1}\sum_{n=1}^{\infty} K^{2n-1}\log\{(2nh)^2 + x^2\}. \tag{2.9.5}$$

Since $K = \frac{1-\epsilon_r}{1+\epsilon_r}$, where ϵ_r is the relative permittivity,

$$\frac{(1-K)^2}{4\pi\epsilon_1} = \frac{1-K^2}{4\pi\epsilon_0}, \text{ and } \frac{1-K}{4\pi\epsilon_1} = \frac{1+K}{4\pi\epsilon_0}. \tag{2.9.6}$$

Substituting these expressions into (2.9.5),

$$V_s(x) = -\frac{(1+K)q}{4\pi\epsilon_0}\log(x^2) + \frac{q}{4\pi\epsilon_0}(1-K^2)\sum_{n=1}^{\infty} K^{2n-1}\log\{(2nh)^2 + x^2\}, \tag{2.9.7}$$

which is identical to (2.8.2).

The above exercise was carried out for two purposes. First, as mentioned above, to demonstrate that the potential on the surface of the dielectric can be calculated by letting $a \to 0$ either in the expression of the potential in the center region or the one in the right region. Second, it is a confidence test on the validity of both expressions.

2.2 GREEN'S FUNCTIONS FOR CONDUCTORS PRINTED ON THE SUBSTRATE

2.2.1 Structure with a ground plane

In integrated circuits (IC), conductors are usually placed on a dielectric substrate with a ground plane. The calculation of the Green's function associated with a conductor on an integrated circuit substrate or a microstrip line can be achieved by the method outlined in the previous section. The presence of a ground plane can be tackled by replacing the ground plane with the image of the dielectric and the conductor as depicted in Figure 2.5.

The Green's function can be calculated either by taking the voltage at the right of the charge q placed at $y = h + a$ (equation (2.8)) and the voltage at the left (equation (2.10)) of the charge $-q$ placed at $-(h + a)$, or the equivalent image representation valid in the center region for both charges. For simplicity (the contribution of each pair to the total potential is that of a dipole), the equivalent image representation valid in the center region is adopted, as illustrated in Figure 2.6.

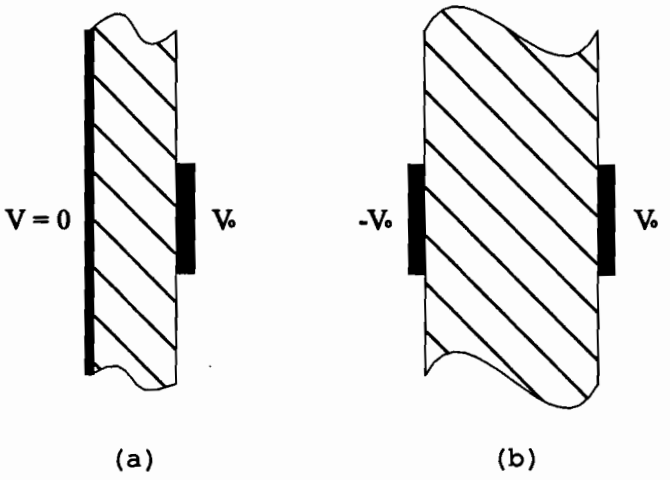

Figure 2.5 Microstrip line. (a) Conductor on the surface of the dielectric above the ground plane. (b) Electrically equivalent two line structure.

Based on Figure 2.6, the potential in the center region is given by

$$V(x,y) = -\frac{(1-K)q}{4\pi\epsilon_1}\sum_{n=0}^{\infty} K^n \log\{[(2n+1)h + a - y]^2 + x^2\}$$
$$+\frac{(1-K)q}{4\pi\epsilon_1}\sum_{n=0}^{\infty} K^n \log\{[(2n+1)h + a + y]^2 + x^2\}. \tag{2.11}$$

Factorizing (2.11),

$$V(x,y) = \frac{(1-K)q}{4\pi\epsilon_1}\sum_{n=0}^{\infty} K^n \log\frac{[(2n+1)h + a + y]^2 + x^2}{[(2n+1)h + a - y]^2 + x^2}. \tag{2.12}$$

The potential at the surface of the strip, $V_s(x)$, is then

$$\lim_{a\to 0} V(x,h) = \frac{(1-K)q}{4\pi\epsilon_1}\sum_{n=0}^{\infty} K^n \log\frac{[(2n+1)h+h]^2+x^2}{[(2n+1)h-h]^2+x^2}. \tag{2.13}$$

Simplifying,

$$V_s(x) = \frac{(1-K)q}{4\pi\epsilon_1}\sum_{n=0}^{\infty} K^n \log\frac{[(n+1)2h]^2+x^2}{(2nh)^2+x^2}. \tag{2.14}$$

Normalizing x with respect to $2h$,

$$V_s(x) = \frac{(1-K)q}{4\pi\epsilon_1}\sum_{n=0}^{\infty} K^n \log\frac{(n+1)^2+(\frac{x}{2h})^2}{n^2+(\frac{x}{2h})^2}, \tag{2.15}$$

or,

$$V_s(\overline{x}) = \frac{(1-K)q}{4\pi\epsilon_1}\sum_{n=0}^{\infty} K^n \log\frac{(n+1)^2+\overline{x}^2}{n^2+\overline{x}^2}, \tag{2.16}$$

where $\overline{x} = \frac{x}{2h}$.

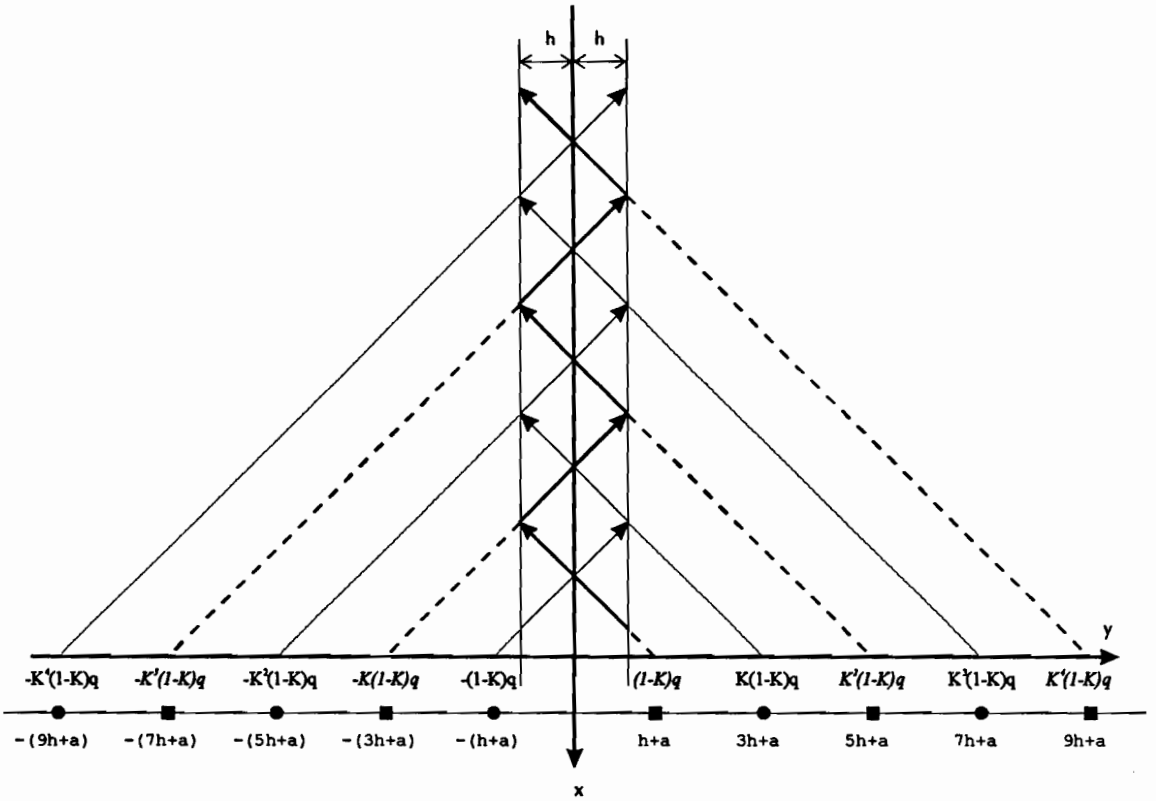

Figure 2.6 Image representation valid in the center region for the surface conductors.

By replacing the image coefficient with its value, $K = \frac{1-\epsilon_r}{1+\epsilon_r}$, where ϵ_r is the relative permittivity, an alternative form will be

$$V_s(\bar{x}) = \frac{1}{2\pi\epsilon_0(\epsilon_r+1)} \sum_{n=0}^{\infty} K^n \log \frac{(n+1)^2+\bar{x}^2}{n^2+\bar{x}^2}. \tag{2.17}$$

When the observation point P and the source point q are both located on the dielectric surface, $P = (x,h)$ and $q = (\xi,h)$, the electric Green's function is

$$G_E(\bar{x};\bar{\xi}) = \frac{1}{2\pi\epsilon_0(\epsilon_r+1)} \sum_{n=0}^{\infty} K^n \log \frac{(n+1)^2+\left(\bar{x}-\bar{\xi}\right)^2}{n^2+\left(\bar{x}-\bar{\xi}\right)^2}. \tag{2.18}$$

For brevity, write the series as

$$G_E(\bar{x};\bar{\xi}) = \frac{1}{2\pi\epsilon_0(\epsilon_r+1)} \sum_{n=0}^{\infty} K^n \log \frac{(n+1)^2+\zeta^2}{n^2+\zeta^2}, \tag{2.19}$$

where $\zeta = \frac{x-\xi}{2h} = \bar{x}-\bar{\xi}.$ (2.20)

For $\bar{x} = \bar{\xi}$ this Green's function has the expected logarithmic singularity. This can cause numerical instability, indeed it represents a major hindrance to effective numerical integration. Therefore it may be desirable to isolate the singular term from the remainder of the series. The simplest possible form that isolates the singularity is to separate the leading term:

$$G_E(\bar{x};\bar{\xi}) = \frac{1}{2\pi\epsilon_0(\epsilon_r+1)} \log \frac{1+\zeta^2}{\zeta^2} + \frac{1}{2\pi\epsilon_0(\epsilon_r+1)} \sum_{n=1}^{\infty} K^n \log \frac{(n+1)^2+\zeta^2}{n^2+\zeta^2}. \tag{2.21}$$

This is in fact a very effective form since each term of the form $\log(a/b)$ physically corresponds to a source-image pair. The contribution of each pair to the total potential is that of a dipole. As the distance between the source-image pair increases (e.g. large ζ or large n), the logarithm approaches zero. Therefore, the effects of two distant sources that make up the dipole cancel each other.

Furthermore, this form turns out to be numerically stable. A numerical computation that calculates the value of each dipolar term $\log\{(n+1)^2+\zeta^2\}/\{n^2+\zeta^2\}$ and adds dipoles to form the Green's function, is numerically stable; a computation that adds terms due to individual charges, e.g.,

$\log\{(n+1)^2+\zeta^2\}$ to $-\log\{n^2+\zeta^2\}$ is not. Indeed, for large ζ or large n, the two logarithmic terms are very similar but oppositely signed, so they suffer a major loss of significant figures on addition. This point is exhibited by consideration of alternative forms and their numerical stability in Appendix A.

The magnetic Green's function $G_M(\bar{x};\bar{\xi})$ is easier to obtain, so long as the substrate is taken to be nonmagnetic, $\mu = \mu_0$. Its form coincides with that of $G_E(\bar{x};\bar{\xi})$ when $\epsilon_r = 1$; its magnitude is $\epsilon_0\mu_0$ times larger:

$$G_M(\bar{x};\bar{\xi}) = \frac{1}{c_0^2} G_E(\bar{x};\bar{\xi})\Big|_{\epsilon_r = 1} \tag{2.22}$$

for $c_0^2\epsilon_0\mu_0 = 1$. The explicit expression is then

$$G_M(\bar{x};\bar{\xi}) = \frac{\mu_0}{4\pi}\log\frac{1+\zeta^2}{\zeta^2} \tag{2.23}$$

which accounts for the source and its single image in the ground plane.

Probably the easiest way of actually computing $G_M(\bar{x};\bar{\xi})$ is to use the program for $G_E(\bar{x};\bar{\xi})$ with ϵ_r set to unity. However, this function is needed frequently, so it may be more efficient to provide a separate, though similar, program for its calculation.

2.2.2 Structure with no ground plane

In printed circuit boards (PCB), conductors are usually placed on dielectric substrate with no ground plane. One can easily calculate the Green's function for such structures by taking the potential at the surface of the strip, $V_s(x)$, given by (2.9.7). Expanding terms in (2.9.7),

$$\begin{aligned} V_s(x) = \; & -\frac{q}{4\pi\epsilon_0}\log(x^2) - \frac{Kq}{4\pi\epsilon_0}\log(x^2) \\ & + \frac{q}{4\pi\epsilon_0}(1-K^2)\sum_{n=1}^{\infty} K^{2n-1}\log\{(2nh)^2+x^2\}. \end{aligned} \tag{2.24}$$

In order to reach a numerically stable and effective form, the image coefficient K

needs to be replaced by

$$K = (1-K^2)\sum_{n=1}^{\infty} K^{2n-1}. \tag{2.25}$$

Substituting (2.25) into (2.24) and factorizing,

$$V_s(x) = -\frac{q}{4\pi\epsilon_0}\log(x^2) + \frac{q}{4\pi\epsilon_0}(1-K^2)\sum_{n=1}^{\infty} K^{2n-1}\log\frac{(2nh)^2+x^2}{x^2}. \tag{2.26}$$

Normalizing x with respect to $2h$,

$$\begin{aligned} V_s(x) = & -\frac{q}{4\pi\epsilon_0}\log\{\left(\frac{x}{2h}\right)^2(2h)^2\} \\ & + \frac{q}{4\pi\epsilon_0}(1-K^2)\sum_{n=1}^{\infty} K^{2n-1}\log\frac{n^2+\left(\frac{x}{2h}\right)^2}{\left(\frac{x}{2h}\right)^2}, \end{aligned} \tag{2.27}$$

or alternatively,

$$V_s(\overline{x}) = -\frac{q}{4\pi\epsilon_0}\log\{\overline{x}^2(2h)^2\} - \frac{q}{4\pi\epsilon_0}(1-K^2)\sum_{n=1}^{\infty} K^{2n-1}\log\frac{\overline{x}^2}{n^2+\overline{x}^2}, \tag{2.28}$$

where $\overline{x} = \frac{x}{2h}$. Thus,

$$V_s(\overline{x}) = -\frac{q}{4\pi\epsilon_0}\left(\log(\overline{x}^2) + \log(4h^2) + (1-K^2)\sum_{n=1}^{\infty} K^{2n-1}\log\frac{\overline{x}^2}{n^2+\overline{x}^2}\right). \tag{2.29}$$

Once again, when the observation point P and the source point q are both located on the dielectric surface, $P=(x,h)$ and $q=(\xi,h)$, the electric Green's function is expressed by

$$\begin{aligned} G_E(\overline{x};\overline{\xi}) = & -\frac{1}{4\pi\epsilon_0}\Big(\log((\overline{x}-\overline{\xi})^2) + \log(4h^2) + \\ & (1-K^2)\sum_{n=1}^{\infty} K^{2n-1}\log\frac{(\overline{x}-\overline{\xi})^2}{n^2+(\overline{x}-\overline{\xi})^2}\Big). \end{aligned} \tag{2.30}$$

For brevity, write the series as

$$G_E(\overline{x};\overline{\xi}) = -\frac{1}{4\pi\epsilon_0}\left(\log(\zeta^2) + \log(4h^2) + (1-K^2)\sum_{n=1}^{\infty} K^{2n-1}\log\frac{\zeta^2}{n^2+\zeta^2}\right), \tag{2.31}$$

where ζ is given by (2.20) ($\zeta = \overline{x} - \overline{\xi}$).

By replacing the image coefficient with its value ($K = (1-\epsilon_r)/(1+\epsilon_r)$, where ϵ_r is the relative permittivity) an alternative form will be

$$G_E(\overline{x};\overline{\xi}) = -\frac{1}{4\pi\epsilon_0}\log(\zeta^2) - \frac{1}{4\pi\epsilon_0}\log(4h^2) - \frac{\epsilon_r}{\pi\epsilon_0(1+\epsilon_r)^2}\sum_{n=1}^{\infty} K^{2n-1}\log\frac{\zeta^2}{n^2+\zeta^2}. \tag{2.32}$$

Once again, for $\overline{x} = \overline{\xi}$ this Green's function has the expected logarithmic singularity. Furthermore, this Green's function is expected to produce a spurious mode which must be ignored (see section 4.2.1 for more details).

For a nonmagnetic substrate, the magnetic Green's function $G_M(\overline{x};\overline{\xi})$ is easier to obtain as described in section 2.2.1. The explicit expression is then,

$$G_M(\overline{x};\overline{\xi}) = -\frac{\mu_0}{4\pi}\Big(\log(\zeta^2) + \log(4h^2)\Big) \tag{2.33}$$

which accounts for a single source.

2.3 GREEN'S FUNCTIONS FOR CONDUCTORS EMBEDDED IN THE SUBSTRATE

In integrated circuits (IC), conductors might sometimes be embedded in the substrate which in turn is placed above a ground plane as depicted in Figure 2.7.

Even though the structure with no ground plane is rarely encountered, its Green's function can be used to approximate other structures such as a ribbon cable.

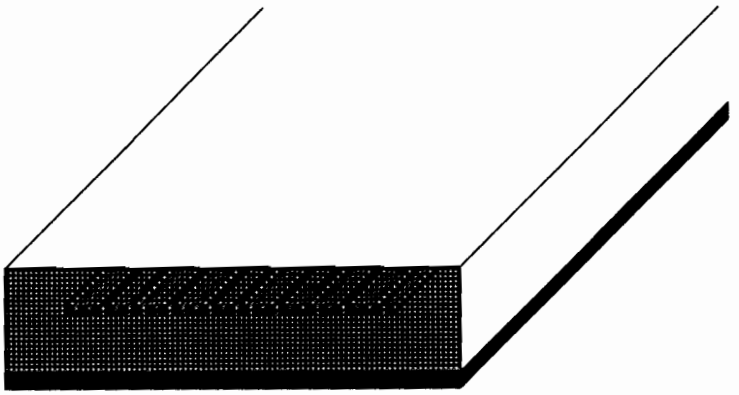

Figure 2.7 Conductors embedded in a substrate.

Therefore, both structures are discussed in this section. Once again, the calculation of the Green's function of such structures can be achieved by the method outlined in the previous sections. As mentioned previously, the presence of a ground plane can be tackled by replacing the ground plane with the image of the dielectric and the conductors.

2.3.1 Structure with a ground plane

The image representation of this structure is depicted in Figure 2.8. Orienting the x-axis towards the bottom and the y-axis to the right in the case of Figure 2.8 is adopted for practical reasons. Indeed, all the figures in Chapter 2 with an infinite image representation across the horizontal boundaries are rotated -90° with the objective of providing more space to draw the images on a single page.

The Green's functions obtained for this structure can be checked for accuracy by reducing them to the case when the interconnections are printed on the substrate by setting $a = y = h$ and ensuring that the resulting expression for the surface potential or Green's function agrees with those found in section 2.2.1.

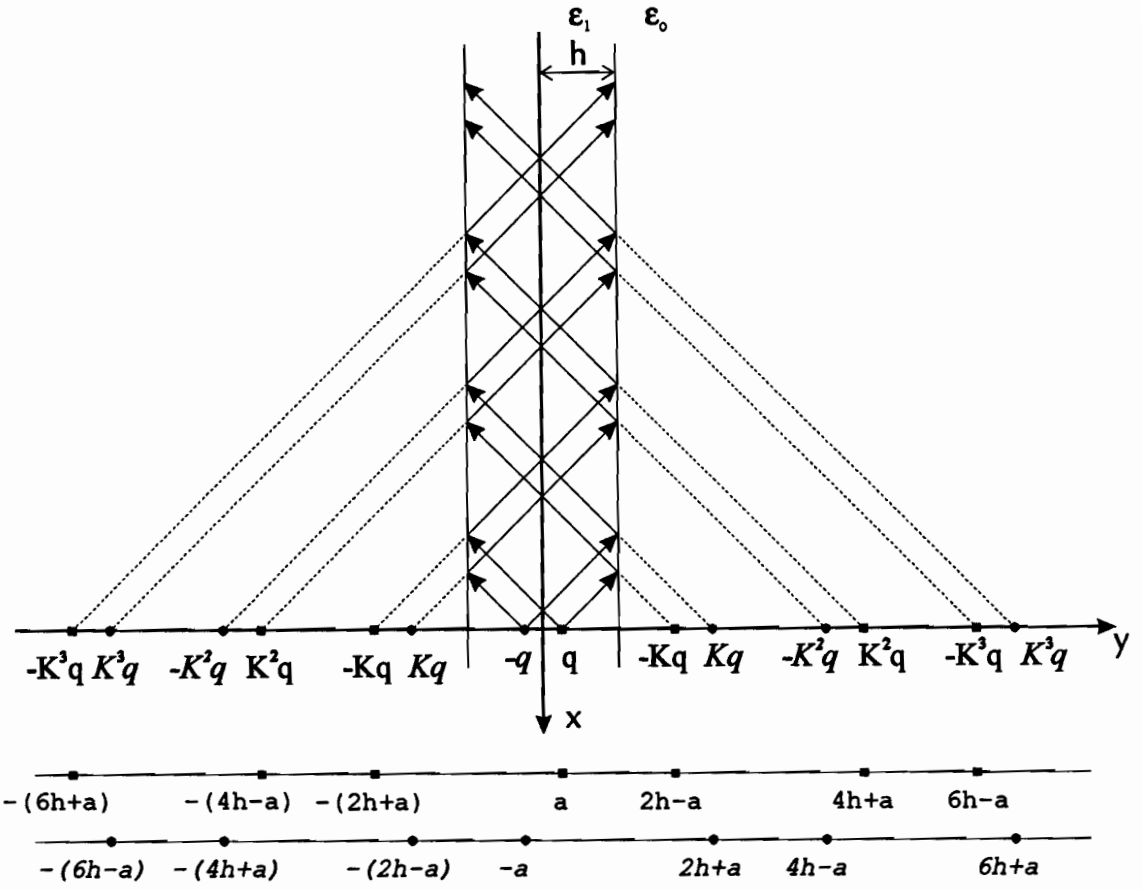

Figure 2.8 Image representation valid in the center region for the embedded conductors with a ground plane.

From Figure 2.8, it follows that the potential for $0 < y < h$ is

$$V(x,y) = \frac{q}{4\pi\epsilon_1}\log\frac{x^2+(y+a)^2}{x^2+(y-a)^2} + \frac{q}{4\pi\epsilon_1}\sum_{n=0}^{\infty} K^{n+1}\log\frac{[(n+1)2h-a-y]^2+x^2}{[(n+1)2h+a-y]^2+x^2}$$
$$+\frac{q}{4\pi\epsilon_1}\sum_{n=0}^{\infty} K^{n+1}\log\frac{[(n+1)2h+a+y]^2+x^2}{[(n+1)2h-a+y]^2+x^2}. \qquad (2.34)$$

In order to stay consistent with the previous sections, the image coefficient is considered having the same expression $(K = (1-\epsilon_r)/(1+\epsilon_r))$. Therefore, an incident flux gets reflected by multiplying its value by $-K$ instead of K.

Collecting terms in (2.34),

$$V(x,y) = \frac{q}{4\pi\epsilon_1}\sum_{n=0}^{\infty} K^{n+1}\log\frac{[(n+1)2h-a-y]^2+x^2}{[(n+1)2h+a-y]^2+x^2} + \frac{q}{4\pi\epsilon_1}\sum_{n=0}^{\infty} K^{n}\log\frac{(2nh+a+y)^2+x^2}{(2nh-a+y)^2+x^2}. \tag{2.35}$$

The potential at the surface of the conductors, $V_s(x)$, is obtained by letting $y = a$,

$$V(x,a) = \frac{q}{4\pi\epsilon_1}\left(\sum_{n=0}^{\infty} K^{n+1}\log\frac{[(n+1)2h-a-a]^2+x^2}{[(n+1)2h+a-a]^2+x^2} + \sum_{n=0}^{\infty} K^{n}\log\frac{(2nh+a+a)^2+x^2}{(2nh-a+a)^2+x^2}\right). \tag{2.36}$$

Simplifying (2.36),

$$V_s(x) = \frac{q}{4\pi\epsilon_1}\left(\sum_{n=0}^{\infty} K^{n+1}\log\frac{[(n+1)2h-2a]^2+x^2}{[(n+1)2h]^2+x^2} + \sum_{n=0}^{\infty} K^{n}\log\frac{(2nh+2a)^2+x^2}{(2nh)^2+x^2}\right). \tag{2.37}$$

Since a is proportional to h, it can be replaced by rh, where r is a positive real number bounded by $0 < r < 1$. Thus,

$$V(x) = \frac{q}{4\pi\epsilon_1}\left(\sum_{n=0}^{\infty} K^{n+1}\log\frac{[(n+1)2h-2rh]^2+x^2}{[(n+1)2h]^2+x^2} + \sum_{n=0}^{\infty} K^{n}\log\frac{(2nh+2rh)^2+x^2}{(2nh)^2+x^2}\right). \tag{2.38}$$

Normalizing x with respect to $2h$,

$$V(\overline{x},a) = \frac{q}{4\pi\epsilon_1}\left(\sum_{n=0}^{\infty} K^{n+1}\log\frac{[(n+1)-r]^2+\overline{x}^2}{(n+1)^2+\overline{x}^2} + \sum_{n=0}^{\infty} K^{n}\log\frac{(n+r)^2+\overline{x}^2}{n^2+\overline{x}^2}\right), \tag{2.39}$$

where $\overline{x} = \frac{x}{2h}$ and $0 < r < 1$.

Once again, when the observation point P and the source point q are both located on the surface of the conductors, $P=(x,a)$ and $q=(\xi,a)$, the electric Green's function is

$$G_E(\bar{x};\bar{\xi})=\frac{1}{4\pi\epsilon_1}\left(\sum_{n=0}^{\infty}K^{n+1}\log\frac{[(n+1)-r]^2+\zeta^2}{(n+1)^2+\zeta^2}+\sum_{n=0}^{\infty}K^n\log\frac{(n+r)^2+\zeta^2}{n^2+\zeta^2}\right), \tag{2.40}$$

where ζ is given by (2.20) ($\zeta=\bar{x}-\bar{\xi}$).

In order to check the validity of the (2.40), this structure can be converted into one with conductors printed on the substrate by setting $r=1$,

$$G_E(\bar{x};\bar{\xi})=\frac{1}{4\pi\epsilon_1}\left(\sum_{n=0}^{\infty}K^{n+1}\log\frac{n^2+\zeta^2}{(n+1)^2+\zeta^2}+\sum_{n=0}^{\infty}K^n\log\frac{(n+1)^2+\zeta^2}{n^2+\zeta^2}\right). \tag{2.40.1}$$

Rearranging terms,

$$G_E(\bar{x};\bar{\xi})=\frac{1}{4\pi\epsilon_1}\left(-K\sum_{n=0}^{\infty}K^n\log\frac{(n+1)^2+\zeta^2}{n^2+\zeta^2}+\sum_{n=0}^{\infty}K^n\log\frac{(n+1)^2+\zeta^2}{n^2+\zeta^2}\right). \tag{2.40.2}$$

Factorizing,

$$G_E(\bar{x};\bar{\xi})=\frac{1}{4\pi\epsilon_1}(1-K)\sum_{n=0}^{\infty}K^n\log\frac{(n+1)^2+\zeta^2}{n^2+\zeta^2}. \tag{2.40.3}$$

With $K=(1-\epsilon_r)/(1+\epsilon_r)$, (2.40.3) is identical to (2.19).

Once again, for $\bar{x}=\bar{\xi}$ this Green's function has the expected logarithmic singularity. Therefore it may be desirable to isolate the singular term from the remainder of the series. The simplest possible form that isolates the singularity is to separate the leading term:

$$G_E(\bar{x};\bar{\xi})=\frac{1}{4\pi\epsilon_1}\left(\sum_{n=0}^{\infty}K^{n+1}\log\frac{(n+1-r)^2+\zeta^2}{(n+1)^2+\zeta^2}+\sum_{n=0}^{\infty}K^{n+1}\log\frac{(n+1+r)^2+\zeta^2}{(n+1)^2+\zeta^2}+\log\frac{r^2+\zeta^2}{\zeta^2}\right). \tag{2.41}$$

Factorizing,

$$G_E(\overline{x};\overline{\xi}) = \frac{1}{4\pi\epsilon_1}\left(\log\frac{r^2+\zeta^2}{\zeta^2} + \sum_{n=0}^{\infty} K^{n+1}\log\frac{[(n+1-r)^2+\zeta^2][(n+1+r)^2+\zeta^2]}{[(n+1)^2+\zeta^2]^2}\right). \quad (2.42)$$

For brevity, start the summation at $n = 1$,

$$G_E(\overline{x};\overline{\xi}) = \frac{1}{4\pi\epsilon_1}\left(\log\frac{r^2+\zeta^2}{\zeta^2} + \sum_{n=1}^{\infty} K^{n}\log\frac{[(n-r)^2+\zeta^2][(n+r)^2+\zeta^2]}{(n^2+\zeta^2)^2}\right). \quad (2.43)$$

This is an effective and numerically stable form for the same reasons outlined in section 2.2.1.

For a nonmagnetic substrate, the expression of the magnetic Green's function $G_M(\overline{x};\overline{\xi})$ is given by

$$G_M(\overline{x};\overline{\xi}) = \frac{\mu_0}{4\pi}\log\frac{r^2+\zeta^2}{\zeta^2}. \quad (2.44)$$

Note that (2.44) reduces to (2.23) (the magnetic Green's function of conductors printed on the substrate) when $r = 1$.

It is possible to use the Green's functions given by (2.43) and (2.44) in a single program which accounts for the structure of a surface and embedded conductors with a ground plane.

2.3.2 Structure with no ground plane

The image representation of this structure is depicted in Figure 2.9.

Once again, the results obtained for this structure can be checked for validity by reducing them to the case when the interconnections are printed on the substrate (by setting $a = y = h$) and ensuring that the resulting expression for the surface potential or Green's function agrees with those found in section 2.2.2.

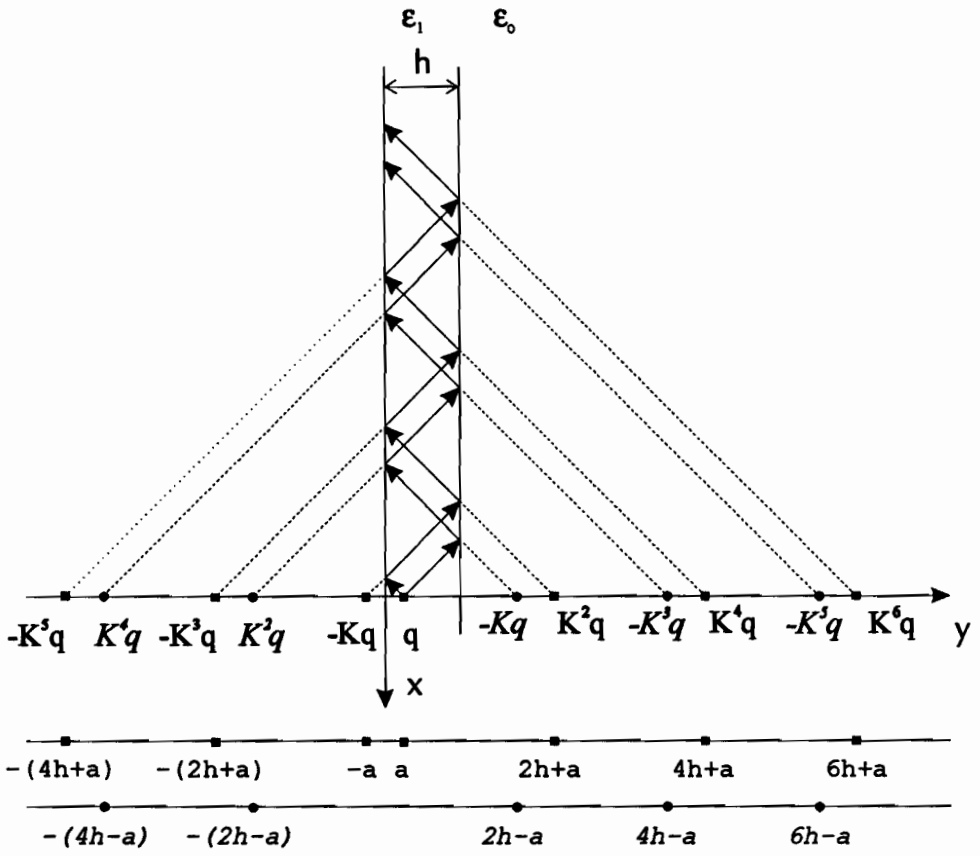

Figure 2.9 Image representation valid in the center region for an embedded conductors with no ground plane.

From Figure 2.9, it follows that the potential for $0 < y < h$ is

$$V(x,y) = -\frac{q}{4\pi\epsilon_1}\log\{(y-a)^2+x^2\}$$
$$+\frac{q}{4\pi\epsilon_1}\sum_{n=1}^{\infty}K^{2n-1}\log\{[(2nh-a-y)^2+x^2][(2(n-1)h+a+y)^2+x^2]\}$$
$$-\frac{q}{4\pi\epsilon_1}\sum_{n=1}^{\infty}K^{2n}\log\{[(2nh+a-y)^2+x^2][(2nh-a+y)^2+x^2]\}. \quad (2.45)$$

At the surface of the strip, the potential, $V_s(x)$, is given by letting $y = a$,

$$V(x,a) = -\frac{q}{4\pi\epsilon_1}\log(x^2)$$
$$+\frac{q}{4\pi\epsilon_1}\sum_{n=1}^{\infty} K^{2n-1}\log\{[(2nh-2a)^2+x^2][(2(n-1)h+2a)^2+x^2]\}$$
$$-\frac{q}{4\pi\epsilon_1}\sum_{n=1}^{\infty} K^{2n}\log\{[(2nh)^2+x^2][(2nh)^2+x^2]\}. \tag{2.46}$$

By fixing $a = h$ in (2.46), it is possible to verify whether the latter is equal to (2.9.2). Therefore, with $a = h$, (2.46) becomes

$$V(x,h) = -\frac{q}{4\pi\epsilon_1}\log(x^2)$$
$$+\frac{q}{4\pi\epsilon_1}\sum_{n=1}^{\infty} K^{2n-1}\log\{[(2nh-2h)^2+x^2][(2nh)^2+x^2]\}$$
$$-\frac{q}{4\pi\epsilon_1}\sum_{n=1}^{\infty} K^{2n}\log\{[(2nh)^2+x^2][(2nh)^2+x^2]\}. \tag{2.46.1}$$

Expanding,

$$V(x,h) = -\frac{q}{4\pi\epsilon_1}\log(x^2)$$
$$+\frac{q}{4\pi\epsilon_1}\sum_{n=1}^{\infty} K^{2n-1}\log\{(2nh-2h)^2+x^2\} - \frac{q}{4\pi\epsilon_1}\sum_{n=1}^{\infty} K^{2n}\log\{(2nh)^2+x^2\}$$
$$+\frac{q}{4\pi\epsilon_1}\sum_{n=1}^{\infty} K^{2n-1}\log\{(2nh)^2+x^2\} - \frac{q}{4\pi\epsilon_1}\sum_{n=1}^{\infty} K^{2n}\log\{(2nh)^2+x^2\}. \tag{2.46.2}$$

Since,

$$\frac{q}{4\pi\epsilon_1}\sum_{n=1}^{\infty} K^{2n-1}\log\{(2nh-2h)^2+x^2\} - \frac{q}{4\pi\epsilon_1}\sum_{n=1}^{\infty} K^{2n}\log\{(2nh)^2+x^2\} =$$
$$\frac{q}{4\pi\epsilon_1}K\log(x^2) - \frac{(1-K)q}{4\pi\epsilon_1}\sum_{n=1}^{\infty} K^{2n}\log\{(2nh)^2+x^2\}, \tag{2.46.3}$$

and

$$\frac{q}{4\pi\epsilon_1}\sum_{n=1}^{\infty} K^{2n-1}\log\{(2nh)^2+x^2\} - \frac{q}{4\pi\epsilon_1}\sum_{n=1}^{\infty} K^{2n}\log\{(2nh)^2+x^2\} =$$
$$\frac{(1-K)q}{4\pi\epsilon_1}\sum_{n=1}^{\infty} K^{2n-1}\log\{(2nh)^2+x^2\}, \tag{2.46.4}$$

therefore, substituting (2.46.3) and (2.46.4) into (2.46.2) yields

$$V(x,h) = -\frac{q}{4\pi\epsilon_1}\log(x^2) + \frac{(1-K)q}{4\pi\epsilon_1}\sum_{n=1}^{\infty} K^{2n-1}\log\{(2nh)^2+x^2\} + \frac{q}{4\pi\epsilon_1}K\log(x^2) - \frac{(1-K)q}{4\pi\epsilon_1}\sum_{n=1}^{\infty} K^{2n}\log\{(2nh)^2+x^2\}. \tag{2.46.5}$$

Factorizing,

$$V(x,h) = \frac{(1-K)q}{4\pi\epsilon_1}\sum_{n=1}^{\infty} K^{2n-1}\log\{(2nh)^2+x^2\} - \frac{(1-K)q}{4\pi\epsilon_1}\sum_{n=0}^{\infty} K^{2n}\log\{(2nh)^2+x^2\}, \tag{2.46.6}$$

which is identical to (2.9.2).

Since a is proportional to h, it can by replaced with rh in (2.46), where r is a positive real number bounded by $0 < r < 1$. Thus, (2.46) becomes

$$V_s(x) = -\frac{q}{4\pi\epsilon_1}\log(x^2) + \frac{q}{4\pi\epsilon_1}\sum_{n=1}^{\infty} K^{2n-1}\log\{[(2nh-2rh)^2+x^2][(2(n-1)h+2rh)^2+x^2]\} - \frac{q}{4\pi\epsilon_1}\sum_{n=1}^{\infty} K^{2n}\log\{[(2nh)^2+x^2][(2nh)^2+x^2]\}. \tag{2.47}$$

Normalizing with respect to $2h$,

$$V_s(\overline{x}) = -\frac{q}{4\pi\epsilon_1}\log(\overline{x}^2) - \frac{q}{4\pi\epsilon_1}\sum_{n=1}^{\infty} K^{2n}\log(n^2+\overline{x}^2)^2 + \frac{q}{4\pi\epsilon_1}\sum_{n=1}^{\infty} K^{2n-1}\log\{[(n-r)^2+\overline{x}^2][(n-1+r)^2+\overline{x}^2]\} + \frac{q}{4\pi\epsilon_1}\left(-\log(2h)^2 + \log(2h)^4\left\{\sum_{n=1}^{\infty} K^{2n-1} - \sum_{n=1}^{\infty} K^{2n}\right\}\right) \tag{2.48}$$

and simplifying,

$$V_s(\bar{x}) = -\frac{q}{4\pi\epsilon_1}\log(\bar{x}^2) - \frac{q}{4\pi\epsilon_1}\epsilon_r\log(4h^2) - \frac{q}{4\pi\epsilon_1}\sum_{n=1}^{\infty}K^{2n}\log(n^2+\bar{x}^2)^2$$
$$+\frac{q}{4\pi\epsilon_1}\sum_{n=1}^{\infty}K^{2n-1}\log\{[(n-1+r)^2+\bar{x}^2][(n-r)^2+\bar{x}^2]\}. \quad (2.49)$$

Once again, when the observation point P and the source point q are both located on the surface of the conductors, $P=(x,a)$ and $q=(\xi,a)$, the electric Green's function is

$$G_E(\bar{x};\bar{\xi}) = -\frac{1}{4\pi\epsilon_1}\Bigg(\log(\zeta^2) + \epsilon_r\log(4h^2) + \sum_{n=1}^{\infty}K^{2n}\log(n^2+\zeta^2)^2$$
$$-\sum_{n=1}^{\infty}K^{2n-1}\log\{[(n-1+r)^2+\zeta^2][(n-r)^2+\zeta^2]\}\Bigg), \quad (2.50)$$

where ζ is given by (2.20) ($\zeta=\bar{x}-\bar{\xi}$).

For $\bar{x}=\bar{\xi}$ this Green's function has the expected logarithmic singularity. Furthermore, as in section 2.2.2, this Green's function is expected to produce a spurious mode which must be ignored (see section 5.2.1 for more details).

A numerically more stable form will be obtained by adding,

$$+\frac{1}{4\pi\epsilon_1}\sum_{n=1}^{\infty}K^{2n-1}\log(\zeta^4) - \frac{1}{4\pi\epsilon_1}\sum_{n=1}^{\infty}K^{2n-1}\log(\zeta^4)$$
$$+\frac{1}{4\pi\epsilon_1}\sum_{n=1}^{\infty}K^{2n}\log(\zeta^4) - \frac{1}{4\pi\epsilon_1}\sum_{n=1}^{\infty}K^{2n}\log(\zeta^4) \quad (2.51)$$

to (2.50). Therefore, substituting (2.51) into (2.50) yields

$$G_E(\bar{x};\bar{\xi}) = -\frac{1}{4\pi\epsilon_1}\log(\zeta^2) - \frac{\epsilon_r}{4\pi\epsilon_1}\log(4h^2) - \frac{1}{4\pi\epsilon_1}\sum_{n=1}^{\infty}K^{2n}\log\frac{(n^2+\zeta^2)^2}{\zeta^4}$$
$$+\frac{1}{4\pi\epsilon_1}\sum_{n=1}^{\infty}K^{2n-1}\log\frac{[(n-r)^2+\zeta^2][(n-1+r)^2+\zeta^2]}{\zeta^4} \quad (2.52)$$
$$+\frac{1}{4\pi\epsilon_1}\log(\zeta^4)\left(\sum_{n=1}^{\infty}K^{2n-1} - \sum_{n=1}^{\infty}K^{2n}\right).$$

However, $$\left(\sum_{n=1}^{\infty}K^{2n-1} - \sum_{n=1}^{\infty}K^{2n}\right) = \frac{K}{1+K} = \frac{1}{2}(1-\epsilon_r). \quad (2.53)$$

Therefore,

$$G_E(\overline{x};\overline{\xi}) = -\frac{1}{4\pi\epsilon_1}\log(\zeta^2) - \frac{\epsilon_r}{4\pi\epsilon_1}\log(4h^2) - \frac{1}{4\pi\epsilon_1}\sum_{n=1}^{\infty} K^{2n}\log\frac{(n^2+\zeta^2)^2}{\zeta^4}$$
$$+\frac{1}{4\pi\epsilon_1}\sum_{n=1}^{\infty} K^{2n-1}\log\frac{[(n-r)^2+\zeta^2][(n-1+r)^2+\zeta^2]}{\zeta^4} \qquad (2.54)$$
$$+\frac{1}{4\pi\epsilon_1}2\log(\zeta^2)\left(\frac{1}{2}(1-\epsilon_r)\right).$$

Factorizing (2.54),

$$G_E(\overline{x};\overline{\xi}) = +\frac{1}{4\pi\epsilon_1}\log(\zeta^2)\,(1-\epsilon_r-1) - \frac{\epsilon_r}{4\pi\epsilon_1}\log(4h^2)$$
$$-\frac{1}{4\pi\epsilon_1}\sum_{n=1}^{\infty} K^{2n}\log\left(\frac{n^2+\zeta^2}{\zeta^2}\right)^2$$
$$+\frac{1}{4\pi\epsilon_1}\sum_{n=1}^{\infty} K^{2n-1}\log\frac{[(n-r)^2+\zeta^2][(n-1+r)^2+\zeta^2]}{\zeta^4}. \qquad (2.55)$$

Alternatively,

$$G_E(\overline{x};\overline{\xi}) = -\frac{1}{4\pi\epsilon_0}\Big(\log(\zeta^2)+\log(4h^2)\Big) - \frac{1}{2\pi\epsilon_1}\sum_{n=1}^{\infty} K^{2n}\log\frac{n^2+\zeta^2}{\zeta^2}$$
$$+\frac{1}{4\pi\epsilon_1}\sum_{n=1}^{\infty} K^{2n-1}\log\frac{[(n-r)^2+\zeta^2][(n-1+r)^2+\zeta^2]}{\zeta^4}. \qquad (2.56)$$

For a nonmagnetic substrate, the expression of the magnetic Green's function is given by

$$G_M(\overline{x};\overline{\xi}) = -\frac{\mu_0}{4\pi}\Big(\log(\zeta^2)+\log(4h^2)\Big). \qquad (2.57)$$

Note that (2.57), which is identical to (2.33) (magnetic Green's function of conductors printed on the substrate with no ground plane), is independent of the position r (or a) of the conductors.

Once again, it is possible to use the Green's functions given by (2.50) (or the

alternative form given by (2.56)) and (2.57) in a single program which accounts for the structure of a surface and embedded conductors without a ground plane.

2.3.3 Structure with a finite dielectric width and with no ground plane

In the previous sections, all of the structures considered consisted of an infinite dielectric width. This section deals with yet another embedded conductor with no ground plane, but contrary to the preceding section, it contains a dielectric of substrate width W_d as depicted in Figure 2.10.

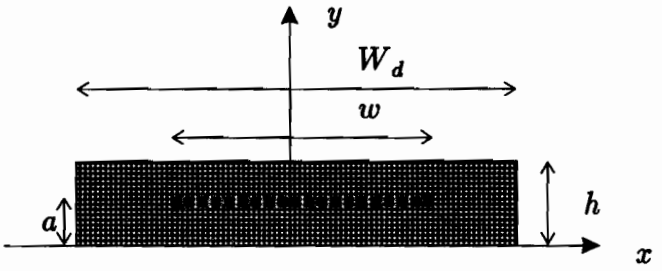

Figure 2.10 Embedded conductors with no ground plane and with finite dielectric width.

Considering first the dielectric width to be infinite, the Green's function will be identical to the one calculated in the previous section (equation (2.46)):

$$\begin{aligned} G_E(x;\xi) = \; & -\frac{1}{4\pi\epsilon_1}\log((x-\xi)^2) \\ & +\frac{1}{4\pi\epsilon_1}\sum_{n=1}^{\infty} K^{2n-1}\log\{(2nh-2a)^2+(x-\xi)^2\} \\ & +\frac{1}{4\pi\epsilon_1}\sum_{n=1}^{\infty} K^{2n-1}\log\{(2(n-1)h+2a)^2+(x-\xi)^2\} \\ & -\frac{1}{4\pi\epsilon_1}\sum_{n=1}^{\infty} K^{2n}\log\{[(2nh)^2+(x-\xi)^2][(2nh)^2+(x-\xi)^2]\}. \end{aligned} \tag{2.58}$$

Next, if the dielectric thickness is considered to be infinite ($h\to\infty$) but the

dielectric width finite, then the image representation of a charge q placed at (ξ, y) is depicted in Figure 2.11.

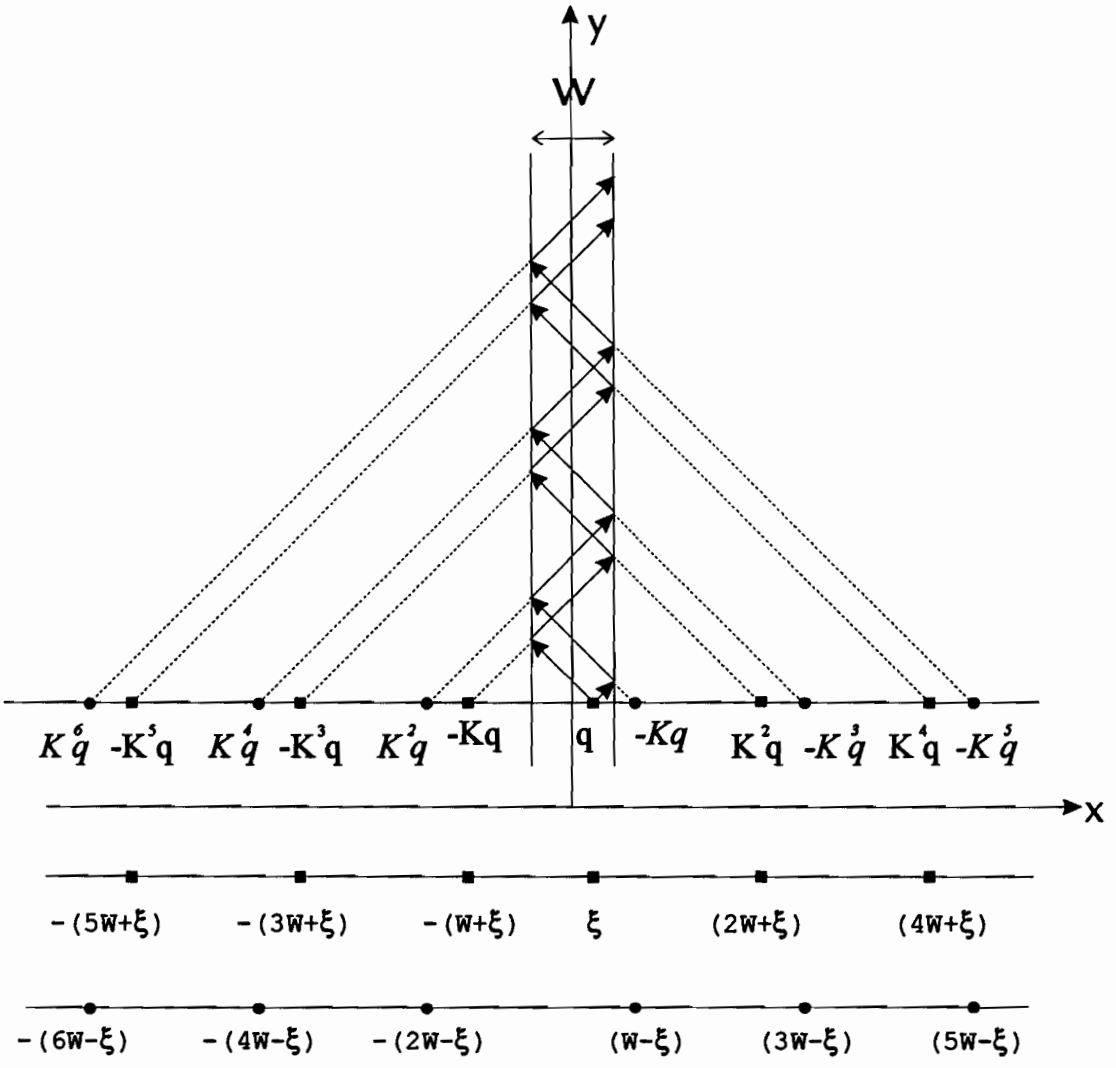

Figure 2.11 Image representation valid in the center region for an embedded conductor for very large h.

Based on Figure 2.11, the potential at a point $P = (x, y_0)$ due to the source point $q = (\xi, y)$ will be given by

$$V(x,y_0) = -\frac{q}{4\pi\epsilon_1}\log\{(x-\xi)^2+(y-y_0)^2\}\}$$
$$+\frac{q}{4\pi\epsilon_1}\sum_{m=1}^{\infty}(-1)^{m+1}K^m\Big(\log\{[mW_d+(-1)^m\xi-x]^2+[y-y_0]^2\}$$
$$+\log\{[mW_d+(-1)^{m+1}\xi+x]^2+[y-y_0]^2\}\Big). \tag{2.59}$$

For convenience, let

$$G_1(x;\xi,y)=\sum_{m=1}^{\infty}(-1)^{m+1}K^m\left(\log\{[mW_d+(-1)^m\xi-x]^2+y^2\}+\log\{[mW_d+(-1)^{m+1}\xi+x]^2+y^2\}\right). \tag{2.60}$$

Thus, (2.59) can now be expressed as

$$V(x,y_0) = -\frac{q}{4\pi\epsilon_1}\log\{(x-\xi)^2+(y-y_0)^2\}+\frac{q}{4\pi\epsilon_1}G_1(x;\xi,y)$$
$$= -\frac{q}{4\pi\epsilon_1}\Big(\log\{(x-\xi)^2+(y-y_0)^2\}-G_1(x;\xi,y)\Big). \tag{2.61}$$

The Green's function of embedded conductors with a finite dielectric width can be obtained using the following reasoning. A single charge, located at $y=0$, will have an infinite image representation (equation (2.58)) across the horizontal boundaries of the dielectric (due to the finite thickness h). Each of the image charges obtained, including the original one located at $y=0$, will have an infinite image representation across the vertical boundaries of the dielectric (due to the finite thickness W_d). Therefore, the electric Green's function (G_R) of the embedded conductors with a finite dielectric width is given by

$$G_R(x;\xi) = -\frac{1}{4\pi\epsilon_1}\log\{(x-\xi)^2\}+\frac{1}{4\pi\epsilon_1}G_1(x;\xi,0)$$
$$+\frac{1}{4\pi\epsilon_1}\sum_{n=1}^{\infty}K^{2n-1}\Big(\log\{(2nh-2rh)^2+(x-\xi)^2\}-G_1(x;\xi,[2nh-2rh])\Big) \tag{2.62}$$
$$+\frac{1}{4\pi\epsilon_1}\sum_{n=1}^{\infty}K^{2n-1}\Big(\log\{(2(n-1)h+2rh)^2+(x-\xi)^2\}-G_1(x;\xi,[2(n-1)h+2rh])\Big)$$
$$-\frac{1}{4\pi\epsilon_1}2\sum_{n=1}^{\infty}K^{2n}\Big(\log\{(2nh)^2+(x-\xi)^2\}-G_1(x;\xi,[2nh])\Big).$$

The first two terms of (2.62) represent a single charge located at $y = 0$ and its infinite image representation through the vertical dielectric boundaries. The remaining terms depict the images of this single charge through the horizontal boundaries and the infinite image representation of each one of them through the vertical boundaries. These two image representations (vertical and horizontal) can be separated and expressed as

$$\begin{aligned} G_R(x;\xi) = \; & G_E(x;\xi) + \frac{1}{4\pi\epsilon_1} G_1(x;\xi,0) \\ & - \frac{1}{4\pi\epsilon_1} \sum_{n=1}^{\infty} K^{2n-1} \{G_1(x;\xi,[2nh - 2rh])\} \\ & - \frac{1}{4\pi\epsilon_1} \sum_{n=1}^{\infty} K^{2n-1} \{G_1(x;\xi,[2(n-1)h + 2rh])\} \\ & + \frac{1}{4\pi\epsilon_1} 2 \sum_{n=1}^{\infty} K^{2n} \{G_1(x;\xi,[2nh])\}, \end{aligned} \tag{2.63}$$

where $G_E(x;\xi)$ is given by (2.58).

Normalizing (2.63) is straightforward. Starting with G_1,

$$\begin{aligned} G_1(\bar{x};\bar{\xi},\bar{y}) = \sum_{m=1}^{\infty} (-1)^{m+1} K^m \Big(& \log\{[m\overline{W}_d + (-1)^m \bar{\xi} - \bar{x}]^2 + \bar{y}^2\} + \\ & \log\{[m\overline{W}_d + (-1)^{m+1} \bar{\xi} + \bar{x}]^2 + \bar{y}^2\} \Big) \\ + \sum_{m=1}^{\infty} (-1)^{m+1} K^m \Big(& \log\{4h^2\} + \log\{4h^2\} \Big), \end{aligned} \tag{2.64}$$

where an overline on a variable indicates normalization with respect to $2h$. But, since

$$\sum_{m=1}^{\infty} (-1)^{m+1} K^m = \frac{K}{1+K}, \tag{2.65}$$

(2.64) becomes

$$G_1(\bar{x};\bar{\xi},\bar{y}) = \sum_{m=1}^{\infty}(-1)^{m+1}K^m\Big(\log\{[m\overline{W}_d+(-1)^m\bar{\xi}-\bar{x}]^2+\bar{y}^2\}+ \log\{[m\overline{W}_d+(-1)^{m+1}\bar{\xi}+\bar{x}]^2+\bar{y}^2\}\Big) + \frac{2K}{1+K}\log(4h^2). \tag{2.66}$$

For convenience, a redefinition of G_1 is in order,

$$G_1(\bar{x};\bar{\xi},\bar{y}) = \sum_{m=1}^{\infty}(-1)^{m+1}K^m\Big(\log\{[m\overline{W}_d+(-1)^m\bar{\xi}-\bar{x}]^2+\bar{y}^2\}+ \log\{[m\overline{W}_d+(-1)^{m+1}\bar{\xi}+\bar{x}]^2+\bar{y}^2\}\Big). \tag{2.67}$$

Equation (2.63) can now be expressed in normalized coordinates as

$$\begin{aligned} G_R(\bar{x};\bar{\xi}) &= G_E(\bar{x};\bar{\xi})+\frac{1}{4\pi\epsilon_1}G_1(\bar{x};\bar{\xi},0)+\frac{2K}{1+K}\frac{1}{4\pi\epsilon_1}\log(4h^2) \\ &-\frac{1}{4\pi\epsilon_1}\sum_{n=1}^{\infty}K^{2n-1}G_1(\bar{x};\bar{\xi},[n-r])-\frac{1}{4\pi\epsilon_1}\sum_{n=1}^{\infty}K^{2n-1}\frac{2K}{1+K}\log(4h^2) \\ &-\frac{1}{4\pi\epsilon_1}\sum_{n=1}^{\infty}K^{2n-1}G_1(\bar{x};\bar{\xi},[(n-1)+r])-\frac{1}{4\pi\epsilon_1}\sum_{n=1}^{\infty}K^{2n-1}\frac{2K}{1+K}\log(4h^2) \\ &+\frac{1}{4\pi\epsilon_1}2\sum_{n=1}^{\infty}K^{2n}G_1(\bar{x};\bar{\xi},[n])+\frac{1}{4\pi\epsilon_1}2\sum_{n=1}^{\infty}K^{2n}\frac{2K}{1+K}\log(4h^2). \end{aligned} \tag{2.68}$$

Factorizing,

$$\begin{aligned} G_R(\bar{x};\bar{\xi}) &= G_E(\bar{x};\bar{\xi})+\frac{1}{4\pi\epsilon_1}G_1(\bar{x};\bar{\xi},0)-\frac{1}{4\pi\epsilon_1}\sum_{n=1}^{\infty}K^{2n-1}G_1(\bar{x};\bar{\xi},[n-r]) \\ &-\frac{1}{4\pi\epsilon_1}\sum_{n=1}^{\infty}K^{2n-1}G_1(\bar{x};\bar{\xi},[(n-1)+r])+\frac{1}{4\pi\epsilon_1}2\sum_{n=1}^{\infty}K^{2n}G_1(\bar{x};\bar{\xi},[n]) \\ &+\frac{2K}{1+K}\frac{1}{4\pi\epsilon_1}\log(4h^2)\left(1-\sum_{n=1}^{\infty}K^{2n-1}-\sum_{n=1}^{\infty}K^{2n-1}+2\sum_{n=1}^{\infty}K^{2n}\right). \end{aligned} \tag{2.69}$$

Since,

$$\left(1-\sum_{n=1}^{\infty}K^{2n-1}-\sum_{n=1}^{\infty}K^{2n-1}+2\sum_{n=1}^{\infty}K^{2n}\right)=\frac{1-K}{1+K}=\epsilon_r, \tag{2.70}$$

and

$$\frac{2K}{1+K}=1-\epsilon_r, \tag{2.71}$$

(2.69) becomes,

$$\begin{aligned} G_R(\overline{x};\overline{\xi}) &= G_E(\overline{x};\overline{\xi})+\frac{1}{4\pi\epsilon_1}G_1(\overline{x};\overline{\xi},0)-\frac{1}{4\pi\epsilon_1}\sum_{n=1}^{\infty}K^{2n-1}G_1(\overline{x};\overline{\xi},[n-r]) \\ &-\frac{1}{4\pi\epsilon_1}\sum_{n=1}^{\infty}K^{2n-1}G_1(\overline{x};\overline{\xi},[(n-1)+r])+\frac{1}{4\pi\epsilon_1}2\sum_{n=1}^{\infty}K^{2n}G_1(\overline{x};\overline{\xi},[n]) \\ &+\frac{\epsilon_r(1-\epsilon_r)}{4\pi\epsilon_1}\log(4h^2), \end{aligned} \tag{2.72}$$

where,

$$\begin{aligned} G_E(\overline{x};\overline{\xi}) = -\frac{1}{4\pi\epsilon_1}\Bigg(&\log(\zeta^2)+\epsilon_r\log(4h^2)+\sum_{n=1}^{\infty}K^{2n}\log(n^2+\zeta^2)^2 \\ &-\sum_{n=1}^{\infty}K^{2n-1}\log\{[(n-1+r)^2+\zeta^2][(n-r)^2+\zeta^2]\}\Bigg), \end{aligned} \tag{2.73}$$

or any alternative representation given in the previous section, and

$$\begin{aligned} G_1(\overline{x};\overline{\xi},\overline{y}) = \sum_{m=1}^{\infty}(-1)^{m+1}K^m\Big(&\log\{[m\overline{W}_d+(-1)^m\overline{\xi}-\overline{x}]^2+\overline{y}^2\}+ \\ &\log\{[m\overline{W}_d+(-1)^{m+1}\overline{\xi}+\overline{x}]^2+\overline{y}^2\}\Big). \end{aligned} \tag{2.74}$$

The Green's function given by (2.72) can be used as an approximation to that applicable to a ribbon cable. Indeed, the Green's function of a ribbon cable is impossible to calculate analytically due to the circular boundaries of the structure. An interesting experiment would be to calculate numerically the Green's function of the ribbon cable, by applying the finite element or finite difference method, and to compare the results with (2.72). Probably, in many applications, the approximation given by (2.72) will prove to be satisfactory.

The magnetic Green's function of this structure is the same as the one given in the previous section (embedded conductors with no ground plane and an infinite dielectric width).

CHAPTER 3
PROJECTION INTEGRALS

The evaluation of the following projection integrals constitutes the most difficult and computationally expensive step in the implementation of the method discussed in Chapter 1:

$$P_{mn} = \int\int G_E(\overline{x};\overline{\xi})\, p_m(\overline{\xi}) p_n(\overline{x})\, d\overline{\xi} d\overline{x} \tag{3.1}$$

$$L_{mn} = \int\int G_M(\overline{x};\overline{\xi})\, p_m(\overline{\xi}) p_n(\overline{x})\, d\overline{\xi} d\overline{x}. \tag{3.2}$$

The singularity of all of the Green's functions calculated in Chapter 2, coupled with the possibility of error occurring during their calculation (as shown in Appendix A) leads to the use of a mixture of analytical and numerical integration methods.

The present chapter describes methods to make the singularity *integrable* by exploiting numerical and analytical schemes.

3.1 SECTIONAL INTEGRATION

Integrations should be performed sectionally. The choice of the basis functions relies on two factors. First, the numerical stability or condition numbers of the matrices must be considered while computing the eigenfunctions. For instance, simple basis functions such as monomials will simplify the implementation of the integration (data structure and the program). Unfortunately, the use of monomials of an order greater than one will result in badly conditioned matrices. Second, the excitations to be applied to transmission structures in due course will very likely be sectionally defined. Therefore, for post-processing considerations, it is better to use polynomials defined sectionally such as Lagrangian polynomials of moderate order. High order Lagrangian polynomials are also likely to give rise to numerical instability since they are not orthogonal but rather linearly independent. Orthogonal polynomials of any kind (Legendre, Chebyshev, $\cdots$) tend

to be the most numerically stable. However, the post-processing with such polynomials is more difficult than Lagrangian polynomials. For generality, the coefficients of the basis functions will be undefined in order to experiment any kind of polynomials or monomials. Thus, since the structures will be sectionally defined and piecewise continuous, it will be convenient to integrate them using the same sectional bases regardless of the fact that each section may have a basis function of a different order.

Sectional treatment of the integrals is straightforward. The normalized width of the structure is hereafter denoted by

$$\overline{w} = \frac{w}{2h}. \tag{3.3}$$

Let the integration ranges in $\overline{x}$ and $\overline{\xi}$, which both cover the structure width $-\frac{\overline{w}}{2} \le \overline{x} \le \frac{\overline{w}}{2}$ and $-\frac{\overline{w}}{2} \le \overline{\xi} \le \frac{\overline{w}}{2}$, be divided into segments. The segments need not be of the same width. This amounts to subdividing the $\overline{x}$-$\overline{\xi}$ plane into a set of nonoverlapping rectangles and integrating over each one in turn as in Figure 3.1. Suppose there are M segments Ω_k that span $\overline{x}_{k-1} \le \overline{x} \le \overline{x}_k$, with $\overline{x}_0 = -\frac{\overline{w}}{2}$ and $\overline{x}_M = \frac{\overline{w}}{2}$. Then

$$P_{mn} = \sum_i \sum_j \int_{\Omega_i} \int_{\Omega_j} G_E(\overline{x};\overline{\xi})\, p_m(\overline{\xi}) p_n(\overline{x})\, d\overline{\xi} d\overline{x}. \tag{3.4}$$

Because L_{mn} is subject to a similar development, the focus of the following will be on the influence matrix P. Furthermore, since all of the Green's functions contain the same kind of singularity, only the Green's function for conductors printed on the substrate with a ground plane (section 2.2.1) will be considered. Substituting the detailed Green's function,

$$P_{mn} = \frac{1}{2\pi\epsilon_0(\epsilon_r+1)} \sum_{n=0}^{\infty} K^n \sum_i \sum_j I_{mnij}(n) \tag{3.5}$$

where

$$I_{mnij}(n) = \int_{\overline{x}_{i-1}}^{\overline{x}_i} \int_{\overline{x}_{j-1}}^{\overline{x}_j} \log \frac{(n+1)^2 + (\overline{x}-\overline{\xi})^2}{n^2 + (\overline{x}-\overline{\xi})^2} p_m(\overline{\xi}) p_n(\overline{x})\, d\overline{\xi} d\overline{x}. \tag{3.6}$$

In the case of polynomials of moderate order (e.g., $p_m(\overline{x})$ and $p_n(\overline{x})$ reasonably

simple) the unexpected but pleasing result is that analytical treatment of these integrals is possible.

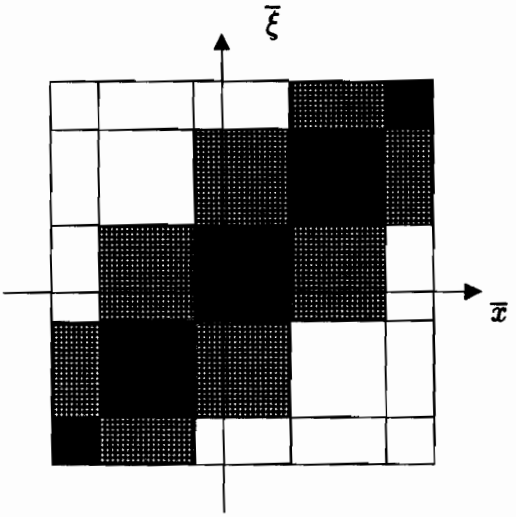

Figure 3.1 Sectional double integration. Line singularities occur in the darkly shaded areas, point singularities are represented in areas of light shading, and no singularities are present elsewhere.

Recall that $\zeta = \overline{x} - \overline{\xi}$. Because $\log\zeta$ is singular at $\zeta = 0$, the integrand of $I_{mnij}(0)$ is singular at all points where $\overline{x} = \overline{\xi}$, i.e., along the diagonal in Figure 3.1 . Three distinct cases therefore arise, as illustrated in Figure 3.1. First, a line singularity arises for $i = j$, i.e., the integrand is singular at all points along a diagonal line in the $\overline{x}$-$\overline{\xi}$ plane. Here the singularity dominates and forms a principal influence on the integral value in the dark squares of Figure 3.1. Second, a point singularity arises if $|i-j| = 1$; the integrand is singular only at a corner point of the region $\Omega_i \times \Omega_j$ i.e., in the lightly shaded rectangles of Figure 3.1. While the point singularity may influence the numerical result, it contributes less strongly than the line singularity of the first case. Third, in all other rectangles of Figure 3.1 $|i-j| > 1$, there is no singularity of any kind. Straightforward numerical quadratures are satisfactory in such cases. Although analytic integration is possible in the third case, numerical quadrature is likely to prove computationally more efficient and equally accurate. In the first two cases, at least partly analytic integration is indicated.

Because their requirements differ in practice, the three cases will now be dealt with separately. It will be assumed that $p_m(\bar{\xi})$ and $p_n(\bar{x})$ are polynomials, for example

$$p_n(\bar{x}) = \sum_{k=0}^{N} a_k \bar{x}^k, \tag{3.7}$$

$$p_m(\bar{\xi}) = \sum_{k=0}^{N} b_k \bar{\xi}^k. \tag{3.8}$$

The algebraic complexity of high-order approximations is immense, therefore sectionally low-order polynomials will be used.

3.2 INTEGRATION THROUGH LINE SINGULARITIES

Regardless of the nature of the polynomial approximants, the singular integrals containing line singularities all take the form

$$I_{mnii}(n) = \int_{\bar{x}_{i-1}}^{\bar{x}_i} \int_{\bar{x}_{i-1}}^{\bar{x}_i} \log \frac{(n+1)^2 + (\bar{x} - \bar{\xi})^2}{n^2 + (\bar{x} - \bar{\xi})^2} p_m(\bar{\xi}) p_n(\bar{x}) \, d\bar{\xi} d\bar{x}. \tag{3.9}$$

It is possible to evaluate these analytically, for suitable closed forms are known in terms of the elementary functions if the integrand functions $p_m(\bar{\xi})$ and $p_n(\bar{x})$ are polynomials. Nevertheless, analytic evaluation is very difficult, for reasons of sheer complexity. In principle, it should be possible to write a program, in the programming language of one of the established symbolic algebra packages (Mathematica, Maple, Derive, etc.), to perform the necessary integrations and algebraic substitutions. In practice however, these fail to perform unless extensive preliminary work is done. Failure may occur in one of several modes. The number of intermediate terms generated in the calculation may prove overwhelming, so that even after many hours of computing, no result is obtained; this form of failure was encountered with Maple for polynomials of order 1, though, oddly enough, correct results were obtained for order 0! Alternatively, the exercise of enough patience may be rewarded with so large a number of pages of computed terms that organizing the results into a useful form presents a near-hopeless task. In principle it is possible to have C or Fortran 77 statements generated directly,

and indeed (in the case of Maple) to have the generated code optimized, in the sense this word is employed by compiler builders (by identifying and extracting any recurring subsidiary terms). Unfortunately, the code thus generated is defective for another reason: symbolic algebra programs do not restrict themselves to the real domain in the same way that numerical programming languages do, hence square roots and logarithms of negative arguments abound in the resulting code. Although the end result may in principle be a pure real quantity, intermediate calculations need to be done in complex arithmetic; and in any case, the existence of roundoff error ensures that cancellation of imaginary parts is rarely carried out to perfection. Calculating the integrations analytically while still producing efficient numeric code therefore requires substantial preliminary work by hand and extensive manual intervention in the algebraic processes. On the other hand, the work reported here is sufficiently demanding algebraically that there is little prospect of it being carried out without the assistance of symbolic computation.

The key to efficient computation lies in the coordinate transformation sketched in Figure 3.2. The normalized geometric coordinates are transformed by $\zeta = \overline{x} - \overline{\xi}$ as previously, and

$$\eta = \overline{x} + \overline{\xi} - \overline{x}_i - \overline{x}_{i-1}. \tag{3.10}$$

For convenience, let

$$\overline{r}_i = \frac{\overline{x}_i + \overline{x}_{i-1}}{2} \tag{3.11}$$

denote the normalized midpoint of the i^{th} segment. Correspondingly, let

$$\overline{w}_i = \overline{x}_i - \overline{x}_{i-1} \tag{3.12}$$

represent the normalized width of the i^{th} segment.
This coordinate transformation may be stated as

$$\zeta = \overline{x} - \overline{\xi} \tag{3.13}$$

$$\eta = \overline{x} + \overline{\xi} - 2\overline{r}_i, \tag{3.14}$$

and inversely

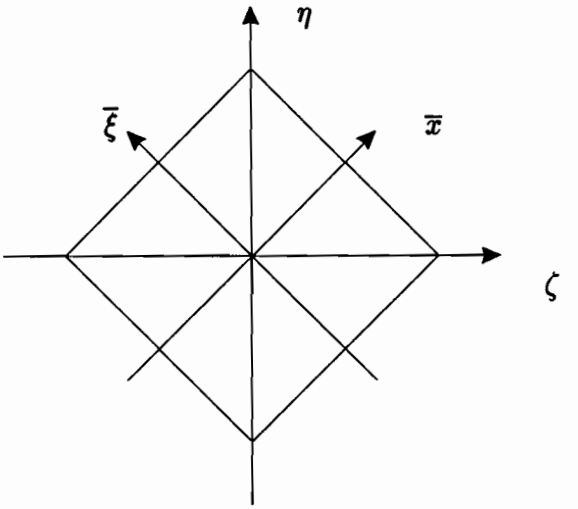

Figure 3.2 Sectional integration: a rotation transformation brings singularities onto a single coordinate axis.

$$\bar{x} = \frac{\zeta + \eta}{2} + \bar{r}_i \tag{3.15}$$

$$\bar{\xi} = \frac{-\zeta + \eta}{2} + \bar{r}_i. \tag{3.16}$$

The Maple program (and probably most of the other symbolic math packages) is capable of producing an analytical result for the integration after the coordinate transformation outlined. Nevertheless, for orders of polynomials higher that 1, the generated output is quite large, resulting in huge files containing several hundred lines of arithmetic evaluations. Even though it is possible to get a numerical answer from the generated output, such endless arithmetic operations may lead to round-off errors. Furthermore, depending on the nature of the polynomial being used (for example in the case of Lagrangian polynomials), the coefficients for distant elements may almost be identical yet with opposite signs. This may result in catastrophic cancellations during the evaluations of the generated arithmetic expressions. Therefore, it is desirable to express the basis function in local coordinate independent of the size and position (simplex coordinates) of the element. By centering the local coordinates at the origin, the midpoint $\bar{r}_i$ will be

equal to 0 which will reduce considerably the number of expressions generated by the symbolic math packages.

Thus, the following coordinate transformation aims at expressing the polynomials in local coordinate,

$$\overline{x} = \frac{\overline{w}_i}{2} u + \overline{r}_i, \tag{3.17}$$

$$\overline{\xi} = \frac{\overline{w}_i}{2} v + \overline{r}_i \tag{3.18}$$

and inversely

$$u = \frac{2}{\overline{w}_i} (\overline{x} - \overline{r}_i), \tag{3.19}$$

$$v = \frac{2}{\overline{w}_i} (\overline{\xi} - \overline{r}_i). \tag{3.20}$$

Thus, the singular integral

$$I_{mnii}(n) = \int_{\overline{x}_{i-1}}^{\overline{x}_i} \int_{\overline{x}_{i-1}}^{\overline{x}_i} \log \frac{(n+1)^2 + (\overline{x} - \overline{\xi})^2}{n^2 + (\overline{x} - \overline{\xi})^2} p_m(\overline{\xi}) p_n(\overline{x}) \, d\overline{\xi} d\overline{x} \tag{3.21}$$

becomes

$$I_{mnii}(n) = \frac{\overline{w}_i^2}{4} \int_{-1}^{+1} \int_{-1}^{+1} \log \frac{(n+1)^2 + \left(\frac{\overline{w}_i}{2}(u-v)\right)^2}{n^2 + \left(\frac{\overline{w}_i}{2}(u-v)\right)^2} p_m(v) p_n(u) \, dv du. \tag{3.22}$$

Note that the polynomials $p_m(\overline{u})$ and $p_n(\overline{v})$ are now expressed in the local coordinates $\overline{u}$ and $\overline{v}$, with no loss of precision. Furthermore, the coefficients of the polynomials need to be calculated once independently of the position of the element.

The second coordinate transformation may now be stated as

$$\zeta = \frac{u - v}{2} \tag{3.23}$$

$$\eta = \frac{u + v}{2}. \tag{3.24}$$

For convenience, the transformation can be stated in matrix notation,

$$\begin{bmatrix} \zeta \\ \eta \end{bmatrix} = \frac{1}{2} \begin{bmatrix} +1 & -1 \\ +1 & +1 \end{bmatrix} \begin{bmatrix} u \\ v \end{bmatrix} \tag{3.25}$$

and inversely,

$$\begin{bmatrix} u \\ v \end{bmatrix} = \begin{bmatrix} +1 & +1 \\ -1 & +1 \end{bmatrix} \begin{bmatrix} \zeta \\ \eta \end{bmatrix}. \tag{3.26}$$

The integration limits are clearly the four edges of the square defined by $v = \pm 1$, $u = \pm 1$, $v = 0, u = 0$ in quadrants 4, 1, 2, 3, respectively. The corresponding expressions in ζ, η are obtained by substitution. In the fourth and second quadrants, v has a fixed value. Thus,

$$\eta = -1 + \zeta \qquad 4^{th} \text{ quadrant}, \tag{3.27}$$

$$\eta = +1 + \zeta \qquad 2^{nd} \text{ quadrant}, \tag{3.28}$$

$$\eta = -1 - \zeta \qquad 3^{rd} \text{ quadrant}, \tag{3.29}$$

$$\eta = +1 - \zeta \qquad 1^{st} \text{ quadrant}. \tag{3.30}$$

Under this transformation, the polynomials in u and v transform into polynomials in ζ, η:

$$f_{mn}(\zeta, \eta) = p_m(\zeta; \eta) p_n(\zeta; \eta). \tag{3.31}$$

The integral given by (3.22) now takes the form,

$$I_{mnii}(n) = \frac{\overline{w}_i^2}{4}\left(\int_{-1}^{0} \int_{-1-\zeta}^{+1+\zeta} \log\frac{(n+1)^2 + (\overline{w}_i\zeta)^2}{n^2 + (\overline{w}_i\zeta)^2} f_{mn}(\zeta,\eta)\, 2\, d\eta\, d\zeta + \right.$$

$$\left. \int_{0}^{1} \int_{-1+\zeta}^{+1-\zeta} \log\frac{(n+1)^2 + (\overline{w}_i\zeta)^2}{n^2 + (\overline{w}_i\zeta)^2} f_{mn}(\zeta,\eta)\, 2\, d\eta\, d\zeta \right). \tag{3.32}$$

The factor 2 attached to the area element $d\eta\, d\zeta$ is the Jacobian of the coordinate transformation. Note that the two halves of the interval in ζ must be treated independently; their integrands can be expressed as polynomials in each half, but they do not have to sustain a continuous polynomial representation over the entire range. This is the result of ζ appearing in the integration limits. To map all integrations onto the right half plane, the first integral is reversed, by substituting ζ for $-\zeta$:

$$I_{mnii}(n) = \frac{\overline{w}_i^2}{2}\left(\int_{0}^{1} \int_{-1+\zeta}^{+1-\zeta} \log\frac{(n+1)^2 + (\overline{w}_i\zeta)^2}{n^2 + (\overline{w}_i\zeta)^2} f_{mn}(-\zeta,\eta)\, d\eta\, d\zeta + \right.$$

$$\left. \int_{0}^{1} \int_{-1+\zeta}^{+1-\zeta} \log\frac{(n+1)^2 + (\overline{w}_i\zeta)^2}{n^2 + (\overline{w}_i\zeta)^2} f_{mn}(\zeta,\eta)\, d\eta\, d\zeta \right). \tag{3.33}$$

With the two integration areas now identical,

$$I_{mnii}(n) = \frac{\overline{w}_i^2}{2}\left(\int_{0}^{1} \log\frac{(n+1)^2 + (\overline{w}_i\zeta)^2}{n^2 + (\overline{w}_i\zeta)^2} \right.$$

$$\left. \int_{-1+\zeta}^{+1-\zeta} (f_{mn}(-\zeta,\eta) + f_{mn}(\zeta,\eta))\, d\eta\, d\zeta \right). \tag{3.34}$$

In computational practice, the work seems to run best if expressions are kept small and compact. To achieve that goal, the inner integral is evaluated, then viewed as a polynomial in ζ,

$$\sum_k C_k \zeta^k = \int_{-1+\zeta}^{+1-\zeta} (f_{mn}(-\zeta,\eta) + f_{mn}(\zeta,\eta))\, d\eta. \tag{3.35}$$

The outer integral is then evaluated term by term and summed:

$$I_{mnii}(n) = \frac{\overline{w}_i^2}{2} \sum_k C_k \int_0^1 \zeta^k \log \frac{(n+1)^2 + (\overline{w}_i \zeta)^2}{n^2 + (\overline{w}_i \zeta)^2} d\zeta. \tag{3.36}$$

The Maple program described in Appendix B, carries out these steps in the sequence outlined above. It generates an output in C (optimized) for polynomials of order 5.

Corresponding results may be obtained for other powers with the above program, by setting N to have the desired value. The same results are also generated by the program as C statements, first by straight translation and then with subexpression optimization. The optimized programs, while generally a little longer, run faster. Equivalent programs in Fortran are available as an alternative to C.

3.3 INTEGRATION THROUGH POINT SINGULARITIES

There is only one possible place that a point singularity can occur in the integrals considered here: at a corner of the rectangular region of integration. That is to say, the integrals now take on the appearance

$$I_{mnij}(n) = \int_{\overline{x}_{i-1}}^{\overline{x}_i} \int_{\overline{x}_{j-1}}^{\overline{x}_j} \log \frac{(n+1)^2 + (\overline{x} - \overline{\xi})^2}{n^2 + (\overline{x} - \overline{\xi})^2} p_m(\overline{\xi}) p_n(\overline{x}) d\overline{\xi} d\overline{x}. \tag{3.37}$$

In this particular case $|i - j| = 1$. In detail, two possibilities arise:

$$I_{mnij}(n) = \int_{\overline{x}_{i-1}}^{\overline{x}_i} \int_{\overline{x}_i}^{\overline{x}_{i+1}} \log \frac{(n+1)^2 + (x - \overline{\xi})^2}{n^2 + (\overline{x} - \overline{\xi})^2} p_m(\overline{\xi}) p_n(\overline{x}) d\overline{\xi} d\overline{x} \tag{3.38}$$

and

$$I_{mnji}(n) = \int_{\overline{x}_i}^{\overline{x}_{i+1}} \int_{\overline{x}_{i-1}}^{\overline{x}_i} \log \frac{(n+1)^2 + (\overline{x} - \overline{\xi})^2}{n^2 + (\overline{x} - \overline{\xi})^2} p_m(\overline{\xi}) p_n(\overline{x}) d\overline{\xi} d\overline{x}. \tag{3.39}$$

These correspond to rectangular regions lying above and below the diagonal $\overline{x} = \overline{\xi}$ respectively, as illustrated in Figure 3.3. However, when Lagrangian interpolation polynomials are chosen to be the basis functions, an integral over the region of interest is still nonsingular if either of the polynomials vanishes at that point. In

other words, a Lagrangian element of order N has interpolation nodes at both endpoints, so only one interpolation function fails to vanish at each end: the last Lagrangian polynomial of the left element and the first Lagrangian polynomial of the right element.

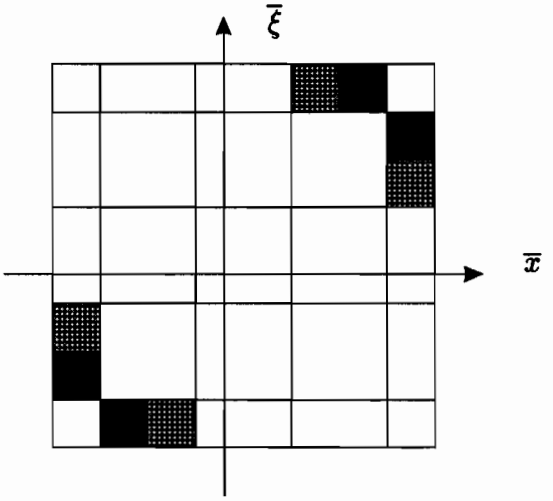

Figure 3.3 Integration touching corner-point singularities: the integration areas occur in complementary pairs.

Because the two singular cases (above and below the diagonal) are subject to a similar development, the focus of the following will be on one of the singular cases: the singularity occurring at the upper left of the rectangle:

$$I_{mnij}(n) = \int_{\overline{x}_i}^{\overline{x}_{i+1}} \int_{\overline{\xi}_{i-1}}^{\overline{\xi}_i} \log \frac{(n+1)^2 + (x-\overline{\xi})^2}{n^2 + (\overline{x}-\overline{\xi})^2} p_m(\overline{\xi}) p_n(\overline{x})\, d\overline{\xi} d\overline{x}. \tag{3.40}$$

Here, as in the integration over line singularities, the actual values of $\overline{x}_i$ and $\overline{\xi}_i$ are the same; they are kept distinct solely to retain traceability in the algebra. To develop an integration technique, let

$$\overline{s}_i = \min(\overline{x}_{i+1} - \overline{x}_i,\ \overline{\xi}_i - \overline{\xi}_{i-1}) \tag{3.41}$$

and

$$\overline{p}_{mn}(\overline{x}, \overline{\xi}) = p_m(\overline{\xi}) p_n(\overline{x}). \tag{3.42}$$

Subdivide the intervals of integration, breaking them into two parts.

If $(\overline{x}_{i+1}-\overline{x}_i) > (\overline{\xi}_i - \overline{\xi}_{i-1})$, then $\overline{s}_i = \overline{\xi}_i - \overline{\xi}_{i-1}$, and

$$I_{mnij}(n) = \int_{\overline{x}_i}^{\overline{x}_i+s_i}\int_{\overline{\xi}_{i-1}}^{\overline{\xi}_i} \log\frac{(n+1)^2+(\overline{x}-\overline{\xi})^2}{n^2+(\overline{x}-\overline{\xi})^2}\overline{p}_{mn}(\overline{x},\overline{\xi})\,d\overline{\xi}d\overline{x} + \int_{\overline{x}_i+s_i}^{\overline{x}_i+1}\int_{\overline{\xi}_{i-1}}^{\overline{\xi}_i} \log\frac{(n+1)^2+(\overline{x}-\overline{\xi})^2}{n^2+(\overline{x}-\overline{\xi})^2}\overline{p}_{mn}(\overline{x},\overline{\xi})\,d\overline{\xi}d\overline{x}. \tag{3.43}$$

If $(\overline{x}_{i+1}-\overline{x}_i) = (\overline{\xi}_i - \overline{\xi}_{i-1})$, then $\overline{s}_i = 0$, and the integral given by (3.40) stays intact.

If $(\overline{x}_{i+1}-\overline{x}_i) < (\overline{\xi}_i - \overline{\xi}_{i-1})$, then $\overline{s}_i = \overline{x}_{i+1} - \overline{x}_i$, and

$$I_{mnij}(n) = \int_{\overline{x}_i}^{\overline{x}_i+1}\int_{\overline{\xi}_{i-1}}^{\overline{\xi}_{i-1}+s_i} \log\frac{(n+1)^2+(\overline{x}-\overline{\xi})^2}{n^2+(\overline{x}-\overline{\xi})^2}\overline{p}_{mn}(\overline{x},\overline{\xi})\,d\overline{\xi}d\overline{x} + \int_{\overline{x}_i}^{\overline{x}_i+1}\int_{\overline{\xi}_{i-1}+s_i}^{\overline{\xi}_i} \log\frac{(n+1)^2+(\overline{x}-\overline{\xi})^2}{n^2+(\overline{x}-\overline{\xi})^2}\overline{p}_{mn}(\overline{x},\overline{\xi})\,d\overline{\xi}d\overline{x}. \tag{3.44}$$

It should be evident on examining (3.44) and (3.43), that, in both cases, the region of integration which is usually rectangular, splits into a square of side $\overline{s}_i$ and a rectangular remainder. The rectangular remainder is nonsingular while the singularity is always located at one corner of the square subregion. Verifying this assertion is relatively straightforward. If $\overline{s}_i = (\overline{\xi}_i - \overline{\xi}_{i-1})$, then the integrals of (3.43) become

$$I_{mnij}(n) = \int_{\overline{x}_i}^{\overline{x}_i+\overline{\xi}_i-\overline{\xi}_{i-1}}\int_{\overline{\xi}_{i-1}}^{\overline{\xi}_i} \log\frac{(n+1)^2+(\overline{x}-\overline{\xi})^2}{n^2+(\overline{x}-\overline{\xi})^2}\overline{p}_{mn}(\overline{x},\overline{\xi})\,d\overline{\xi}d\overline{x} + \int_{\overline{x}_i+s_i}^{\overline{x}_i+1}\int_{\overline{\xi}_{i-1}}^{\overline{\xi}_i} \log\frac{(n+1)^2+(\overline{x}-\overline{\xi})^2}{n^2+(\overline{x}-\overline{\xi})^2}\overline{p}_{mn}(\overline{x},\overline{\xi})\,d\overline{\xi}d\overline{x}, \tag{3.45}$$

and $\overline{x}_i + \overline{\xi}_i - \overline{\xi}_{i-1} - \overline{x}_i = \overline{\xi}_i - \overline{\xi}_{i-1}$.
On the other hand, if $\overline{s}_i = \overline{x}_{i+1} - \overline{x}_i$ then the integrals of (3.44) become

$$I_{mnij}(n) = \int_{\overline{x}_i}^{\overline{x}_{i+1}} \int_{\overline{\xi}_{i-1}}^{\overline{\xi}_i - s_i} \log \frac{(n+1)^2 + (\overline{x} - \overline{\xi})^2}{n^2 + (\overline{x} - \overline{\xi})^2} \overline{p}_{mn}(\overline{x}, \overline{\xi})\, d\overline{\xi} d\overline{x} + \tag{3.46}$$

$$\int_{\overline{x}_i}^{\overline{x}_{i+1}} \int_{\overline{\xi}_i - \overline{x}_{i+1} + \overline{x}_i}^{\overline{\xi}_i} \log \frac{(n+1)^2 + (\overline{x} - \overline{\xi})^2}{n^2 + (\overline{x} - \overline{\xi})^2} \overline{p}_{mn}(\overline{x}, \overline{\xi})\, d\overline{\xi} d\overline{x},$$

and $\overline{x}_{i+1} - \overline{x}_i = \overline{\xi}_i - \overline{\xi}_i + \overline{x}_{i+1} - \overline{x}_i$.

As in the previous section, an analytical solution can be obtained for the singular integral by a coordinate transformation that rotates the square subregion 45°. The rotation can be obtained through many different coordinate transformations. The choice of the appropriate transformation must be made according to its ability to minimize the output generated by the symbolic math package. The coordinate transformation that centers the square at the origin of the ζ-η plane has been adopted as depicted in Figure 3.4.

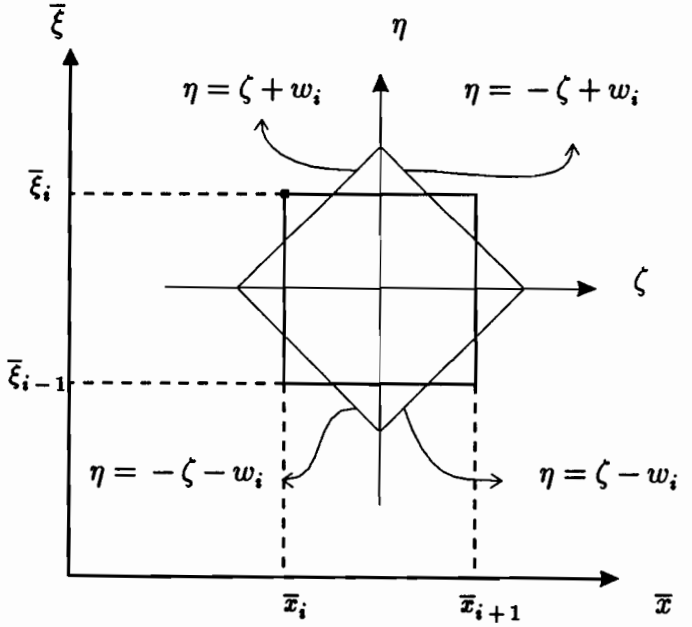

Figure 3.4 Coordinate transformation to create one-dimensional singularity from a corner-point singularity.

For convenience, the region of integration is chosen on a square, thus $\bar{s}_i = 0$. The normalized geometric coordinates are transformed by

$$\zeta = \bar{x} - \bar{\xi} + \bar{\xi}_i - \bar{\xi}_{i-1} - \bar{x}_{i+1} + \bar{x}_i \tag{3.47}$$

and

$$\eta = \bar{x} + \bar{\xi} - (\bar{\xi}_i - \bar{\xi}_{i-1} + \bar{x}_{i+1} - \bar{x}_i). \tag{3.48}$$

For simplicity, let

$$\bar{r}_\xi = \frac{\bar{\xi}_i + \bar{\xi}_{i-1}}{2}, \tag{3.49}$$

and

$$\bar{r}_x = \frac{\bar{x}_{i+1} + \bar{x}_i}{2},$$

denote the normalized midpoint of the two segments respectively. Correspondingly, let

$$\bar{w}_i = \bar{x}_{i+1} - \bar{x}_i = \bar{\xi}_i - \bar{\xi}_{i-1} \tag{3.50}$$

represent the normalized width of both segments. The transformation can now be stated as

$$\zeta = \bar{x} - \bar{\xi} + (\bar{r}_\xi - \bar{r}_x) \tag{3.51}$$

and

$$\eta = \bar{x} + \bar{\xi} - (\bar{r}_\xi + \bar{r}_x). \tag{3.52}$$

Inversely,

$$\bar{x} = \frac{\zeta + \eta}{2} + \bar{r}_x, \tag{3.53}$$

and

$$\bar{\xi} = \frac{-\zeta + \eta}{2} + \bar{r}_{\xi}. \tag{3.54}$$

The integration limits are clearly the four edges of the rotated square as illustrated by Figure 3.4. Thus,

$$\eta = -\zeta + w_i \qquad 1^{st} \text{ quadrant}, \tag{3.55}$$

$$\eta = +\zeta + w_i \qquad 2^{nd} \text{ quadrant}, \tag{3.56}$$

$$\eta = -\zeta - w_i \qquad 3^{rd} \text{ quadrant}, \tag{3.57}$$

$$\eta = +\zeta - w_i \qquad 4^{th} \text{ quadrant}. \tag{3.58}$$

The integral,

$$I_{mnij}(n) = \int_{\bar{x}_i}^{\bar{x}_i+1} \int_{\bar{\xi}_{i-1}}^{\bar{\xi}_i} \log \frac{(n+1)^2 + (\bar{x}-\bar{\xi})^2}{n^2 + (\bar{x}-\bar{\xi})^2} \bar{p}_{mn}(\bar{x}, \bar{\xi})\, d\bar{\xi} d\bar{x}$$

now takes the form

$$I_{mnij}(n) = \frac{1}{2}\left(\int_{-w_i}^{0} \int_{-w_i-\zeta}^{+w_i+\zeta} \log \frac{(n+1)^2 + (\zeta + r_x - r_{\xi})^2}{n^2 + (\zeta + r_x - r_{\xi})^2} f_{mn}(\zeta, \eta)\, d\eta\, d\zeta + \right. \tag{3.59}$$

$$\left. \int_{0}^{w_i} \int_{-w_i+\zeta}^{+w_i-\zeta} \log \frac{(n+1)^2 + (\zeta + r_x - r_{\xi})^2}{n^2 + (\zeta + r_x - r_{\xi})^2} f_{mn}(\zeta, \eta)\, d\eta\, d\zeta \right)$$

where, as in the previous section, $f_{mn}(\zeta, \eta) = p_m(\zeta; \eta) p_n(\zeta; \eta)$. The factor 1/2 attached to the integral is the Jacobian of the coordinate transformation. Since the region of integration is a square, $r_x - r_{\xi} = w_i$. Therefore, the integral can be expressed as

$$I_{mnij}(n) = \frac{1}{2}\left(\int_{-w_i}^{0} \int_{-w_i-\zeta}^{+w_i+\zeta} \log\frac{(n+1)^2+(\zeta+w_i)^2}{n^2+(\zeta+w_i)^2} f_{mn}(\zeta,\eta)\,d\eta\,d\zeta + \right. \tag{3.60}$$

$$\left. \int_{0}^{w_i} \int_{-w_i+\zeta}^{+w_i-\zeta} \log\frac{(n+1)^2+(\zeta+w_i)^2}{n^2+(\zeta+w_i)^2} f_{mn}(\zeta,\eta)\,d\eta\,d\zeta \right).$$

Note that the integrals must be treated independently.

The point singularity is actually weak enough to yield to numerical integration. Figure 3.5 shows the error in evaluating point singular integrals for elements of order 0 through 3 by Gaussian quadrature in the x and ξ directions by ignoring the singularity.

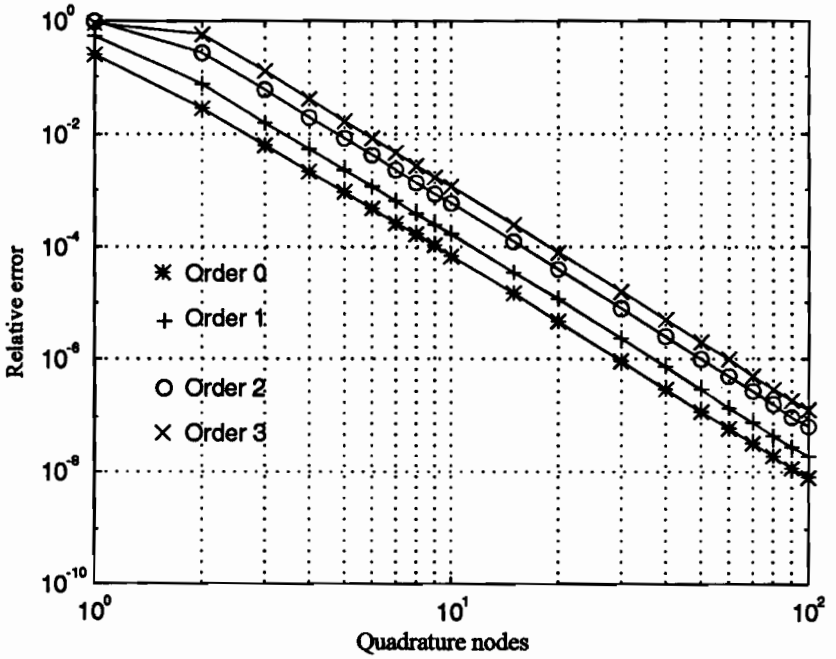

Figure 3.5 Error in evaluating point-singular integrals for elements orders 0 through 3 by Gaussian quadrature.

Evidently, the results are straight lines of the form,

$$\log E = a \log \frac{k}{c} \tag{3.61}$$

where E is the error, a is the slope, c is some constant and k is the number of nodes in the quadrature . Hence

$$E = \exp\left(a \log \frac{k}{c}\right) = \left(\frac{k}{c}\right)^a. \tag{3.62}$$

The slope of the lines is -4 (actually it is -3.9). For an order 0 element $c \simeq 0.87$, for an order 1 element $c \simeq 1.09$, for an order 2 element $c \simeq 1.50$ and for an order 3 element $c \simeq 1.79$. Therefore, the error in k-node quadrature is clearly $O(k^{-4})$ so the use of high-order Gaussian quadrature may be considered reliable at the cost of $O(k^2)$ computing time as against $O(1)$ for analytic integration.

3.4 STABILITY OF DISTANT INTEGRALS

There is no singularity at all when elements do not touch, so in theory there is no difficulty. In practice, numeric precision troubles may arise when the elements are at substantial distances from each other. As previously, let

$$\overline{r}_i = \frac{\overline{x}_i + \overline{x}_{i-1}}{2} \tag{3.63}$$

denote the normalized midpoint of the i^{th} element, and

$$\overline{w}_i = \overline{x}_i - \overline{x}_{i-1} \tag{3.64}$$

the normalized width of the i^{th} element. The integrations between distant elements are then

$$I_{mnij}(n) = \int_{\overline{x}_{i-1}}^{\overline{x}_i} \int_{\overline{x}_{j-1}}^{\overline{x}_j} \log \frac{(n+1)^2 + (\overline{x} - \overline{\xi})^2}{n^2 + (\overline{x} - \overline{\xi})^2} p_m(\overline{\xi}) p_n(\overline{x})\, d\overline{\xi} d\overline{x}. \tag{3.65}$$

Introduce the simple coordinate transformation

$$\overline{x} = \frac{\overline{w}_i}{2} \overline{u} + \overline{r}_i, \tag{3.66}$$

$$\overline{\xi} = \frac{\overline{w}_j}{2}\overline{v} + \overline{r}_j. \tag{3.67}$$

With this change of variables,

$$I_{mnij}(n) = \frac{\overline{w}_i\overline{w}_j}{4}\int_{-1}^{+1}\int_{-1}^{+1} \log\frac{(n+1)^2 + [\frac{1}{2}(\overline{w}_i\overline{u} - \overline{w}_j\overline{v}) + \overline{r}_i - \overline{r}_j]^2}{n^2 + [\frac{1}{2}(\overline{w}_i\overline{u} - \overline{w}_j\overline{v}) + \overline{r}_i - \overline{r}_j]^2} \tag{3.68}$$

$$p_m(\overline{u})p_n(\overline{v})\,d\overline{u}\,d\overline{v}.$$

Note that logarithmic integrand troubles may arise if the distances between elements and/or the image numbers n are enormously large. In either case, $I_{mnij}(n)$ will make only a small contribution to the summed integral P_{mn}, so the loss of precision is not significant. Nevertheless, expressing the polynomials $p_m(\overline{u})$ and $p_n(\overline{v})$ in local coordinates $\overline{u}$ and $\overline{v}$ is very convenient since the coefficients of the polynomials need to be calculated once, regardless of the position and width of the elements.

CHAPTER 4
CONDUCTORS PRINTED ON THE SUBSTRATE

A widely encountered electronics structure both at chip and board level is one where a group of numerous parallel conductors occupy a channel of predetermined width and are placed on the surface of a dielectric substrate. The theory developed in Chapter 1 suggests that the propagation modes of such a structure are substantially independent of structural details. On the other hand, the modes are mainly dependent on the parameters of the transmission channel, the substrate thickness and dielectric permittivity.

The present chapter examines the effect of the parameters on the modal functions and describes the modal spectrum. The Green's functions calculated in Chapter 2 concern very thin conductors where the density variations in the y direction may be neglected and the modeling in the x direction is sufficient. Recall from Chapter 1 that the approximation in terms of a finite basis functions is

$$\psi_k(\overline{x}) = \sum_{m=1}^{N} a_{km} p_m(\overline{x}), \tag{4.1}$$

$$\phi_k(\overline{x}) = \sum_{m=1}^{N} b_{km} p_m(\overline{x}). \tag{4.2}$$

The generalized eigenvalue problem therefore takes the form

$$\mathbf{C}^{-1}\mathbf{a}_k = c_k^2 \mathbf{L}\mathbf{a}_k, \tag{4.3}$$

where $\mathbf{C} = \mathbf{P}^{-1}$ and the matrices are given by

$$P_{mn} = \int\int G_E(\overline{x};\overline{\xi})\, p_m(\overline{\xi}) p_n(\overline{x})\, d\overline{\xi} d\overline{x} \tag{4.4}$$

$$L_{mn} = \int\int G_M(\overline{x};\overline{\xi})\, p_m(\overline{\xi}) p_n(\overline{x})\, d\overline{\xi} d\overline{x}, \tag{4.5}$$

where $\overline{x} = x/2h$. The two Green's functions (G_E and G_M) are calculated in Chapter 2 and integration techniques for evaluating the singular integrals are described in Chapter 3.

4.1 STRUCTURE WITH A GROUND PLANE

The electric Green's function of a structure with a ground plane (calculated in Chapter 2) is given by

$$G_E(\bar{x};\bar{\xi}) = \frac{1}{2\pi\epsilon_0(\epsilon_r+1)} \sum_{n=0}^{\infty} K^n \log \frac{(n+1)^2+\zeta^2}{n^2+\zeta^2}, \tag{4.6}$$

and the magnetic Green's function is

$$G_M(\bar{x};\bar{\xi}) = \frac{\mu_0}{4\pi} \log \frac{1+\zeta^2}{\zeta^2} \tag{4.7}$$

where $\zeta = \dfrac{x-\xi}{2h} = \bar{x}-\bar{\xi}$.

Computing the entries of the two matrices **P** and **L** with the leading constant will result in a matrix **P** with entries of $O(10^{+10})$ and a matrix **L** with entries of $O(10^{-7})$. A more convenient way is to compute the entries of the two matrices **P** and **L** without the leading constants, resulting in entries of the same order of magnitude for both matrices. Similarly, by normalizing the propagation velocities (the eigenvalues) with respect to the velocity of light, the results will be independent of constant though measured values such as ϵ_0. Thus, the entries of the matrix **P** must be computed as

$$P_{mn} = \sum_{n=0}^{\infty} K^n \int\int \log \frac{(n+1)^2+\zeta^2}{n^2+\zeta^2} p_m(\bar{\xi}) p_n(\bar{x})\, d\bar{\xi} d\bar{x}, \tag{4.8}$$

and those of **L** as

$$L_{mn} = \int\int \log \frac{1+\zeta^2}{\zeta^2} p_m(\bar{\xi}) p_n(\bar{x})\, d\bar{\xi} d\bar{x}. \tag{4.9}$$

The velocity v_i of a given mode i, normalized with respect to the free-space velocity, will then be

$$v_i = \sqrt{\frac{2}{(1+\epsilon_r)}\lambda_i} \tag{4.10}$$

where λ_i is the eigenvalue obtained by solving the generalized eigenvalue problem

with the entries of the matrices given by (4.8) and (4.9). From here on, modal velocity refers to the normalized velocity given by (4.10).

When all the finite elements have the same width and order, and in the absence of gaps between the finite elements, the resulting two matrices will be block Toeplitz (positive definite). Therefore, for order N finite elements, the first $N+1$ rows (or columns) of the matrices need to be calculated.

The number of terms for the series of the electric Green's function is chosen as follows. Since the image coefficient K is less than unity and always negative, the resulting alternating series converges faster than the corresponding geometric series. Thus, the number of terms required for a given accuracy can be obtained by calculating that required for a similar accuracy in the geometric series. Therefore, the number of terms is calculated as

$$K^n = 10^{-p} \tag{4.11}$$

where p is the required precision. Thus,

$$n = \frac{\log(10^{-p})}{\log(K)}. \tag{4.12}$$

The number of Gaussian quadrature nodes must be chosen according to several factors. The order of elements is an important factor since it is well known that k-node quadrature give exact solution to polynomials of order up to $2k-1$.

Whether the integration is taking place on adjacent or non-adjacent elements must also be taken into account. Finally, the index of the summation n plays a role in choosing the number of quadrature nodes. For example, on adjacent elements, when $n=0$, if numerical integration is adopted as opposed to analytical, the number of nodes must be chosen according to Figure 3.5.

For adjacent and non-adjacent elements of order 0, for $0 < n < 10$ in order to obtain an accurate answer up to 10^{-15}, 10-node quadrature is required. For $n \geq 10$, 5-node quadrature is sufficient to obtain the same accuracy.

An alternative, more efficient method of performing the integration is the use of an adaptive Gaussian quadrature such as Gauss-Kronrod.

Figure 4.1 illustrates the computing time for calculating the entries of the matrices for elements of order 0 through 3.

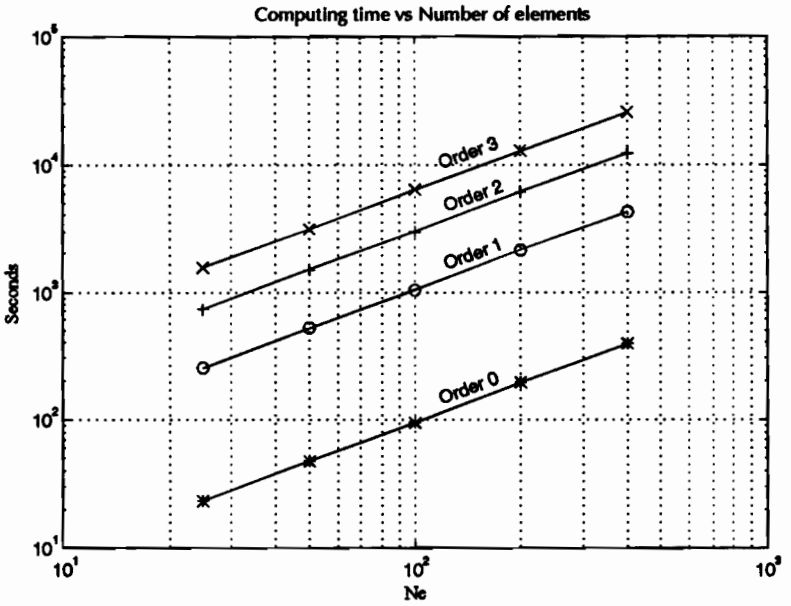

Figure 4.1 Computing time for calculating the entries of the matrices.

The computing times of Figure 4.1 are calculated on a computer with 486 microprocessor with 256K cache. The duration depends on the computer used as well as on the compiler. Indeed, the level of optimization reached in a compiler and the use of extended or conventional memory under MSDOS operating system are factors that might affect the computing time. All of the results obtained in this work, including Figure 4.1, are done by setting the precision p in (4.12) equal to 15. Figure 4.1 has been computed with ϵ_r equal to 9, resulting in a number of terms of the series equal to 154. The width of the channel is fixed to 10.0 times the substrate thickness h. The number of quadrature nodes is fixed to 15 regardless of the order of the elements, the integration region and the index of the summation n. Obviously, Figure 4.1 suggests that order 0 elements are the least time consuming despite the fact that a lesser number of higher order elements is required to obtain the same accuracy. Therefore, order 0 elements will be used to calculate the results.

4.1.1 Results of generalized eigenvalue problem

For the structure illustrated in Figure 4.2, where substrate relative permittivity ϵ_r is set to 9 and a width of the channel w 10.0 times the substrate thickness h, the first eight modal function pairs are illustrated in Figure 4.3. All of the x-axes in Figure 4.3 range between $[-1;1]$ and the y-axes range between $[-0.1;0.1]$. The potential eigenfunctions ϕ_i are continuous and bounded and have the "k wiggles in the k^{th} function". The current eigenfunctions ψ_i resemble the potential eigenfunctions, but show a singularity at the structure's edges. This behavior was expected since current and charge densities usually are singular at sharp edges. The unexpected result is that this singular behavior is not limited to only a few dominant modes but applies to *all* of them.

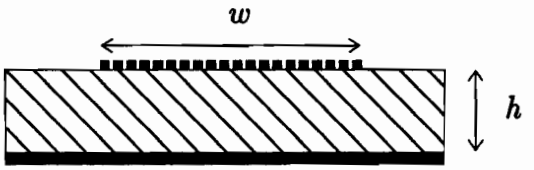

Figure 4.2 Parallel conductors printed on a dielectric substrate with a ground plane.

The modes can be separated in two groups: even and odd. A surprising observation is that not only does the first even mode have an average value different from 0, but this characteristic is present in all of the even modes. The odd modes have 0 average value as expected. Figure 4.4 illustrates the integral of the first 50 even eigenfunctions ($\int \psi_i(x)dx$ and $\int \phi_i(x)dx$ for $i = 1,3,5,...,99$). The integral of the current eigenfunctions seems to be decreasing for higher modes while the integral of the potential eigenfunctions remains relatively high.

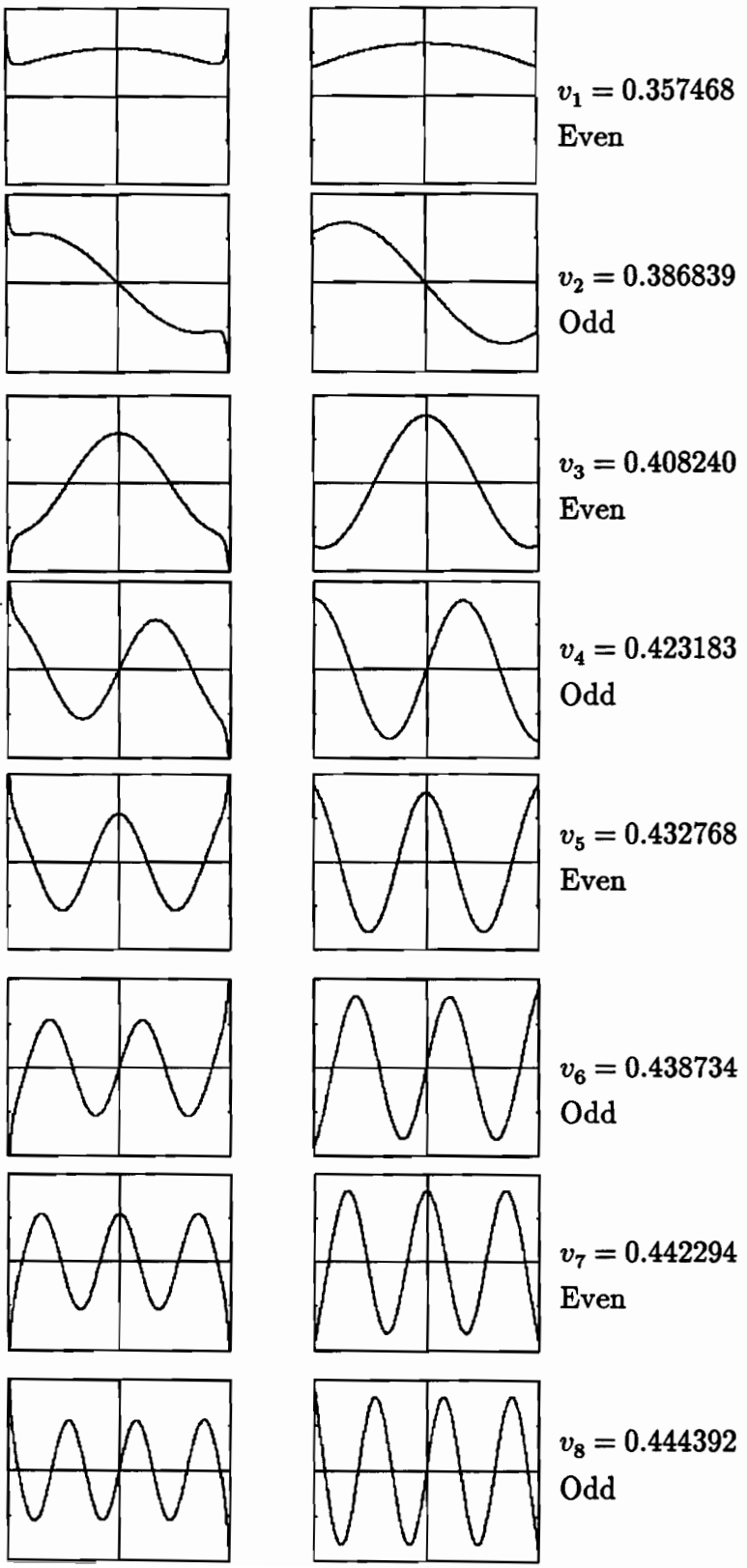

Figure 4.3 The first eight current (left) and potential (right) modal functions for thin parallel conductors printed on a dielectric substrate with a ground plane.

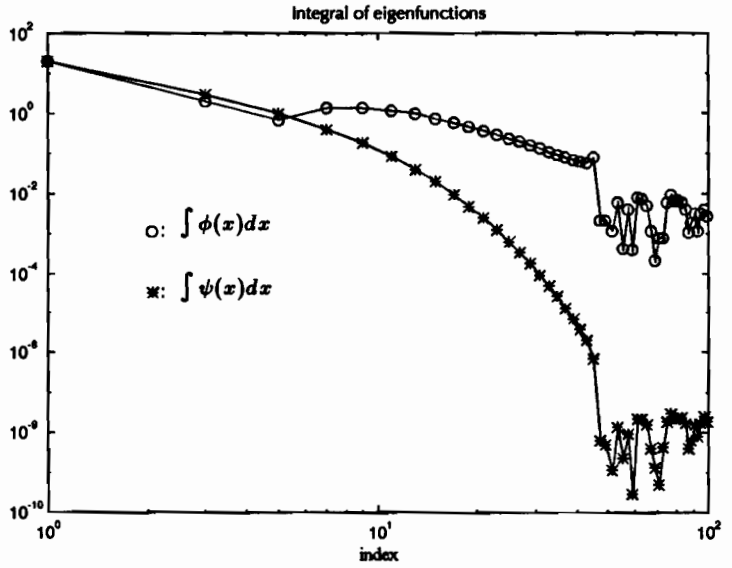

Figure 4.4 Integral of the even eigenfunctions.

Figure 4.5 shows the distribution of the first 25 modal velocities (normalized with respect to the free-space velocity of light). All modal velocities must lie between the velocity of a wave traveling in air alone and the velocity of a wave traveling in the substrate material alone. Since $\epsilon_r = 9$, these limits are 1 and 1/3. The first mode clearly carries a large proportion of its field energy in the substrate material since its velocity is barely higher than 1/3. Higher modes transport a larger proportion of their field energy in the air. After the 15^{th} velocity, the values are identical to four or more significant digits.

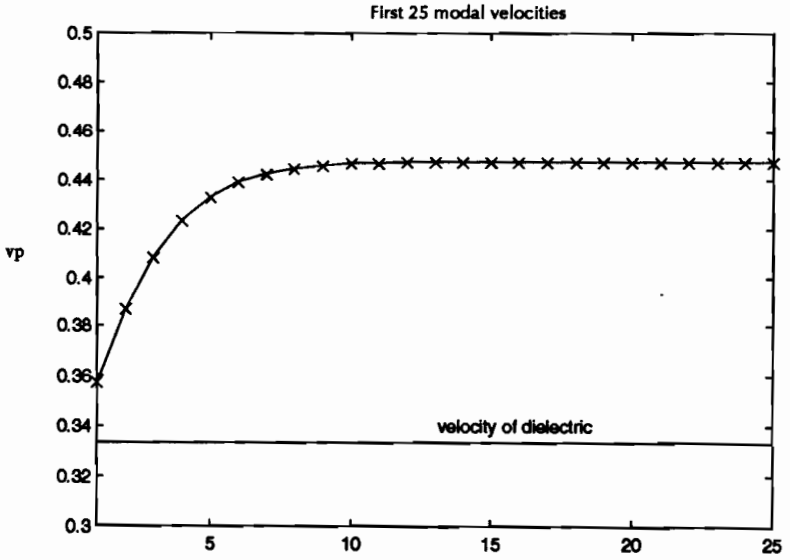

Figure 4.5 Modal velocities of a structure with $w/h = 10, \epsilon_r = 9$.

Figure 4.6 illustrates the effect of the w/h ratio on the number of distinct modal velocities for different ϵ_r as a function of w/h ratio. All the structures of Figure 4.6 (for a given relative permittivity and w/h ratio) are discretized using 200 elements. Two modal velocities are considered to be equal when their difference is less than or equal to 10^{-6}.

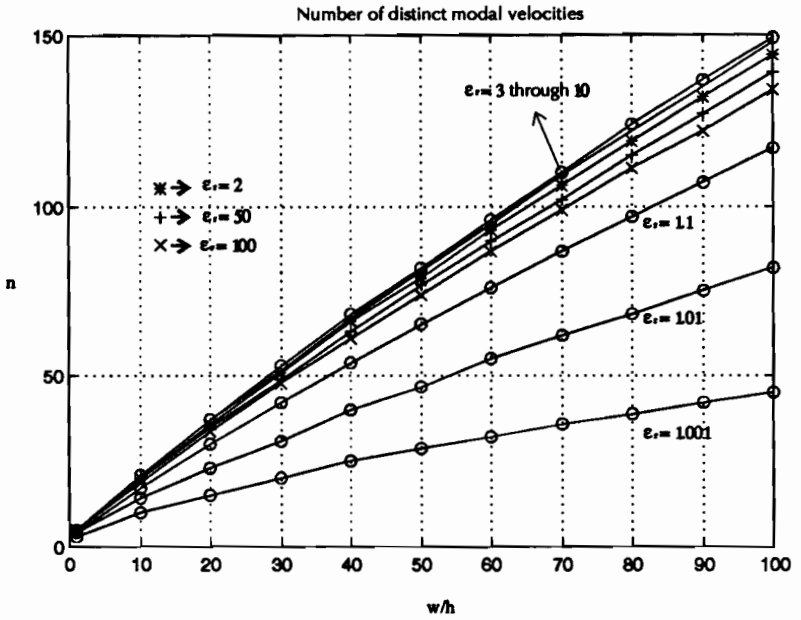

Figure 4.6 Number of distinct modal velocities as a function of w/h ratio.

Obviously, the relation between the w/h ratio and the number of distinct modes is almost linear. For practical structures (ϵ_r greater than or equal to 2), the number of distinct modal velocities can be considered as independent of the relative permittivity. Figure 4.7 illustrates the spectrum of the first 25 modal velocities for two structures with different w/h ratio. Figure 4.7 suggests that the spectrum increases as w/h ratio increases. Therefore, it is interesting to see the effect of ϵ_r on the difference between the smallest and largest modal velocities.

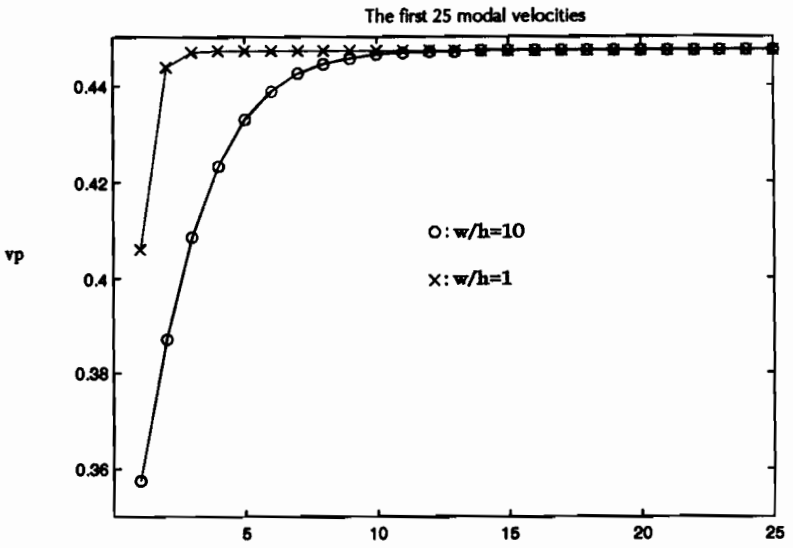

Figure 4.7 Modal velocities for two structures with $\epsilon_r = 9$.

Figure 4.8 illustrates the ratio of the maximum and the minimum of the velocities (v_{max}/v_{min}).

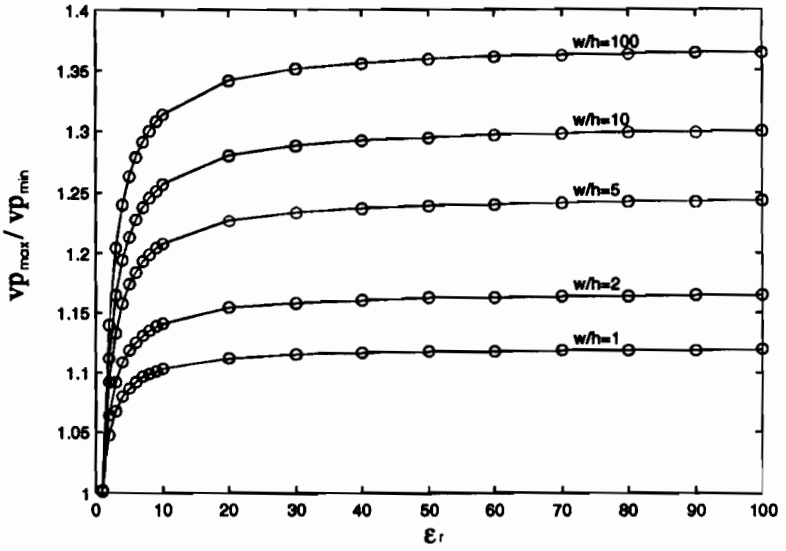

Figure 4.8 The ratio v_{max}/v_{min} as a function of ϵ_r.

In order to have a feeling for what the ratio in Figure 4.8 represents, the following reasoning can be adopted: for sinusoidal excitations (phasor), over a given distance d, the phase shift θ between two signals is given by

$$\theta = (\beta_1 - \beta_2)\, d \tag{4.13}$$

where the phase constant $\beta = \frac{2\pi}{\lambda} = \frac{2\pi f}{v}$, f being the frequency and v the velocity of the signal. Therefore, over a quarter wavelength ($d = \lambda/4$), the phase shift is given by

$$\theta = 2\pi f(\frac{1}{v_{min}} - \frac{1}{v_{max}})\frac{v_{min}}{4f}. \tag{4.14}$$

Expressing v_{max} as a ratio of v_{min} ($v_{max} = r v_{min}$, r being the ratio), the phase shift in degrees is given by

$$\theta = 90^{\circ}(1 - \frac{1}{r}). \tag{4.15}$$

Thus, a ratio r of 1.125, 1.2 and 1.5 will result in a phase shift of 10°, 15° and 30° respectively. These phase shifts can be considerable depending on the applications. Figure 4.8 suggests that the spectrum of the modal velocities increases with the w/h ratio. Also, the difference between the maximum and minimum modal velocities can be considered as constant for ϵ_r greater than 20.

4.1.2 An upper and lower bound for the eigenvalue spectrum

As mentioned above, all modal velocities must lie between the velocity of a wave traveling in air alone and the velocity of a wave traveling in the substrate material alone. It will be practical to narrow this interval in order to get an acceptable initial guess of the slowest and fastest modal velocities of a given structure. Those estimates of the eigenvalues can also be used as shifts in the *shifted QR algorithm* or the shifted *inverse power method* in order to accelerate the convergence of the eigenvalue problem. Therefore it is interesting to compare the modal velocities with the TEM wave velocity to verify if the latter has any meaningful significance (if the TEM velocity is a lower bound) in the group of numerous parallel conductors. This parameter is investigated in great depth in the literature. For example, in Silvester [1968] the velocities have been calculated using 30 elements of order 0 and using symmetry (with a four image-term Green's function). Therefore, it corresponds to 60 elements of order 0. The same results have been obtained in the present work using 22 elements of order 1 or 15 elements of order 2.

As in the case of modal velocities, in order to calculate in an appropriate

manner, the normalized TEM wave velocity, described in Chapter 1, should also be calculated by factoring out the leading constant. Thus, the two matrices can be written as

$$\mathbf{P} \quad \text{as} \quad \frac{1}{2\pi\epsilon_0(1+\epsilon_r)}\mathbf{P} \quad \text{and} \quad \mathbf{L} \quad \text{as} \quad \frac{\mu_0}{4\pi}\mathbf{L}. \tag{4.16}$$

By defining,

$$\mathbf{b} = \begin{bmatrix} \int p_1(\overline{x})\, d\overline{x} \\ \cdots \\ \int p_n(\overline{x})\, d\overline{x} \end{bmatrix}, \tag{4.17}$$

and

$$t_1 = \mathbf{b}^{\mathrm{T}}\mathbf{P}^{-1}\mathbf{b}, t_2 = \mathbf{b}^{\mathrm{T}}\mathbf{L}^{-1}\mathbf{b}, \tag{4.18}$$

where T denotes transposition, the line capacitance per unit length C is obtained by

$$C = 2\pi\epsilon_0(1+\epsilon_r)\mathbf{b}^{\mathrm{T}}\mathbf{P}^{-1}\mathbf{b} = 2\pi\epsilon_0(1+\epsilon_r)t_1. \tag{4.19}$$

The capacitance per unit length C_0 for a similar line with $\epsilon_r = 1$ is

$$C_0 = \frac{4\pi}{\mu_0}\mathbf{b}^{\mathrm{T}}\mathbf{L}^{-1}\mathbf{b} = \frac{4\pi}{\mu_0}t_2. \tag{4.20}$$

The inductance per unit length is then

$$L = \frac{1}{C_0} = \frac{\mu_0}{4\pi}\frac{1}{t_2}. \tag{4.21}$$

The TEM velocity is given by

$$v = \frac{1}{\sqrt{LC}} = \frac{1}{\sqrt{\frac{\mu_0}{4\pi t_2}\, 2\pi\epsilon_0(1+\epsilon_r)t_1}} = \frac{1}{\sqrt{\epsilon_0\mu_0}}\sqrt{\frac{2t_2}{(1+\epsilon_r)t_1}}. \tag{4.22}$$

Therefore, the TEM velocity, normalized with respect to c, is given by

$$\frac{v}{c} = \sqrt{\frac{2t_2}{(1+\epsilon_r)t_1}}\,. \tag{4.23}$$

The characteristic impedance of a TEM transmission line is given by

$$Z = \sqrt{\frac{L}{C}} = \sqrt{\frac{\mu_0}{4\pi t_2}\,\frac{1}{2\pi\epsilon_0(1+\epsilon_r)t_1}} = \sqrt{\frac{\mu_0}{\epsilon_0}}\,\frac{1}{2\pi\sqrt{2}\,\sqrt{t_1 t_2(1+\epsilon_r)}}\,. \tag{4.24}$$

Therefore, the TEM impedance, normalized with respect to the free-space impedance Z_0, is given by

$$\frac{Z}{Z_0} = \frac{1}{2\pi\sqrt{2}\,\sqrt{t_1 t_2(1+\epsilon_r)}}. \tag{4.25}$$

The two expressions given by (4.23) and (4.25) respectively represent the TEM velocity and impedance when *all* conductors are connected to the same source, i.e., when the structure is electrically equivalent to a flat strip. The TEM wave velocity of the structure ($w/h = 10, \epsilon_r = 9$) is 0.358789. This is somewhat higher than the velocity of the slowest (dominant) mode which is $v_1 = 0.357468$. Clearly, when the conductors are joined to make a single strip, the great majority of energy is transported by the first mode.

Table I outlines the difference between the first modal velocity and the TEM velocity. Since the relative error does not decrease as the number of elements (Ne) increases, it can be stated that the TEM velocity does not represent a lower bound. Nevertheless, it can give a good estimate of the propagation velocity of the dominant mode (the first eigenvalue).

Ne	TEM velocity v	first modal velocity (v_1)	Relative error $(v-v_1)/v$
50	3.598422e-01	3.575308e-01	6.423396e-03
100	3.598145e-01	3.574963e-01	6.442910e-03
150	3.598038e-01	3.574839e-01	6.447652e-03
200	3.597981e-01	3.574775e-01	6.449692e-03
300	3.597923e-01	3.574711e-01	6.451512e-03
400	3.597893e-01	3.574678e-01	6.452339e-03

Table I. Comparison between the TEM velocity and first modal velocity.

Another interesting experiment is to excite the structure by a delta-function (a single element at potential 1, the rest at 0). Figure 4.9 illustrates the TEM velocity applicable to a single conductor in a multi-line structure as a function of conductor position which is normalized with respect to h. Table II compares the average of the TEM velocities where each conductor is excited by a delta-function with the TEM velocity (when all conductors are connected to the same source).

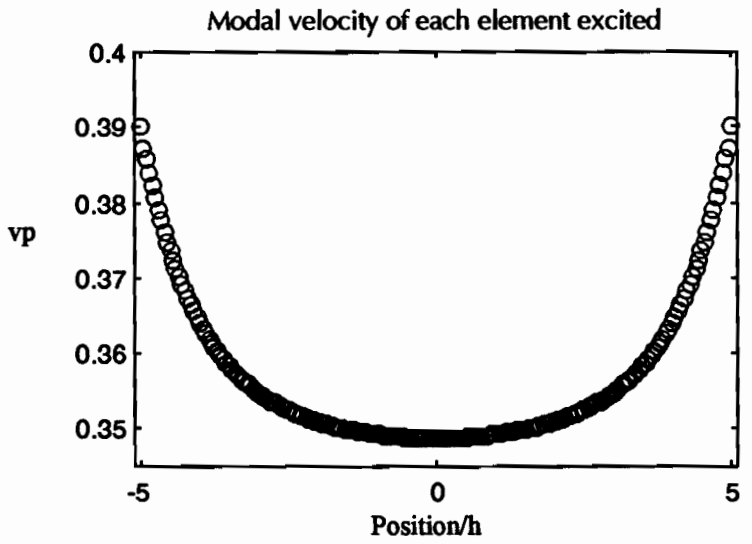

Figure 4.9 TEM velocities of the structure excited by a delta function.

Ne	TEM velocity v	average $\overline{v}$	Relative error $(v-\overline{v})/v$
25	3.598774e-01	3.573825e-01	6.932584e-03
50	3.598422e-01	3.572623e-01	7.169706e-03
100	3.598145e-01	3.571920e-01	7.288681e-03
200	3.597981e-01	3.571502e-01	7.359454e-03

Table II. Comparison between the TEM velocity and the average of the TEM velocities where each conductor is excited by the delta function.

Once again, since the relative error is not decreasing as the number of elements (Ne) increases, the concluding remark is that there is no obvious relation between the modal velocities of a multi-line structure and the TEM velocity.

In order to get an estimate of the propagation velocity of higher modes, one can reason as follows: each high-order mode has its currents and charges distributed more or less sinusoidally except at the edges. In other words, the charges appear as more or less equal packets, alternately positive and negative, and more or less equally spaced. For the higher modes, the spacing between negative and positive charges is smaller than the thickness of the substrate, so the existence of a ground plane is not very important. This point will be proven when the velocities of the structure with no ground plane will be calculated and indeed the degenerate velocities for both structures will be shown to be equal. Therefore, one can get a good estimate of the velocity of higher modes by taking an approximated eigenfunction $\mathbf{V}_{apr}$ with an alternating $+1$ and -1 as entries:

$$\mathbf{V}_{apr} = \begin{bmatrix} +1 \\ -1 \\ \cdots \\ -1 \\ +1 \end{bmatrix}. \tag{4.26}$$

Thus, an estimate of the fastest normalized modal velocity will be

$$v_{apr} = \sqrt{\frac{2}{(1+\epsilon_r)} \frac{\mathbf{V}_{apr}^{\mathbf{T}} \mathbf{P} \mathbf{V}_{apr}}{\mathbf{V}_{apr}^{\mathbf{T}} \mathbf{L} \mathbf{V}_{apr}}} \tag{4.27}$$

where $\mathbf{P}$ and $\mathbf{L}$ are considered without the leading constants. For a structure with $w/h = 10, \epsilon_r = 9$, Table III compares the relative error between the modal velocity calculated by solving the generalized eigenvalue problem (v_{Ne}) and the one calculated using (4.27). Even though the relative error is better when the discretization is denser, the approximation can be considered as a good estimate for any discretization.

Ne	last modal velocity: v_{Ne}	Approximated velocity: v_{apr}	Relative error $(v_{Ne}-v_{apr})/v_{Ne}$
50	4.472136e-01	4.462842e-01	2.078141e-03
100	4.472136e-01	4.467421e-01	1.054375e-03
150	4.472136e-01	4.468972e-01	7.073715e-04
200	4.472136e-01	4.469755e-01	5.324245e-04
300	4.472136e-01	4.470542e-01	3.563522e-04
400	4.472136e-01	4.470938e-01	2.678425e-04

Table III. Comparison between the velocities of the higher modes and an approximated one.

Thus, in order to get an estimate of the modal velocity spectrum prior to solving any problem, a practical approach is to consider as the lower bound either the TEM velocity (with a relative error of 0.6%) or simply the velocity of the substrate (with a relative error of 7%) and the estimate given by (4.27) as the upper bound of the modal velocities. When these limits are satisfactory for a given application, then the eigenvalue problem can be solved and those estimates can be used as shifts in order to accelerate the convergence.

Note that the calculation of the TEM velocity is not so computationally expensive due to the Toeplitz characteristic of the matrices. Therefore, solving a system of equations (in order to find the inverse of a matrix) can be achieved by the use of so-called *"new, fast"* algorithms which require only $N(\log N)^2$ operations, compared to N^2 for Levinson's method.

Tables I, II and III also illustrate the sensitivity of the modal velocities to discretisation. They are certainly very stable since in Table I, the relative error between 50 and 400 elements is 0.02% while in Table III, there is no difference with the number of digits tabulated.

4.1.3 Crosstalk problem

The modal theory can be usefully applied to calculate the crosstalk problem of a multi-line structure consisting of many closely spaced fine lines. It is assumed that the structure of Figure 4.2 is semi-infinite in the direction of propagation z,

and that it comprises a large number N of similar and equally spaced conductors, with conductor m occupying $x_{m-1} < x < x_m$. Also, the conductors are driven by N independent voltage sources, one for each conductor. The *crosstalk problem* may be stated as follows: if all the sources are held at zero except for the source feeding conductor m, what voltage appears at time t at position z on conductor n? The receiving end is assumed to be infinitely far away (or, what is equivalent, terminated in its characteristic impedance) so that no reflections can exist and the energy can only propagate in the $+z$ direction. If $v(x,z,t)$ represents the potential distribution on all the conductors, the sending–voltage is now given by

$$\begin{aligned} V(x,0,t) &= \mathrm{V}_e u(t), \qquad x_{m-1} < x < x_m \\ &= 0 \qquad\qquad \text{elsewhere,} \end{aligned} \tag{4.28}$$

where $u(t)$ represents any function. It is assumed that the conductors are much thinner than the substrate, and the plane $y = 0$ coincides with the top surface of the dielectric. Waves will now propagate in the $+z$ direction but, as mentioned above, due to the infinite length of the structure, there will be no reflections and no traveling waves in the $-z$ direction.

As developed in detail in Chapter 1, any wave capable of propagating in the $+z$ direction in this structure may be expressed by describing its voltage and current as

$$V(x,z,t) = \sum_k V_k \phi_k(x) h_k(z - c_k t), \tag{4.29}$$

$$J(x,z,t) = \sum_k J_k \psi_k(x) h_k(z - c_k t). \tag{4.30}$$

The current and potential eigenfunctions ($\psi_k(x)$ and $\phi_k(x)$ respectively) and their corresponding modal velocities c_k, can be regarded as known. At the sending end, the wave must exactly match the impressed voltage. Thus,

$$\mathrm{V}_e u(t) = \sum_k V_k \phi_k(x) h_k(-c_k t). \tag{4.31}$$

The potential and current eigenfunctions are biorthogonal. The coefficients V_k of (4.31) can therefore be determined by multiplying both sides by one of the current eigenfunctions and integrating over the width of the structure:

$$V_e \int \psi_j(x) u(t)\, dx = \sum_k V_k h_k(-c_k t) \int \psi_j(x) \phi_k(x)\, dx. \tag{4.32}$$

Because the eigenfunctions are biorthogonal, the summation on the right collapses to a single term. In the left-hand integral $u(t)$ is nonzero only on $x_{m-1} < x < x_m$ and therefore permits immediate integration to yield

$$V_j h_j(-c_j t) = \frac{V_e \int_{x_{m-1}}^{x_m} \psi_j(x) u(t)\, dx}{\int \psi_j(x) \phi_j(x)\, dx}. \tag{4.33}$$

With the conventionally abbreviated notation

$$\langle \phi, \psi \rangle = \int \phi(x,y) \psi(x,y)\, dx, \tag{4.34}$$

(4.33) becomes

$$V_j h_j(-c_j t) = \frac{V_e \int_{x_{m-1}}^{x_m} \psi_j(x) u(t)\, dx}{\langle \phi_j, \psi_j \rangle}. \tag{4.35}$$

For a wave traveling in the $+z$ direction, the current and voltage expansion coefficients are related by

$$\frac{V_k}{J_k} = c_k \frac{\langle \psi_k, \Omega \psi_k \rangle}{\langle \psi_k, \phi_k \rangle}, \tag{4.36}$$

so that

$$J_j h_j(-c_j t) = \frac{1}{c_j} \frac{V_e \int_{x_{m-1}}^{x_m} \psi_j(x) u(t)\, dx}{\langle \phi_j, \psi_j \rangle} \frac{\langle \psi_j, \phi_j \rangle}{\langle \psi_j, \Omega \psi_j \rangle} \tag{4.37}$$

which, after simplification, becomes

$$J_j h_j(-c_j t) = \frac{1}{c_j} \frac{V_e \int_{x_{m-1}}^{x_m} \psi_j(x) u(t)\, dx}{\langle \psi_j, \Omega \psi_j \rangle}. \tag{4.38}$$

The pairs of coefficients V_j, J_j provide a full description of the wave propagating along the multi-wire structure. Note that the time functions $h_j(-c_j t)$ are directly implied by (4.38): to within a scalar multiplier,

$$h_j(-c_j t) = u(t). \tag{4.39}$$

In other words, the time distributions of voltages, currents, and power in the various modes all mirror the source behavior. They do not depend on each other.

When the eigenfunctions are scaled to be biorthonormal and the structure has been discretized using elements of the same width, then

$$\langle \psi_j, \phi_j \rangle = \Delta_i \tag{4.40}$$

where Δ_i is the width of an element. Furthermore, if the eigenfunctions are piecewise linear (or the conductors are very narrow), then the voltage coefficients can be expressed as

$$V_j = \frac{V_e \Delta_m \psi_j(\bar{x}_m)}{\Delta_i} = V_e \psi_j(\bar{x}_m) \tag{4.41}$$

where $\bar{x}_m$ is the midpoint of conductor m and Δ_m is the space it occupies ($\Delta_m = x_m - x_{m-1}$). Substituting (4.41) into (4.29) yields

$$V(x,z,t) = V_e \sum_k \phi_k(x) \psi_k(\bar{x}_m) h_k(z - c_k t). \tag{4.42}$$

Therefore, the voltage on conductor n is given by

$$V(\bar{x}_n,z,t) = V_e \sum_k \phi_k(\bar{x}_n) \psi_k(\bar{x}_m) h_k(z - c_k t). \tag{4.43}$$

Close examination of (4.43) shows that the contribution of two modes can be minimized, or even totally eliminated, by selecting m and n so that $\bar{x}_n$ and $\bar{x}_m$ coincide with zeros of ϕ_k and ψ_k. This suggests that minimum-crosstalk positions can be located in a structure even if the total number of conductors and their exact placement are unknown.

Figure 4.10 shows the voltages on conductors 177 ($\bar{x}_n = -0.575h$), 193 ($\bar{x}_n = -0.175h$), 361 ($\bar{x}_n = 4.025h$), and 396 ($\bar{x}_n = 4.9h$) at some point $z > 0$ in a structure that extends over $-5h \le x \le +5h$ (h being the substrate thickness) where a pulse of short duration and unity amplitude is applied on conductor 300

($\overline{x}_m = 2.5h$). It must be emphasized that none of the voltages on those lines arise from reflections; the lines are infinite, so ***there are no reflections.*** In reality, the conductors outlined in Figure 4.10 are grounded at $t = 0$ and $z = 0$. Therefore, pulses are appearing on a grounded conductor due to the electromagnetic interference between the lines.

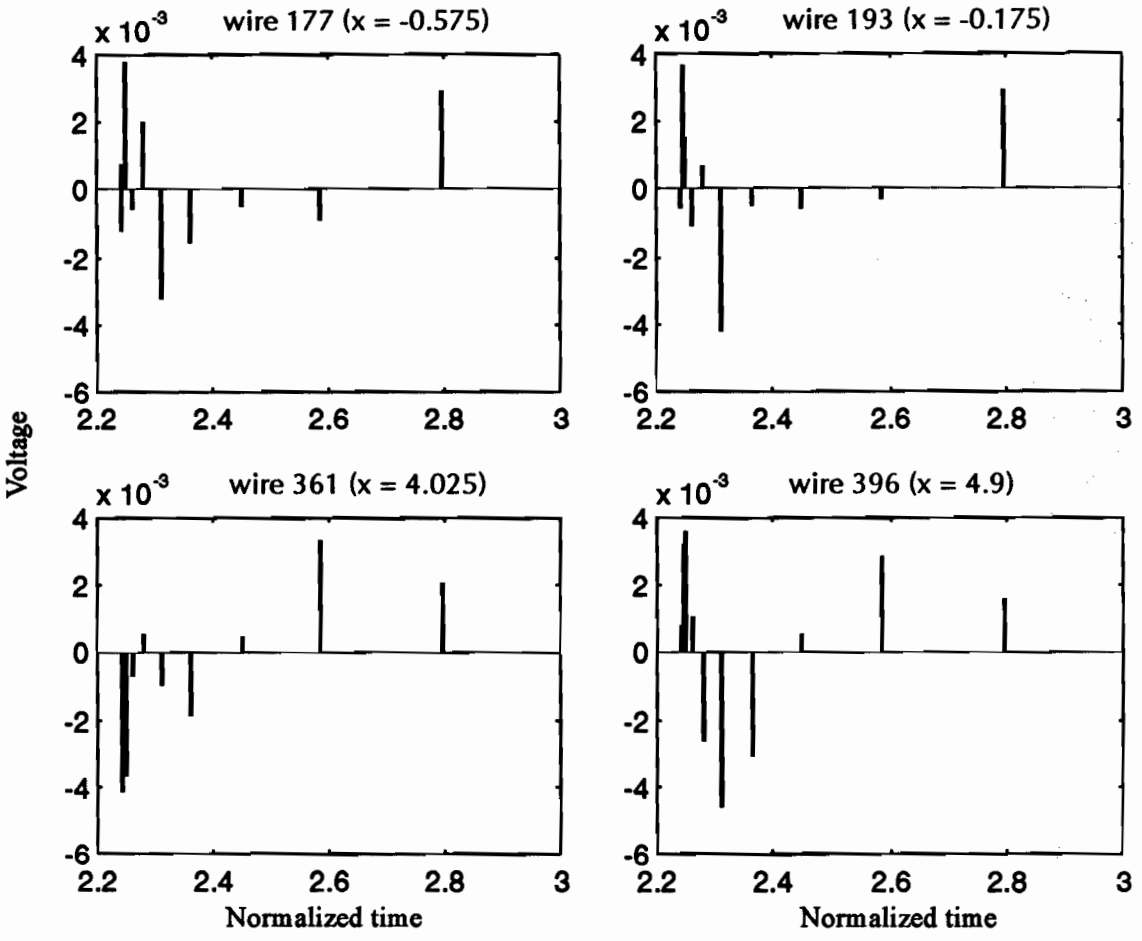

Figure 4.10 Voltage distribution as a function of time for an impulse excitation.

The time scale of Figure 4.10 is normalized to the velocity of light in air (c) and z. To obtain the time in seconds for a given distance z in meters, the normalized time axis needs to be multiplied by z/c.

At time 2.3 a substantial number of small pulses are crowded together, as the fast–traveling high–order modes arrive. Subsequently, longer periods of time elapse between the pulses carried in the slower low–order modes. At time 2.8, the

lowest–order mode arrives and the process is completed. Each distinct pulse represents a packet of energy traveling in a different mode hence at a different velocity, arriving at a different time. Thus, the original pulse is *spatially* decomposed into the orthogonal modes of the transmission structure and the individual modal components are propagated at different speeds, arriving at different times.

If there was a boundary further away on the structure, then each of the incident pulses would have been scattered and reflected to another group of pulses which would then be traveling to the left. These left traveling pulses would get mixed with the incident pulses that did not reach the boundary yet.

The same approach can be applied to an excitation of a step function. Figure 4.11 illustrates the voltages at some point $z > 0$ on different conductors for the same structure ($-5h \leq x \leq +5h$).

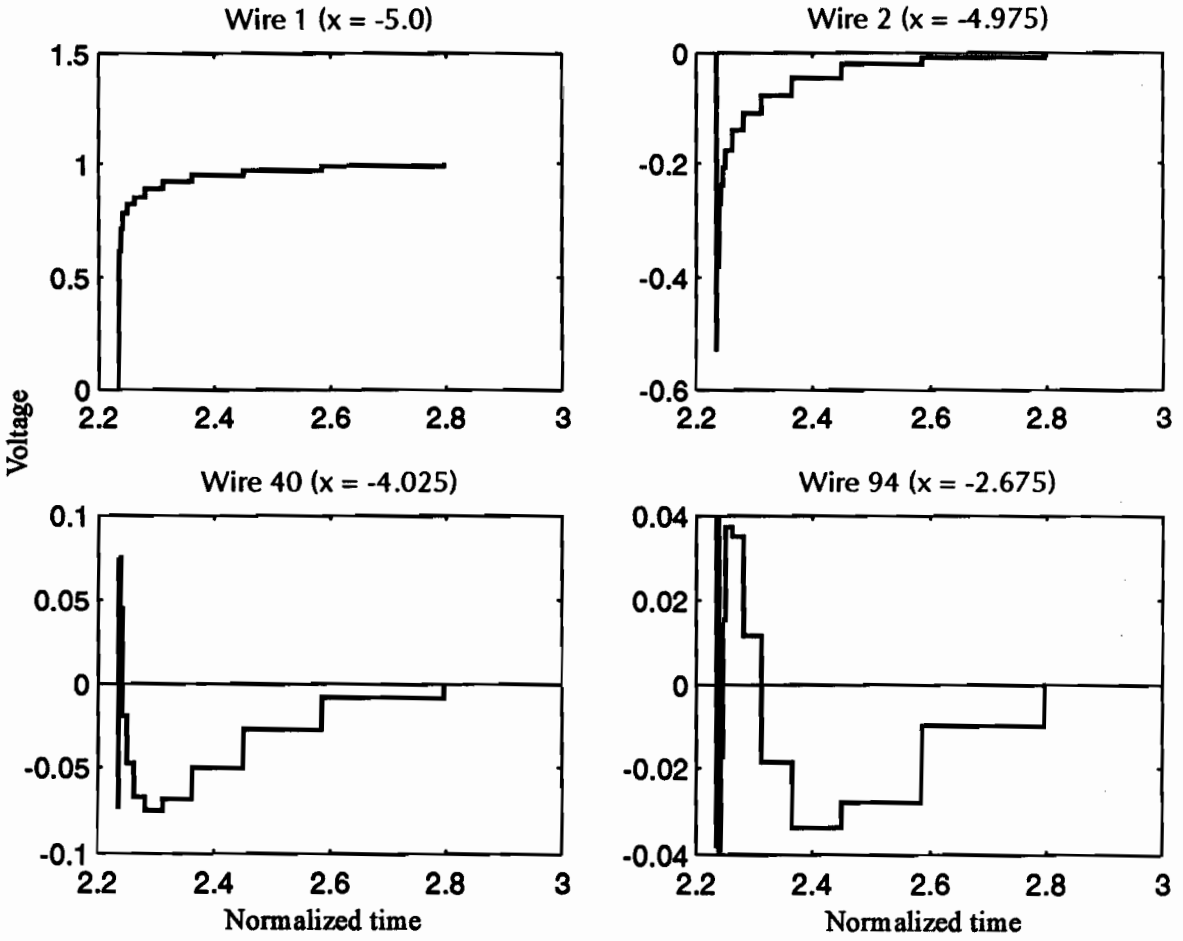

Figure 4.11 Voltage distribution as a function of time for a step excitation.

Here, a step function of unity amplitude is applied on conductor 1 ($\bar{x}_m = -5h$) at $t = 0$ and $z = 0$, while all the other conductors are grounded. Once again, voltages appear on all the conductors not because of reflections but due to crosstalk. Since all the conductors are grounded except one, their final voltage is zero, while the first conductor reaches 1v gradually. Figure 4.11 illustrates the voltages on conductors 1 ($\bar{x}_n = -5h$), 2 ($\bar{x}_n = -4.975h$), 40 ($\bar{x}_n = -4.025h$), and 94 ($\bar{x}_n = -2.675h$) at some point $z > 0$. As in the case of a pulse excitation, the time scale is normalized to the velocity of light in air (c) and z. Once again, a substantial number of high–order fast–traveling modes arrive at time 2.3, resulting in an abrupt voltage change in a short period of time. This period of time is so short that it is imperceptible to the excited conductor and to those which are nearby. On conductors located at a greater distance, it is more apparent. Subsequently, the slower low–order modes arrive and the voltage gradually gets to its steady state value. Once again, it must be emphasized that none of the voltages on those lines arise from reflections; the lines are infinite, so ***there are no reflections.***

4.1.4 Modal energy distribution

It is next of interest to enquire how the transmitted power in multimode propagation is divided between the various modes. The total power is clearly given by the voltage-current product,

$$W(z,t) = \int V(x,z,t)J(x,z,t)\,dx. \tag{4.44}$$

Substituting (4.29) and (4.30) into (4.44) yields

$$W(z,t) = \sum_k \sum_j V_k J_j h_k(z - c_k t)\, h_j(z - c_j t) \int \phi_k(x)\psi_j(x)\,dx. \tag{4.45}$$

Once again, biorthogonality of the eigenfunctions implies that the only term different from zero in (4.45) is for $j = k$, thus,

$$W(z,t) = \sum_j V_j J_j h_j^2(z - c_k t) \int \phi_j(x)\psi_j(x)\,dx. \tag{4.46}$$

Since

$$\frac{V_k}{J_k} = c_k \frac{\langle \psi_k, \Omega \psi_k \rangle}{\langle \psi_k, \phi_k \rangle}, \tag{4.47}$$

substituting (4.47) into (4.46) yields

$$W(z,t) = \sum_j \frac{1}{c_j} \frac{\langle \psi_j, \phi_j \rangle^2}{\langle \psi_j, \Omega \psi_j \rangle} V_j^2 h_j^2(z - c_k t). \tag{4.48}$$

Since the modes are orthogonal, the total power given by (4.48) can be viewed as a summation of modal powers W_j,

$$W(z,t) = \sum_j W_j(z,t) \tag{4.49}$$

where the power of each mode j is given by

$$W_j(z,t) = \frac{1}{c_j} \frac{\langle \psi_j, \phi_j \rangle^2}{\langle \psi_j, \Omega \psi_j \rangle} V_j^2 h_j^2(z - c_k t). \tag{4.50}$$

Therefore, the power of each mode depends on the excitation $u(t)$ since

$$V_j h_j(z - c_j t) = \frac{\mathrm{V}_e \int_{x_{m-1}}^{x_m} \psi_j(x) u(\frac{z}{c_j} - t)\, dx}{\langle \psi_j, \phi_j \rangle} \tag{4.51}$$

Equation (4.50) becomes

$$W_j(z,t) = \frac{1}{c_j} \frac{\langle \psi_j, \phi_j \rangle^2}{\langle \psi_j, \Omega \psi_j \rangle} \frac{\mathrm{V}_e^2 u^2(\frac{z}{c_j} - t) \left(\int_{x_{m-1}}^{x_m} \psi_j(x)\, dx \right)^2}{\langle \psi_j, \phi_j \rangle^2} \tag{4.52}$$

or after simplification,

$$W_j(z,t) = \mathrm{V}_e^2 \frac{\left(\int_{x_{m-1}}^{x_m} \psi_j(x)\, dx \right)^2}{c_j \langle \psi_j, \Omega \psi_j \rangle} u^2(\tfrac{z}{c_j} - t). \tag{4.53}$$

Note that the power carried by a single mode is a function of the position of the energized conductor x ($x_{m-1} < x < x_m$). It is therefore appropriate to identify the

energy of each mode by writing $W_j(x,z,t)$, rather than $W_j(z,t)$.

Each mode carries power independently of the others, and at its own propagation speed c_j. At the sending end $z=0$, the source power is divided into modal fractions and each fraction is transmitted independently. Therefore, a good way of describing the relative importance of modes is to give the fraction $\eta_j(x)$ of the power allocated to each,

$$\eta_j(x) = \frac{W_j(x,0,t)}{\sum_k W_k(x,0,t)}. \tag{4.54}$$

In detail, (4.54) can be written as

$$\eta_j(x) = \frac{\dfrac{\left(\int_{x_{m-1}}^{x_m} \psi_j(x)\,dx\right)^2}{c_j\langle\psi_j,\Omega\psi_j\rangle}}{\sum_k \dfrac{\left(\int_{x_{m-1}}^{x_m} \psi_k(x)\,dx\right)^2}{c_k\langle\psi_k,\Omega\psi_k\rangle}}. \tag{4.55}$$

Note that (4.55) is independent of time and the excitation $u(t)$, so it characterizes the modes. However, $\eta_j(x)$ depends on the energized conductor.

When the eigenfunctions are piecewise linear (or the conductors are very narrow), then

$$\int_{x_{m-1}}^{x_m} \psi_j(x)\,dx = \Delta_m \psi_j(\bar{x}_m) \tag{4.56}$$

where $\bar{x}_m$ is the midpoint of the energized conductor m and Δ_m is the space it occupies ($\Delta_m = x_m - x_{m-1}$). Therefore, substituting (4.56) into (4.55) yields

$$\eta_j(\bar{x}_m) = \frac{\dfrac{\psi_j^2(\bar{x}_m)}{c_j\langle\psi_j,\Omega\psi_j\rangle}}{\sum_k \dfrac{\psi_j^2(\bar{x}_m)}{c_k\langle\psi_k,\Omega\psi_k\rangle}}. \tag{4.57}$$

It is interesting to draw curves of power partitioning between modes for any given structure. Since $\eta_j(\bar{x}_m)$ gives the *fraction* of power allocated to mode j, it is

clear that

$$\sum_j \eta_j(\bar{x}_m) = 1.$$

The power division, and its dependence on conductor position, can therefore be exhibited in a *power distribution diagram* as shown in Figure 4.12; the abscissa is normalized with respect to h ($-5h \leq \bar{x}_m \leq +5h$, h being the substrate thickness) and the ordinate is the fraction $\eta_j(\bar{x}_m)$.

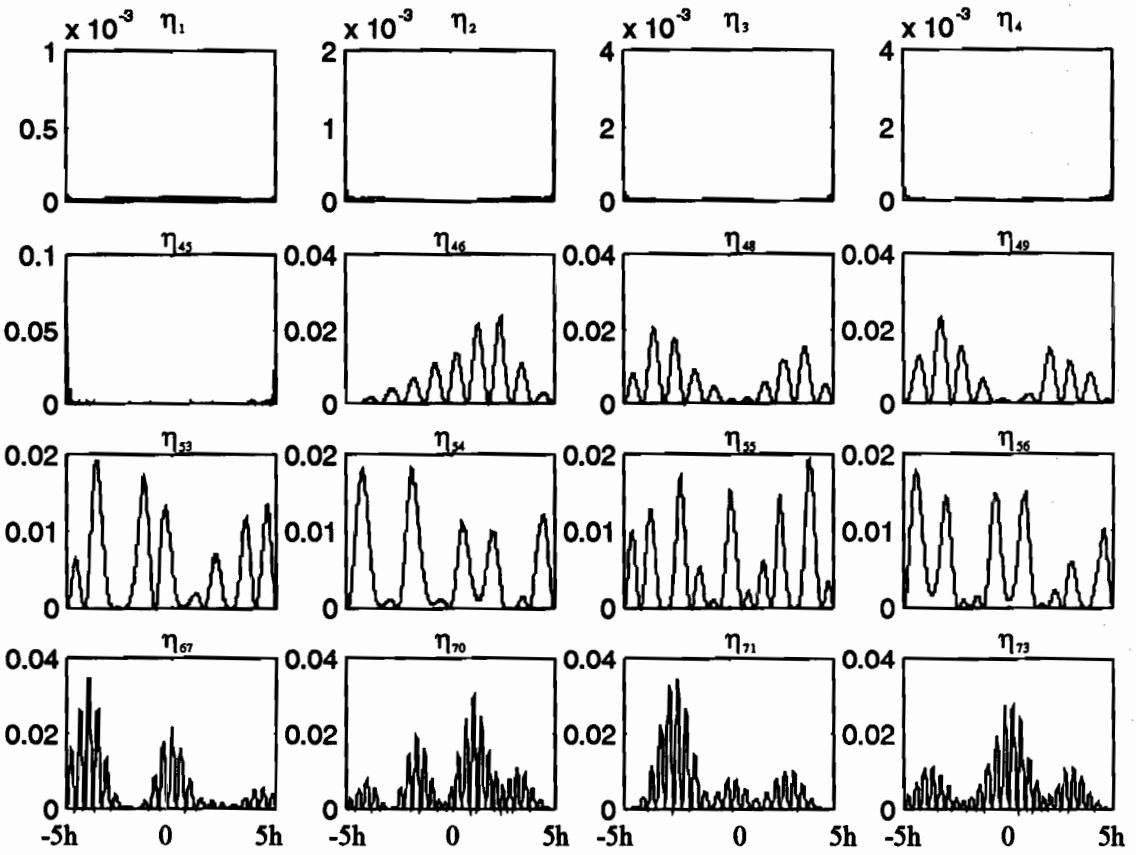

Figure 4.12 Modal power distribution diagram.

Figure 4.12 gives the power distribution between modes along any vertical line (corresponding to a particular $\bar{x}_m$).

The energy content is about 3% for the first 10 modes (it varies between 2

and 4) of the total, in all cases except at the edges and 97% of the energy travels in the higher (crinklier) modes for which the velocities are just about equal throughout. Finding a large part of the energy in a few modes for the edge, but not the interior, is not as surprising as it might seem and can be explained by analogy with Fourier series. If the charge distributions are more or less sinusoidal in the high modes (but not at the edges!) then the eigenfunctions are behaving like the Fourier series. Indeed, since only a single line is excited, the quasi-impulsive (spatially impulsive) excitation causes energy to split up between the various modes. Thus, the dominant harmonics do not contribute as much as the higher harmonics for the Fourier series of an impulse.

In fact, having a large part of the energy residing in high-order modes is potentially valuable. Since all the high-order modes have just about the same velocity, it is reasonable approximation to call the velocities equal and to treat and describe all the high order modes by just one modal function.

The lowest mode does carry most of the energy. Proving this is quite simple by exciting the whole structure (all elements) with potential 1. In this case the power calculation integrals do not contain the delta function any more. Therefore, the power carried by a single mode is no longer a function of the position of the energized conductor. In other words, the power integrals cease to sample the eigenfunctions but rather compute averages. The power of mode j will now be given by

$$\eta_j = \frac{\dfrac{\left(\int \psi_j(x)\,dx\right)^2}{c_j\langle\psi_j, \Omega\psi_j\rangle}}{\displaystyle\sum_k \frac{\left(\int \psi_k(x)\,dx\right)^2}{c_k\langle\psi_k, \Omega\psi_k\rangle}}. \tag{4.58}$$

Table IV illustrates how the total power divides among the modes. Obviously, the large part of the power propagates in the lowest mode. This point will be more apparent in the next section where equipotential lines produced by each mode will be computed. Note that the power is propagating in even modes. Indeed, the first mode, which is even, has 95% of the power while the second even mode has the

next 3% and the remaining 2% is divided among the rest of the even modes.

Mode	Percentage of power per mode
1	9.55e+01
2	3.34e-29
3	3.66e+00
4	1.21e-32
5	6.19e-01
6	1.34e-29
7	1.37e-01
8	3.20e-29
9	3.38e-02
10	4.22e-28
11	8.73e-03

Table IV. Percentage of power divided among the modes.

This is not so surprising since the odd modes have a zero average value and in the case of the even modes, the average decreases for the higher modes (refer to Figure 4.4).

Once again, this behavior is similar to the Fourier series of a step function where the fundamental and first couple of harmonics will characterize the function while the higher harmonics will have less influence.

4.1.5 Equipotential lines

Equipotential lines can be computed with the objective to observe the fields produced by the eigenfunctions. Referring back to Chapter 2, the potential at a point P to the right of the strip (i.e $y > h + a$), due to a charge q placed at $y = h + a$, is given by

$$V_1(x,y) = -\frac{q}{4\pi\epsilon_0}\log\{(y-(h+a))^2+x^2\} - \frac{Kq}{4\pi\epsilon_0}\log\{(y-(h-a))^2+x^2\} + \frac{q(1-K^2)}{4\pi\epsilon_0}\sum_{n=0}^{\infty} K^n \log\{(y+(2n+1)h+a)^2+x^2\}. \quad (4.59)$$

When $a = 0$, this potential becomes

$$V_1(x,y) = -\frac{q}{4\pi\epsilon_0}\log\{(y-h)^2+x^2\} - \frac{Kq}{4\pi\epsilon_0}\log\{(y-h)^2+x^2\} + \frac{q(1-K^2)}{4\pi\epsilon_0}\sum_{n=0}^{\infty} K^n \log\{(y+(2n+1)h)^2+x^2\}. \quad (4.60)$$

Therefore, for $y > h$ (in air),

$$V_1(x,y) = -\frac{q(1+K)}{4\pi\epsilon_0}\log\{(y-h)^2+x^2\} + \frac{q(1-K^2)}{4\pi\epsilon_0}\sum_{n=0}^{\infty} K^n \log\{(y+(2n+1)h)^2+x^2\}. \quad (4.61)$$

For, for $y < h$ (in the substrate),

$$V_2(x,y) = \frac{q(1-K)}{4\pi\epsilon_1}\sum_{n=0}^{\infty} K^n \log\frac{((2n+1)h+y)^2+x^2}{((2n+1)h-y)^2+x^2}. \quad (4.62)$$

On the surface of the substrate ($y = h$), the expression of the potential can be computed by letting $y = h$ in (4.62) or (4.61). Starting with (4.62), the expression of the potential at the surface of the substrate will be

$$V_3(x,h) = \frac{q(1-K)}{4\pi\epsilon_1}\sum_{n=0}^{\infty} K^n \log\frac{((n+1)2h)^2+x^2}{(2nh)^2+x^2}. \quad (4.63)$$

At first glance, obtaining the same expression as (4.63) starting with (4.61) may seem highly unlikely. However, the following lines demonstrates that this is quite possible. Starting with (4.61),

$$V_1(x,h) = -\frac{q(1+K)}{4\pi\epsilon_0}\log(x^2) + \frac{q(1-K^2)}{4\pi\epsilon_0}\sum_{n=0}^{\infty} K^n \log\{(2h(n+1))^2+x^2\}. \quad (4.64)$$

Factorizing (4.64),

$$V_1(x,h) = \frac{q(1+K)}{4\pi\epsilon_0}\left(-\log(x^2) + (1-K)\sum_{n=0}^{\infty} K^n \log\{(2h(n+1))^2 + x^2\}\right). \quad (4.65)$$

Since $K = \frac{1-\epsilon_r}{1+\epsilon_r}$, where ϵ_r is the relative permittivity, therefore,

$$\frac{1+K}{4\pi\epsilon_0} = \frac{1-K}{4\pi\epsilon_1}, \quad (4.66)$$

and obviously

$$\log(x^2) = \log(x^2) - \sum_{n=0}^{\infty} K^{n+1}\log\{(2(n+1)h)^2 + x^2\} + \sum_{n=0}^{\infty} K^{n+1}\log\{(2(n+1)h)^2 + x^2\} \quad (4.67)$$

or,

$$\log(x^2) = -K\sum_{n=0}^{\infty} K^n \log\{(2(n+1)h)^2 + x^2\} + \sum_{n=0}^{\infty} K^n \log\{(2nh)^2 + x^2\}. \quad (4.68)$$

Substituting (4.66) and (4.68) into (4.65) will give the same expression as (4.63). Although there might be other methods of proving the validity of the equations for the potentials, this exercise is nevertheless a confidence test of the validity of the expressions.

Using the above expressions for the potentials of the three regions of interest, equipotential lines can be computed when the charge distributions are represented by the eigenfunctions. Therefore, for any given point (x_0, y_0), the potential can be calculated as follows. For $y_0 > h$

$$V_1(x_0,y_0) = -\frac{1+K}{4\pi\epsilon_0}\int \phi_i(x)\log\{(y_0-h)^2 + (x-x_0)^2\}\,dx + \frac{1-K^2}{4\pi\epsilon_0}\sum_{n=0}^{\infty} K^n \int \phi_i(x)\log\{(y_0+(2n+1)h)^2 + (x-x_0)^2\}\,dx, \quad (4.69)$$

for $y_0 < h$

$$V_2(x_0,y_0) = \frac{1-K}{4\pi\epsilon_1}\sum_{n=0}^{\infty} K^n \int \phi_i(x)\log\frac{((2n+1)h+y_0)^2 + (x-x_0)^2}{((2n+1)h-y_0)^2 + (x-x_0)^2}\,dx, \quad (4.70)$$

and for $y_0 = h$

$$V_3(x_0, y_0) = \frac{1-K}{4\pi\epsilon_1} \sum_{n=0}^{\infty} K^n \int \phi_i(x) \log \frac{((n+1)2h)^2 + (x-x_0)^2}{(2nh)^2 + (x-x_0)^2} dx, \tag{4.71}$$

where ϕ_i is the i^{th} potential eigenfunctions. The latter gives the behavior of the electric field. By substituting ϕ_i with ψ_i (the current eigenfunction), the magnetic field behavior can be observed.

Figure 4.13 illustrates equipotential lines associated with the electromagnetic fields produced by the first potential and current eigenfunctions. The odd modes have a zero average value, that is

$$V(x_0, y_0) = -V(-x_0, y_0) \tag{4.72}$$

while the even modes are symmetrical,

$$V(x_0, y_0) = V(-x_0, y_0). \tag{4.73}$$

The first two equipotential lines associated with the potential and current eigenfunctions are identical. A slight difference begins to appear after the third mode. It is also noted that since the "k^{th} function has k wiggles", there are k concentrations of equipotential lines associated with the k^{th} eigenfunction. The number of concentrations will reveal if the equipotential lines are associated with an even or odd eigenfunction. Also, a zero at the origin of the axis is another indication that the lines are generated by an odd mode.

The effect of the edges on the equipotential lines are also evident, especially for the first three equipotential lines.

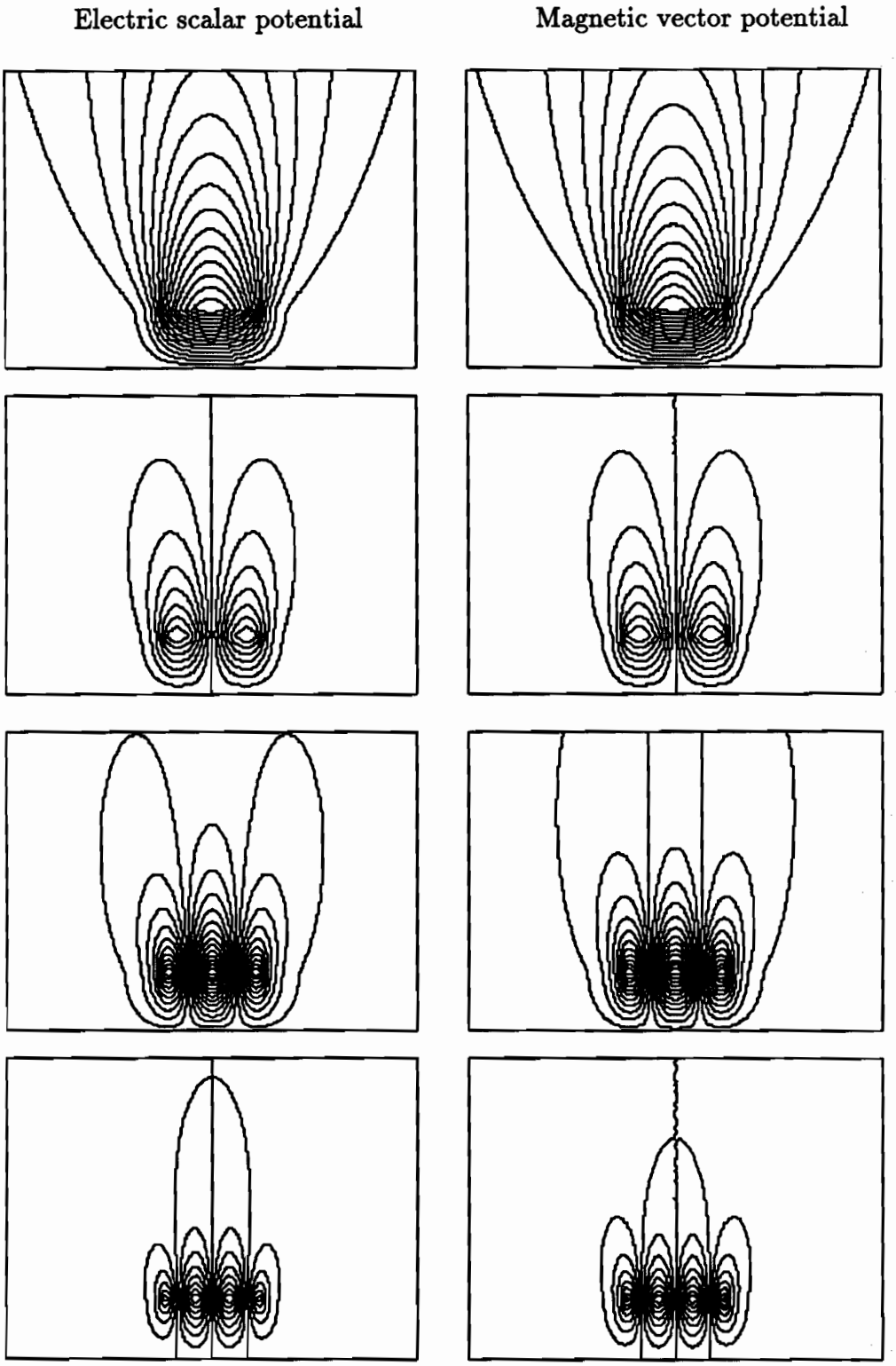

Figure 4.13 Equipotential lines due to the first four voltage and current charge distributions.

Figure 4.14 illustrates the equipotential lines produces by the eigenfunctions five through eight. Once again, k concentration of equipotential lines are associated with the k^{th} eigenfunction. In Figure 4.14, the difference between the equipotential lines produced by the potential and current eigenfunctions is more obvious.

As mentioned in previous sections, it is evident that the energy travels in both mediums (air and substrate) for the first few modes. For higher modes, the energy is particularly concentrated around the dielectric surface. Therefore the existence of a ground plane is not relevant.

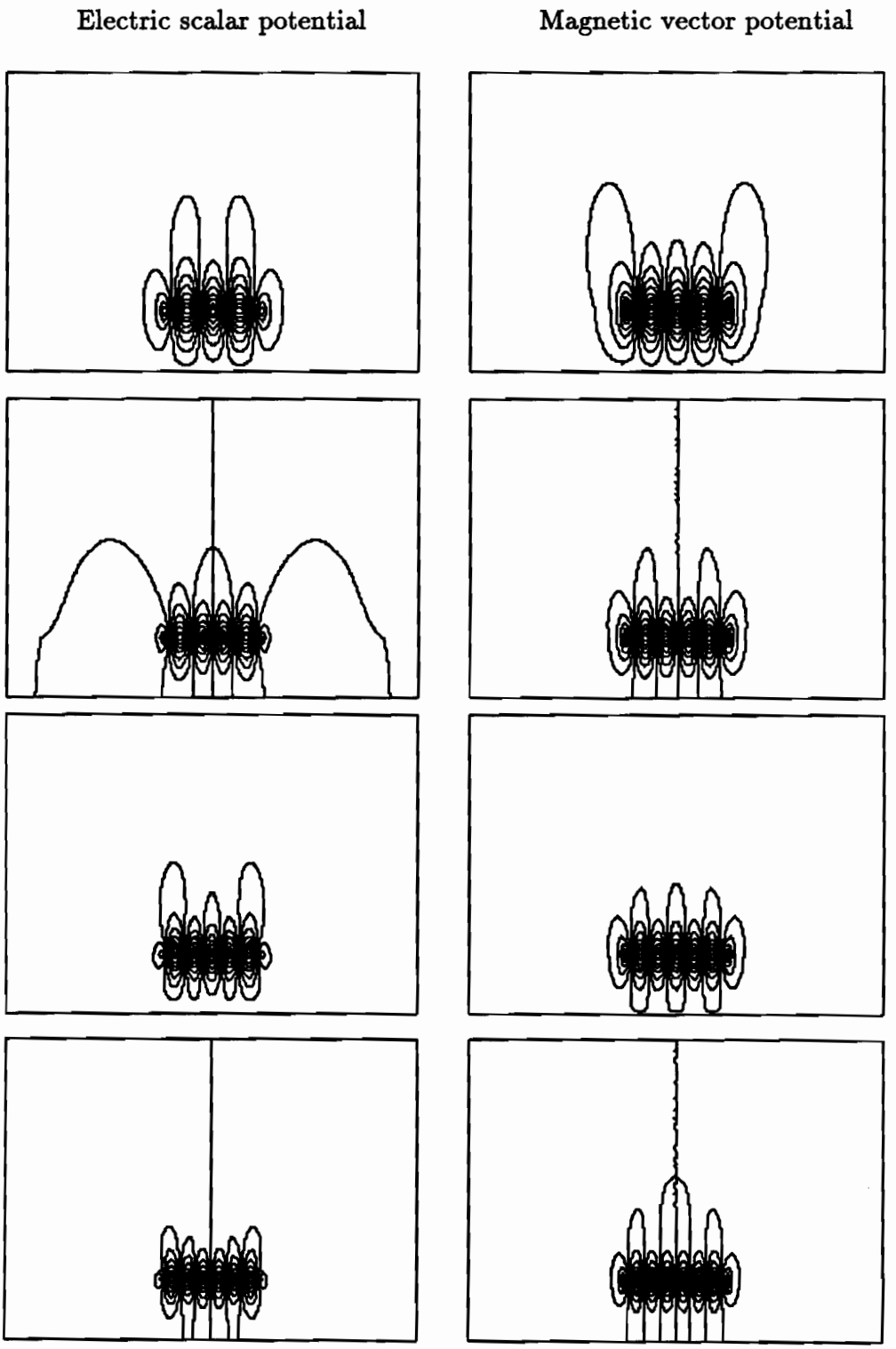

Figure 4.14 Equipotential lines due to the voltage and current charge distributions (5 through 8).

4.2 STRUCTURE WITH NO GROUND PLANE

The electric Green's function of a structure with no ground plane (calculated in Chapter 2) is given by

$$G_E(\overline{x};\overline{\xi}) = -\frac{1}{4\pi\epsilon_0}\left(\log(\zeta^2)+\log(4h^2)+(1-K^2)\sum_{n=1}^{\infty}K^{2n-1}\log\frac{\zeta^2}{n^2+\zeta^2}\right), \quad (4.74)$$

and the magnetic Green's function is

$$G_M(\overline{x};\overline{\xi}) = -\frac{\mu_0}{4\pi}\Big(\log(\zeta^2)+\log(4h^2)\Big), \quad (4.75)$$

where $\zeta = \dfrac{x-\xi}{2h} = \overline{x}-\overline{\xi}$.

Once again, it is preferable, as in the case of the structure with a ground plane, to compute the entries of the two matrices **P** and **L** without the leading constants, resulting in entries of the same order of magnitude for both matrices. Similarly, by normalizing the propagation velocities (the eigenvalues) with respect to the velocity of light, the results will be independent of constant though measured values such as ϵ_0. Thus, the entries of the matrix **P** must be computed as

$$P_{mn} = \int\int\Big(\log(\zeta^2)+\log(4h^2)\Big)p_m(\overline{\xi})p_n(\overline{x})\,d\overline{\xi}d\overline{x} + (1-K^2)\sum_{n=1}^{\infty}K^{2n-1}\int\int\log\frac{\zeta^2}{n^2+\zeta^2}p_m(\overline{\xi})p_n(\overline{x})\,d\overline{\xi}d\overline{x}, \quad (4.76)$$

and those of **L** as

$$L_{mn} = \int\int\Big(\log(\zeta^2)+\log(4h^2)\Big)p_m(\overline{\xi})p_n(\overline{x})\,d\overline{\xi}d\overline{x}. \quad (4.77)$$

The velocity v_i of a given mode i, normalized with respect to the free-space velocity, will then be

$$v_i = \sqrt{\lambda_i}, \quad (4.78)$$

where λ_i is the eigenvalue obtained by solving the generalized eigenvalue problem

with the entries of the matrices given by (4.76) and (4.77).

The resulting matrices **P** and **L** are no longer positive definite as in the case of the structure with a ground plane. Therefore, the generalized eigenvalue problem must be solved using the *LU* decomposition which, in the context of eigenvalue problems, is traditionally called the *LR* decomposition.

4.2.1 Results of generalized eigenvalue problem

For a structure where substrate relative permittivity ϵ_r is set to 9 and a width of the channel w 10.0 times the substrate thickness h, the last seven modal function pairs (associated with the non-degenerate eigenvalues) are illustrated in Figure 4.15. As in the case of Figure 4.3, all of the x-axes in Figure 4.15 range between $[-1;1]$ and the y-axes range between $[-0.1;0.1]$. It is obvious that for the structure with no ground plane, the eigenfunctions associated with the non-degenerate eigenvalues resemble those of the structure with a ground plane.

As mentioned in Chapter 2, this structure leads to one spurious mode which must be eliminated. The latter was expected since the conservation of charge was not respected during the calculation of the Green's function, i.e. the contribution of each charge to the total potential is not that of a dipole. The spurious modal velocity is either greater than the speed of light or less than the velocity of a wave traveling in the substrate material alone. Sometimes, depending on the w/h ratio, the spurious mode is imaginary (negative eigenvalue). The spurious eigenfunction, which is not depicted in Figure 4.15, resembles the first eigenfunction of the structure with a ground plane.

Table V compares the non-spurious current eigenfunctions obtained with the two structures. The comparison is illustrated using several methods: the angle between them, the standard deviation (STD) and the Euclidean norm of the difference. Table V suggests that the non-degenerate eigenfunctions do look alike especially when the difference between the modal velocities decreases. Those with a larger difference have a more significant, though moderate, standard deviation among them.

Note that the decrease follows a different rate depending on whether the eigenfunctions are odd or even.

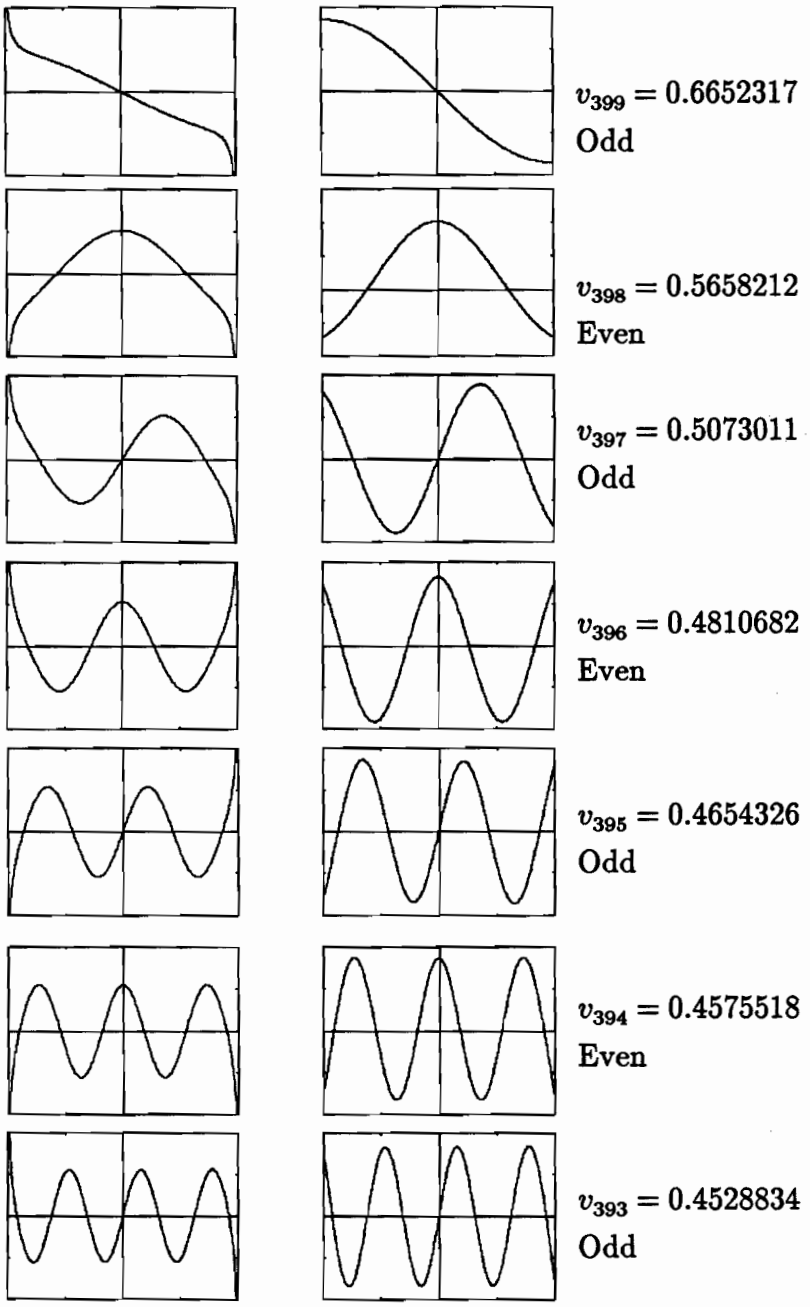

Figure 4.15 The current and potential modal functions associated with the first seven non-degenerate eigenvalues for conductors printed on a dielectric substrate with no ground plane.

velocity with GND	velocity with NOGND	angle °	STD $(\psi_{gnd} - \psi_{nognd})$	$\|\psi_{gnd} - \psi_{nognd}\|_2$
3.868390e-01	6.652317e-01	19.15	0.016651	0.332594
4.082398e-01	5.658212e-01	17.56	0.012480	0.305212
4.231830e-01	5.073011e-01	11.90	0.010376	0.207256
4.327676e-01	4.810682e-01	11.45	0.009572	0.199455
4.387339e-01	4.654326e-01	8.23	0.007181	0.143439
4.422935e-01	4.575518e-01	8.16	0.007031	0.142257
4.443919e-01	4.528834e-01	6.07	0.005304	0.105955
4.456027e-01	4.504319e-01	6.18	0.005371	0.107733
4.462993e-01	4.489925e-01	4.72	0.004125	0.082396
4.466955e-01	4.482222e-01	4.91	0.004284	0.085688
4.469209e-01	4.477734e-01	3.84	0.003354	0.066989
4.470483e-01	4.475307e-01	4.08	0.003559	0.071127
4.471205e-01	4.473901e-01	3.28	0.002870	0.057321
4.471611e-01	4.473136e-01	3.63	0.003174	0.063411
4.471841e-01	4.472695e-01	3.37	0.002944	0.058809
4.471970e-01	4.472454e-01	4.35	0.003803	0.075967
4.472042e-01	4.472316e-01	5.58	0.004872	0.097320
4.472083e-01	4.472240e-01	8.04	0.007023	0.140283
4.472106e-01	4.472197e-01	11.34	0.009894	0.197626

Table V. Comparison between the current eigenfunctions of the two structures associated with the non-degenerate modal velocities.

Figure 4.16 shows the distribution of the non-degenerate modal velocities for the two structures. As mentioned in previous sections, once the spurious mode is eliminated, all modal velocities must lie between the velocity of a wave traveling in air alone and the velocity of a wave traveling in the substrate material alone. Since $\epsilon_r = 9$, these limits are 1 and 1/3. It is interesting to note that the modal velocities have a different behavior in each of these two structures. In the

structure with a ground plane, the non-degenerate modal velocities are slower than the degenerate ones. On the other hand, in the structure with no ground plane, the non-degenerate modal velocities are faster than the degenerate ones. As mentioned in previous sections, degenerate modal velocities of the two structures are equal. That is, the fastest modal velocities of the structure with a ground plane are equal to the slowest ones for the structure with no ground plane. This behavior has already been explained in previous sections: for higher modes, the energy is particularly concentrated around the dielectric surface, thus rendering the existence of a ground plane irrelevant. It is interesting to note that the ground plane seems to "*slow down*" the propagation of the modes.

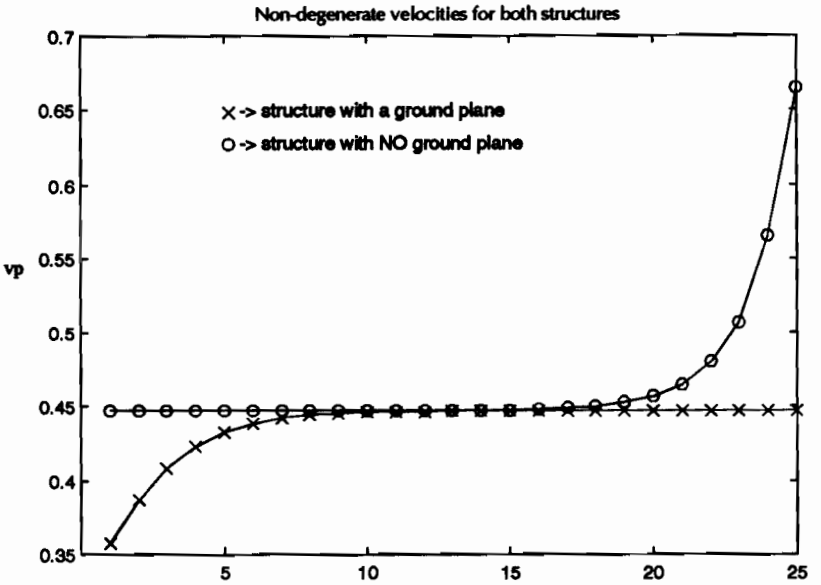

Figure 4.16 Modal velocities of the two structures (with and without a ground plane) for $w/h = 10, \epsilon_r = 9$.

As in the case of the structure with a ground plane, the effect of the w/h ratio and ϵ_r on the modal velocities is hereby investigated. Figure 4.17 illustrates the effect of the w/h ratio on the number of distinct modal velocities for different ϵ_r. All the structures of Figure 4.17 (for a given relative permittivity and w/h ratio) are discretized using 200 elements. Once again, two modal velocities are considered to be equal when their difference is less than or equal to 10^{-6}.

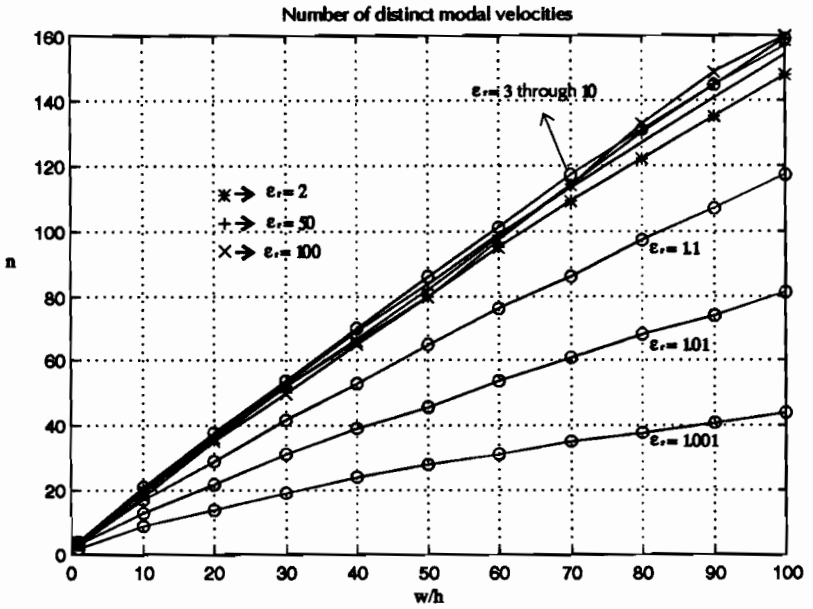

Figure 4.17 Number of distinct modal velocities as a function of w/h ratio for the structure with no ground plane.

The number of distinct modes can be considered as being the same for both structures. Therefore, all the remarks stated in section 4.1.1 apply to this particular case as well.

Figure 4.18 illustrates the effect of ϵ_r on the ratio between the smallest and largest modal velocities for both structures.

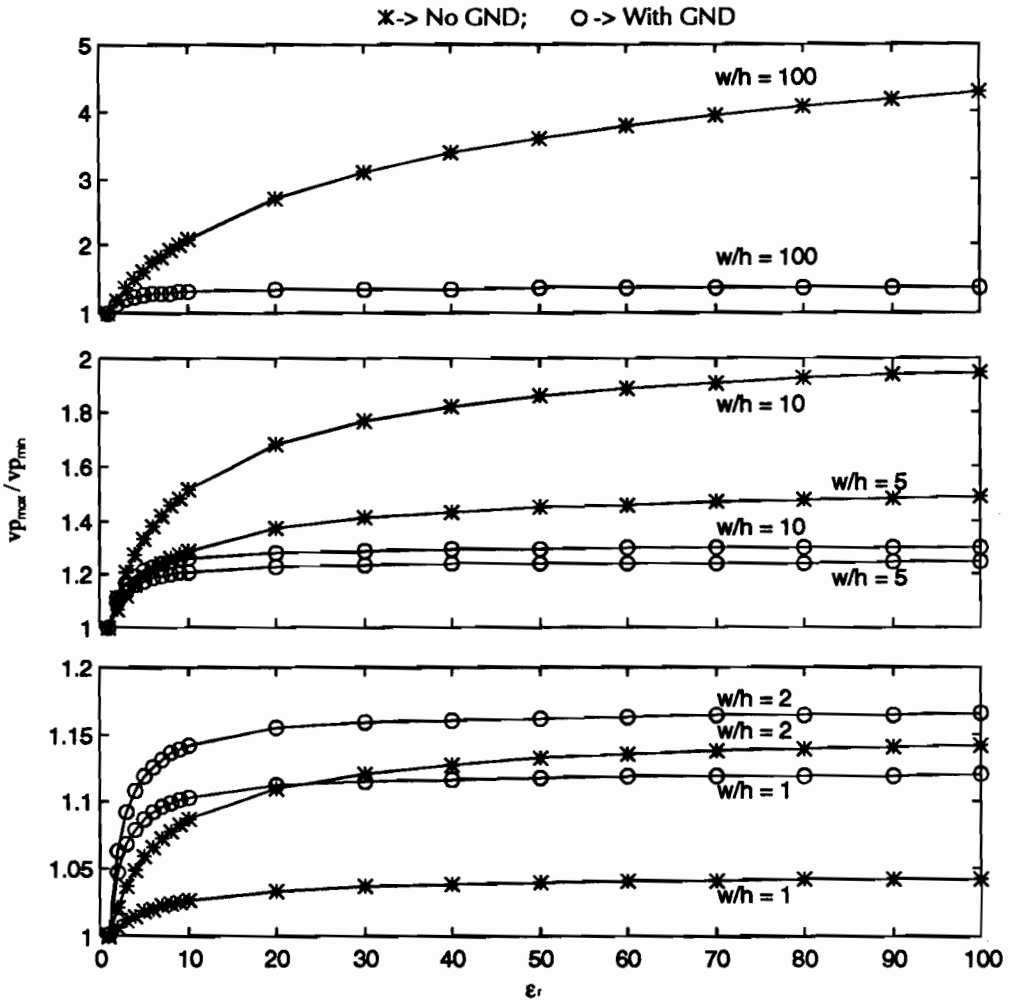

Figure 4.18 The ratio v_{max}/v_{min} as a function of ϵ_r for the structure with no ground plane.

Clearly, the dispersion between the modes in this structure is more important than in the structure with a ground plane (except for $w/h = 1$ and $w/h = 2$). If the analogy with phasor is adopted again, the structure with a ground gives a phase shift between 10° (for $w/h = 1, \epsilon_r = 100$) and 24° (for $w/h = 100, \epsilon_r = 100$) while this structure gives a phase shift between 4° (for $w/h = 1, \epsilon_r = 100$) and 69° (for $w/h = 100, \epsilon_r = 100$). Once again, the difference between the maximum and minimum modal velocities can be considered as constant for ϵ_r greater than 20.

4.2.2 Upper and lower estimates of the eigenvalue spectrum for the structure with no ground plane

As in the structure with a ground plane, it will be practical to narrow the interval of the eigenvalue spectrum in order to get an acceptable initial guess of the slowest and fastest modal velocities for a given structure. Once again, those estimates of the eigenvalues can be used as shifts (*shifted QR algorithm* or *inverse power method*) in order to accelerate the convergence of the eigenvalue problem.

In order to get an estimate of the propagation velocity of higher modes (associated with degenerate velocities), the same reasoning of section 4.1.2 can be adopted: by taking an approximated eigenfunction $\mathbf{V}_{apr}$ with an alternating $+1$ and -1 as entries. Thus, an estimate of the fastest normalized modal velocity will be

$$v_{apr} = \sqrt{\frac{\mathbf{V}_{apr}^{\mathbf{T}}\mathbf{P}\mathbf{V}_{apr}}{\mathbf{V}_{apr}^{\mathbf{T}}\mathbf{L}\mathbf{V}_{apr}}}, \tag{4.79}$$

where $\mathbf{P}$ and $\mathbf{L}$ are considered without the leading constants. For a structure with $w/h = 10, \epsilon_r = 9$, Table VI compares the relative error between the modal velocity calculated by solving the generalized eigenvalue problem (v_1) and the modal velocity calculated using (4.79).

Ne	first modal velocity: v_1	Approximated velocity: v_{apr}	Relative error $(v_1 - v_{apr})/v_1$
50	4.471998e-01	4.569660e-01	2.183860e-02
100	4.471998e-01	4.522343e-01	1.125788e-02
150	4.471998e-01	4.505952e-01	7.592760e-03
200	4.471998e-01	4.497622e-01	5.730015e-03
300	4.471998e-01	4.489194e-01	3.845249e-03
400	4.471998e-01	4.484940e-01	2.894007e-03

Table VI. Comparison between the velocities of the higher modes and the approximation for the structure with no ground plane.

Table VI suggests that the approximated velocity can give an estimate of the

slowest modal velocity despite the fact that the relative error is higher than the one obtained in Table III. It is also obvious, as in the case of Table III, that the approximated velocity is sensitive, to some extent, to the discretization of the problem. On the other hand, the velocities obtained by solving the generalized eigenvalue problem are less sensitive (or almost completely insensitive) to discretization.

In order to get an approximation of the fastest modal velocity (associated with the first, non-spurious and non-degenerate velocity) one can consider the first odd eigenfunction as a vector containing $+1$ (or -1) the first half of the structure and -1 (or $+1$) the second half:

$$\mathbf{V}_{apr} = \begin{bmatrix} +1 \\ +1 \\ \cdots \\ -1 \\ -1 \end{bmatrix}. \tag{4.80}$$

Thus, an estimate of the fastest normalized modal velocity will be, once again, the use of (4.79). For a structure with $w/h = 10, \epsilon_r = 9$, Table VII compares the relative error between the modal velocity calculated by solving for the generalized eigenvalue problem (v_{Ne}) and the modal velocity calculated using (4.79) where $\mathbf{V}_{apr}$ is given by (4.80).

Ne	last modal velocity: v_{Ne}	Approximated velocity: v_{apr}	Relative error $(v_{Ne} - v_{apr})/v_{Ne}$
50	6.646641e-01	6.469013e-01	2.672436e-02
100	6.649839e-01	6.469012e-01	2.719272e-02
150	6.650932e-01	6.469012e-01	2.735260e-02
200	6.651484e-01	6.469012e-01	2.743326e-02
300	6.652038e-01	6.469011e-01	2.751441e-02
400	6.652317e-01	6.469011e-01	2.755516e-02

Table VII. Comparison between the first non-spurious and non-degenerate velocity and an approximated one.

It is interesting to note that the approximated velocity is not sensitive to the number of elements of the problem. On the other hand, the modal velocity obtained by solving the generalized eigenvalue problem is sensitive to discretisation: the relative error between 50 and 400 elements is 0.1%. The relative error between the calculated and approximated modal velocity can be considered as being constant (2.7%). Therefore, the approximation can be considered as a good estimate for any discretization.

This same approach, e.g., forming an approximate eigenfunction by placing the right number of ± 1 in a vector, can be applied to get an initial guess of the eigenvalue associated with the remaining non-degenerate eigenfunctions. These initial guesses can thereafter be used as shifts (in *shifted QR algorithm* or the shifted *inverse power method*) to accelerate the convergence of the eigenvalue problem.

4.2.3 Removal of the spurious mode

It is possible (though not necessary) to remove the spurious mode prior to solving the generalized eigenvalue problem. Since the currents must all add up to zero, one can impose the following property on all the current eigenfunctions:

$$\int \psi_i(x) = 0, \ \forall i. \tag{4.81}$$

In other words, one can require all the eigenfunctions to be orthogonal to 1. Recall from Chapter 1, section 1.6 that the current eigenfunction is approximated by a set of basis functions

$$\psi_i(x) = \sum_j a_{i,j}\alpha_j(x). \tag{4.82}$$

Thus, given a set of functions $\{\alpha_j(x) \mid j = 1,\ldots,n\}$, find a set of functions $\{\beta_j(x) \mid j = 1,\ldots,m\}$ with $m = n-1$, all orthogonal to $f(x) = 1$. The conventional procedure is to set

$$\beta_i = \sum_{j=1}^{n} a_{i,j}\alpha_j(x) \tag{4.83}$$

and require

$$\int f(x)\beta_i dx = \sum_{j=1}^{n} a_{ij} \int f(x)\alpha_j(x)dx = 0, \qquad \forall i,\ 1 \le i \le m. \tag{4.84}$$

Therefore, what is required is a rectangular matrix $\mathbf{A}$ of m rows and n columns, such that

$$\boldsymbol{\beta}_{m\times 1} = \mathbf{A}_{m\times n}\boldsymbol{\alpha}_{n\times 1}. \tag{4.85}$$

Alternatively,

$$\mathbf{A}^{\mathbf{T}}_{n\times m}\boldsymbol{\beta}_{m\times 1} = \mathbf{A}^{\mathbf{T}}_{n\times m}\mathbf{A}_{m\times n}\boldsymbol{\alpha}_{n\times 1}. \tag{4.86}$$

Ideally, if there exists a matrix $\mathbf{A}$ such that

$$\mathbf{A}^{\mathbf{T}}_{n\times m}\mathbf{A}_{m\times n} = \mathbf{I}, \tag{4.87}$$

i.e., an orthogonal matrix, then the eigenvalue problem becomes

$$\mathbf{P}_{n\times n}\mathbf{A}^{\mathbf{T}}_{n\times m}\mathbf{A}_{m\times n}\boldsymbol{\alpha}_{n\times 1} = \lambda\,\mathbf{L}_{n\times n}\mathbf{A}^{\mathbf{T}}_{n\times m}\mathbf{A}_{m\times n}\boldsymbol{\alpha}_{n\times 1}. \tag{4.88}$$

However, by replacing $\mathbf{A}_{m\times n}\boldsymbol{\alpha}_{n\times 1}$ by $\boldsymbol{\beta}_{m\times 1}$, (4.88) becomes

$$\mathbf{P}_{n\times n}\mathbf{A}^{\mathbf{T}}_{n\times m}\boldsymbol{\beta}_{m\times 1} = \lambda\,\mathbf{L}_{n\times n}\mathbf{A}^{\mathbf{T}}_{n\times m}\boldsymbol{\beta}_{m\times 1}, \tag{4.89}$$

or,

$$\mathbf{A}_{m\times n}\mathbf{P}_{n\times n}\mathbf{A}^{\mathbf{T}}_{n\times m}\boldsymbol{\beta}_{m\times 1} = \lambda\,\mathbf{A}_{m\times n}\mathbf{L}_{n\times n}\mathbf{A}^{\mathbf{T}}_{n\times m}\boldsymbol{\beta}_{m\times 1}. \tag{4.90}$$

In other words, $\mathbf{A}_{m\times n}\mathbf{P}_{n\times n}\mathbf{A}^{\mathbf{T}}_{n\times m}$ is a *similarity transformation*, therefore the eigenvalues of the original problem are preserved. Unfortunately, it is impossible to find an orthogonal matrix $\mathbf{A}_{m\times n}$ since $m = n-1$, therefore, the best one can do is to have the dimension of the rank of $\mathbf{A}$ equal to m (under-determined system). Consequently, with the set of β functions, the eigenvalue problem

$$\mathbf{P}_{n\times n}\boldsymbol{\alpha}_{n\times 1} = \lambda\mathbf{L}_{n\times n}\boldsymbol{\alpha}_{n\times 1} \tag{4.91}$$

is expressed as

$$\mathbf{A}_{m\times n}\mathbf{P}_{n\times n}\mathbf{A}^{\mathbf{T}}_{n\times m}\boldsymbol{\beta}_{m\times 1} = \lambda'\mathbf{A}_{m\times n}\mathbf{L}_{n\times n}\mathbf{A}^{\mathbf{T}}_{n\times m}\boldsymbol{\beta}_{m\times 1} \tag{4.92}$$

where λ' is different from λ. If the numerical values are close, it is due to the physics of the problem.

Method 1: One simple choice of the matrix $\mathbf{A}$ is of the form

$$\mathbf{A} = \begin{bmatrix} \mathbf{a}_1 & \mathbf{A}' \end{bmatrix} \tag{4.93}$$

$\mathbf{A}'$ is square $M \times M$ and equal to the identity matrix. This makes it easy to find $\mathbf{a}_1$,

$$\sum_{j=1}^{N} a_{ij}\int f(x)\alpha_j(x)\,dx = a_{1i}\int f(x)\alpha_1(x)\,dx + a'_{ii}\int f(x)\alpha_i(x)\,dx = 0 \tag{4.94}$$

thus,

$$a_{1i} = -\frac{a'_{ii}\int f(x)\alpha_i(x)\,dx}{\int f(x)\alpha_1(x)\,dx} \tag{4.95}$$

where a'_{ii} is equal to 1 for all i. When the basis functions are piecewise constant, i.e., order zero finite elements, then

$$\begin{bmatrix}\beta_1\\ \beta_2\\ \cdots\\ \beta_M\end{bmatrix} = \begin{bmatrix} -1 & 1 & 0 & 0 & 0\\ -1 & 0 & 1 & 0 & 0\\ -1 & 0 & 0 & 1 & 0\\ -1 & 0 & 0 & 0 & 1\end{bmatrix}\begin{bmatrix}\alpha_1\\ \alpha_2\\ \alpha_3\\ \cdots\\ \alpha_N\end{bmatrix}. \tag{4.96}$$

Table VIII compares the modal velocities of the two generalized eigenvalue problems given by (4.91) and (4.92).

λ	λ'	$\lambda-\lambda'$
1.352911		
0.664664	0.664664	-6.661338e-16
0.565283	0.562211	3.071965e-03
0.506897	0.506897	-6.661338e-16
0.480761	0.480319	4.418347e-04
0.465220	0.465220	6.106227e-16
0.457399	0.457311	8.812559e-05
0.452781	0.452781	1.110223e-16
0.450361	0.450341	2.000880e-05
0.448946	0.448946	4.440892e-16
0.448191	0.448186	4.856895e-06
0.447753	0.447753	-1.110223e-15
0.447518	0.447517	1.226156e-06
0.447382	0.447382	1.665335e-16
0.447309	0.447308	3.172690e-07
0.447267	0.447267	-4.996004e-16

Table VIII. Modal velocities of two eigenproblems with method 1.

Method 2: Another choice of **A** will be

$$\begin{bmatrix}\beta_1\\ \beta_2\\ \cdots\\ \beta_M\end{bmatrix}=\begin{bmatrix}1 & -1 & 0 & 0 & 0\\ 0 & +1 & -1 & 0 & 0\\ 0 & 0 & +1 & -1 & 0\\ 0 & 0 & 0 & +1 & -1\end{bmatrix}\begin{bmatrix}\alpha_1\\ \alpha_2\\ \alpha_3\\ \cdots\\ \alpha_N\end{bmatrix}. \tag{4.97}$$

Table IX compares the modal velocities of the two generalized eigenvalue problems given by (4.91) and (4.92).

λ	λ'	$\lambda - \lambda'$
1.352911		
0.664664	0.664664	-5.551115e-16
0.565283	0.562211	3.071965e-03
0.506897	0.506897	-8.881784e-16
0.480761	0.480319	4.418347e-04
0.465220	0.465220	3.330669e-16
0.457399	0.457311	8.812559e-05
0.452781	0.452781	-5.551115e-17
0.450361	0.450341	2.000880e-05
0.448946	0.448946	3.330669e-16
0.448191	0.448186	4.856895e-06
0.447753	0.447753	-7.216450e-16
0.447518	0.447517	1.226156e-06
0.447382	0.447382	4.996004e-16
0.447309	0.447308	3.172690e-07
0.447267	0.447267	-2.775558e-16

Table IX. Modal velocities of two eigenproblems with method 2.

Note:

1) Both methods give the same results. The odd eigenvalues have "zero" difference (1e-16) whereas even ones are gradually decreasing.

2) The new matrix $\mathbf{A}_{m\times n}\mathbf{L}_{n\times n}\mathbf{A}^{\mathbf{T}}_{n\times m}$ is still not positive definite. Therefore LR decomposition must be used to solve the eigenproblem.

Figure 4.19 illustrates the eigenfunctions obtained with methods 1 and 2.

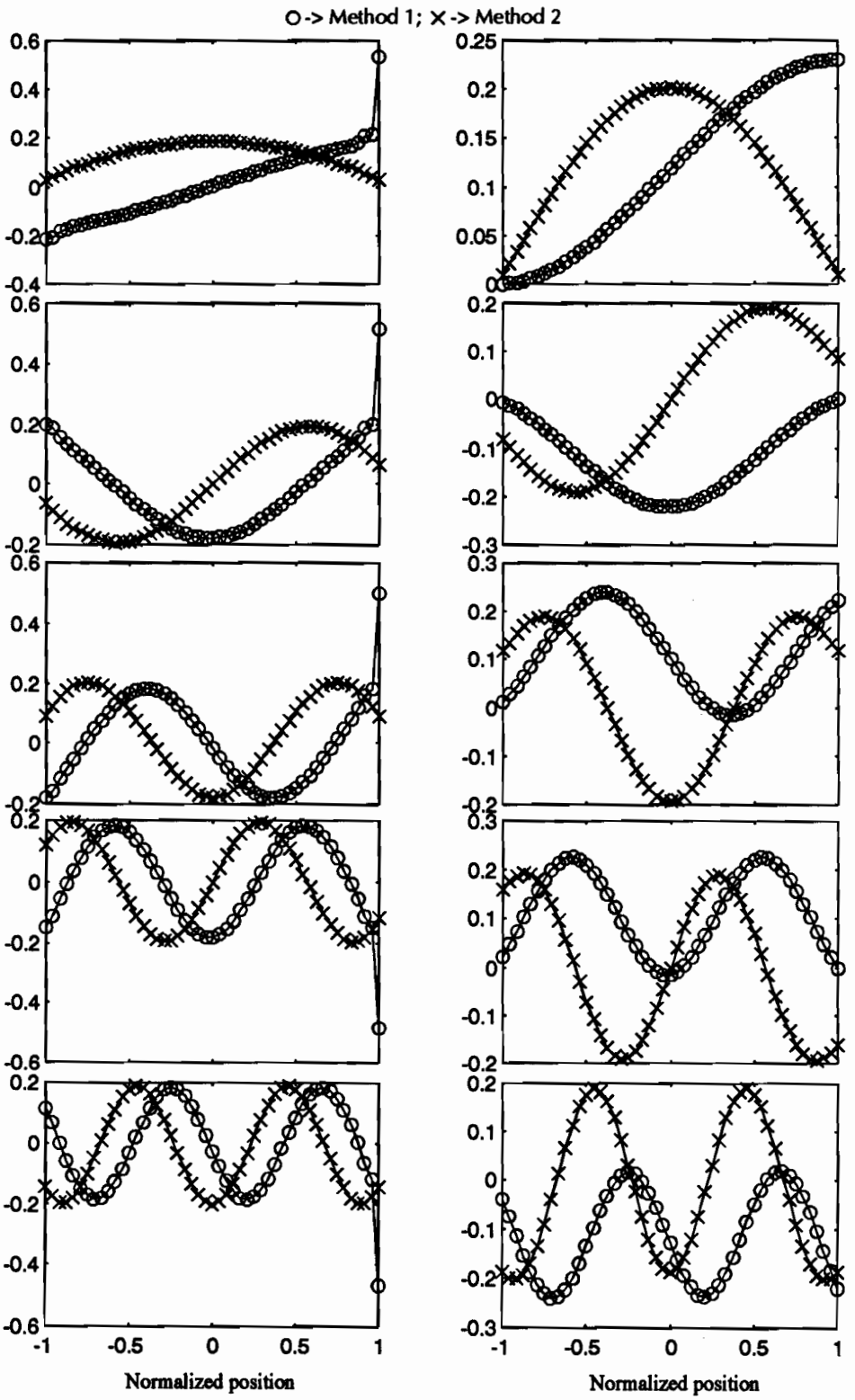

Figure 4.19 Eigenfunctions obtained with methods 1 and 2.

Method 3: Another method will be to force one eigenfunction to be spurious. Therefore, one can consider square matrices instead of rectangular ones. Without loss of generality, suppose elements of order zero are used, i.e., rectangular pulses, as the set of functions $\{\alpha_j(x) \mid j = 1,\ldots,n\}$. Then define another basis for the span of $\{\alpha_j\}$, say $\{\beta_j(x) \mid j = 1,\ldots,n\}$. Now any finite element functions, including those of zero order, form a partition of unity, i.e.,

$$\sum_{j=1}^{n} \alpha_j(x) = 1. \tag{4.98}$$

Set

$$\beta_1 = \sum_{j=1}^{n} \alpha_j(x) \tag{4.99}$$

and

$$\beta_i = \alpha_{i-1}(x) - \alpha_i(x). \tag{4.100}$$

In matrix notation,

$$\begin{bmatrix} \beta_1 \\ \beta_2 \\ \cdots \\ \beta_{n-1} \\ \beta_n \end{bmatrix} = \begin{bmatrix} 1 & 1 & 1 & \cdots & 1 & 1 \\ 1 & -1 & 0 & \cdots & 0 & 0 \\ & & & \cdots & & \\ 0 & 0 & 0 & \cdots & -1 & 0 \\ 0 & 0 & 0 & \cdots & +1 & -1 \end{bmatrix} \begin{bmatrix} \alpha_1 \\ \alpha_2 \\ \cdots \\ \alpha_{n-1} \\ \alpha_n \end{bmatrix}. \tag{4.101}$$

In this method, all the β_i are orthogonal to β_1 for $i \geq 2$. Equation (4.101) can be expressed as

$$\boldsymbol{\beta}_{n\times 1} = \mathbf{A}_{n\times n}\boldsymbol{\alpha}_{n\times 1}. \tag{4.102}$$

Since $\mathbf{A}$ is square and nonsingular, the eigenvalue problem can be stated as

$$\mathbf{P}\mathbf{A}^{-1}\mathbf{A}\boldsymbol{\alpha} = \lambda\mathbf{L}\mathbf{A}^{-1}\mathbf{A}\boldsymbol{\alpha}. \tag{4.103}$$

However, $\boldsymbol{\beta}$ is equal to $\mathbf{A}\boldsymbol{\alpha}$, thus (4.103) becomes

$$\mathbf{P}\mathbf{A}^{-1}\beta = \lambda \mathbf{L}\mathbf{A}^{-1}\beta. \tag{4.104}$$

Therefore, in this method, the eigenvalues are unaltered. Just to glance at the accuracy obtained, Table X illustrates the eigenvalues obtained by solving equations (4.91) and (4.104).

$\mathbf{P}\alpha = \lambda \mathbf{L}\alpha$	$\mathbf{P}\mathbf{A}^{-1}\beta = \lambda \mathbf{L}\mathbf{A}^{-1}\beta$	Difference
1.352911	1.352911	8.881784e-16
0.664664	0.664664	-7.771561e-16
0.565283	0.565283	-1.443290e-15
0.506897	0.506897	-3.330669e-16
0.480761	0.480761	1.665335e-15
0.465220	0.465220	4.440892e-16
0.457399	0.457399	-2.775558e-16
0.452781	0.452781	3.885781e-16
0.450361	0.450361	9.436896e-16
0.448946	0.448946	1.221245e-15
0.448191	0.448191	-2.220446e-16
0.447753	0.447753	-2.775558e-16
0.447518	0.447518	-7.216450e-16
0.447382	0.447382	1.720846e-15
0.447309	0.447309	-1.665335e-15
0.447267	0.447267	8.326673e-16
0.447244	0.447244	1.110223e-16
0.447231	0.447231	2.831069e-15
0.447224	0.447224	1.443290e-15
0.447220	0.447220	7.771561e-16
0.447218	0.447218	-1.498801e-15

Table X. Modal velocities of two eigenproblems with method 3.

With this method, the spurious mode is made sure to be the first one (β_1). Figure 4.20 illustrates the eigenfunctions obtained with the original eigenproblem and those obtained with method 3.

All these methods are in fact not necessary since unlike spurious modes encountered in waveguide discontinuities where it is spotted after a perturbation analysis, the spurious mode in multiconductor lines can be easily found. Once the eigenvalues are sorted in ascending or descending order, the spurious mode is always either the first one or the last one. In most practical cases, the spurious velocity is higher than the speed of light. Therefore, it is arguable if it is necessary to go through the trouble of removing the spurious mode via the transformation given with the three methods outlined above which are all computationally more expensive then sorting the resulting eigenvalues. Figures 4.19 and 4.20 illustrate the eigenfunctions obtained with the three methods. Note that each method gives a different representation of the eigenfunctions. All of them are valid representations.

With the three methods outlined above, the matrix of the right hand side is still not positive definite. Therefore, *LR* decomposition is used to compute the eigenvalues. Thus, the generalized eigenvalue problem

$$\mathbf{E}\mathbf{x} = \lambda \mathbf{F}\mathbf{x} \tag{4.105}$$

is expressed as

$$\mathbf{C}\mathbf{y} = \lambda \mathbf{y} \tag{4.106}$$

where $\mathbf{E}$ and $\mathbf{F}$ are the $\mathbf{P}$ and $\mathbf{L}$ matrices or the matrices obtained after the transformations ($\mathbf{P}\mathbf{A}^{-1}, \mathbf{L}\mathbf{A}^{-1}$ or $\mathbf{A}\mathbf{P}\mathbf{A}^{\mathrm{T}}, \mathbf{A}\mathbf{L}\mathbf{A}^{\mathrm{T}}$), $\mathbf{y} = \mathbf{U}\mathbf{x}$, $\mathbf{C} = \mathbf{R}^{-1}\mathbf{E}\mathbf{U}^{-1}$ and $\mathbf{U}$ and $\mathbf{R}$ are the *LU* decomposition of the matrix $\mathbf{F}$. Since the matrix $\mathbf{C}$ is not symmetric, mathematically it is not guaranteed to get real eigenvalues. However real eigenvalues are obtained for a simple reason: the matrices are the mathematical representation of a physical problem. The latter necessarily yields real velocities. In fact, even when the matrices are completely changed so that

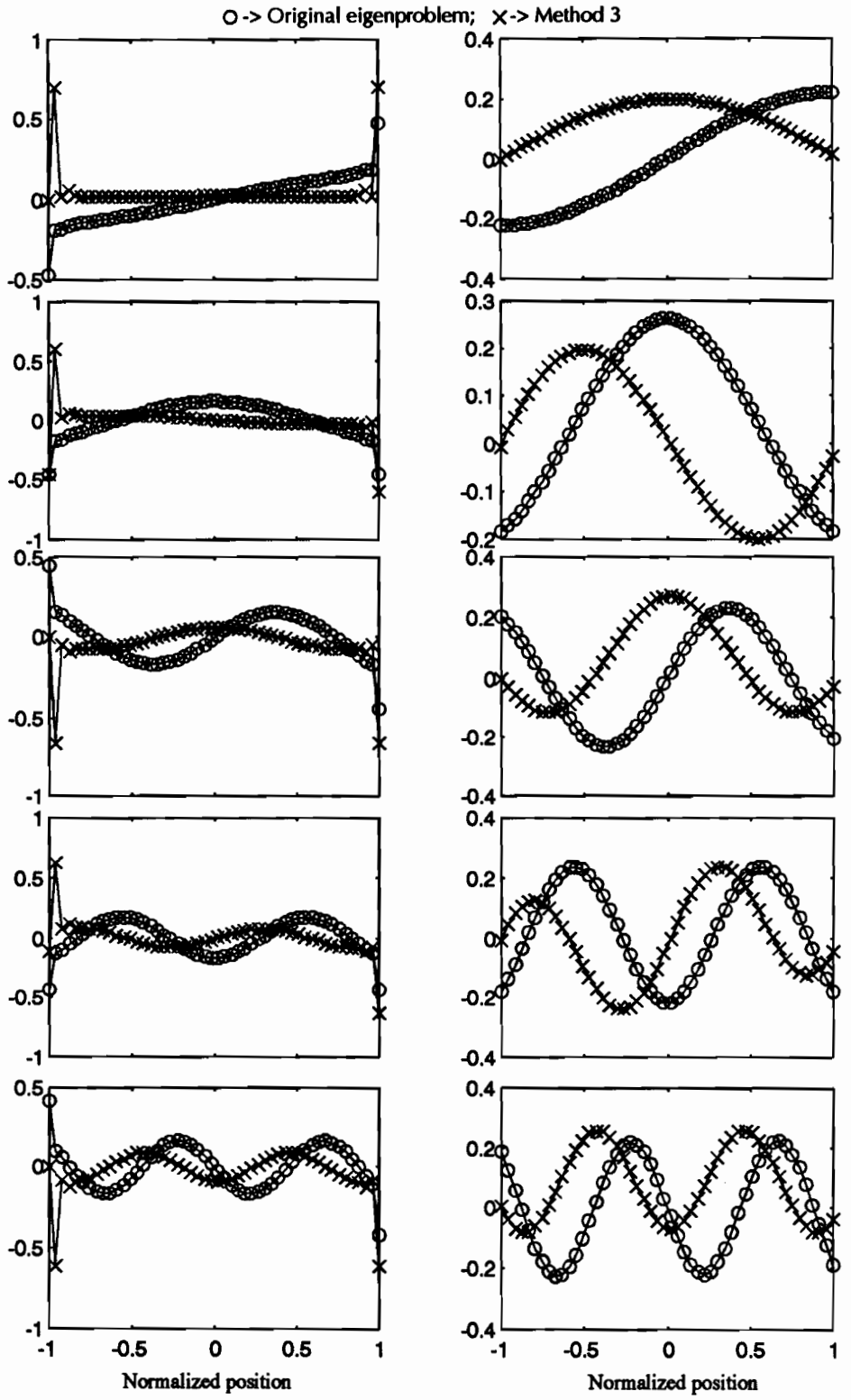

Figure 4.20 Eigenfunctions obtained with the original eigenproblem and method 3.

mathematically it is not guaranteed to get the same eigenvalues (methods 1 and 2), the resulting eigenvalues are still not too different from the original problem with a maximum absolute error of 3.1e-3. This is due to the connection of the matrices to a physical representation.

Therefore, it will be justifiable to use any transformation on the matrices **P** and **L** if it can be insured to have a positive definite matrix in the right hand side so that Cholesky decomposition can be used instead of *LU* decomposition ensuring a symmetric matrix **C**. In other words, to seek a square matrix **A**, such that $\mathbf{LA}^{-1}$ or $\mathbf{A}^t\mathbf{LA}^{-1}$ is positive definite and the new set of basis functions are all orthogonal to 1. Nevertheless, even with symmetric positive matrices, it is possible to obtain imaginary eigenvalues if the resulting positive definite matrix is ill conditioned.

Method 4: Circuit formulation.

The formulation of the problem with the field approach which gives a spurious mode is not wrong. The entries of the matrices are determined as *static field solutions in the two-dimensional transverse plane of the conductors.* Nevertheless, when the circuit approach is taken, the solution will become awkward since it is impossible to have floating sources. In other words, any voltage or current that must be forced on a conductor must be done with respect to a reference point. Therefore, with the circuit approach, it is important to select a reference point. The latter can be chosen to be one of the conductors to which all the voltages are referenced. Although the choice of reference conductor is arbitrary, choosing one of the conductor over another as reference may facilitate the computation of the new matrices. In order to do so, a similar reasoning can be adopted as by Paul and Feather [1976] by expressing all voltages of the lines with respect to one of the conductors.

Let ϕ_i be the potential of each of the $(n+1)$ conductors with respect to some reference point or line parallel to the z axis. The total charge per unit of line length, q_i, of each of the $(n+1)$ conductors is related to their potential, ϕ_i, for $i = 0,1,2,\cdots,n$ with the $(n+1)\times(n+1)$ generalized matrix, $\mathcal{P}$, as,

$$\boldsymbol{\phi} = \mathcal{P}\boldsymbol{q} \tag{4.107}$$

or, in expanded form, as

$$\begin{aligned}
\phi_0 &= \mathcal{P}_{00}q_0 + \mathcal{P}_{01}q_1 + \cdots + \mathcal{P}_{0n}q_n \\
\phi_1 &= \mathcal{P}_{10}q_0 + \mathcal{P}_{11}q_1 + \cdots + \mathcal{P}_{1n}q_n \\
&\vdots \qquad\qquad\qquad\qquad \vdots \\
\phi_n &= \mathcal{P}_{n0}q_0 + \mathcal{P}_{n1}q_1 + \cdots + \mathcal{P}_{nn}q_n
\end{aligned} \tag{4.108}$$

Note that the matrix $\mathcal{P}$ is $(n+1)\times(n+1)$. This matrix is nothing but the original matrix which gives rise to a spurious mode. It has been renamed to uppercase script in order to differentiate it from the new matrix $\mathbf{P}$ yet to be determined. The latter should be $n \times n$ and should not contain any spurious mode.

Without loss of generality, suppose that the zeroth conductor is chosen as being the reference. In order to obtain the new matrix $\mathbf{P}$ from the original matrix $\mathcal{P}$, define the line voltages with respect to this zeroth reference conductor as

$$V_i = \phi_i - \phi_0 \quad \text{for } i = 1,2,\cdots,n. \tag{4.109}$$

If it is assumed that the entire system of $(n+1)$ conductors is charge neutral, then the zeroth conductor's charge can be written in terms of the n other conductors as

$$q_0 = -\sum_{k=1}^{n} q_k. \tag{4.110}$$

Substituting (4.110) and (4.109) into (4.108) and expanding gives

$$\begin{aligned}
\phi_0 &= q_1(\mathcal{P}_{01} - \mathcal{P}_{00}) + q_2(\mathcal{P}_{02} - \mathcal{P}_{00}) \cdots + q_n(\mathcal{P}_{0n} - \mathcal{P}_{00}) \\
V_1 + \phi_0 &= q_1(\mathcal{P}_{11} - \mathcal{P}_{10}) + q_2(\mathcal{P}_{12} - \mathcal{P}_{10}) + \cdots + q_n(\mathcal{P}_{1n} - \mathcal{P}_{10}) \\
&\vdots \qquad\qquad\qquad\qquad \vdots \\
V_n + \phi_0 &= q_1(\mathcal{P}_{n1} - \mathcal{P}_{n0}) + q_2(\mathcal{P}_{n2} - \mathcal{P}_{n0}) + \cdots + q_n(\mathcal{P}_{nn} - \mathcal{P}_{n0})
\end{aligned} \tag{4.111}$$

Substituting the first equation of (4.111) into the last n equations of (4.111) yields the potential of the n conductors with respect to the zeroth (reference) conductor:

$$
\begin{aligned}
V_1 &= q_1(\mathcal{P}_{11} - \mathcal{P}_{10} - \mathcal{P}_{01} + \mathcal{P}_{00}) + q_2(\mathcal{P}_{12} - \mathcal{P}_{10} - \mathcal{P}_{02} + \mathcal{P}_{00}) + \cdots + \\
&\qquad q_n(\mathcal{P}_{1n} - \mathcal{P}_{10} - \mathcal{P}_{0n} + \mathcal{P}_{00}) \\
&\vdots \qquad\qquad\qquad\qquad \vdots \\
V_n &= q_1(\mathcal{P}_{n1} - \mathcal{P}_{n0} - \mathcal{P}_{01} + \mathcal{P}_{00}) + q_2(\mathcal{P}_{n2} - \mathcal{P}_{n0} - \mathcal{P}_{02} + \mathcal{P}_{00}) + \cdots + \\
&\qquad q_n(\mathcal{P}_{nn} - \mathcal{P}_{n0} - \mathcal{P}_{0n} + \mathcal{P}_{00})
\end{aligned}
\tag{4.112}
$$

or,

$$\mathbf{V} = \mathbf{P}\mathbf{q}$$

where the dimensions of the matrix and vectors are n. The entries of the matrix $\mathbf{P}$ are given by

$$\mathrm{P}(i,j) = \mathcal{P}(i,j) - \mathcal{P}(i,0) + \mathcal{P}(0,0) - \mathcal{P}(0,j) \quad i,j = 1,\cdots,n. \tag{4.113}$$

Note that the new matrix $\mathbf{P}$ is also symmetric.

The inductance matrix $\mathbf{L}$ can be obtained in a similar fashion since it is computed from the potential matrix with the dielectric removed, $\mathcal{P}_0$. Once the latter is computed, the new matrix $\mathbf{L}$ will be found to be $\mathbf{L} = \mu\epsilon_0\mathcal{P}_0$.

Note that if any other conductor is chosen to be the reference, the new matrices can always be calculated from these so called *generalized* matrices. This definition is given by Paul and Feather [1976] even though their formulation is based on the capacitance matrix rather than the potential.

As mentioned above, this method has a strong circuit-theoretic formulation while this work was based on a field-theoretical approach. Nevertheless, it has been introduced in order to show that it is always possible to switch from field approach to circuit. Table XI illustrates the modal velocities obtained by solving the generalized eigenvalue problem with the *generalized* matrices and the ones with the new matrices with the zeroth conductor as the reference.

$\mathcal{P}\alpha = \lambda \mathcal{L}\alpha$	$\mathbf{P}\alpha = \lambda \mathbf{L}\alpha$	Difference
1.352911e+00		
6.646641e-01	6.611969e-01	3.467159e-03
5.652830e-01	5.592344e-01	6.048617e-03
5.068973e-01	5.047686e-01	2.128739e-03
4.807606e-01	4.788259e-01	1.934672e-03
4.652198e-01	4.642316e-01	9.882114e-04
4.573991e-01	4.566588e-01	7.402997e-04
4.527810e-01	4.523661e-01	4.149382e-04
4.503609e-01	4.500771e-01	2.838589e-04
4.489460e-01	4.487826e-01	1.633943e-04
4.481909e-01	4.480848e-01	1.061068e-04
4.477534e-01	4.476919e-01	6.148283e-05
4.475177e-01	4.474791e-01	3.861099e-05
4.473822e-01	4.473598e-01	2.236998e-05
4.473088e-01	4.472951e-01	1.372770e-05
4.472668e-01	4.472589e-01	7.937145e-06
4.472440e-01	4.472392e-01	4.793458e-06
4.472311e-01	4.472283e-01	2.768995e-06
4.472240e-01	4.472223e-01	1.659939e-06
4.472200e-01	4.472190e-01	9.709647e-07
4.472177e-01	4.472171e-01	6.007410e-07

Table XI. Modal velocities of two eigenproblems with method 4.

Once again, this method results in a matrix **L** which is not positive definite. Perhaps, for another reference conductor, it might turn up to be positive definite. This assertion is subject to further investigation.

Figure 4.21 illustrates the eigenfunctions obtained with the original eigenproblem (with the *generalized* matrices) and those obtained with method 4.

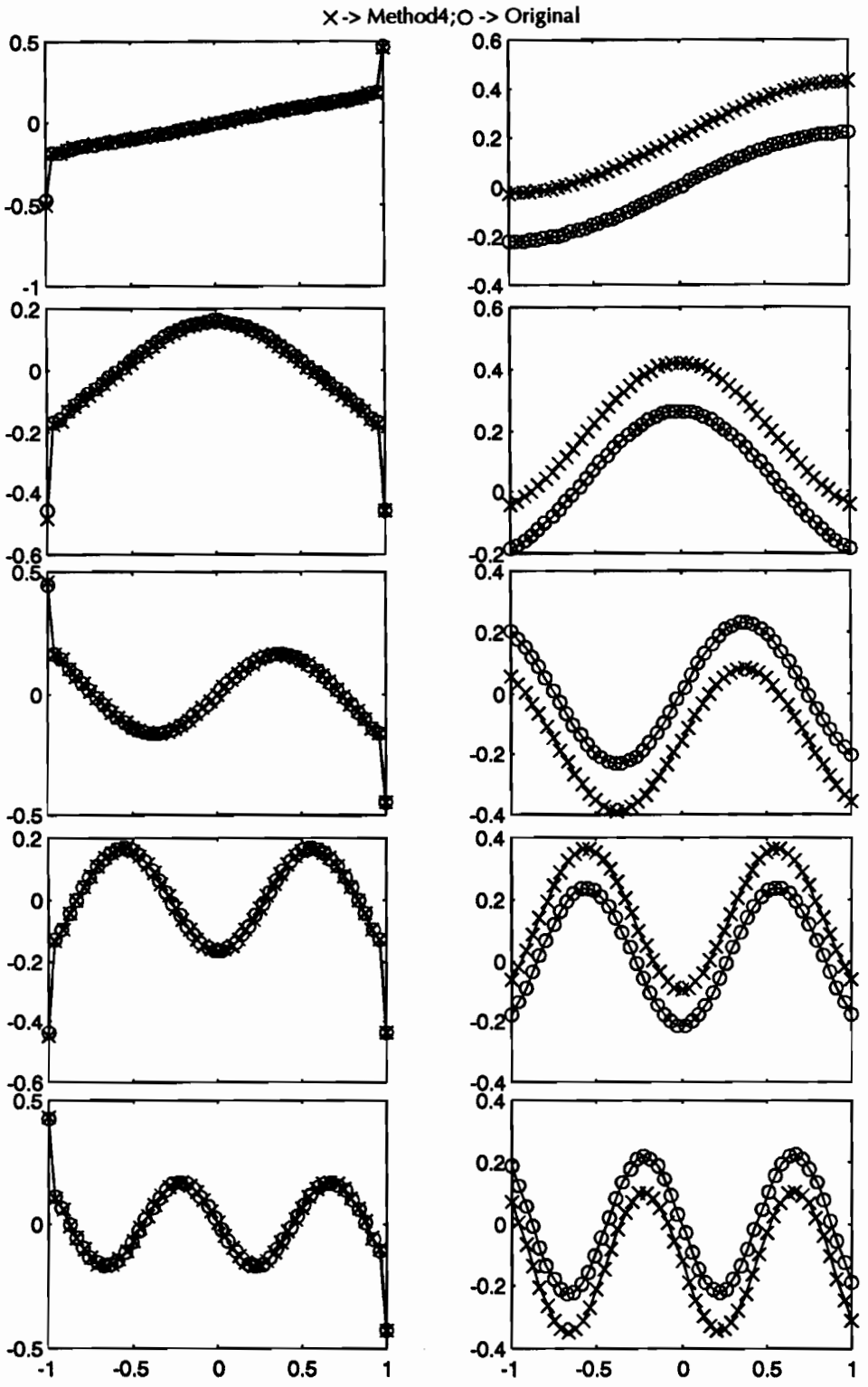

Figure 4.21 Eigenfunctions obtained with the original eigenproblem and method 4.

Conclusion:

Method 2 expresses physics with absolute correctness. It is therefore a correct representation of the problem.

Method 1 is an alternative to method 2. It only differs in computation and gives the same results.

Both methods 1 and 2 give undesirable matrix properties.

The original problem (section 4.2) and method 3 give nice matrix properties (symmetric) but the physics is dubious.

Thus, since almost all the bad physics is swept into one spurious mode while the remaining modes are reasonable approximation to truth, the original problem can be used as an approximation.

CHAPTER 5
CONDUCTORS EMBEDDED IN THE SUBSTRATE

The present chapter is very similar to the previous one as it describes the modal spectrum but for the structure of embedded conductors in the substrate. Once again, the propagation modes are shown to be substantially independent of structural details as the theory suggests in Chapter 1. On the other hand, the modes are mainly dependent on the parameters of the transmission channel, the substrate thickness, dielectric permittivity and, particular to embedded structures, the position of the conductors within the dielectric.

Therefore, the present chapter examines the effect of the parameters on the modal functions and describes the modal spectrum. Once again, since very thin conductors are concerned, the density variations in the y direction may be neglected and the modeling in the x direction is sufficient. Recall from Chapter 1 or Chapter 4 that the generalized eigenvalue problem takes the form

$$\mathbf{C}^{-1}\mathbf{a}_k = c_k^2 \mathbf{L}\mathbf{a}_k, \tag{5.1}$$

where $\mathbf{C} = \mathbf{P}^{-1}$ and the matrices are given by

$$P_{mn} = \int\int G_E(\overline{x};\overline{\xi})\, p_m(\overline{\xi}) p_n(\overline{x})\, d\overline{\xi} d\overline{x} \tag{5.2}$$

$$L_{mn} = \int\int G_M(\overline{x};\overline{\xi})\, p_m(\overline{\xi}) p_n(\overline{x})\, d\overline{\xi} d\overline{x}, \tag{5.3}$$

where $\overline{x} = x/2h$. The two Green's functions (G_E and G_M) are calculated in Chapter 2 and integration techniques for evaluating the singular integrals are described in Chapter 3.

5.1 STRUCTURE WITH A GROUND PLANE

The electric Green's function of a structure with a ground plane, as illustrated

in Figure 5.1, is given by

$$G_E(\bar{x};\bar{\xi}) = \frac{1}{4\pi\epsilon_1}\left(\log\frac{r^2+\zeta^2}{\zeta^2} + \sum_{n=1}^{\infty} K^n \log\frac{[(n-r)^2+\zeta^2][(n+r)^2+\zeta^2]}{(n^2+\zeta^2)^2}\right), \tag{5.4}$$

and the magnetic Green's function is

$$G_M(\bar{x};\bar{\xi}) = \frac{\mu_0}{4\pi}\log\frac{r^2+\zeta^2}{\zeta^2}, \tag{5.5}$$

where $\zeta = \dfrac{x-\xi}{2h} = \bar{x}-\bar{\xi}$, $K = (1-\epsilon_r)/(1+\epsilon_r)$ and $0 < r < 1$.

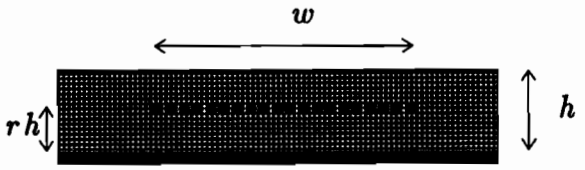

Figure 5.1 Parallel conductors embedded in a dielectric substrate with a ground plane.

Once again, computing the entries of the two matrices **P** and **L** with the leading constant will result in a matrix **P** with entries of $O(10^{+10})$ and a matrix **L** with entries of $O(10^{-7})$. A more convenient way is to compute the entries of the two matrices **P** and **L** without the leading constants, resulting in entries of the same order of magnitude for both matrices. Similarly, by normalizing the propagation velocities (the eigenvalues) with respect to the velocity of light, the results will be independent of constant though measured values such as ϵ_0. Thus, the entries of the matrix **P** must be computed as

$$P_{mn} = \int\int \log\frac{r^2+\zeta^2}{\zeta^2} p_m(\bar{\xi}) p_n(\bar{x})\, d\bar{\xi} d\bar{x} + \sum_{n=1}^{\infty} K^n \int\int \log\frac{[(n-r)^2+\zeta^2][(n+r)^2+\zeta^2]}{(n^2+\zeta^2)^2} p_m(\bar{\xi}) p_n(\bar{x})\, d\bar{\xi} d\bar{x}, \tag{5.6}$$

and those of **L** as

$$L_{mn} = \int\int \log\frac{r+\zeta^2}{\zeta^2} p_m(\bar{\xi}) p_n(\bar{x})\, d\bar{\xi} d\bar{x}. \tag{5.7}$$

The velocity v_i of a given mode i, normalized with respect to the free-space velocity, will then be

$$v_i = \sqrt{\frac{1}{\epsilon_r}\lambda_i} \tag{5.8}$$

where λ_i is the eigenvalue obtained by solving the generalized eigenvalue problem with the entries of the matrices given by (5.6) and (5.7). From here on, modal velocity refers to the normalized velocity given by (5.8).

As in the previous chapter, when all the finite elements have the same width and order, and in the absence of gaps between the finite elements, the resulting two matrices will be block Toeplitz (positive definite). Therefore, for order N finite elements, the first $N+1$ rows (or columns) of the matrices need to be calculated.

The number of terms for the series of the electric Green's function is chosen using the same reasoning as described in section 4.1. Also, the number of Gaussian quadrature nodes must be chosen based on the same reasoning as section 4.1. Therefore, order 0 finite elements will be used to calculate the results.

5.1.1 Results of generalized eigenvalue problem

For the structure illustrated in Figure 5.1, where substrate relative permittivity ϵ_r is set to 9, a width of the channel w 10.0 times the substrate thickness h, and the position of the conductors r set to 0.5, the eight modal function pairs associated with the first eight non-degenerate modal velocities are illustrated in Figure 5.2. All of the x-axes in Figure 5.2 range between $[-1;1]$ and the y-axes range between $[-0.1;0.1]$. The potential and current eigenfunctions, ϕ_i and ψ_i respectively have the same behavior, though they differ in shape from the structure described in the previous chapter. Indeed, the current eigenfunctions ψ_i resemble the potential eigenfunctions, but show a singularity at the structure's edges.

Figure 5.3 shows the distribution of the last 35 modal velocities (normalized with respect to the free-space velocity of light) associated with the non-degenerate eigenvalues. All modal velocities must lie between the velocity of a wave traveling in air alone and the velocity of a wave traveling in the substrate material alone.

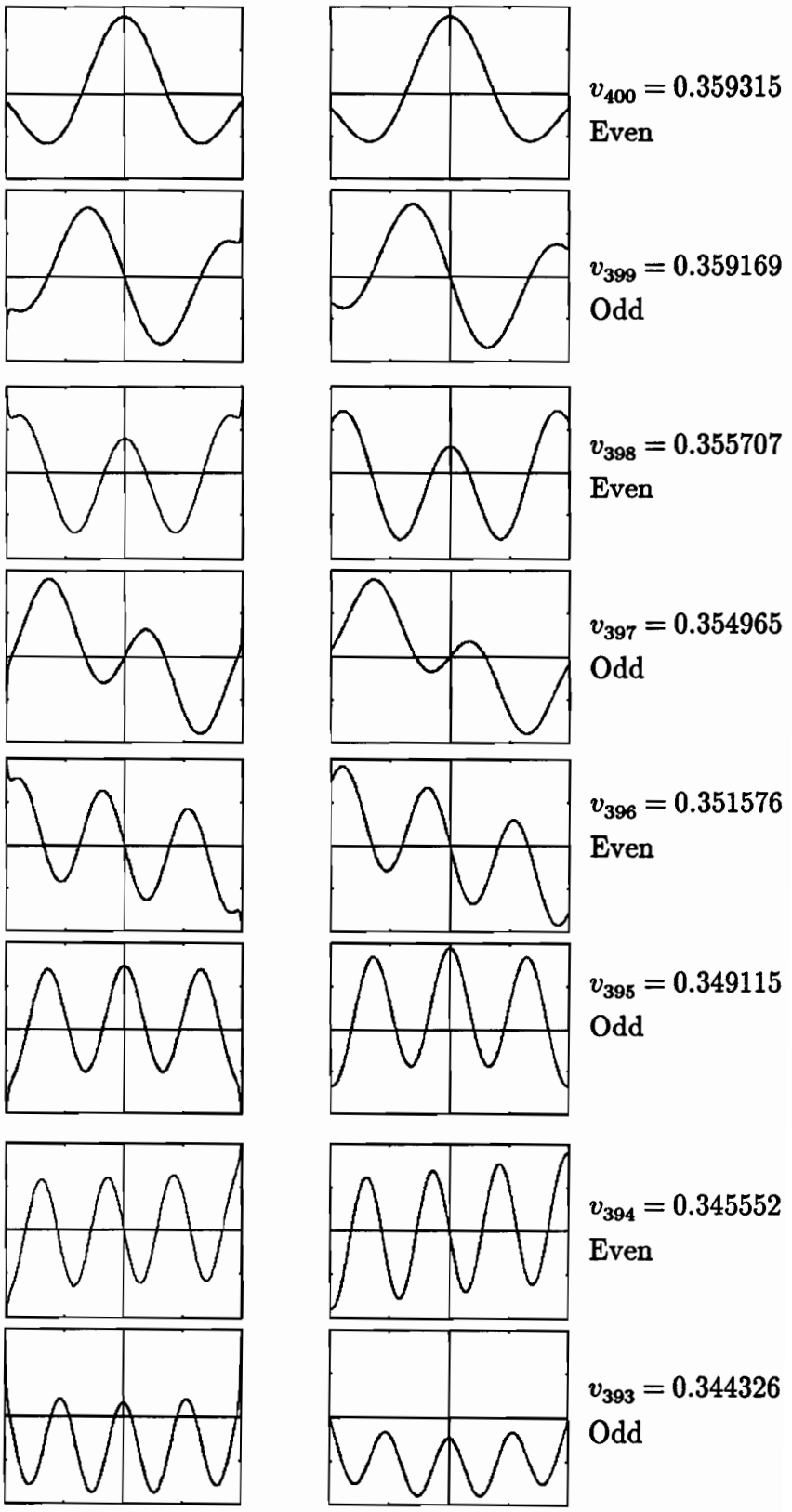

Figure 5.2 The first eight current (left) and potential (right) modal functions for thin parallel conductors embedded in a dielectric substrate with a ground plane ($w/h = 10, \epsilon_r = 9$, $r = 0.5$).

Since $\epsilon_r = 9$, these limits are 1 and 1/3. It is interesting to note that the behavior of the modal velocities bears a clear resemblance to that of a structure of the conductors printed on the surface with no ground plane rather than to one with a ground plane. Indeed, the degenerate modal velocities are slower than the non-degenerate ones. Therefore, unlike the structure of conductors printed on the surface with a ground plane, in this structure the ground plane does not "*slow down*" the propagation of the modes. On the other hand, the *dispersion* between the modes of this structure is so small that it can almost be ignored in some particular applications. Indeed, the fastest modal velocity is 0.359 while the slowest is equal to the velocity of a wave traveling in the substrate material alone. Thus, if the analogy with phasor is adopted again (as in section 4.1.1), this particular structure ($w/h = 10, \epsilon_r = 9$ and $r = 0.5$) has a phase shift of 6.4° between the fastest and slowest modes.

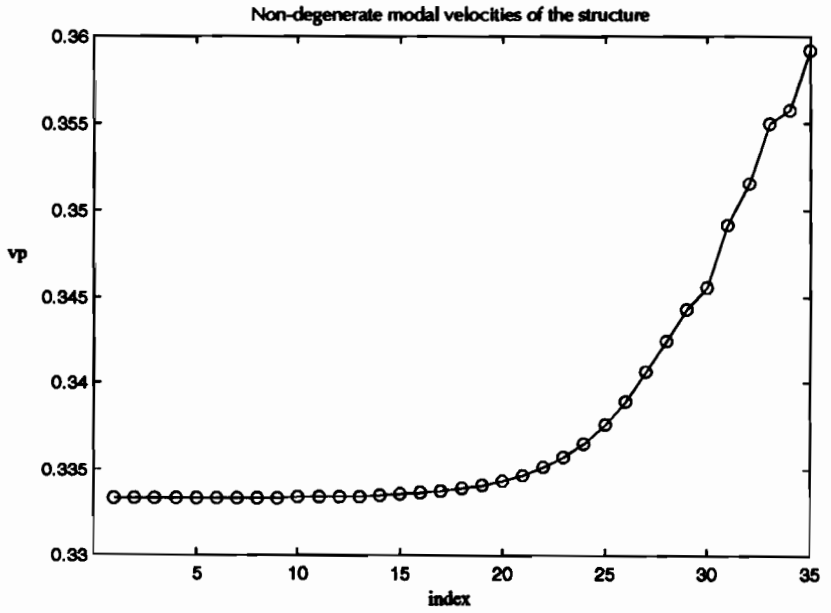

Figure 5.3 Modal velocities of a structure with $w/h = 10, \epsilon_r = 9$ and $r = 0.5$.

Figure 5.4 illustrates the effect of ϵ_r on the ratio of the maximum and the minimum of the velocities (v_{max}/v_{min}).

Clearly, the *dispersion* between modes for this structure is the least significant compared to all the structures seen thus far (in the previous chapter). Indeed, if

the analogy with phasor is adopted again, the minimum ratio is 1.0004 (for $w/h = 1$, $\epsilon_r = 1.01$ and $r = 0.5$) and the maximum 1.092 (for $w/h = 10$, $\epsilon_r = 100$ and $r = 0.5$) resulting in phase shifts of 0.036° and 7.59° respectively.

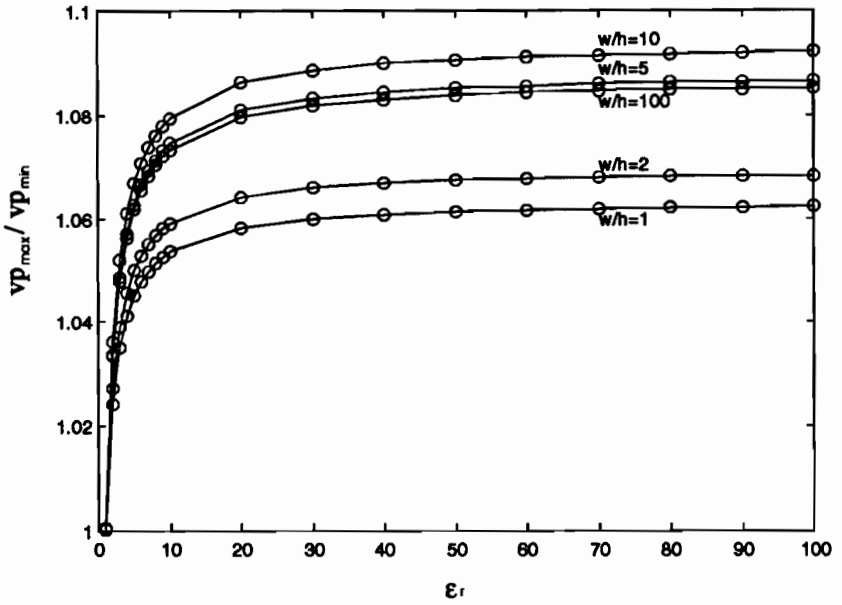

Figure 5.4 The ratio v_{max}/v_{min} as a function of ϵ_r for a structure with $r = 0.5$.

Once again, the difference between the maximum and minimum modal velocities can be considered as almost constant for ϵ_r greater than 20.

5.1.2 Effect of the position of the conductors on the eigenvalue spectrum

The effect of the position (r) of the conductors on the eigenvalue spectrum is an important aspect that needs investigation. Figure 5.5 illustrates the modal velocities of a structure where substrate relative permittivity ϵ_r is set to 9, the width of the channel w 10.0 times the substrate thickness h for different values of the position of the conductors r.

Obviously, the ratio between the maximum and minimum modal velocities increases as the conductors get closer to the surface of the dielectric substrate (as r gets closer to 1).

It is interesting to inquire at which value of r close to 1 the behavior (degenerate modal velocities faster than the non-degenerate ones) of the structure

with surface conductors will be observed. Figure 5.6 illustrates the modal velocities for r set to 0.9, 0.99, 0.999 and 0.999.

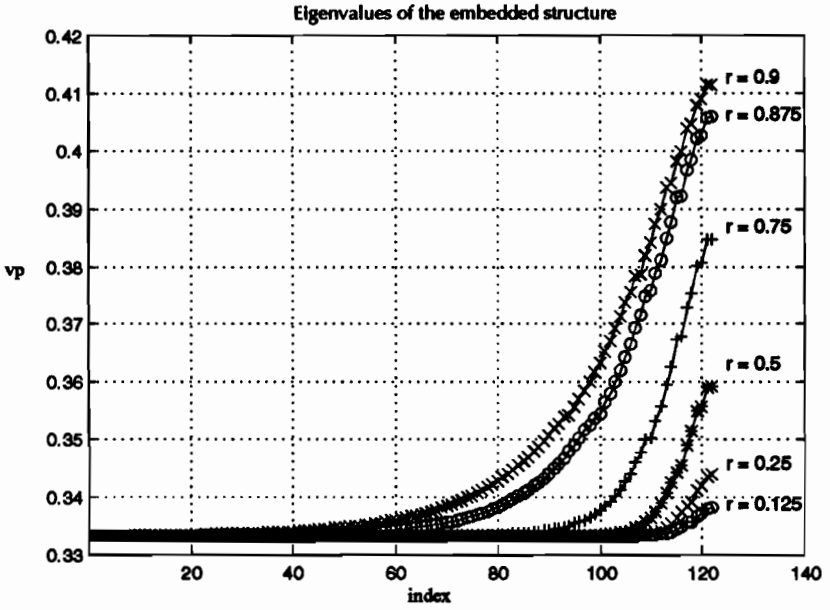

Figure 5.5 Modal velocities of a structure with $w/h = 10, \epsilon_r = 9$ and different values of r.

Figure 5.6 suggests that the behavior of surface conductors is observed when the position of the conductors of this structure is very close to the surface ($r \geq 0.999$).

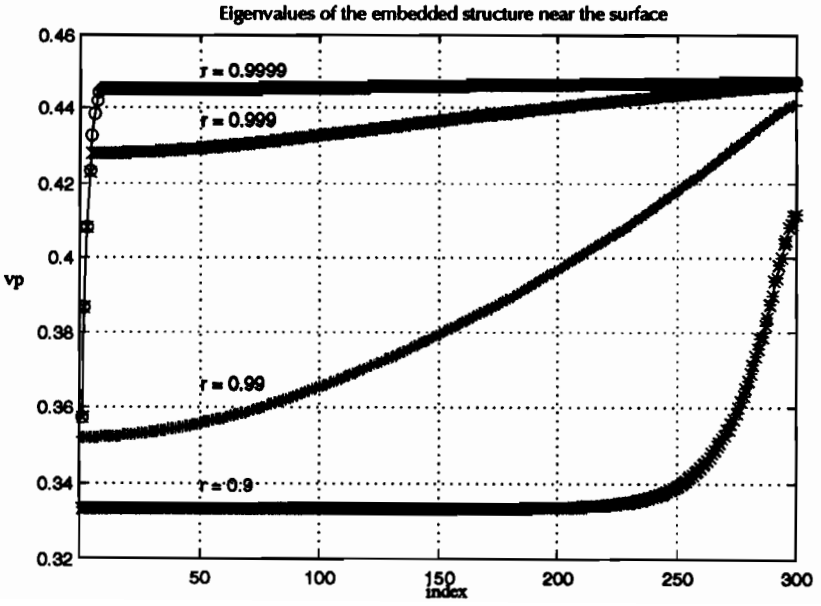

Figure 5.6 Modal velocities of a structure with $w/h = 10, \epsilon_r = 9$ and for $r \geq 0.9$.

Precautions must be taken when r is fixed to a value close to 1. Recall that the electric Green's function of this structure is given by

$$G_E(\bar{x};\bar{\xi}) = \frac{1}{4\pi\epsilon_1}\left(\log\frac{r^2+\zeta^2}{\zeta^2} + \sum_{n=1}^{\infty} K^n \log\frac{[(n-r)^2+\zeta^2][(n+r)^2+\zeta^2]}{(n^2+\zeta^2)^2}\right). \tag{5.9}$$

The first term of (5.9) is integrated analytically after removing the singularity with the coordinate transformation outlined in Chapter 3. On the other hand, numerical quadrature is used for each integral in the summation of (5.9). However, the first integral ($n=1$) is singular for $r=1$ when integration is performed to calculate the self capacitance of a conductor. Thus, with r set to a value close to 1 such as 0.9999, a numerical integration is performed very close to a singular point. Therefore, either high-order Gaussian quadrature or analytical solution (obtained by a symbolic math package) must be used. Figure 5.7 illustrates the modal velocities of the structure with surface conductors (Chapter 4) and this structure with r set to 0.9999. The modal velocities of this structure have been obtained using the analytical solution for the integrals.

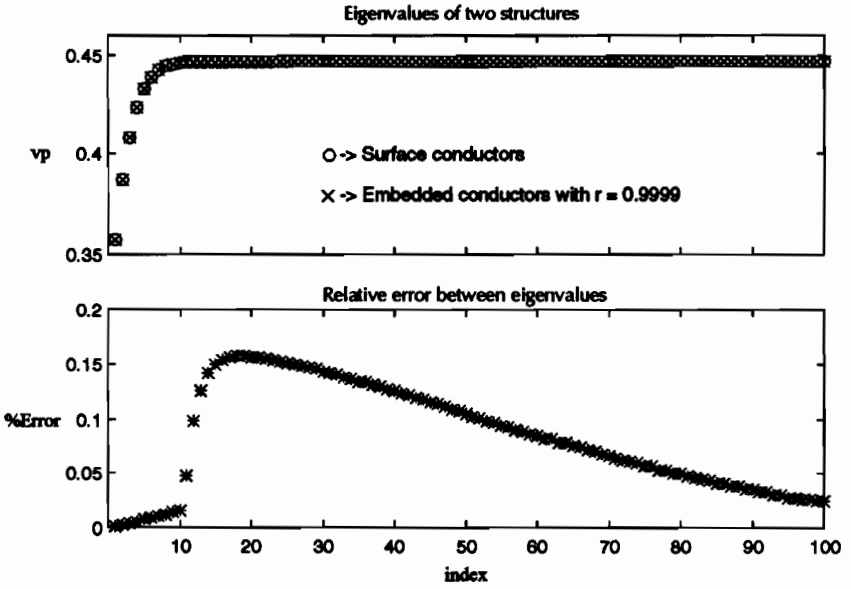

Figure 5.7 Top graph: modal velocities of surface conductors and embedded with $r = 0.9999$. Bottom graph: relative error between the modal velocities.

Obviously, the results are very satisfactory since the maximum relative error (relative to the modal velocities of the surface conductors) is 0.16%. Therefore, as mentioned in Chapter 2, it is possible to use the Green's functions of this structure, given by (5.9), in a single program which accounts for the structure of a surface and embedded conductors with a ground plane.

Figure 5.5 suggests that the *dispersion* between modes increases with the position of the conductors. Figure 5.8 outlines this behavior with a *dispersion diagram* where the effect of ϵ_r on the ratio of the maximum and the minimum of the velocities (v_{max}/v_{min}) is depicted for a structure $w/\mathrm{h} = 10$ for different values of the position of the conductors.

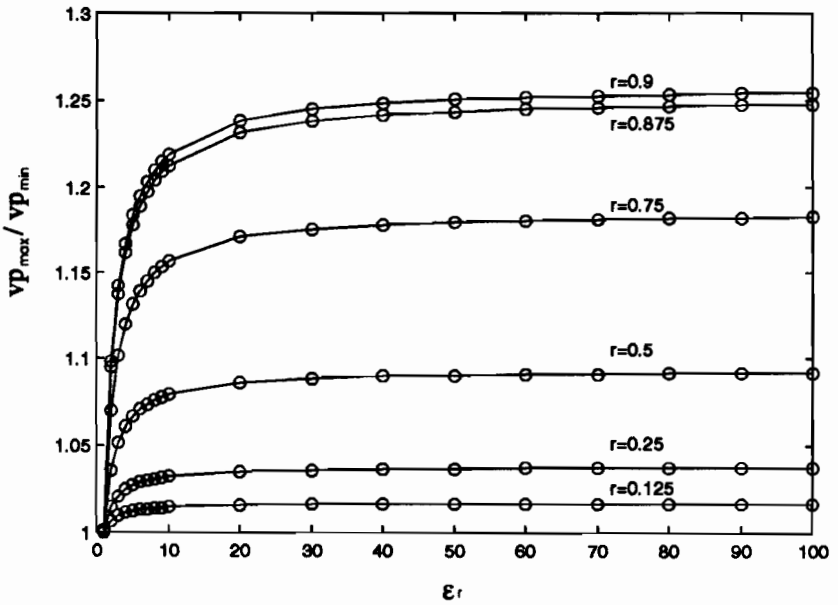

Figure 5.8 The ratio v_{max}/v_{min} as a function of ϵ_r for a structure with $w/h = 10$, for different values of r.

As mentioned earlier, for $r < 0.5$, the ratio is so small that the modes can almost be considered as having the same modal velocities (TEM propagation). As the distance between the conductors and the surface of the dielectric decreases, the ratio becomes more important. For instance, if the analogy with phasor is adopted again (as in section 4.1.1), for $r = 0.875$ the ratio is close to 1.25, resulting in a phase shift of 18°.

5.1.3 Upper and lower estimates for the eigenvalue spectrum

The lower estimate of the modal velocity spectrum is already known. In fact, it is not an estimate but rather an exact value. Indeed, for any realistic structure ($r \leq 0.9$), the lower modal velocity is equal to the velocity of a wave traveling in the substrate material alone. This exact value becomes an estimate for r greater than 0.9.

It is interesting to compare the fastest modal velocity with the TEM wave velocity to verify if the latter can be used as an estimate for the first non-degenerate (fastest) modal velocity. As in the case of modal velocities, a convenient way of calculating the normalized TEM wave velocity is to factor out the leading constant. Thus, the two matrices can be written as

$$\mathbf{P} \text{ as } \frac{1}{4\pi\epsilon_0\epsilon_r}\mathbf{P} \text{ and } \mathbf{L} \text{ as } \frac{\mu_0}{4\pi}\mathbf{L}. \tag{5.10}$$

By defining,

$$\mathbf{b} = \begin{bmatrix} \int p_1(\overline{x})\, d\overline{x} \\ \cdots \\ \int p_n(\overline{x})\, d\overline{x} \end{bmatrix}, \tag{5.11}$$

and

$$t_1 = \mathbf{b}^{\mathrm{T}}\mathbf{P}^{-1}\mathbf{b}, t_2 = \mathbf{b}^{\mathrm{T}}\mathbf{L}^{-1}\mathbf{b}, \tag{5.12}$$

where T denotes transposition, the line capacitance per unit length C is obtained by

$$C = (4\pi\epsilon_0\epsilon_r)\,\mathbf{b}^{\mathrm{T}}\mathbf{P}^{-1}\mathbf{b} = (4\pi\epsilon_0\epsilon_r)\,t_1. \tag{5.13}$$

The capacitance per unit length C_0 for a similar line with $\epsilon_r = 1$ is

$$C_0 = \frac{4\pi}{\mu_0}\mathbf{b}^{\mathrm{T}}\mathbf{L}^{-1}\mathbf{b} = \frac{4\pi}{\mu_0}t_2. \tag{5.14}$$

The inductance per unit length is then

$$L = \frac{1}{C_0} = \frac{\mu_0}{4\pi}\frac{1}{t_2}. \tag{5.15}$$

The TEM velocity is given by

$$v = \frac{1}{\sqrt{LC}} = \frac{1}{\sqrt{\frac{\mu_0}{4\pi t_2}(4\pi\epsilon_0\epsilon_r)t_1}} = \frac{1}{\sqrt{\epsilon_0\mu_0}}\sqrt{\frac{t_2}{\epsilon_r t_1}}\,. \tag{5.16}$$

Therefore, the TEM velocity, normalized with respect to c, is given by

$$\frac{v}{c} = \sqrt{\frac{t_2}{\epsilon_r t_1}}\,. \tag{5.17}$$

Table I outlines the difference between the first non-degenerate modal velocity (the fastest) for a structure with $w/h = 10$, $\epsilon_r = 9$ and $r = 0.5$ and the TEM velocity.

Ne	TEM velocity v	modal velocity (v_{Ne})	Relative error $(v_{Ne} - v)/v_{Ne}$
50	0.343728	0.359313	4.337362e-02
100	0.343708	0.359315	4.343456e-02
200	0.343700	0.359315	4.345758e-02
400	0.343696	0.359315	4.346888e-02

Table I. Comparison between the TEM velocity and the first non-degenerate (fastest) modal velocity for a structure with $w/h = 10$, $\epsilon_r = 9$ and $r = 0.5$.

The relative error between the TEM velocity and the first non-degenerate modal velocity is not as promising as it was for the surface conductors. In other words, the relative error is somewhat considerable (4%).

Table I also illustrates the sensitivity of the modal velocities to discretisation. They are certainly very stable since in the relative error between 50 and 400 elements is 6.5e-04%.

5.1.4 Crosstalk problem

Recall from section 4.1.3 that when all the sources connected to the conductors are held at zero except for the source feeding conductor m, the voltage on conductor n will be given by

$$V(\overline{x}_n, z, t) = \mathrm{V}_e \sum_k \phi_k(\overline{x}_n)\psi_k(\overline{x}_m)h_k(z - c_k t). \tag{5.18}$$

Figure 5.9 illustrates the crosstalk for the structure where $w/h = 10$ ($-5h \leq x \leq +5h$), $\epsilon_r = 9$ and $r = 0.5$. The voltages on conductors 1 ($\overline{x}_n = -5h$), 2 ($\overline{x}_n = -4.975h$), 40 ($\overline{x}_n = -4.025h$), and 94 ($\overline{x}_n = -2.675h$) at some point $z > 0$ are illustrated when a step function of unity amplitude is applied on conductor 1 ($\overline{x}_m = -5h$) at $t = 0$ and $z = 0$, while all the other conductors are grounded. Once again, the conductors are considered to have infinite length. Therefore, voltages appear on all the conductors not because of reflections but due to crosstalk. Since all the conductors are grounded except one, their final voltage is zero, while the first conductor reaches 1v gradually.

Once again, the time scale is normalized to the velocity of light in air and z.

The crosstalk outlined in Figure 5.9 can be compared to Figure 4.11 since the structures are almost alike. Indeed, $w/h = 10$, $\epsilon_r = 9$ and the voltages are drawn for the same conductors. The only difference is that in Figure 4.11 the conductors are on the surface of the dielectric while in Figure 5.9, they are right in the middle ($r = 0.5$). In Figure 5.9, the effect of the modal velocity behavior is made clear. Since the dominant modes, associated with the non-degenerate modal velocities, are faster than the high–order modes, associated with degenerate modal velocities, the shape of the voltages are the image of those depicted in Figure 4.11. The fast–order modes arrive first, followed by a substantial number of high–order slow–traveling modes, resulting in an abrupt voltage change in a short period of time. In Figure 4.11, this abrupt change of voltage was observed first since the high–order modes were the faster ones.

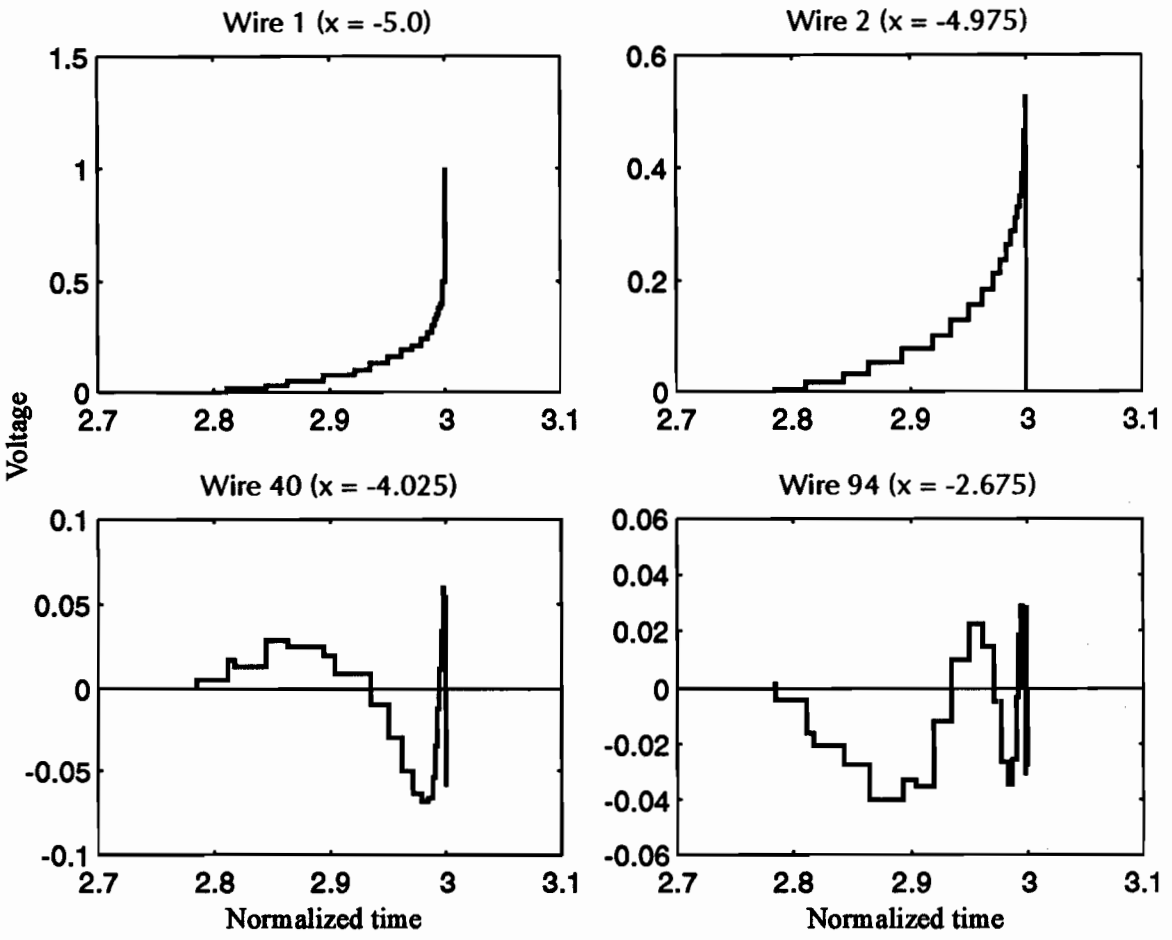

Figure 5.9 Voltage distribution as a function of time for a step excitation.

It should also be noted that the duration of the crosstalk (the range of the normalized time) is shorter in Figure 5.9 than in Figure 4.11. Indeed, the duration of the normalized time in Figure 4.11 was 0.6 (between 2.2 and 2.8) while in Figure 5.9, the duration is 0.3 (between 2.7 and 3.0). This behavior is due to the fact that the ratio between the fastest and slowest modal velocity in the structure with surface conductors was more important than the ratio of this structure.

5.1.5 Equipotential lines

Equipotential lines can be computed with the objective to observe the fields produced by the eigenfunctions. Referring back to Chapter 2, the potential at a point P in the dielectric (i.e $y < h$), due to a charge q placed at $y = a$, is given by

$$V_1(x,y) = \frac{q}{4\pi\epsilon_1}\log\frac{x^2+(y+a)^2}{x^2+(y-a)^2} + \frac{q}{4\pi\epsilon_1}\sum_{n=0}^{\infty} K^{n+1}\log\frac{[(n+1)2h-a-y]^2+x^2}{[(n+1)2h+a-y]^2+x^2}$$
$$+\frac{q}{4\pi\epsilon_1}\sum_{n=0}^{\infty} K^{n+1}\log\frac{[(n+1)2h+a+y]^2+x^2}{[(n+1)2h-a+y]^2+x^2}, \tag{5.19}$$

and for $y > h$ (in air),

$$V_2(x_0,y_0) = (1+K)V_1(x_0,y_0), \tag{5.20}$$

where $K = \frac{1-\epsilon_r}{1+\epsilon_r}$, ϵ_r being the relative permittivity of the substrate.

Using the above expressions, equipotential lines can be computed when the charge distributions are represented by the eigenfunctions. Therefore, for any given point (x_0, y_0), the potential can be calculated as follows.
For $y_0 > h$

$$V_1(x_0,y_0) = \frac{1}{4\pi\epsilon_1}\int \phi_i(x)\log\frac{(x-x_0)^2+(y_0+a)^2}{(x-x_0)^2+(y_0-a)^2}\,dx$$
$$+\frac{1}{4\pi\epsilon_1}\sum_{n=1}^{\infty} K^n\int \phi_i(x)\log\frac{[2nh-a-y_0]^2+(x-x_0)^2}{[2nh+a-y_0]^2+(x-x_0)^2}\,dx$$
$$+\frac{1}{4\pi\epsilon_1}\sum_{n=1}^{\infty} K^n\int \phi_i(x)\log\frac{[2nh+a+y_0]^2+(x-x_0)^2}{[2nh-a+y_0]^2+(x-x_0)^2}\,dx, \tag{5.21}$$

and for $y_0 > h$

$$V_2(x_0,y_0) = (1+K)V_1(x_0,y_0), \tag{5.22}$$

where $\phi_i(x)$ is the i^{th} potential eigenfunction. The latter gives the behavior of the electric field. By substituting $\phi_i(x)$ with $\psi_i(x)$ (the current eigenfunction), the magnetic field behavior can be observed. Note that, for brevity the summations start at $n = 1$ rather than 0.

Figure 5.10 illustrates equipotential lines associated with the electromagnetic fields produced by the first four potential and current eigenfunctions associated with the non-degenerate modal velocities for a structure with $w/h = 10$, $\epsilon_r = 9$ and $r = 0.5$.

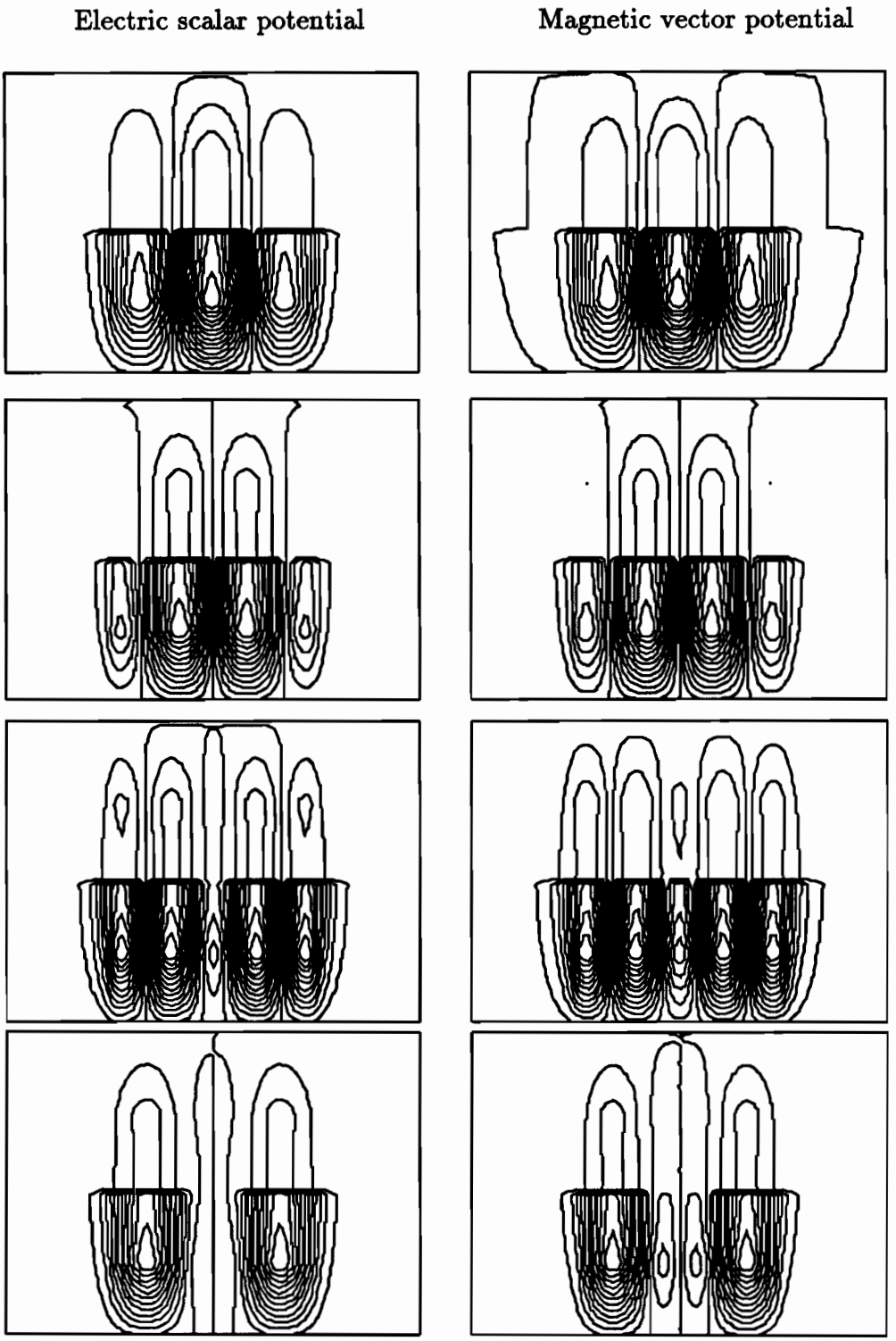

Figure 5.10 Equipotential lines due to the first four voltage and current charge distributions.

Figure 5.10 makes more evident the difference between this structure and the structure where the conductors are printed on the surface of the dielectric substrate. It can be seen from Figure 5.10 that most of the electromagnetic fields travel in the dielectric substrate. The equipotential lines have been calculated for a grid of points where y_0 ranges between the ground and $2h$ (conductors are placed at $0.5h$) while x_0 ranges between $-w$ to $+w$ (conductors occupy a region from $-w/2$ to $+w/2$).

It is interesting to note that not only the first few dominant modes are capable to extend a small percentage of their fields in air but even the higher modes have this characteristic. This assertion is substantiated when equipotential lines of higher modes are depicted.

Figure 5.11 illustrates the equipotential lines produced by the next four eigenfunctions associated with the non-degenerate modal velocities for the same structure ($w/h = 10$, $\epsilon_r = 9$ and $r = 0.5$).

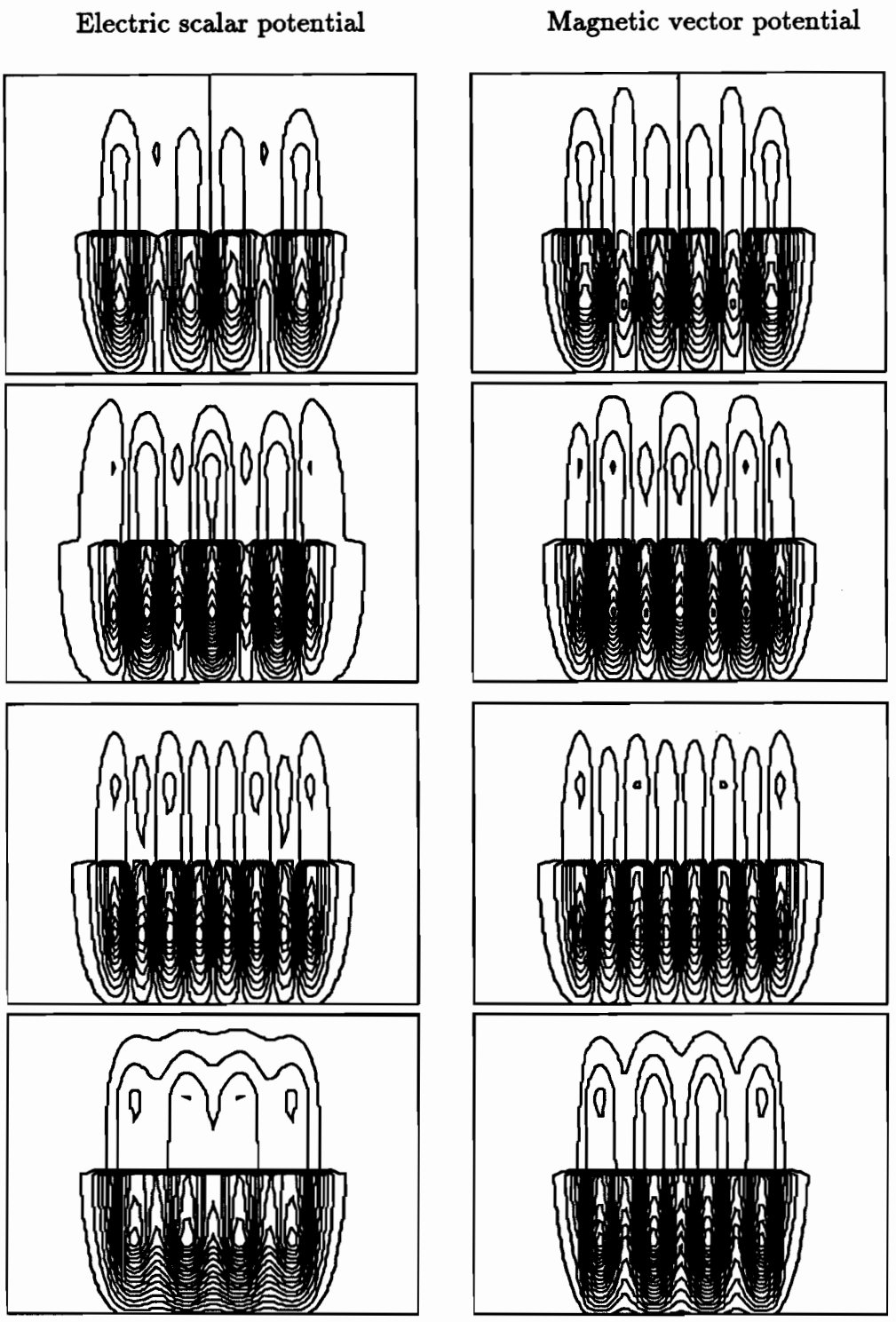

Figure 5.11 Equipotential lines due to the voltage and current charge distributions (5 through 8).

5.2 STRUCTURE WITH NO GROUND PLANE

The electric Green's function of a structure with no ground plane (calculated in Chapter 2) is given by

$$G_E(\overline{x};\overline{\xi}) = -\frac{1}{4\pi\epsilon_1}\Bigg(\log(\zeta^2) + \epsilon_r \log(4h^2) + 2\sum_{n=1}^{\infty} K^{2n}\log(n^2+\zeta^2) - \sum_{n=1}^{\infty} K^{2n-1}\log\{[(n-1+r)^2+\zeta^2][(n-r)^2+\zeta^2]\}\Bigg), \quad (5.23)$$

and the magnetic Green's function is

$$G_M(\overline{x};\overline{\xi}) = -\frac{\mu_0}{4\pi}\Big(\log(\zeta^2) + \log(4h^2)\Big), \quad (5.24)$$

where $\zeta = \dfrac{x-\xi}{2h} = \overline{x} - \overline{\xi}$.

Once again, it is preferable, as in the case of the structure with a ground plane, to compute the entries of the two matrices **P** and **L** without the leading constants. Thus, the entries of the matrix **P** must be computed as

$$\begin{aligned} P_{mn} = {} & \int\int \Big(\log(\zeta^2) + \epsilon_r \log(4h^2)\Big) p_m(\overline{\xi}) p_n(\overline{x})\, d\overline{\xi} d\overline{x} + \\ & - \sum_{n=1}^{\infty} K^{2n-1} \int\int \log\{[(n-1+r)^2+\zeta^2][(n-r)^2+\zeta^2]\, p_m(\overline{\xi}) p_n(\overline{x})\, d\overline{\xi} d\overline{x} \\ & + 2\sum_{n=1}^{\infty} K^{2n} \int\int \log(n^2+\zeta^2)\, p_m(\overline{\xi}) p_n(\overline{x})\, d\overline{\xi} d\overline{x}, \end{aligned} \quad (5.25)$$

and those of **L** as

$$L_{mn} = \int\int \Big(\log(\zeta^2) + \log(4h^2)\Big) p_m(\overline{\xi}) p_n(\overline{x})\, d\overline{\xi} d\overline{x}. \quad (5.26)$$

The velocity v_i of a given mode i, normalized with respect to the free-space velocity, will then be

$$v_i = \sqrt{\frac{1}{\epsilon_r \lambda_i}}, \quad (5.27)$$

where λ_i is the eigenvalue obtained by solving the generalized eigenvalue problem

with the entries of the matrices given by (5.25) and (5.26).

The resulting matrices **P** and **L** are no longer positive definite as in the case of the structure with a ground plane. Therefore, the generalized eigenvalue problem must be solved using the LU decomposition which, in the context of eigenvalue problems, is traditionally called the LR decomposition.

5.2.1 Results of generalized eigenvalue problem

Figure 5.12 illustrates the last seven modal function pairs (associated with the non-degenerate eigenvalues) for a structure where substrate relative permittivity ϵ_r is set to 9, the width of the channel w is 10.0 times the substrate thickness h, and the position of the conductors r is set to 0.5. As in the case of Figure 5.2, all of the x-axes in Figure 5.12 range between $[-1;1]$ and the y-axes range between $[-0.1;0.1]$. It is surprising to note that, as mentioned in section 5.1.1, the eigenfunctions for an embedded structure with a ground plane differ in shape from those of surface conductors with a ground plane. On the other hand, the eigenfunctions of this structure resemble those of surface conductors with or without a ground plane (since the two structures of surface conductors have eigenfunctions that look alike).

As mentioned in Chapter 2, this structure leads to one spurious mode which must be eliminated. The latter was expected since the conservation of charge was not respected during the calculation of the Green's function, i.e. the contribution of each charge to the total potential is not that of a dipole. The spurious modal velocity is either greater than the speed of light or less than the velocity of a wave traveling in the substrate material alone. Note that the spurious eigenfunction is omitted from Figure 5.12.

Table II demonstrates a comparison between the non-spurious current eigenfunctions obtained with this structure (ψ_e) and the structure with surface conductors with no ground plane (ψ_s, previous chapter). The comparison is illustrated using three methods: the angle between them, the standard deviation (STD) and the Euclidean norm of the difference. Table II suggests that the non-degenerate eigenfunctions do look alike especially when the difference between the modal velocities decreases. Those with a larger difference have a more significant, though still moderate, standard deviation.

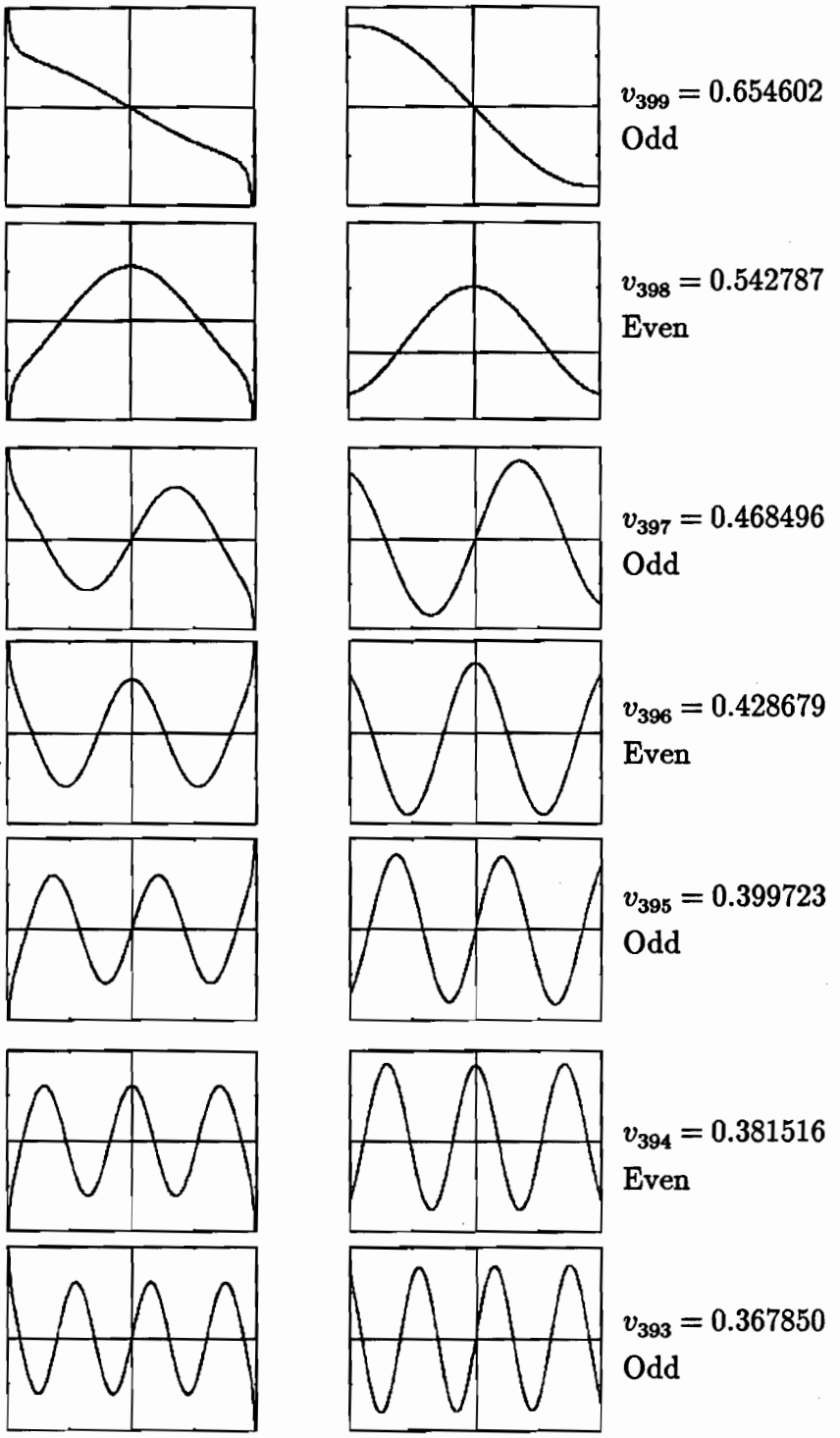

Figure 5.12 The current and potential modal functions associated with the first seven non-degenerate eigenvalues for conductors embedded in a dielectric substrate with no ground plane ($w/h = 10, \epsilon_r = 9$ and $r = 0.5$).

velocity surface	velocity embedded	angle °	STD $(\psi_s - \psi_e)$	$\|\psi_s - \psi_e\|_2$
6.652317e-01	6.546024e-01	3.15	0.002755	0.055029
5.658212e-01	5.427872e-01	4.59	0.004012	0.080144
5.073011e-01	4.684964e-01	6.16	0.005382	0.107497
4.810682e-01	4.286795e-01	7.47	0.006525	0.130344
4.654326e-01	3.997231e-01	9.01	0.007862	0.157041
4.575518e-01	3.815160e-01	10.32	0.009007	0.179928
4.528834e-01	3.678500e-01	11.91	0.010385	0.207441
4.504319e-01	3.586850e-01	13.27	0.011568	0.231082
4.489925e-01	3.517348e-01	14.90	0.012981	0.259286
4.482222e-01	3.469233e-01	16.30	0.014197	0.283586
4.477734e-01	3.432651e-01	17.95	0.015623	0.312072
4.475307e-01	3.406874e-01	19.39	0.016860	0.336769
4.473901e-01	3.387284e-01	21.04	0.018285	0.365236
4.473136e-01	3.373330e-01	22.50	0.019536	0.390230
4.472695e-01	3.362742e-01	24.18	0.020975	0.418975
4.472454e-01	3.355147e-01	25.74	0.022302	0.445488
4.472316e-01	3.349395e-01	27.64	0.023917	0.477746
4.472240e-01	3.345249e-01	29.68	0.025647	0.512296
4.472197e-01	3.342114e-01	32.54	0.028053	0.560348

Table II. Comparison between the current eigenfunctions associated with the non-degenerate modal velocities of the surface (ψ_s) and embedded (ψ_e) conductors with no ground plane.

Figure 5.13 shows the distribution of the non-degenerate modal velocities for three structures: surface and embedded conductors with no ground plane and embedded conductors with a ground plane. As mentioned in previous sections, once the spurious mode is eliminated, all modal velocities must lie between the velocity of a wave traveling in air alone and the velocity of a wave traveling in the substrate material alone. Since $\epsilon_r = 9$, these limits are 1 and 1/3. As noticed in the previous chapter, the ground plane seems to "*slow down*" the propagation of the modes. Indeed, the dominant modes of the embedded structure with no ground plane are faster than the ones with a ground plane.

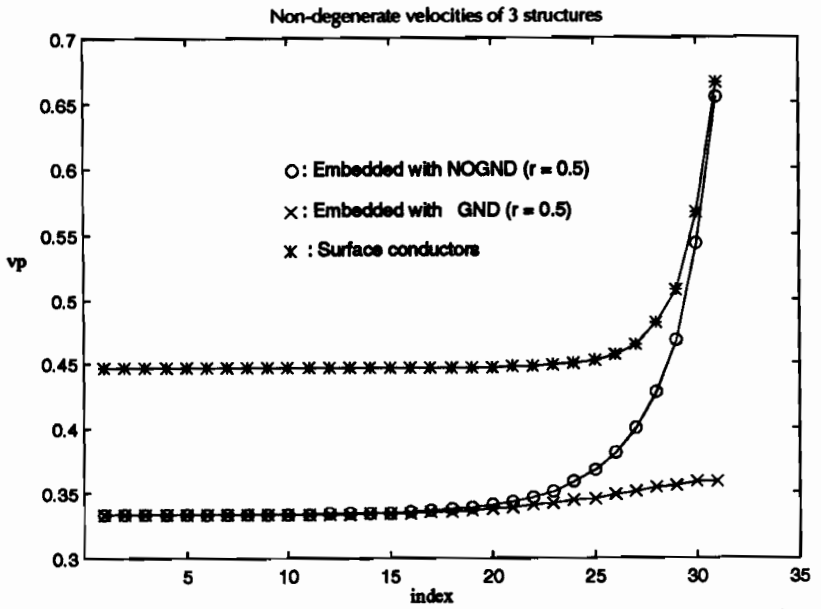

Figure 5.13 Modal velocities of three structures: surface and embedded with no ground plane and embedded with a ground plane. All the structures have $w/h = 10, \epsilon_r = 9$. The embedded ones have $r = 0.5$.

The modes associated with the degenerate modal velocities of the embedded structures are slower than the those of the surface conductors. This behavior was somewhat predictable because, when conductors are placed at the surface, the high-order modes, concentrated around the conductors, travel both in air and in the substrate while those of the embedded structures travel entirely in the substrate. The very fact that the higher-modes are concentrated around the conductors results in having the lower bound of the modal velocities of embedded structures equal to the velocity of a wave traveling in the substrate material alone. What is interesting to note is that the modal velocities of the dominant modes of the embedded structure with no ground plane reach the values of the modal velocities of the surface conductors with no ground plane. Therefore, the *dispersion* of the modes for this structure is the most important one found in all of the structures investigated thus far. Figure 5.14 illustrates the effect of the w/h ratio and ϵ_r on the ratio between the smallest and largest modal velocities for both structures: surface and embedded conductors with no ground plane.

If the analogy with phasor is adopted again, recall from section 4.2.1 that the

surface conductors with no ground plane gives a phase shift between 4° (for $w/h = 1, \epsilon_r = 100$) and 69° (for $w/h = 100, \epsilon_r = 100$), while this structure gives a phase shift between 11° (for $w/h = 1, \epsilon_r = 100$) and 72° (for $w/h = 100, \epsilon_r = 100$).

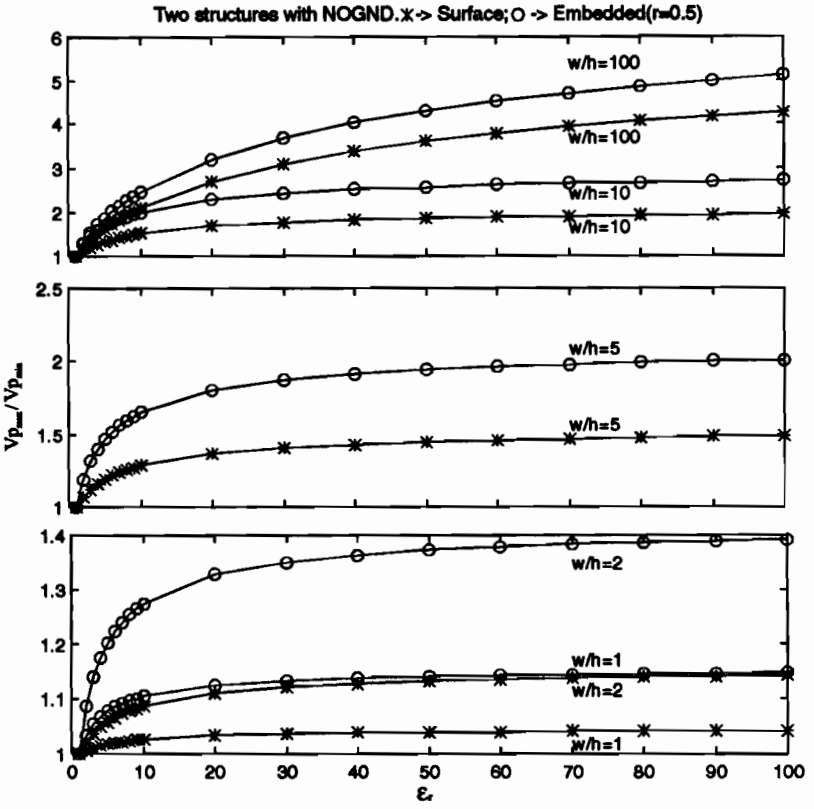

Figure 5.14 The ratio v_{max}/v_{min} as a function of ϵ_r for the surface and embedded ($r = 0.5$) structures with no ground plane.

5.2.2 Effect of the position of the conductors on the eigenvalue spectrum

As for the embedded structure with a ground plane, the effect of the position of the conductors (r) on the eigenvalue spectrum is an important aspect that needs investigation. Figure 5.15 illustrates the modal velocities of this structure where substrate relative permittivity ϵ_r is set to 9, the width of the channel w 10.0 times the substrate thickness h for different values of the position of the conductors r.

In the absence of a ground plane, the structure is symmetric with respect to the center ($r = 0.5$). This behavior is illustrated in Figure 5.15 where it can be seen that the eigenspectrum is identical for r equal to 0.125 and 0.875 (similarly

for $r = 0.75$ and 0.25). Therefore, the lower limit of the spectrum occurs when $r = 0.5$ and the upper limit occurs when r is close to the top or bottom surfaces ($r = 0.9$ or 0.1).

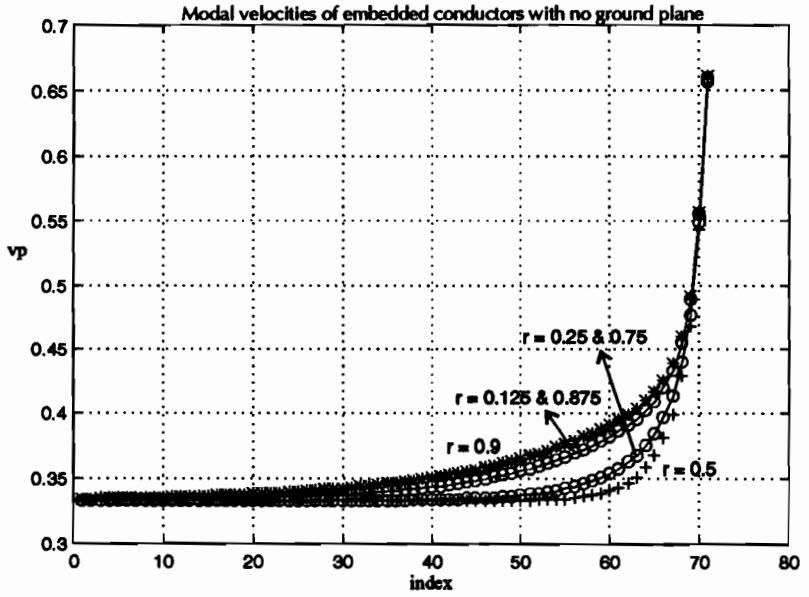

Figure 5.15 Modal velocities of an embedded structure with no ground plane with $w/h = 10, \epsilon_r = 9$ and different values of r.

The interesting and distinctive behavior of this structure is that the ratio between the maximum and minimum modal velocities is almost constant regardless if the conductors are getting closer to the top or bottom surface of the dielectric substrate (as r gets closer to 1 or 0). Figure 5.16 depicts this assertion.

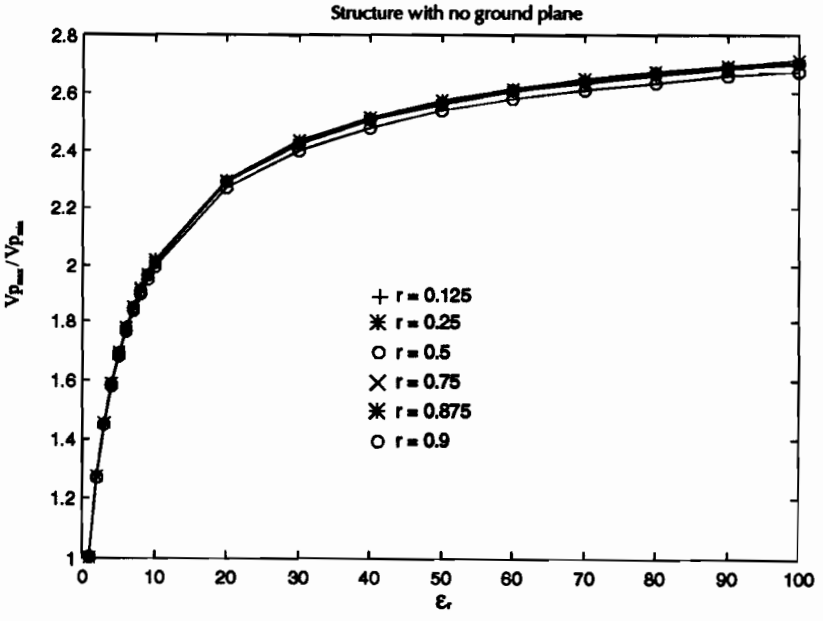

Figure 5.16 The ratio v_{max}/v_{min} as a function of ϵ_r for an embedded structure with $w/h = 10$, for different values of r.

Once again, it is interesting to inquire at which value of r close to 1 the modal velocities of this structure are equal to those of surface conductors with no ground plane. Figure 5.17 illustrates the modal velocities for r set to 0.9, 0.99, 0.999 and 0.9999.

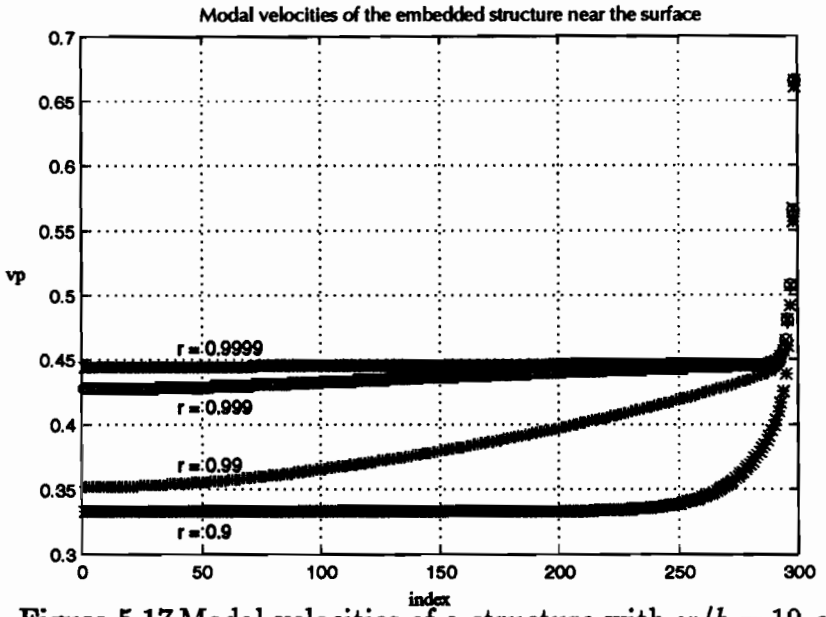

Figure 5.17 Modal velocities of a structure with $w/h = 10, \epsilon_r = 9$ and for $r \geq 0.9$.

Figure 5.17 suggests that the behavior of surface conductors is observed when the position of the conductors is very close to the surface ($r \geq 0.999$). Once again, as for the embedded structure with a ground plane, precautions must be taken while performing numerical quadrature to calculate the self capacitance of a conductor. Indeed, the first integral ($n = 1$) of the summation (equation (5.25)) is singular for $r = 1$. Figure 5.18 illustrates the modal velocities of the structure with surface conductors with no ground plane (using the expression of the Green's function given in Chapter 4) and this structure with r set to 0.9999. The modal velocities of this structure have been obtained using the analytical solution (obtained with a symbolic math package) for the integrals.

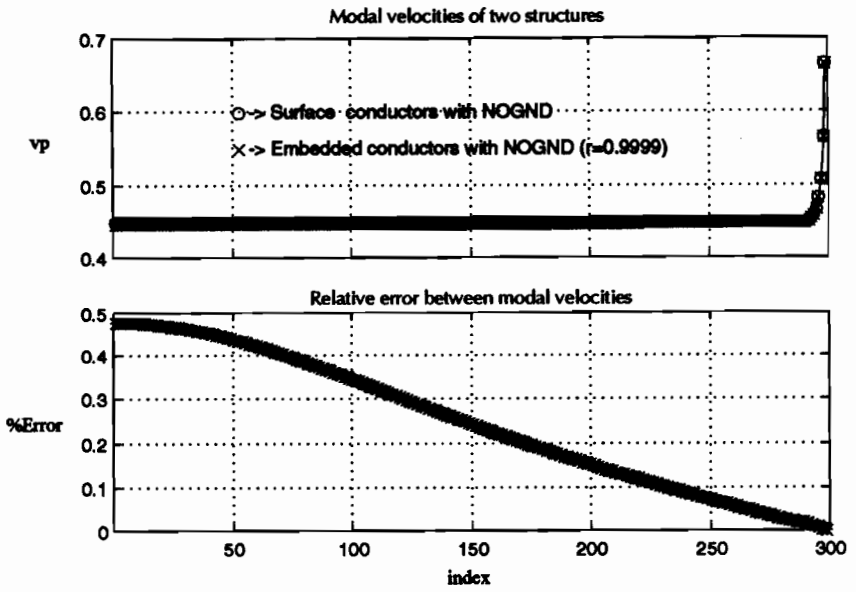

Figure 5.18 Top graph: modal velocities of surface conductors and embedded with $r = 0.9999$. Bottom graph: relative error between the modal velocities.

Obviously, the results are very satisfactory since the maximum relative error (relative to the modal velocities of the surface conductors) is 0.48%. This error is somewhat higher than the relative error (0.16%) obtained for the surface and embedded structures with a ground plane (section 5.1.2), the reason being the numerical stability of the expression of the Green's function in use. Indeed, the expressions of the Green's functions for the structures with a ground plane are of the form $\log(a/b)$. Therefore, as explained in Chapter 2, a computation that adds terms of the form of a dipole is numerically stable; a computation that adds terms due to individual charges, e.g., $\log(a) - \log(b)$ is not. One can overcome this difficulty by considering the alternative form of the Green's function (Chapter 2) of this structure for which special care has been taken in order to express the function in the form of $\log(a/b)$.

Despite the fact that the relative error obtained with the expression given by (5.25) is somewhat higher than the structures with a ground plane, it is still very reasonable. Therefore, as mentioned in Chapter 2, it is possible to use the Green's functions of this structure, given by (5.25) or an alternative more stable form given in Chapter 2, in a single program which accounts for the structure of a

surface and embedded conductors with no ground plane.

5.2.3 Upper and lower estimates of the eigenvalue spectrum for the embedded structure with no ground plane

As in the structure with a ground plane, it will be practical to narrow the interval of the eigenvalue spectrum in order to get an acceptable initial guess of the slowest and fastest modal velocities for a given structure. Those estimates can be used as shifts (in *shifted QR algorithm* or the shifted *inverse power method*) in order to accelerate the convergence of the eigenvalue problem.

As in the case of the embedded structure with a ground plane, the lower estimate of the modal velocity spectrum is already known. For realistic structures ($r \leq 0.9$), the lower modal velocity is equal to the velocity of a wave traveling in the substrate material alone.

In order to get an estimate for the fastest and slowest with $r > 0.9$ modal velocities, the same reasoning found in Chapter 4 (section 4.2.2) can be adopted: by placing the right number of ± 1 in an approximated eigenfunction $\mathbf{V}_{apr}$ and calculating the estimate of the modal velocity by

$$v_{apr} = \sqrt{\frac{1}{\epsilon_r} \frac{\mathbf{V}_{apr}^T \mathbf{P} \mathbf{V}_{apr}}{\mathbf{V}_{apr}^T \mathbf{L} \mathbf{V}_{apr}}}, \tag{5.28}$$

where $\mathbf{P}$ and $\mathbf{L}$ are considered without the leading constants.

For the estimate of the slowest modal velocity (with $r > 0.9$), $\mathbf{V}_{apr}$ is formed with an alternating $+1$ and -1 as entries since the energy is concentrated around the conductors. For the estimate of the fastest modal velocity, $\mathbf{V}_{apr}$ is formed by considering the first odd eigenfunction as a vector containing $+1$ (or -1) the first half of the structure and -1 (or $+1$) the second half.

With regard to a structure with $w/h = 10, \epsilon_r = 9$, Table III compares the relative error between the modal velocity calculated by solving the generalized eigenvalue (v_1) and the modal velocity calculated using (5.28).

As already observed in Figure 5.17, the first modal velocity is very sensitive to the position of the conductors (r). Table III re-demonstrates this behavior. The disappointing observation is that the first modal velocity (slowest, associated with

the least dominant mode) is sensitive also to discretisation. Indeed, for $r = 0.99$, the relative error between 50 finite elements and 300 is 18.6%. For $r = 0.999$, the relative error between the same two discretisations is 3.6% and for $r = 0.9999$, it is 0.4%.

r	Ne	first modal velocity: v_1	Approximated velocity: v_{apr}	Relative error $\lvert(v_1 - v_{apr})\rvert/v_1$
	50	4.174492e-01	4.295685e-01	2.903174e-02
0.99	100	3.958726e-01	4.032699e-01	1.868588e-02
	200	3.677501e-01	3.723864e-01	1.260707e-02
	300	3.520725e-01	3.555438e-01	9.859677e-03
	50	4.436737e-01	4.537143e-01	2.263053e-02
0.999	100	4.403007e-01	4.456433e-01	1.213409e-02
	200	4.339617e-01	4.368551e-01	6.667282e-03
	300	4.280737e-01	4.301315e-01	4.807068e-03
	50	4.468496e-01	4.566428e-01	2.191615e-02
0.9999	100	4.464876e-01	4.515537e-01	1.134662e-02
	200	4.457711e-01	4.483689e-01	5.827777e-03
	300	4.450630e-01	4.468199e-01	3.947517e-03

Table III. Comparison between the slowest modal velocity and the approximated one for a structure with $w/h = 10$, $\epsilon_r = 9$.

Therefore, when conductors need to be placed near the surface ($r > 0.9$), a finer discretisation is recommended. Bear in mind that this behavior is encountered only near the surface, i.e. when the Green's functions of this structure are used to account for the structure of a surface and embedded conductors with no ground plane. For practical embedded structures, r is usually less than or equal to 0.9 ($0.5 \leq r \leq 0.9$ or $0.1 \leq r \leq 0.5$, since the structure is symmetric). In this case, the first modal velocity is completely independent of discretisation and is equal to the velocity of a wave traveling in the substrate material alone.

The relative error between the approximated velocity and the one calculated by solving the generalized eigenvalue is satisfactory for any discretisation, though

it improves with a finer one.

Table IV compares the relative error between the last modal velocity (associated with the dominant mode) calculated by solving the generalized eigenvalue problem (v_{Ne}) and the modal velocity calculated using (5.28). The structure has $w/h = 10, \epsilon_r = 9$.

r	Ne	last modal velocity: v_{Ne}	Approximated velocity: v_{apr}	Relative error $(v_{Ne} - v_{apr})/v_{Ne}$
	50	6.539905e-01	6.352301e-01	2.868594e-02
	100	6.543329e-01	6.352301e-01	2.919431e-02
0.5	200	6.545114e-01	6.352301e-01	2.945896e-02
	300	6.545719e-01	6.352301e-01	2.954877e-02
	400	6.546024e-01	6.352301e-01	2.959398e-02
	50	6.641117e-01	6.463995e-01	2.667052e-02
0.99	100	6.644062e-01	6.463995e-01	2.710191e-02
	200	6.645530e-01	6.463995e-01	2.731694e-02
	300	6.646021e-01	6.463995e-01	2.738873e-02
	50	6.646058e-01	6.468501e-01	2.671618e-02
0.999	100	6.649216e-01	6.468501e-01	2.717844e-02
	200	6.650821e-01	6.468501e-01	2.741316e-02
	300	6.651354e-01	6.468501e-01	2.749116e-02
	50	6.646580e-01	6.468960e-01	2.672356e-02
0.9999	100	6.649775e-01	6.468960e-01	2.719122e-02
	200	6.651415e-01	6.468960e-01	2.743107e-02
	300	6.651968e-01	6.468960e-01	2.751183e-02

Table IV. Comparison between the fastest modal velocity and the approximated one for a structure with $w/h = 10, \epsilon_r = 9$.

It is pleasing to note that, unlike the slowest modal velocity, the fastest one (associated with the dominant mode) is less sensitive to the position of the conductors and discretisation. The fact that it is not too sensitive to the position of the conductors was already observed in Figure 5.15 and 5.17. For $r = 0.5$, the

relative error between the modal velocities obtained with 50 and 400 finite elements is 0.093%. For $r = 0.99$, the relative error between 50 and 300 elements is 0.074%. For $r = 0.999$, the relative error between the same two discretisations is 0.080% and for $r = 0.9999$, it is 0.081%.

The relative error between the approximated velocity and the one calculated by solving the generalized eigenvalue problem can be considered as being constant regardless of the position of the conductors and the discretisation. Despite the fact that it is not so promising ($\simeq 2.8\%$), it can still be considered as an estimate. Note that the approximated velocities are completely insensitive to discretisation.

5.3 STRUCTURE WITH A FINITE DIELECTRIC WIDTH AND WITH NO GROUND PLANE

The electric Green's function of this structure is given by

$$\begin{aligned} G_E(\overline{x};\overline{\xi}) = G_{E1}(\overline{x};\overline{\xi}) + \frac{1}{4\pi\epsilon_1} G_1(\overline{x};\overline{\xi},0) - \frac{1}{4\pi\epsilon_1}\sum_{n=1}^{\infty} K^{2n-1} G_1(\overline{x};\overline{\xi},[n-r]) \\ - \frac{1}{4\pi\epsilon_1}\sum_{n=1}^{\infty} K^{2n-1} G_1(\overline{x};\overline{\xi},[(n-1)+r]) + \frac{1}{4\pi\epsilon_1} 2\sum_{n=1}^{\infty} K^{2n} G_1(\overline{x};\overline{\xi},[n]) \\ + \frac{\epsilon_r(1-\epsilon_r)}{4\pi\epsilon_1}\log(4h^2), \end{aligned} \tag{5.29}$$

where,

$$\begin{aligned} G_{E1}(\overline{x};\overline{\xi}) = -\frac{1}{4\pi\epsilon_1}\Big(\log(\zeta^2) + \epsilon_r \log(4h^2) + \sum_{n=1}^{\infty} K^{2n}\log(n^2+\zeta^2)^2 \\ - \sum_{n=1}^{\infty} K^{2n-1}\log\{[(n-1+r)^2+\zeta^2][(n-r)^2+\zeta^2]\}\Big), \end{aligned} \tag{5.30}$$

and

$$\begin{aligned} G_1(\overline{x};\overline{\xi},\overline{y}) = \sum_{m=1}^{\infty}(-1)^{m+1}K^m \Big(\log\{[m\overline{W}_d + (-1)^m\overline{\xi} - \overline{x}]^2 + \overline{y}^2\} + \\ \log\{[m\overline{W}_d + (-1)^{m+1}\overline{\xi} + \overline{x}]^2 + \overline{y}^2\}\Big). \end{aligned} \tag{5.31}$$

The magnetic Green's function is the same as the one for the embedded structure with no ground plane (section 5.2):

$$G_M(\overline{x};\overline{\xi}) = -\frac{\mu_0}{4\pi}\Big(\log(\zeta^2) + \log(4h^2)\Big), \tag{5.32}$$

where $\zeta = \dfrac{x-\xi}{2h} = \overline{x} - \overline{\xi}$.

Once again, it is preferable to compute the entries of the two matrices **P** and **L** without the leading constants (without $1/4\pi\epsilon_1$ for **P** and $\mu_0/4\pi$ for **L**). The velocity v_i of a given mode i, normalized with respect to the free-space velocity, will then be

$$v_i = \sqrt{\frac{1}{\epsilon_r}\lambda_i}, \tag{5.33}$$

where λ_i is the eigenvalue obtained by solving the generalized eigenvalue problem.

It can be seen from the Green's function of this structure (equation (5.29)) that computing the entries of the matrix **P** is computationally very demanding. Therefore, crafty methods should be adopted in order to accelerate the computation. Evidently, it is inconceivable to use finite elements with orders different than 0 unless a powerful computer is available.

First, notice that the first term of the Green's function ($G_{E1}(\overline{x};\overline{\xi})$), given by (5.30), is the same as the one for the embedded structure. Therefore, it is a Toeplitz matrix. It can be evaluated independently from the remaining terms by computing only the first row of a matrix. After computing another matrix with the remaining terms, it can be added to the Toeplitz matrix.

Second, all integrations can be computed analytically. With order 0 finite elements, this is possible since the generated output files from Maple are in acceptable sizes. Therefore, the computing time to calculate the Toeplitz matrix (using analytical solutions) is negligible (a few seconds for 400 elements). Note that computing analytically non-singular integrals is not more accurate than numerical quadrature. It is nevertheless slightly faster due to the absence of overheads in the program.

Third, the number of terms in the summations, especially the double ones, can be cleverly chosen. Recall from Chapter 4 that the number of terms required for a given accuracy can be obtained by calculating that required for a similar accuracy in the geometric series. Indeed, since the image coefficient K is less than unity and always negative, the resulting alternating series converges faster than the corresponding geometric series. Therefore, the number of terms is calculated as

$$K^n = 10^{-p} \tag{5.34}$$

where p is the required precision. Since $G_{E1}(\overline{x};\overline{\xi})$, given by (5.30), has an index n that runs with a step of 2, therefore, the number of terms ($Nterms$) required for the index n is

$$Nterms = \frac{1}{2}\frac{\log(10^{-p})}{\log(K)}. \tag{5.35}$$

The number of terms required for the index m ($Mterms$) in the second term of the Greens function ($G_1(\overline{x};\overline{\xi},0)$) is consequently $2\times Nterms$. The remaining double summations can therefore have an index m running from 1 to $2\times(Nterms-n)$, where $n = 1\cdots Nterms$. In fact, this is not as complicated as it appears. When the precision p is fixed to 15, the last term of the summations with index n ($K^{2n} = K^{2\times Nterms}$) gives a vanishingly small number. Therefore, there is no need for a second summation with index m ranging from 1 to $2\times Nterms$.

In terms of images, this procedure corresponds to a diamond image representation of charges. The first charge, located at $y = a$ will have $2\times Nterms$ (*infinite* in a numerical sense) image representation throughout the vertical boundaries. The second image ($n = 1$) due to the horizontal boundaries, located at $y = -a$ will have $(2\times Nterms-2)$ images throughout the vertical boundaries. This process will continue until the last two images located at $y = \pm(2\times Nterms\times h + a)$ and with a straight of $K^{2\times Nterms}$. These two images which have very little contribution on the source point, will not have any images throughout the vertical boundaries. Later in this chapter, the effect of the number of images throughout the vertical boundaries (fixed number of images independent of n) will be investigated.

With the three methods outlined, namely: evaluation of two matrices (Toeplitz and remainder), analytical evaluation of integrals and the appropriate number of terms of the summations, the evaluation of each entry of the matrix **P** requires roughly 7 seconds on a 486, 66MHz computer. Since the matrix is no longer Toeplitz, $N^2/2$ (symmetric) entries need to be evaluated. Thus, for 50, 100 and 200 finite elements, it requires 2.4 hours, 9.7 hours and 1.6 days respectively. Exploitation of geometrical symmetries of the problem provides also the

possibility of a decrease of computing time. Nevertheless, this decrease will be relatively insignificant.

Since the resulting matrices **P** and **L** are no longer positive definite, the generalized eigenvalue problem must be solved using the LR decomposition.

5.3.1 Results of generalized eigenvalue problem

For the structure illustrated in Figure 5.19, where substrate relative permittivity ϵ_r is set to 9 and a width of the channel w 10.0 times the substrate thickness h, the position of the conductors r set to 0.5, and the spacing between the vertical boundaries s set to 0.5, the last seven modal function pairs (associated with the non-degenerate eigenvalues) of this structure and those of the embedded structure with infinite dielectric thickness ($s \to \infty$, section 5.2) are illustrated in Figure 5.20.

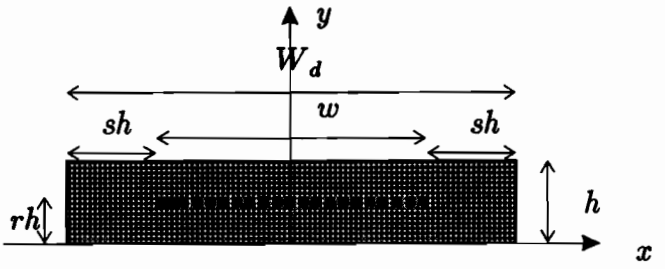

Figure 5.19 Embedded conductors with no ground plane and with a finite dielectric width.

All of the x-axes in Figure 5.20 range between $[-1;1]$ and the y-axes range between $[-0.15;0.15]$. As expected, the eigenfunctions of this structure resemble those of embedded conductors with no ground plane. The distinction of the eigenfunctions is apparent only for the first 3 or 4 dominant modes.

As in the case of the embedded structure with no ground plane, this structure has also (as expected) a spurious mode which must be eliminated.

Table V compares the non-spurious modal velocities and associated current eigenfunctions obtained with this structure (v_r, ψ_r) and with the embedded structure with infinite dielectric width (v_e, ψ_e from section 5.2). The difference between the modal velocities as well as the standard deviation (STD) and the

angle among the eigenfunctions are illustrated.

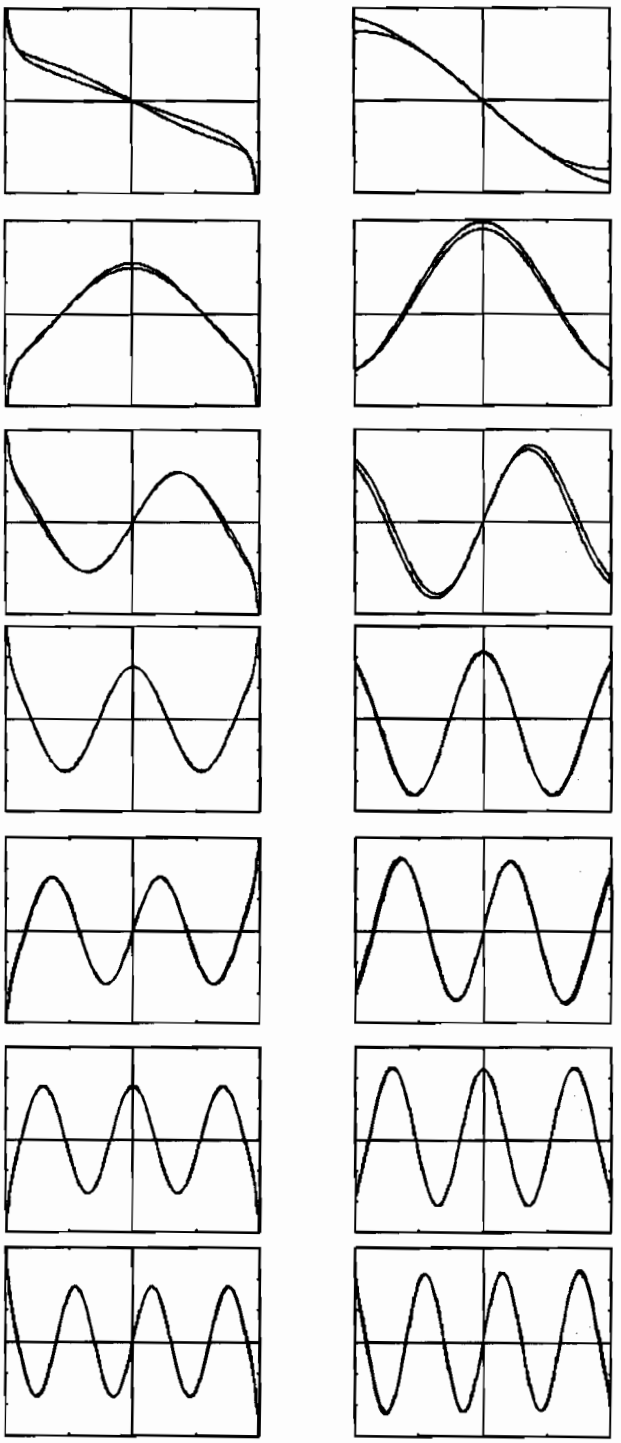

Figure 5.20 The current and potential modal functions associated with the first seven non-degenerate eigenvalues for two embedded structures with no ground plane: finite and infinite dielectric width. Both structures have $w/h = 10, \epsilon_r = 9$ and $r = 0.5$. The structure with finite dielectric width has $s = 0.5$.

Table V suggests that only the first few modal velocities present differences among themselves. The remainder have an insignificant difference and the associated eigenfunctions have a moderate standard deviation. Note that the decrease follows a different rate depending on whether the eigenfunctions are odd or even.

velocity v_r	velocity v_e	difference $v_r - v_e$	angle °	STD $(\psi_r - \psi_e)$
7.291280e-01	6.545114e-01	7.461663e-02	9.91	0.012252
5.516677e-01	5.431740e-01	8.493652e-03	4.34	0.004844
4.753236e-01	4.684141e-01	6.909504e-03	4.79	0.005928
4.303076e-01	4.286675e-01	1.640118e-03	2.07	0.002479
4.015418e-01	3.996625e-01	1.879354e-03	3.39	0.004197
3.820343e-01	3.814794e-01	5.549651e-04	1.53	0.001866
3.685003e-01	3.678071e-01	6.931678e-04	2.67	0.003307
3.588872e-01	3.586541e-01	2.331057e-04	1.29	0.001589
3.520008e-01	3.517053e-01	2.954602e-04	2.25	0.002786
3.470104e-01	3.469007e-01	1.096734e-04	1.17	0.001448
3.433821e-01	3.432452e-01	1.369556e-04	1.99	0.002464
3.407271e-01	3.406718e-01	5.533022e-05	1.12	0.001382
3.387822e-01	3.387151e-01	6.711749e-05	1.83	0.002264
3.373518e-01	3.373225e-01	2.928166e-05	1.10	0.001366
3.362997e-01	3.362654e-01	3.426001e-05	1.74	0.002147
3.355238e-01	3.355077e-01	1.604726e-05	1.12	0.001388
3.349518e-01	3.349338e-01	1.805648e-05	1.69	0.002092
3.345294e-01	3.345203e-01	9.025766e-06	1.17	0.001443
3.342175e-01	3.342078e-01	9.767800e-06	1.69	0.002086

Table V. Comparison between the modal velocities and associated current eigenfunctions for the embedded structure with infinite dielectric width (v_e, ψ_e from section 5.2) and the structure with finite dielectric width (v_r, ψ_r). Both structures have $w/h = 10, \epsilon_r = 9$ and $r = 0.5$. The structure with finite dielectric width has $s = 0.5$.

In order to get an idea on the sensitivity of the modal velocities to discretisation, Table VI compares the fastest and slowest modal velocities of two structures with finite dielectric width: $s = 0.5$ and $s = 2.5$, for two different discretisations. Both structures have $w/h = 10, \epsilon_r = 9, r = 0.5$. The errors are computed relative to the finer discretisation. The slowest modal velocities seem to be insensitive to discretisation with a relative error of 1.68e-5%. On the other hand, the fastest modal velocity, associated with the dominant mode, is more sensitive to discretisation and the spacing s.

s		$Ne = 50$	$Ne = 100$	$Ne = 200$	Relative error
0.5	min	3.333334e-01		3.333333e-01	1.686565e-07
	max	7.280325e-01		7.291280e-01	1.502451e-03
2.5	min	3.333334e-01	3.333333e-01		1.682219e-07
	max	6.969768e-01	6.975135e-01		7.695125e-04

Table VI. Sensitivity of the slowest and fastest modal velocities to discretisation for the embedded structure with finite dielectric width ($w/h = 10, \epsilon_r = 9$ and $r = 0.5$).

When this spacing increases, the fastest modal velocity becomes less sensitive to discretisation.

5.3.2 Effect of the width of the dielectric on the eigenvalue spectrum

It is expected that the difference between the modal velocities of this structure and the structure with an infinite dielectric width will decrease as the spacing between the conductors and the vertical edges (s) increases. The spacing between the conductors and the vertical edges can also be expressed in terms of W_d/w ratio. Indeed, if the problem is centered at the origin, then

$$s = \frac{1}{2h}(W_d - w) = \frac{w}{2h}(W_d/w - 1). \tag{5.36}$$

Figure 5.21 illustrates the modal velocity spectrum of the structure with an infinite dielectric width (section 5.2) and this structure for different values of s. It

can be seen from Figure 5.21 that only the first two or three modal velocities seem to have a difference among themselves, with the largest difference associated with the fastest velocity (associated with the dominant mode). As s increases, this difference decreases. Note that the dominant modes (especially the first one) are faster in this structure (for small s) than in the structure with an infinite dielectric width. This can be explained by the following reasoning. The dominant mode carries enough energy to allow its electric and magnetic fields to reach the air, thus to travel faster. For the structure with infinite dielectric width, the fields travel in the air only from the top and bottom due to the finite thickness of the substrate.

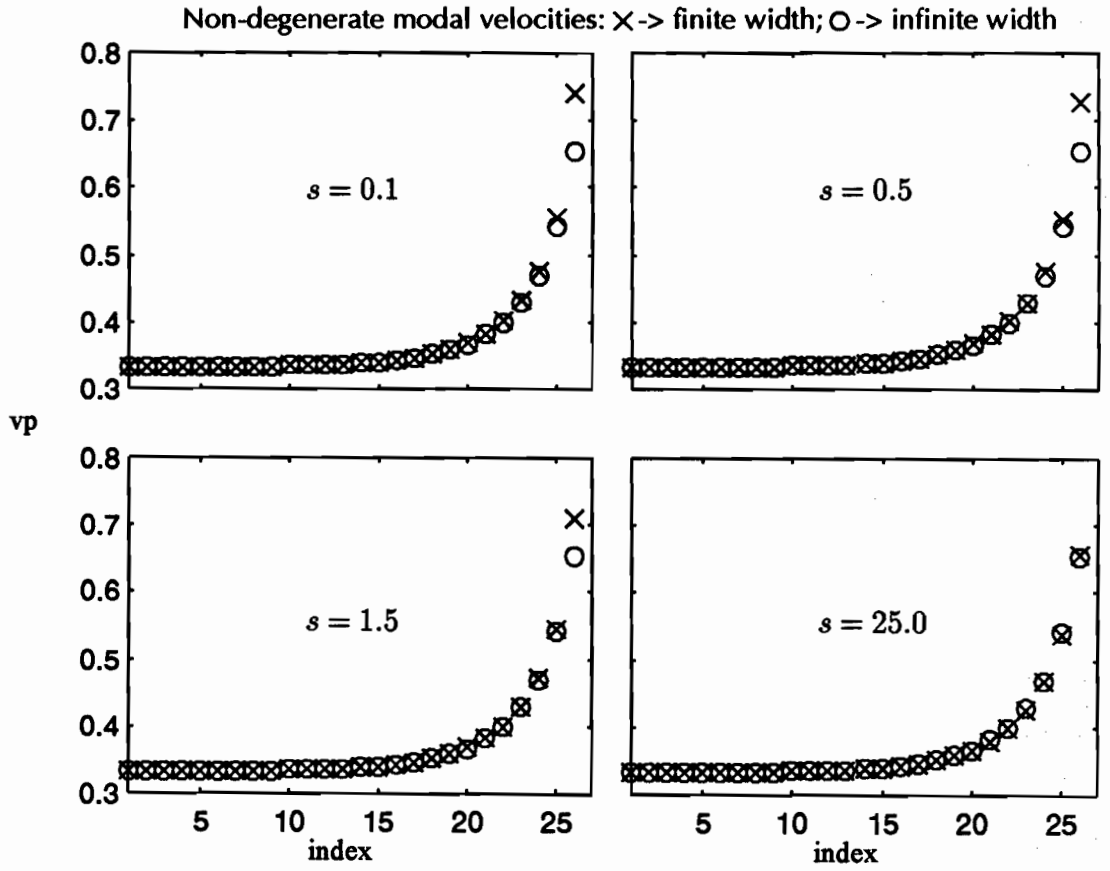

Figure 5.21 The last 26 modal velocities of two embedded structures with no ground plane: finite and infinite dielectric width. Both structures have $w/h = 10, \epsilon_r = 9$ and $r = 0.5$.

In this structure, in addition to the top and bottom, the fields are also in air from the left and right sides of the structure due to the finite width of the substrate. Therefore, the dominant mode has a faster velocity. When the spacing s is relatively small, the second dominant mode is capable also of reaching the air region. As a result, the second modal velocity is slightly faster than the one for the structure with an infinite dielectric width. As mentioned above, the two structures become alike as the spacing s increases.

It is interesting to inquire at which value of s the two structures will have almost equal modal velocities. Figure 5.22 illustrates the largest difference between the modal velocities of the infinite dielectric width structure (section 5.2) and this structure as a function of s.

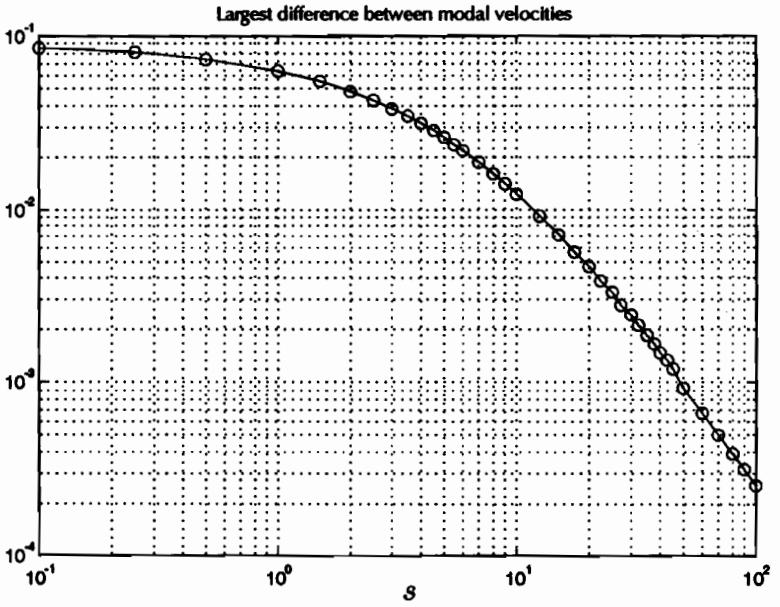

Figure 5.22 The largest difference between the modal velocities as a function of s for the two embedded structures with no ground plane: finite and infinite dielectric width. Both structures have $w/h = 10, \epsilon_r = 9$ and $r = 0.5$.

It is interesting to note that the largest difference does not decrease at a fast rate. Indeed, for $s = 100$, the difference is only 2.7e-4. In some particular applications,

this can be considered insignificant and therefore this structure can be approximated by the structure with infinite dielectric width (section 5.2). Consequently, the computing time for the matrices (block Toeplitz) are negligible due to the simplicity of the expression of the Green's function. In other applications, this difference can be considerable. This requires other clever methods in order to reduce the computing time for the evaluation of the matrix P. The next section gives such a solution.

5.3.3 Effect of the number of images throughout the vertical boundaries

Until now, all the results have been obtained by adopting the diamond image representation described at the beginning of the section. Thus, the indices n of the summations ranged from $n = 1 \cdots Nterms$ and the indices m from $m = 1 \cdots 2 \times (Nterms - n)$. It is interesting to inquire whether there is a fixed number of images throughout the vertical boundaries that will give a reasonable accuracy of the calculated modal velocities. In other words, to seek a constant integer value $Mterms$ (independent from the index n) such that the index m of the inner summation will range from $m = 1 \cdots Mterms$. This corresponds to having a rectangle image representation.

Figure 5.23 illustrates the largest difference between the modal velocities obtained with the diamond image representation and those obtained with a constant value of $Mterms$ ($m = 1 \cdots Mterms$). Obviously, as the number $Mterms$ increases, the difference decreases while the computing time increases. It is very surprising and unexplainable and yet extremely beneficial that the difference is at its smallest when $Mterms$ is equal to 2 or 4. The expected result was to have the largest difference decrease monotonically as $Mterms$ increases. It would probably have been best to compute the largest difference between the modal velocities obtained when $m = 1 \cdots 2 \times Nterms$ and those obtained with $m = 1 \cdots Mterms$ for different values of $Mterms$ less than $2 \times Nterms$. Perhaps the latter experiment would have resulted in the expected monotonic decrease of the largest difference between the modal velocities.

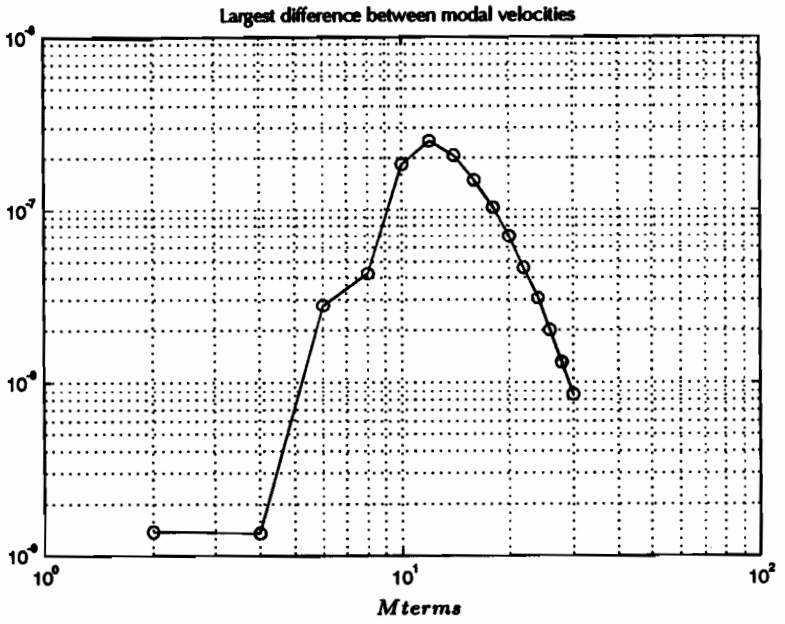

Figure 5.23 The largest difference between the modal velocities as a function of *Mterms*. The structure has $w/h = 10$, $\epsilon_r = 9, r = 0.5$ and $s = 0.5$.

In any case, for any even value of *Mterms* between 2 and 30, the largest difference (obtained for $Mterm = 12$) is less than 2.5e-7 (it is actually 2.486e-7). Therefore, in order to shorten the computing time of the matrix **P**, it is recommended to use two images throughout the vertical boundaries for each image charge (including the *real* charge) throughout the horizontal boundaries.

5.3.4 Approximation to a ribbon cable

As mentioned in Chapter 2, this structure can be used as an approximation of the ribbon cable. There are several kinds of ribbon cables. Figure 5.24 and 5.25 illustrate the photos of two ribbon cables along with a sketch of the contour lines.

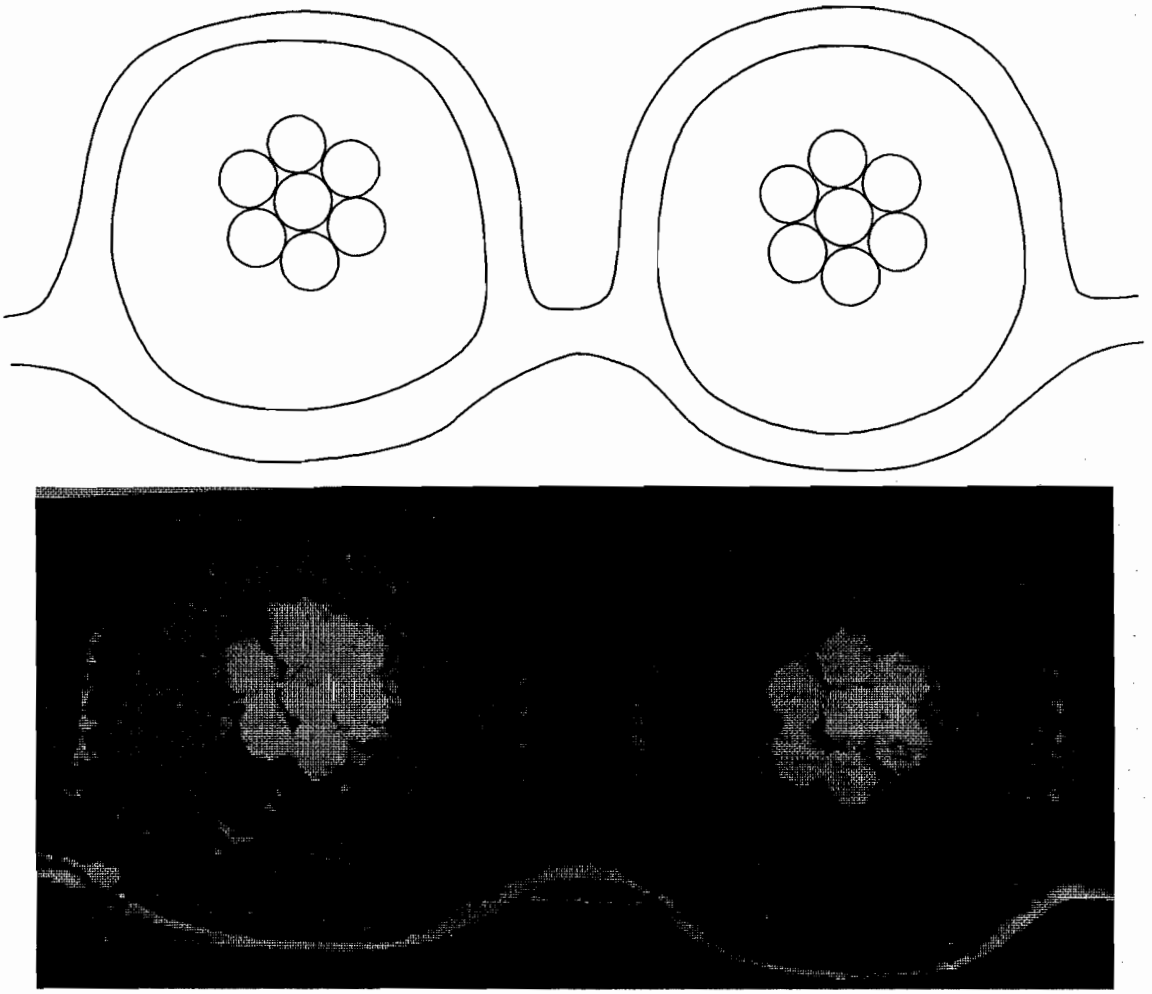

Figure 5.24 *Colored cable:* colored insulated wires placed in an enveloping matrix designed to hold them together.

It is as yet unknown how to calculate the analytical expression of the Green's function of a ribbon cable due to the circular surfaces of the structure. An approximation can be achieved by considering the surfaces as being flat. Therefore, the structure with a finite dielectric width and with no ground plane can be used as an approximation of the ribbon cable. The effect of the circular surfaces on the modal spectrum has yet to be determined, and the results have so far not been compared to this approximation.

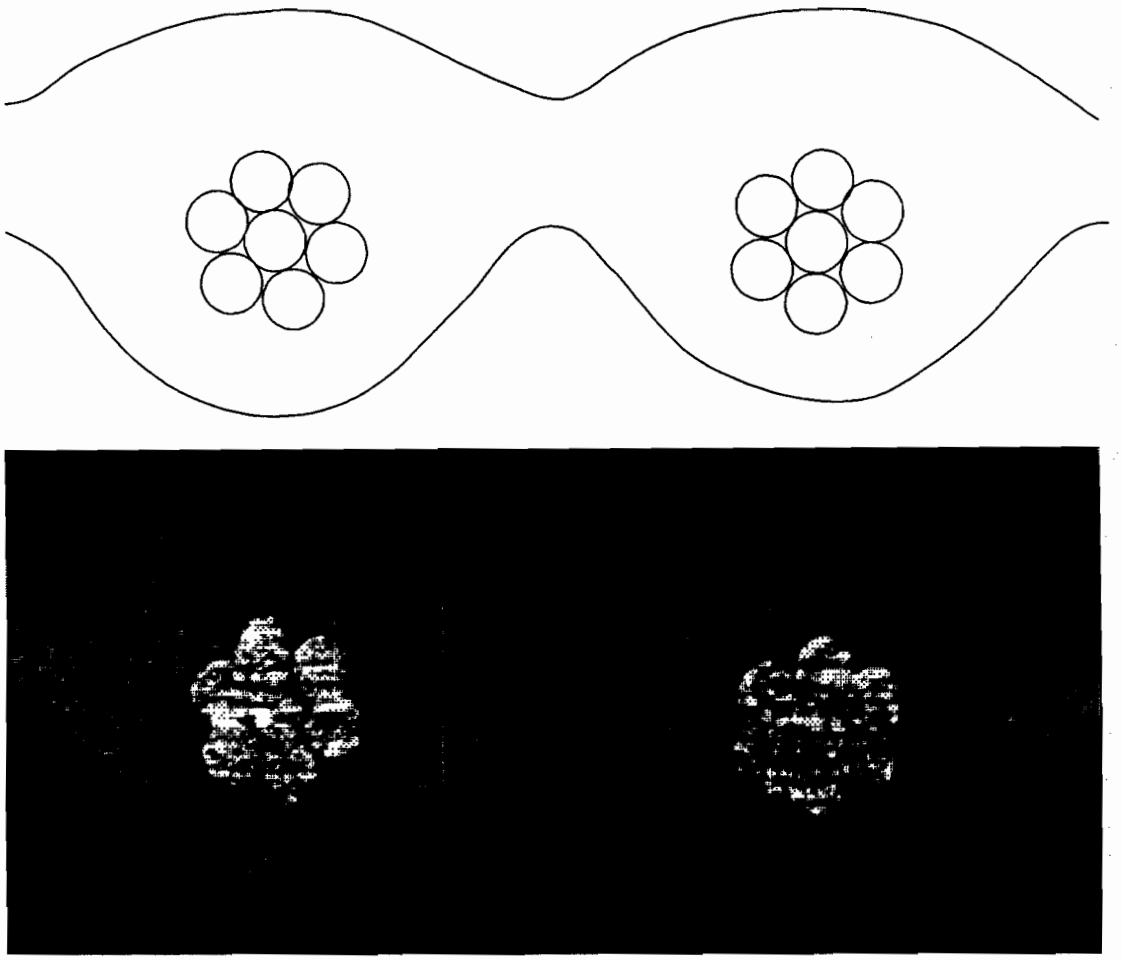

Figure 5.25 *Gray cable:* conductors molded into a single dielectric, suitably shaped.

Paul [1978] has investigated to see if accurate predictions can be achieved by using the multiconductor transmission line model. To this effect, he compared experimental results obtained for a 20 wire ribbon cable with the multiconductor transmission line model. He found that it is possible and the prediction accuracy is within ± 1dB for frequencies for which the line is electrically short (length of

the line $L < \lambda/10$) and ± 6dB for higher frequencies. He investigated several scenarios. In summary, he concluded that in most cases, conductor losses and the insulation dielectric can be neglected. In others, namely for frequencies where the line is electrically long ($L > \lambda/10$), conductor losses can be neglected but wire insulation must be considered. In all experimented scenarios, he found that in order to get an accurate prediction in ribbon cables one must consider interactions between all wires in the cable rather than only the driven wire (generator wire) and the pickup wire (receptor wire).

In this section, the only feature left out is the conductor losses. Indeed, the interaction between all wires and the dielectric are considered. Therefore, probably in most applications, this approximation will prove to be satisfactory. Nevertheless, these conclusions cannot be generalized absolutely, thus further investigations are in order.

CHAPTER 6
CONCLUSION AND FURTHER WORK

The objective of this work was to develop a field theory of propagating TEM modes for a theoretically infinite number of extremely thin conductors on a flat dielectric substrate. It has been shown that electromagnetic energy propagates along multiwire structure in an infinite set of normal modes, each mode having a distinct velocity of its own. Each mode comprises a characteristic current distribution and a characteristic potential distribution. These distributions are bi-orthogonal with respect to power. In other words, no power can be shared between two modes.

The mode functions and velocities depend only on the total conductive material in the structure, rather than on the way conductors are placed in a transmission pathway, cable, or channel. Therefore, they characterize the channel, not the individual wires in it.

The transmission properties, such as crosstalk, of any individual conductor are strongly dependent on the placement of the conductor, and on its relationship to the spectrum of modal functions. Therefore, optimal positions of conductors can be found in order to minimize or even totally eliminate the crosstalk between conductors by selecting positions that coincide with zeros of the current and potential eigenfunctions. Consequently, minimum-crosstalk positions can be located in a structure even if the total number of conductors and their exact placement are unknown.

The existing methods, despite the fact that they give the ability to consider the compatibility problem through all the phases of development of a design, have failed to produce a rigorous method for optimizing the design (reducing the EMI or *crosstalk*) due to the *bottom-up* characteristic. Indeed, any new configuration of the interconnections requires the re-computation of the solution from scratch.

The present work, by taking a field theory viewpoint and a *top-down* approach, can be used for optimization. Indeed, when the modal theory was applied to calculate the crosstalk problem of a multi-line structure, it was shown that optimum positions of conductors can be found in order to reduce the EMI.

Furthermore, the problem needs to be solved once and the results can be used for optimizing the design in order to minimize the EMI for different numbers and positions of conductors.

The modal analysis adopted in this study still requires some work before becoming a powerful optimization method for reducing EMI in transmission lines. In the following, some further work is suggested.

1) In order to calculate the modes only once and use them to optimize a design, one needs to perform a *perturbation* analysis. The word perturbation might be confusing somewhat since what is meant is to reduce the problem from infinite number to a finite number of conductors with gaps in-between. A less encountered definition of such problems is *downdating* (as opposed to *updating*) since the problem is to reduce the original generalized eigenvalue problem

$$\mathbf{A}\mathbf{x} = \lambda \mathbf{B}\mathbf{x} \tag{6.1}$$

to a problem with smaller dimensions

$$\mathbf{A}'\mathbf{x}' = \lambda' \mathbf{B}'\mathbf{x}'. \tag{6.2}$$

Once the eigenfunctions are calculated for the infinite problem, one needs to obtain the new modal functions as well as their corresponding velocities without recomputing the new generalized eigenvalue problem.

2) To produce a rigorous proof that it is always possible (if at all) to realize a network at the end of the line in order to eliminate all reflections of the modes. In order to do so, one needs to prove that the characteristic admittance matrix is diagonally dominant.

3) The behavior of the modes must be analyzed when discontinuities are encountered in multiconductor lines. Typical discontinuities encountered in various levels of packaging are bends (right-angle, T junctions, crossings), stubs, through-hole vias, tapered etches, etc. While circuit theory approach suggests that the current follows the conductor, the modeling of multiline discontinuities poses a

rather difficult and challenging task because one must first solve a complicated electromagnetic field problem. The available experimental data and literature for bends are scarce.

4) Losses in conductors might be of interest to some designers. Therefore, new but similar formulations of the problem must be made to take into account conductor and/or dielectric losses. This can be done rather easily when skin effect is ignored. The formulation will become quite difficult when skin effect has to be taken into consideration.

5) The theory suggested in this work requires the Green's function of a structure under investigation. While it is always possible to compute numerically Green's functions of any structure, it is preferable, where possible, to have an analytical expression of the Green's function of a structure. Due to formation of images, the Green's functions of complicated structures are usually computed in frequency domain which can be done very easily. On the other hand, analytical expression of structures, as for instance a structure with multilayered dielectric, is unknown. Indeed, for N dielectric layers, the Green's function consist of N^2 expressions, each containing $N-1$ infinite series. Therefore, using the method of image theory to obtain the Green's function to more than two or three dielectric layers is impractical. Other methods must therefore be adopted to obtain the Green's function perhaps in a recursive form. Symbolic math packages can be of primary importance in the development of such methods.

APPENDIX A
ALTERNATIVE FORMS OF GREEN'S FUNCTIONS

Speedy and effective numerical work requires isolating the singularity in the electric Green's function so as to permit analytic integration. Several methods are available. The expression adopted in Chapter 2 was

$$G_E(\bar{x};\bar{\xi}) = \frac{1}{2\pi\epsilon_0(\epsilon_r+1)} \log\frac{1+\zeta^2}{\zeta^2} + \frac{1}{2\pi\epsilon_0(\epsilon_r+1)} \sum_{n=1}^{\infty} K^n \log\frac{(n+1)^2+\zeta^2}{n^2+\zeta^2}. \tag{A.1}$$

One, which might be termed the "obvious" way, is arrived at by the following method. Begin by writing out the first few terms:

$$\begin{aligned} G_E(\bar{x};\bar{\xi}) = \frac{1}{2\pi\epsilon_0(\epsilon_r+1)} \Bigg\{ & \log\frac{1+\zeta^2}{\zeta^2} + K\log\frac{4+\zeta^2}{1+\zeta^2} + K^2\log\frac{9+\zeta^2}{4+\zeta^2} \\ & + K^3\log\frac{16+\zeta^2}{9+\zeta^2} + \sum_{k=4}^{\infty} K^k \log\frac{(k+1)^2+\zeta^2}{k^2+\zeta^2} \Bigg\}. \end{aligned} \tag{A.2}$$

Rewrite to expose the structure of this series:

$$\begin{aligned} G_E(\bar{x};\bar{\xi}) = \frac{1}{2\pi\epsilon_0(\epsilon_r+1)} \Bigg\{ & -\log\zeta^2 \\ & + \log(1+\zeta^2) - K\log(1+\zeta^2) \\ & + K\log(4+\zeta^2) - K^2\log(4+\zeta^2) \\ & + K^2\log(9+\zeta^2) - K^3\log(9+\zeta^2) \\ & + K^3\log(16+\zeta^2) \ldots - K^k\log[k^2+\zeta^2] \\ & + K^k\log[(k+1)^2+\zeta^2] - K^{k+1}\log[(k+1)^2+\zeta^2] + \ldots \Bigg\}. \end{aligned} \tag{A.3}$$

Collect like terms:

$$G_E(\bar{x};\bar{\xi}) = \frac{1}{2\pi\epsilon_0(\epsilon_r+1)}\Big\{-\log\zeta^2 + (1-K)\log(1+\zeta^2) + K(1-K)\log(4+\zeta^2) + K^2(1-K)\log(9+\zeta^2) + K^3(1-K)\log(16+\zeta^2) + \ldots + K^{k-1}(1-K)\log(k^2+\zeta^2) + \ldots\Big\}. \tag{A.4}$$

Identifying the typical term, the summation may now be collected into a new form:

$$G_E(\bar{x};\bar{\xi}) = \frac{1}{2\pi\epsilon_0(\epsilon_r+1)}\Big\{-\log\zeta^2 + \sum_{k=1}^{\infty} K^{k-1}(1-K)\log(k^2+\zeta^2)\Big\}. \tag{A.5}$$

Substitute $K = (1-\epsilon_r)/(1+\epsilon_r)$, so that

$$1-K = \frac{1+\epsilon_r}{1+\epsilon_r} - \frac{1-\epsilon_r}{1+\epsilon_r} = \frac{2\epsilon_r}{1+\epsilon_r}, \tag{A.6}$$

hence

$$G_E(\bar{x};\bar{\xi}) = \frac{-1}{2\pi\epsilon_0(\epsilon_r+1)}\log\zeta^2 + \frac{\epsilon_r}{\pi\epsilon_0(\epsilon_r+1)^2}\sum_{k=1}^{\infty} K^{k-1}\log(k^2+\zeta^2). \tag{A.7}$$

In this form the summation is regular everywhere, while the separate leading term contains the entire singularity. If desired, this may be rewritten as

$$G_E(\bar{x};\bar{\xi}) = \frac{-1}{2(1+\epsilon_r)\pi\epsilon_0}\log\zeta^2 + \frac{\epsilon_r}{(1-\epsilon_r^2)\pi\epsilon_0}\Big\{\sum_{k=1}^{\infty} K^k\log(k^2+\zeta^2)\Big\}. \tag{A.8}$$

This form is more attractive, but has the disadvantage that near $\epsilon_r = 1$ it approaches the indeterminate form $0/0$. For practical computation, it is therefore probably less desirable.

Note that in both rewritten forms, the Green's function consists of two parts. The term in braces is always regular, any singularity appears in the first term only. Because K is always negative, the series in braces is an alternating

series. If the series is truncated at N terms the truncation error is therefore always less than the last term included, so it is fairly easy to estimate the required number of terms, and to bound the remaining error.

Table I				
ζ	GE1	Rerror of GE1	GE2	Rerror of GE2
0.20	2.505299e+00	7.733781e-11	2.505299e+00	4.966391e-08
0.60	7.091113e-01	2.732217e-10	7.091114e-01	1.754642e-07
1.20	1.429784e-01	1.354837e-09	1.429786e-01	8.702426e-07
2.00	2.738551e-02	7.070786e-09	2.738564e-02	4.543693e-06
3.00	8.230219e-03	2.350970e-08	8.230344e-03	1.512013e-05
4.20	3.745420e-03	5.159266e-08	3.745545e-03	3.323000e-05
5.60	2.036807e-03	9.467499e-08	2.036931e-03	6.111986e-05
7.20	1.214645e-03	1.582671e-07	1.214770e-03	1.025259e-04
9.00	7.716514e-04	2.480338e-07	7.717758e-04	1.614641e-04
11.00	5.143892e-04	3.698592e-07	5.145137e-04	2.423801e-04
13.20	3.563007e-04	5.297490e-07	3.564253e-04	3.502334e-04
15.60	2.546856e-04	7.335922e-07	2.548103e-04	4.905297e-04
18.20	1.869125e-04	9.868600e-07	1.870375e-04	6.693498e-04
21.00	1.402874e-04	1.294266e-06	1.404125e-04	8.933831e-04
24.00	1.073510e-04	1.659410e-06	1.074764e-04	1.169965e-03

Table I Relative error for different expressions of the Green's function.

Perhaps surprisingly, the rewritings (A.5) and (A.8) are numerically less stable than the form (A.1). This is readily demonstrated numerically. Table I shows the results of a numerical experiment, in which values of the expressions (A.1) and (A.5) are computed without the leading constants $(1/(2\pi\epsilon_0(\epsilon_r+1))$. Here $\epsilon_r = 9$, so the series was carried out to a conservative 80 terms. GE1 is the value obtained by the more accurate representation (A.1); it has been checked by multi-precision computation and is believed correct to all figures tabulated. GE2 is

computed by the less robust series (A.5). The relative errors of both expressions are with respect of the result calculated using 160 terms double precision. Most interestingly, both these series give the same results, to within about ± 3 in the low-order digit. At close distances, where the lateral distance amounts to a few substrate thicknesses, four or five correct significant figures are obtained. As the distance increases, accuracy degrades.

The reason for accuracy loss is clear enough. In essence, the A.1 representation is a summation of dipoles, hence suffers little from cancellation error. The A.5 representation consists of two separately computed logarithmic terms. The logarithmic terms are of similar size but opposite sign, so the error in the result is dominated by the subtraction error in the two logarithmic potentials. The clear conclusion is that the sum-of-dipoles form (A.1) is much to be preferred.

APPENDIX B
Maple program for integration through line singularities

```
#   Electric Green's function integrals: Line-singular terms
#
# Calculates the general projection integrals
#
#                          (k+1)^2 + (wk z)^2
#    int( pm(u) pn(v) log ------------------ )
#                           k^2 + (wk z)^2
#
# between limits  -1 < u < +1 and   -1 < v < +1.  Here
# pm(u) and pn(v) are polynomials of order N,
#
#    pm(u) = a0 + a1 u + ..., aN u^N,
#
# similarly for v with coefficients b0, ..., bN.
#
#  Output is in C version which appears in GREENn.C (optimized);
#
# The FINAL RESULT MUST BE MULTIPLIED BY wk^2/2
#
# Notation:
# rk  is the mid-point of the two integration ranges.
# wk  is the width of both ranges (range in u).
# N   is the maximum power of u and v.
#
   restart;
    N := 5;

    pm := a0;
    pn := b0;
```

```
    for i from 1 to N do
        pm := pm + a.i * (u)^i;
        pn := pn + b.i * (v)^i;
    od:

#
    u  := (et + zt) :
    v  := (et - zt) :
    pmpn := collect(expand(pm * pn), et):
#
# Integrate with respect to et; left right halves separately.
# Then collect powers of zt.
#
    F := simplify(subs(zt=-zt,pmpn)):
    F := int(F,    et=-1+zt..1-zt):
    F := int(pmpn, et=-1+zt..1-zt) + F:
    pmpn := 0:
    F  := collect(expand(F), zt):
    for i from 2*(N+1) by -1 to 0 do
       cF[i] := coeff(F,zt,i);
    od;
    F:=0:
#
# Integrate with respect to zt, taking each power in turn.
#
    intg := 0:
    for i from 0 to 2*(N+1) do
       if (cF[i] <> 0) then
             temp := int(zt^i*ln(((k+1)^2+(wk*zt)^2)/(k^2+(wk*zt)^2)),
                                              zt=0..1):
             intg := intg + cF[i] * temp:
       fi
    od:
```

```
# Collect like powers of log(wk), produce output files

    temp := collect(expand(coeff(intg,ln(wk),1)),wk)*ln(wk):
    intg := temp + collect(expand(coeff(intg,ln(wk),0)),wk):

    readlib(C);
    C([GreenE=intg], filename=GREEN.N.`.C`, optimized);
    intg := 0:
#
# Put a delimiter in the program to distiguish the case where k = 0
#
    delim:=delimdelimdelimdelimdelimdelim;

    C([delim=delim],filename=GREEN.N.`.C`);
#
#  Now let's do the same thing with k = 0
#
    intg0 := 0:
    k := 0;
    for i from 0 to 2*(N+1) do
       if(cF[i] <> 0) then
           temp := int(zt^i*ln(((k+1)^2+(wk*zt)^2)/(k^2+(wk*zt)^2)),
                                          zt=0..1):
           intg0 := intg0 + cF[i] * temp:
       fi:
    od:

#
    readlib(C);
    C([GreenE0=intg0], filename=GREEN.N.`.C`, optimized);

    intg0 := 0;
    temp := 0;
```

BIBLIOGRAPHY

E.E. Antonova and P.P Silvester: "Finite element analysis of resonance shift in piezoelectric crystals," *COMPEL - Second International Workshop on Finite Element Methods for Electromagnetics,* vol. 13, Supplement A, pp. 277–282, 1994.

K. Araki and Y. Naito: "Upper bound calculations on capacitance of microstrip line using variational method and spectral domain approach," *IEEE Transactions on Microwave Theory and Techniques*, vol. **MTT–26**, pp. 506–509, 1978.

K.J. Binns and P.J. Lawerson: *Analysis and Computation of Electric and Magnetic Field Problems,* (2nd ed.). Oxford, New York, Pergamon Press, 1973.

J.A. Brando Faria: *Multiconductor transmission–line structures. Modal Analysis Techniques.* New York: Wiley, 1994.

F.H. Branin, Jr.: "Transient analysis of lossless transmission lines," *Proceedings of the IEEE*, vol. 55, pp. 2012–2013, 1967.

J.R. Brews: "Characteristic impedance of microstrip lines," *IEEE Transactions on Microwave Theory and Techniques*, vol. **MTT–35**, pp. 30–34, 1987.

T.G. Bryant and J.A. Weiss: "Parameters of microstrip transmission lines and of coupled pairs of microstrip lines," *IEEE Transactions on Microwave Theory and Techniques*, vol. **MTT–16**, pp. 1021–1027, 1968.

I. Catt: "Crosstalk (Noise) in digital systems," *IEEE Transactions on Electronic Computers*, vol. **EC–16**, pp. 743–763, 1967.

G. Cerri, R. De Leon, V. M. Primiany and A. Schiavoni: "FDTD analysis of crosstalk in multilayer printed circuits," *International Journal of Numerical Modeling: Electronic Networks, Devices and Fields*, vol. 7, pp. 209–221, 1994.

R.E. Collin: *Field theory of guided waves,* 2d ed., IEEE Press, New York: 1991.

P.J.B. Clarricoats and K.R. Slinn: "Numerical solution of waveguide–discontinuity problems," *Proceedings IEE*, vol. 114, no. 7, pp. 878–886, 1967.

R. Crampagne, M. Ahmadpanah and J.L. Guiraud: "A simple method for determining the Green's function for a large class of MIC lines having multilayered dielectric structures," *IEEE Transactions on Microwave Theory and Techniques*, vol. **MTT–26**, no. 2, pp. 82–87, 1978.

A. El–Zein, S. Chowdhury: "An analytical method for finding the maximum crosstalk in lossless–coupled transmission lines," *IEEE/ACM International Conference on Computer–aided Design. Digest of technical papers,* pp. 443–448, 1992.

A. Farrar and A.T. Adams: "Multilayer microstrip transmission line," *IEEE Transactions on Microwave Theory and Techniques*, vol. **MTT–22**, pp. 889–891, 1974.

S. Frankel: *Multiconductor transmission line analysis.* Dedham, Mass.: Artech House, 1977.

A.S. Goel: *Hish–speed VLSI interconnections. Modeling, analysis and simulation.* New York: Wiley, 1994.

S.L. Handy and J.L. Barlow: "Numerical solution of the eigenproblem for banded, symmetric Toeplitz matrices," *SIAM Journal on Matrix Analysis and Applications*, vol. 15, no. 1, pp. 205–214, 1994.

R.J. Hannemann, A.D. Krauss and M. Pecht: *Physical architecture of VLSI systems.* New York: Wiley, 1994.

M. Horno: "Quasistatic characteristic of microstrip on arbitrary anisotropic substrates," *Proceedings of the IEEE*, vol. 68, no. 8, pp. 1033–1034, 1980.

D. Kahaner, C. Moler and S. Nash: *Numerical methods and softwares.* New Jersey: Prentice Hall, 1977.

R.L. Khan and G.I. Costache: "Consideration on modelling crosstalk on printed circuit boards," *IEEE International Symposium on Electromagnetic Compatibility*, pp. 279–281, 1987.

R.L. Khan and G.I. Costache: "Finite element method applied to modeling crosstalk problems on printed circuit boards," *IEEE Transactions on Electromagnetic Compatibility*, vol. 31, no. 1, pp. 5–15, 1989.

P.I. Kuznetsov and R.L. Stratonovich: *The propagation of electromagnetic waves in multiconductor transmission lines.* [1F.F. Kelleher, trans.] Oxford: Macmillan, 1964.

D.N. Ladd and G.I. Costache: "SPICE simulation used to characterize the cross-talk reduction effect of additional tracks grounded with vias on printed circuits boards," *IEEE Transactions on Circuits and Systems II: Analog and digital signal processing*, vol. 39, no. 6, pp. 342–347, 1992.

R. Laroussi and G.I. Costache: "Finite element method applied to EMC problems," *IEEE Transactions on Electromagnetic Compatibility*, vol. 35, no.2, pp. 178–184, 1993.

K.D. Marx: "Propagation modes, equivalent circuits, and characteristic terminations for multiconductor transmission lines with inhomogeneous dielectrics," *IEEE Transactions on Microwave Theory and Techniques*, vol. **MTT–21**, pp. 450–457, 1973.

G.L. Mattaei, L. Young, and E.M.T. Jones: *Microwave filters: impedance-matching networks, and coupling structures.* New York: McGraw–Hill, 1964.

L. Monroe, C.R. Paul and D.H. Colvin: "Lumped circuit modeling of transmission lines," *IEEE International Symposium on Electromagnetic Compatibility*, pp. 282–286, 1985.

H.W. Ott: "Ground– A path for current flow," *IEEE International Symposium on Electromagnetic Compatibility*, pp. 167–170, 1979.

H.W. Ott: "Digital circuit grounding and interconnection," *IEEE International Symposium on Electromagnetic Compatibility*, pp. 292–297, 1981.

H.W. Ott: "EMC education– The missing link," *IEEE International Symposium on Electromagnetic Compatibility*, pp. 359–361, 1981.

H.W. Ott: *Noise reduction techniques in electronic systems*, 2nd edition, New York: Wiley, 1988.

B.N. Parlett: *The symmetric eigenvalue problem.* Englewood Cliffs, N.J. : Prentice-Hall, 1980.

C.R. Paul and A.E. Feather: "Computation of the transmission line inductance and capacitance matrices from the generalized capacitance matrix," *IEEE Transactions on Electromagnetic Compatibility*, vol. **EMC**–18, pp. 175–183, 1976.

C.R. Paul: "Prediction of crosstalk in ribbon cables," *IEEE Transactions on Electromagnetic Compatibility*, vol. **EMC**–20, pp. 36–43, 1978.

C.R. Paul: "Solution of the transmission line equations for three conductor lines in homogeneous media," *IEEE Transactions on Electromagnetic Compatibility*, vol. **EMC**–20, pp. 216–222, 1978.

C.R. Paul: "On the superposition of inductive and capacitive coupling in crosstalk-prediction models," *IEEE Transactions on Electromagnetic Compatibility*, vol. **EMC**–24, no. 3, pp. 335–343, 1982.

C.R. Paul and W.W. Everett: "Printed circuit board crosstalk," *IEEE International Symposium on Electromagnetic Compatibility*, pp. 452–459, 1985.

C.R. Paul: "A simple SPICE model for coupled transmission lines," *IEEE International Symposium on Electromagnetic Compatibility*, pp. 327–333, 1988.

C.R. Paul: "Modeling electromagnetic interference properties of printed circuit boards," *IBM J. Research and Development*, vol. 33, pp. 33–50, 1989.

C.R. Paul: "Literal solutions for time-domaine crosstalk on lossless transmission lines," *IEEE Transactions on Electromagnetic Compatibility*, vol. **EMC**–34, no. 4, pp. 433–444, 1992.

C.R. Paul: *Analysis of multiconductor transmission lines.* New York: Wiley, 1994.

L.A. Pipes: "Matrix theory of multiconductor transmission lines," *Philosophical Magazine*, vol. 24, pp. 97–113, 1937.

G.N. Polozhii: *The method of summary representation for numerical solution of problems of mathematical physics.* Oxford, New York, Pergamon Press, 1965.

W.H. Press, S.A. Teukolsky, W.T. Vetterling and B.P. Flannery: *Numerical recipies in C: the art of scientific computing.* 2nd edition, Cambridge: Cambridge University Press, 1992.

S. Ramo, J.R. Whinnery and T. Van Duzer: *Fields and waves in communication electronics.* 2nd edition, New York: Wiley, 1984.

F. Rellich, assisted by J. Berkowitz: *Perturbation theory of eigenvalue problems.* New York , Gordon and Breach, 1969.

A.E. Ruehli: "Inductance calculations in complex integrated circuit environment," *IBM J. Research and Development*, vol. 16, no. 5, pp. 470–481, 1972.

A.E. Ruehli and P.A. Brennan: "Efficient capacitance calculations for three dimensional multiconductor systems," *IEEE Transactions on Microwave Theory and Techniques*, vol. **MTT–21**, no. 2, pp. 76–82, 1973.

A.E. Ruehli: "Equivalent circuit models for three dimensional multiconductor systems," *IEEE Transactions on Microwave Theory and Techniques*, vol. **MTT–22**, no. 3, pp. 216–221, 1974.

A.E. Ruehli and P.A. Brennan: "Capacitance models for integrated circuit metallization wires," *IEEE Journal of Solid-state Circuits*, vol. **SC–10**, no. 6, pp. 530–536, 1975.

A.E. Ruehli: "Survey of computer-aided electrical analysis of integrated circuit interconnections," *IBM J. Research and Development*, vol. 23, no. 6, pp. 626–639, 1979.

L.P. Schmidt and T. Itoh: "Spectral domain analysis of dominant and higher order modes in fin-lines," *IEEE Transactions on Microwave Theory and Techniques*, vol. **MTT–28**, pp. 981–985, 1980.

K.J. Scott: *Practical simulation of printed circuit boards and related structures.* New York: Wiley, 1994.

P.P. Silvester: "Modal network theory of skin effect in flat conductors," *Proceedings of the IEEE*, vol. 54, no. 9, pp. 1147–1151, 1966.

P.P. Silvester: "Dynamic resistance and inductance of slot-embedded conductors," *IEEE Transactions on Power Apparatus and Systems*, vol. **PAS-87**, no. 1, pp. 250–256, 1968.

P.P. Silvester: "The accurate calculation of skin effect in conductors of complicated shape," *IEEE Transactions on Power Apparatus and Systems*, vol. **PAS-87**, no. 3, pp. 735–742, 1968.

P.P. Silvester: "TEM wave properties of microstrip transmission lines," *Proceedings IEE*, vol. 115, no. 1, pp. 43–48, 1968.

P.P. Silvester: "Skin effect in multiple and polyphase conductors," *IEEE Transactions on Power Apparatus and Systems*, vol. **PAS-88**, no. 3, pp. 231–238, 1969.

P.P. Silvester and M.S. Hsieh: "Projective solution of integral equations arising in electric and magnetic field problems," *Journal of Computational Physics*, vol. 8, pp. 73–82, 1971.

P.P. Silvester and P. Benedek: "Equivalent capacitances of microstrip open circuits," *IEEE Transactions on Microwave Theory and Techniques*, vol. **MTT–20**, no. 8, pp. 511–516, 1972.

P.P. Silvester and P. Benedek: "Equivalent capacitances for microstrip gaps and steps," *IEEE Transactions on Microwave Theory and Techniques*, vol. **MTT–20**, no. 11, pp. 729–733, 1972.

P.P. Silvester and P. Benedek: "Microstrip discontinuity capacitances for right-angle bends, T junctions, and crossings," *IEEE Transactions on Microwave Theory and Techniques*, vol. **MTT–21**, no. 5, pp. 341–346, 1973.

P.P. Silvester and K.K. Chan: "Analysis of antenna structures assembled from arbitrarily located straight wires," *Proceedings IEE*, vol. 120, no. 1, pp. 21–26, 1973.

P.P Silvester, A. Konrad, J.L. Coulomb and J.C. Sabonnadiere: "Modal network representation of slot-embedded conductors," *Electric Machines and Electromechanics: An international quarterly*, vol. 1, pp. 107–122, 1977.

P.P. Silvester and R.L. Ferrari: *Finite Elements for Electrical Engineers*, 2nd edition, Cambridge: Cambridge University Press, 1990.

P.P. Silvester: "Computer algebra in finite element software construction," *International Journal for Applied Electromagnetics in Materials*, vol. 3, pp. 169–177, 1992.

P.P. Silvester and V.S. Chamlian: "Symbolic generation of finite elements for skin–effect integral equations," *IEEE Transactions on Magnetics*, vol. 30, pp. 3594–3597, 1994.

P.P. Silvester and V.S. Chamlian: "TEM modes in parallel–line transmission structures," *IEEE Transactions on Electromagnetic Compatibility*, vol. **EMC–37**, no. 3, pp. 384–391, 1995.

J.P. Simpson, R.R. Goulette and G.I. Costache: "Radiation from microstrip lines," *IEEE International Symposium on Electromagnetic Compatibility*, pp. 340–343, 1988.

C.E. Smith and R.S. Chang: "Microstrip transmission line with a finite-width dielectric," *IEEE Transactions on Microwave Theory and Techniques*, vol. **MTT–28**, no. 2, pp. 90–94, 1980.

I. Stakgold: *Boundary value problems of mathematical physics.* New York: Macmillan, 1967.

G.W. Stewart: "On the sensitivity of the eigenvalue problem $Ax = \lambda Bx$," *SIAM Journal on Numerical Analysis*, vol. 9, no. 4, pp. 669–686, 1972.

G.W. Stewart: *Introduction to matrix computation.* New York: Academic press, 1973.

D. Szyld: "Criteria for combining inverse and Raleigh quatient iteration," *SIAM Journal on Numerical Analysis*, vol. 25, no. 6, pp. 1369–1375, 1988.

T. Itoh and R. Mittra: "Spectral domain approach for calculating the dispersion characteristics of microstrip lines," *IEEE Transactions on Microwave Theory and Techniques* (short papers), vol. **MTT–21**, pp. 496–499, 1973.

T. Itoh (Edited by): *Planar Transmission Line Structures.* New York: IEEE Press. 1987.

W. Thomson: "On peristaltic induction by electric currents," *Proceedings of the Royal Society of London*, vol. 8, pp. 121–132, 1856. [Reprinted in: Lord Kelvin (Sir William Thomson), *Mathematical and Physical Papers*, vol. 2, pp. 79–91. Cambridge: Cambridge University Press, 1884.]

W.F. Trench: "Numerical solution of the eigenvalue problem for Hermitian Toeplitz matrices," *SIAM Journal on Matrix Analysis and Applications*, vol. 10, no. 2, pp. 135–146, 1989.

W.F. Trench: "Interlacement of the even and odd spectra of real symmetric Toeplitz matrices," *Linear Algebra and its Applications*, vol. 195, pp. 59–68, 1993.

D.S. Watkins: *Fundamentals of matrix computation.* New York: Wiley, 1991.

W.T Weeks: "Calculation of coefficients of capacitance of multiconductor transmission lines in the presence of a dielectric interface," *IEEE Transactions on Microwave Theory and Techniques*, vol. **MTT–18**, no. 1, pp. 35–43, 1970.

C. Wei, R.F. Harrington, J.R. Mautz and T.K. Sarkar: "Multiconductor transmission lines in multilayered dielectric media," *IEEE Transactions on Microwave Theory and Techniques*, vol. **MTT–32**, no. 4, pp. 439–449, 1984.

L. Weinberg: *Network analysis and synthesis.* New York: McGraw–Hill, 1962.

A. Wexler: "Solution of waveguide discontinuities by modal analysis," *IEEE Transactions on Microwave Theory and Techniques*, vol. **MTT–15**, pp. 508–517, 1967.

H.A. Wheeler: "Transmission–line properties of parallel wide strips by conformal–mapping approximation," *IEEE Transactions on Microwave Theory and Techniques*, vol. **MTT–12**, pp. 280–289, 1964.

H.A. Wheeler: "Transmission–line properties of parallel strips by separated by dielectric sheet," *IEEE Transactions on Microwave Theory and Techniques*, vol. **MTT–13**, pp. 172–185, 1965.

H.A. Wheeler: "Transmission–line properties of a strip on a dielectric sheet on a plane," *IEEE Transactions on Microwave Theory and Techniques*, vol. **MTT–25**, no. 8, pp. 631–647, 1977.

J.H. Wilkinson: *The algebraic eigenvalue problem.* Oxford: Clarendo press, 1965.